TESIS DE LA UNIVERSIDAD
DE ZARAGOZA

2018

5

Eduardo Sánchez Burillo

One-dimensional few-photon scattering: Numerical and analytical techniques

Departamento

Física de la Materia Condensada

Director/es

Zueco Lainez, David
Martín Moreno, Luis

ISSN 2254-7606

Prensas de la Universidad
Universidad Zaragoza

Servicio de Publicaciones

ISSN 2254-7606

Tesis Doctoral

ONE-DIMENSIONAL FEW-PHOTON SCATTERING: NUMERICAL AND ANALYTICAL TECHNIQUES

Autor

Eduardo Sánchez Burillo

Director/es

Zueco Lainez, David
Martín Moreno, Luis

UNIVERSIDAD DE ZARAGOZA
Física de la Materia Condensada

2017

One-dimensional few-photon scattering: Numerical and analytical techniques

Colección de Estudios de Física
Vol. 140

Esta colección recoge las tesis presentadas en el Departamento de Física de la Materia Condensada de la Universidad de Zaragoza desde su constitución en 1987.

Colección de Estudios de Física Vol. 140

One-dimensional few-photon scattering: Numerical and analytical techniques

Eduardo Sánchez Burillo

1542
Prensas de la Universidad
Universidad Zaragoza

Aquí va la hoja de créditos.

A mis padres

Contents

Abstract

In this thesis, we have studied few-photon scattering in waveguide quantum electrodynamics (waveguide QED), where photons propagate through a one-dimensional medium interacting with some scatterers, such as two-level atoms.

The methods we use to tackle these problems are explained in Chap. 2. We have applied for the first time the numerical technique of matrix-product states (MPS) to this field. Besides, we have used previously known analytical methods, such as the input-output formalism.

We have characterized the spectrum of archetypical models of waveguide QED in Chap. 3, both in the rotating-wave approximation (RWA) and in the ultrastrong-coupling regime. These models support bound states, in which photonic excitations are confined around the scatterers. These states are essential for understanding some dynamical properties. We illustrate this by studying the spontaneous decay of a two-level atom in the RWA.

We have determined some analytical properties of the scattering matrix in Chap. 4, the most important mathematical object in this field. In particular, we have shown that the cluster-decomposition principle for the scattering amplitudes, which arises in quantum field theories because those are relativistic, also holds in our case, even though we are dealing with nonrelativistic models. We have generalized the cluster principle to scatterers with memory, finding the structure of the scattering matrix compatible with this principle. We have also considered scattering in linear systems, that is, systems in which the Heisenberg equations of motions are linear in the operators. We have shown that this scattering matrix induces no correlations and neither annihilation nor creation of photons are allowed. We support our mathematical results with some simulations using MPS. We are able to control how *nonlinear* the scatterers are, finding a suppression of the nonlinear features of the scattering when the scatterers are linear.

We have studied several instances of few-photon scattering in Chap. 5 using the methods introduced in Chap. 2. We have fully characterized the one-photon scattering from a two-level atom in the ultrastrong regime, where deterministic inelastic scattering is possible. We have found also deterministic two-photon generation in the one-photon scattering from a cyclic three-level atom. The one- and two-photon scattering from a generalized V atom has been studied, where we can have perfect transmission both for one and two photons; besides, we can switch on and off the generation of photon-photon correlations in the two-photon scattering. We propose an implementation of a two-qubit quantum phase gate. In order to do so, we have considered two-photon scattering with nonmonochromatic wave packets from different instances of point-like scatterers. Unfortunately, even though the process is feasible, the efficiency is too low. Finally, we have studied the effects of interqubit distance in two-photon scattering.

Resumen

En esta tesis hemos estudiado scattering de pocos fotones en electrodinámica cuántica en guías de onda, donde los fotones se propagan a través de un medio unidimensional interaccionando con algunos scatterers, tales como átomos de dos niveles.

Los métodos utlizados para tratar estos problemas se explican en el capítulo 2. Por primera vez, hemos aplicado la técnica numérica estados producto de matriz (MPS, por sus siglas en inglés) a este campo. Además, hemos utilizado métodos analíticos ya conocidos, tales como el formalismo input-output.

Hemos caracterizado el espectro de estos modelos en el capítulo 3, tanto en la aproximación de onda rotatoria (RWA, por sus siglas en inglés) como en el régimen de acoplo ultrafuerte. Estos espectros contienen estados ligados, en los cuales algunas excitaciones fotónicas están confinadas en torno a los scatterers. Estos estados son esenciales para comprender algunas propiedades dinámicas. Ilustramos esto estudiando el decaimiento espontáneo de un átomo de dos niveles en la RWA.

Hemos determinado algunas propiedades analíticas de la matriz de scattering en el capítulo 4, la cual es el objeto matemático más importante de este campo. En particular, hemos demostrado que el principio de descomposición de cluster para las amplitudes de scattering, el cual se da en teoría cuántica de campos al ser esta una teoría relativista, también se da en nuestro caso, pese a estar tratando con modelos no relativistas. Hemos generalizado el principio de cluster a scatterers con memoria, encontrando la estructura de la matriz de scattering compatible con esta generalización. También hemos estudiado scattering en sistemas lineales, es decir, sistemas en los que las ecuaciones de Heisenberg son lineales en los operadores. Hemos demostrado que la matriz de scattering en estos sistemas no induce correlaciones y que ni creación ni aniquilación de partículas están permitidas. Confirmamos estos resultados matemáticos con varias simulaciones usando MPS. Al ser capaces de controlar cuan *no lineales* son los scatterers, hemos encontrado una supresión de los efectos no lineales del scattering cuando los scatterers tienden a ser lineales.

Hemos estudiado varios problemas de scattering de pocos fotones en el capítulo 5 utilizando los métodos introducidos en el capítulo 2. Hemos caracterizado por completo el scattering de un fotón a través de un átomo de dos niveles en el régimen de acoplo ultrafuerte, donde hemos encontrado que scattering inelástico determinista es posible. Hemos hallado generación de dos fotones también determinista en el scattering de un fotón a través de un átomo cíclico de tres niveles. El scattering de uno y dos fotones a través de un átomo V generalizado ha sido tratado, donde podemos tener transmisión perfecta en ambos casos; además, podemos suprimir la generación de correlaciones entre fotones en el scattering de dos fotones. La posibilidad de implementar una puerta cuántica de fase de dos qubits se ha considerado usando scattering de dos fotones con paquetes de onda no monocromáticas a través de varios scatterers puntuales; desafortunadamente, pese a que el proceso es posible, la eficiencia es demasiado baja. Finalmente, hemos estudiado los efectos de la distancia entre qubits en el scattering de dos fotones.

Chapter 1

Introduction

> *The good thing about science is that it's true whether or not you believe in it.*
>
> Neil deGrasse Tyson in an interview with Bill Maher [1].

Light-matter interaction is one of the most relevant interactions in physics. It dominates a lot of phenomena for a broad energy scale, from atomic physics to solid-state systems, making the other fundamental interactions negligible in many situations.

Quantum description of light-matter interaction is one of the most successful scientific theories to date. In the early times of quantum mechanics, it was able to explain the discrete atomic spectra [2], to say an example. Quantum electrodynamics (QED), where both the atomic degrees of freedom and the electromagnetic field are quantized [3], is the most accurate theory so far. For instance, it is able to predict the anomalous magnetic dipole moment of the electron with more than 10 significant figures.

Genuine quantum effects, such as quantum superposition or entanglement, are routinely measured in the laboratory. Together with the fact that it is possible to deal with few photons interacting with atoms experimentally, signals that we are living a revolution in the study of light-matter interaction at the quantum level. This kind of physics, first developed in cavity-QED, where atoms interact with confined modes of the electromagnetic field [4], is nowadays realized in several platforms. Some instances are superconducting qubits [5–7], quantum dots [8–10], or nitrogen-vacancy (NV) centers [11]. These studies have potential applications in quantum technologies [12] to do computation, simulations, cryptography, or metrology [13–24].

Typical photonic implementations for quantum technologies consist of a network, in which flying photons introduced with single-photon sources [25–

29] carry the information between the artificial atoms, which are the nodes of the network [12, 20, 30–33]. Photonic networks are promising candidates for quantum technologies since photons are highly robust information carriers both in the optical [34, 35] and microwave regime [36, 37] and artificial atoms are easy to manipulate in order to implement quantum gates [17].

A particularly simple instance of a quantum network is a one-dimensional photonic medium coupled to a few atomic systems. This is the field of waveguide QED (wQED) [38]. As in cavity QED, photons interact with localized impurities, being the main difference that now photons propagate. Experimentally, there is a whole zoo of different platforms in which wQED can be implemented, such as photonic crystals [39–46], superconducting transmission lines [7, 47–55], nanofibers [56–58], plasmonic waveguides [59–68], dielectric waveguides [69, 70], diamond structures [71, 72], cold atoms [73, 74], surface acoustic waves [75–80] or coupled cavities [81], to say a few. The reduced dimensionality drastically enhances the interference effects between the flying photons. This allows bringing nonlinear optics to the quantum regime [82–84]. A goal of this field is to perform tasks at the minimum power, such as parametric down conversion, router, lasing, etc. We can also generate photon-photon interactions mediated by the atomic systems (or vice versa) in a controlled way in order to do quantum gates or generate entangled states. Another objective of the field is to perform quantum simulations, since these systems can model many-body Hamiltonians in condensed-matter physics [18]. For instance, a lattice formed by coupled cavities interacting with two-level atoms mimics a spin chain [85, 86]. Even though we are not focused on quantum simulations in this thesis, inspired by this we can solve wQED problems by means of tools typically used in many-body physics. We will illustrate this with the particular example of matrix-product states (MPS) [87–94] in Chap. 2.

In this thesis, we have studied several problems in waveguide QED, focusing on scattering of few photons interacting with few atoms with different level structures. We have employed several methods, both numerical and analytical. We have adapted MPS to this field for the first time, as well as we have adapted previously known methods to solve new problems, such as the input-output formalism [95, 96]. The methods are introduced in Chapter 2. We have characterized the eigenstates of a linear array of cavities coupled to a two-level atom for different ranges of coupling, as well as the influence of the bound states on a spontaneous-decay situation (see Chapter 3). We have determined the structure of the N-photon scattering matrix in general (see Chapter 4), generalizing the already known result in quantum-field theories to the nonrelativistic framework of wQED (see Sect. 4.1), as well as we have studied how linear scattering emerges with several nonlinear scatterers (see Sect. 4.2). In Chapter 5 we solve several scattering problems, finding nonlinear phenomena with potential applications: one-photon scattering in the ultrastrong coupling regime (which allows us to deterministically convert the frequency of the input photon, see Sect. 5.1), also deterministic two-photon generation with a single input photon (see Sect. 5.2), one- and two-photon scattering from a generalized V-atom, with perfect two-photon transmission (see Sect. 5.3), we propose a protocol to perform a quantum phase gate with waveguide QED (see Sect. 5.4), and we study the interqubit distance in two-photon scattering (see Sect. 5.5). We end up with the conclusions, both in English (Chapter 6) and Spanish (Chapter. 7).

In this first chapter, apart from this introduction to motivate the topic, we introduce the kind of models we solve in Sect. 1.1 and expose some generalities on scattering theory in Sect. 1.2.

1.1 Waveguide-QED model

Through this thesis, we consider a one-dimensional photonic medium interacting with some few-level systems. The Hamiltonian reads (we work in units such that $\hbar = 1$)

$$H = \int dk\ \omega_k a_k^\dagger a_k + H_{\mathrm{sc}} + H_{\mathrm{int}}, \tag{1.1}$$

where a_k ($a_k^\dagger$) destroys (creates) a photon with momentum k ($[a_k, a_{k'}^\dagger] = \delta(k-k')$ and $[a_k, a_{k'}] = 0$), ω_k is the photonic dispersion relation, H_{sc} describes the scatterer, that is, some few-level systems interacting with the photons, and H_{int} is the light-matter interaction Hamiltonian. We show a sketch of this kind of systems in Fig. 1.1.

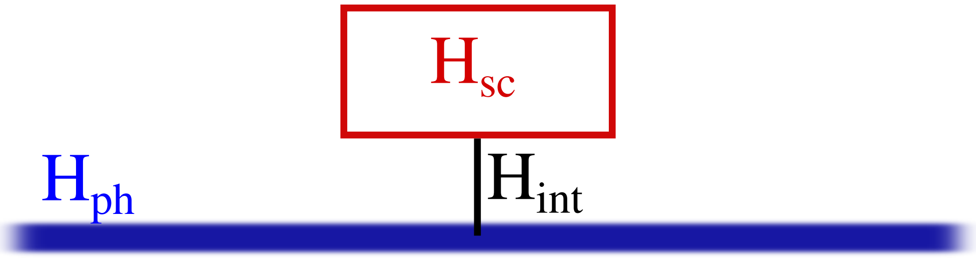

Figure 1.1: Sketch of the system described by the Hamiltonian (1.1), formed by a photonic one-dimensional waveguide (blue), some scatterers (red), and some light-matter interaction (black).

Solving the Hamiltonian (1.1) is usually a hard task, since in general is a many-body problem. The ground state can be nontrivial, scattering of photons can result in photon generation, highly correlated states, etc. In this work, we consider several instances of (1.1) and solve it by means of a bunch of numerical and analytical techniques, which will be presented in the following chapter.

For the photonic part of (1.1), H_{ph}, we consider different models. A realization well suited for our numerical simulations is a cavity array (see Fig. 1.2) with tight-binding interactions

$$H_{\mathrm{ph}} = \epsilon \sum_x a_x^\dagger a_x - J \sum_x (a_x^\dagger a_{x+1} + \mathrm{H.c.}), \tag{1.2}$$

being a_x ($a_x^\dagger$) the annihilation (creation) operator at position x ($[a_x, a_{x'}^\dagger] = \delta_{xx'}$ and $[a_x, a_{x'}] = 0$), ϵ the bare frequency of each cavity, and J the hopping constant. Taking the Fourier transform

$$a_x = \frac{1}{\sqrt{L}} \sum_k e^{ikx} a_k, \tag{1.3}$$

we get the dispersion relation, $\omega_k = \epsilon - 2J\cos k$. This lattice Hamiltonian is either an auxiliary description or it can model bona fide coupled cavities with frequency ϵ and coupling J. We show a sketch of this system and the dispersion relation in Fig. 1.2.

Another important example is a nondispersive medium: $\omega_k = c|k|$, with c the light speed in the medium. This models, for instance, superconducting transmission lines. This will be useful in our analytical calculations, since it allows us to Fourier transform between time and energy spaces easily.

The interaction Hamiltonian between the photons and each scatterer is dipolar [3]

$$H_{\mathrm{int}} = \int (g_k G^\dagger a_k + g_k^* G a_k^\dagger) dk, \tag{1.4}$$

where g_k is the coupling strength between the scatterer and the modes with momentum k and G is some operator of the Hilbert space of the scatterer. In order to be more precise, let us consider the case of a two-level system placed at $x = x_{\mathrm{sc}}$, whose Hamiltonian is given by $H_{\mathrm{sc}} = \Delta \left|1\right\rangle \left\langle 1\right|$, being Δ the level splitting of the qubit and $\left|1\right\rangle$ the excited state of the qubit; its ground state is $\left|0\right\rangle$. We take point-like coupling: $g_k \propto e^{ikx_{\mathrm{sc}}}$. Choosing $G = \sigma^+ + \sigma^-$, which is the dipole operator for the two-level system, with $\sigma^+ = \left|1\right\rangle \left\langle 0\right|$ and $\sigma^- = \left|0\right\rangle \left\langle 1\right|$ [1], the interaction Hamiltonian reads

$$H_{\mathrm{int}} = g(\sigma^- + \sigma^+)(a_{x_{\mathrm{sc}}} + a_{x_{\mathrm{sc}}}^\dagger), \tag{1.5}$$

---

[1] Even though σ^+ and σ^- act on the two-level-system Hilbert space, we consider from now on they are extended operators, *e.g.*, $\sigma^+ = \left|1\right\rangle \left\langle 0\right| \otimes \mathbb{I}_{\mathrm{ph}}$, with $\mathbb{I}_{\mathrm{ph}}$ the identity operator in the photonic space. In the same way, the bosonic operators also belong to the extended Hilbert space.

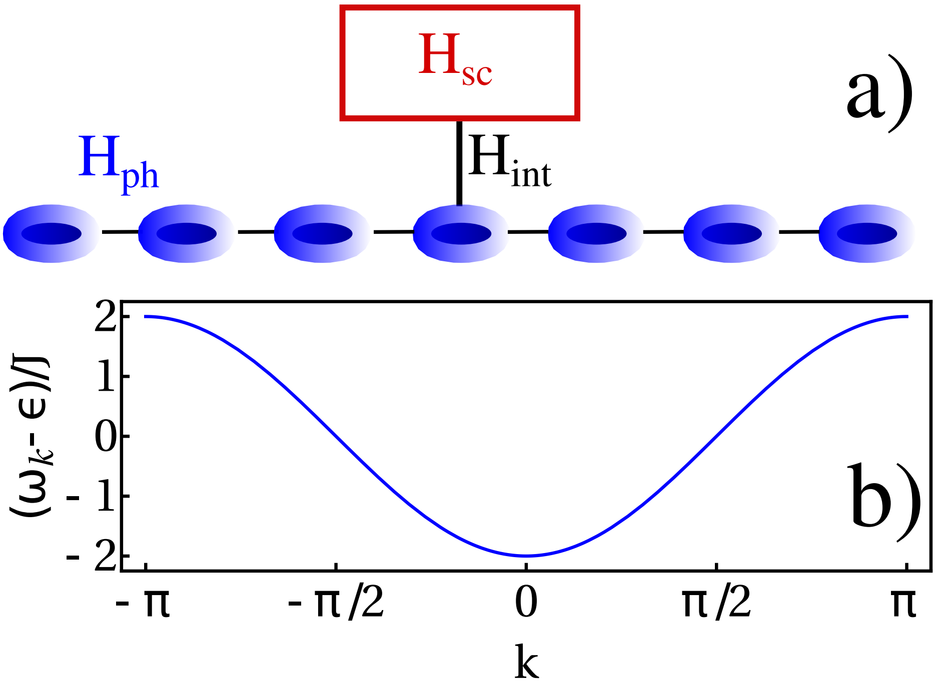

Figure 1.2: a) Sketch of the system described by the Hamiltonian (1.1), when the photonic part is given by Eq. (1.2). b) Dispersion relation $\omega_k = \epsilon - 2J \cos k$ of (1.2) as a function of k.

where the bosonic operators are now in position space and g is the coupling. This Hamiltonian can be split

$$H_{\text{int}} = H_{\text{RW}} + H_{\text{CR}}, \tag{1.6}$$

with,

$$H_{\text{RW}} = g(\sigma^- a^\dagger_{x_{\text{sc}}} + \sigma^+ a_{x_{\text{sc}}}), \tag{1.7}$$

$$H_{\text{CR}} = g(\sigma^+ a^\dagger_{x_{\text{sc}}} + \sigma^- a_{x_{\text{sc}}}). \tag{1.8}$$

The first one, Eq. (1.7), is the so-called Jaynes-Cummings Hamiltonian in cavity QED and the second one, Eq. (1.8), consists of the so-called counter-rotating terms. When the coupling constant g is small enough compared to the other energies of the whole system, the counter-rotating Hamiltonian H_{CR} (1.8) can be neglected. This is the *rotating-wave approximation* (RWA) [97, 98]. In this case, the interaction Hamiltonian preserves the number of excitations, $[H_{\text{int}}, N] = 0$, with

$$N = \int dk\, a^\dagger_k a_k + \sigma^+ \sigma^-. \tag{1.9}$$

This presents a great simplification. In particular, the ground state of the model is $|\phi_0\rangle = |0\rangle\,|\text{vac}\rangle$, with $|0\rangle$ the ground state of the two-level system and

$a_k \left|\mathrm{vac}\right\rangle = 0 \ \forall k$. We can split the Hilbert space in subspaces with different number of particles. Thus, we can restrict our computations to the subspace in which we are interested. The RWA is omnipresent in quantum optics. In particular, it is very common in scattering in waveguide QED [38, 96, 99–105]. However, there are certain systems, such as superconducting circuits [53, 106–108] or some molecular systems [109, 110], where this picture breaks down and we need the full interaction Hamiltonian, including the counter-rotating terms (1.8). In such a case, the number of excitations is not a conserved quantity anymore, $[H_{\mathrm{int}}, N] \neq 0$. This regime of parameters is known as *ultrastrong* [111–119]. In this text, we will consider both the RWA and the ultrastrong regime, depending on the problem we are dealing with.

1.2 Scattering theory

In this work, we solve scattering problems of few photons interacting with few-level systems, described by the Hamiltonian (1.1). In a typical scattering geometry, one usually assume that far away from the interaction region the state is asymptotically a linear combination of free-particle states (generated via creation operators on the noninteracting vacuum) even in the presence of the scatterer-waveguide interaction.

The free-particle states $|\Psi\rangle$ must satisfy the asymptotic condition [120]:

$$\| U(t)|\Psi\rangle - U_{\mathrm{ph}}(t)|\Psi_{\mathrm{in/out}}\rangle \| \overset{t\to\mp\infty}{\longrightarrow} 0, \tag{1.10}$$

where $U(t)$ is the evolution operator of the full Hamiltonian (1.1) and $U_{\mathrm{ph}}(t) = e^{-iH_{\mathrm{ph}}t}$ is the free-evolution operator. We illustrate these states in Fig. 1.3.

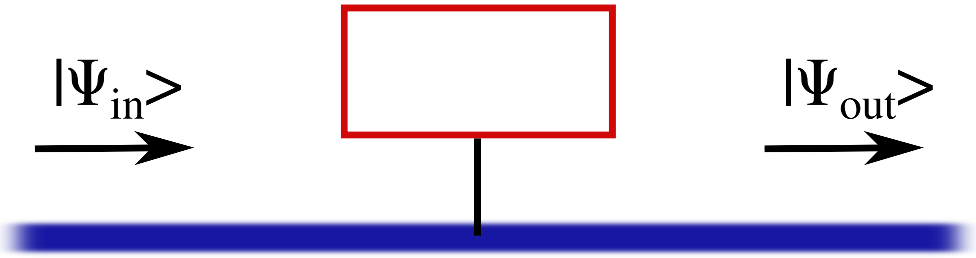

Figure 1.3: A free state $|\Psi_{\mathrm{in}}\rangle$ defined in the far past turns into $|\Psi_{\mathrm{out}}\rangle$ in the far future after interacting with the scatterer.

The scattering operator S relates the amplitude of the output and input fields through

$$\left|\Psi_{\mathrm{out}}\right\rangle = S\left|\Psi_{\mathrm{in}}\right\rangle , \tag{1.11}$$

which, using (1.10), has the formal expression:

$$S = \lim_{\substack{t_{\rm in}\to-\infty \\ t_{\rm out}\to+\infty}} U_I(t_{\rm out}, t_{\rm in}) \ . \tag{1.12}$$

Here, $U_I(t_{\rm out}, t_{\rm in}) = e^{iH_0 t_{\rm in}}\, e^{-iH(t_{\rm out}-t_{\rm in})}\, e^{-iH_0 t_{\rm out}}$ is the evolution operator in the interaction picture. Using again Eq. (1.10) leads to

$$|\Psi_{\rm in/out}\rangle = U^{\dagger}_{\rm ph}(t_{\rm in/out}) U(t_{\rm in/out}) |\Psi\rangle = |\Psi(t_{\rm in/out})\rangle_I, \tag{1.13}$$

which shows that the input and output states, as defined by Eq. (1.10), are in the interaction picture. These states can be defined as flying photons created on the ground state of the model, or even in excited localized states, as we show in Sect. 4.1.

Chapter 2

Methods

It is like being lost in a jungle and trying to use all the knowledge that you can gather to come up with some new tricks — and with some luck you might find a way out.

Maryam Mirzakhani [121].

Solving the dynamics under the Hamiltonian (1.1) is not trivial. In this chapter, we discuss the different methods we have used. Our analytical techniques are based on the input-output formalism [95]. In Sect. 2.1, we introduce the formalism and derive the S matrix. In Sect. 2.2, we set a connection between the quantum-optics master equation and the input-output formalism, which enables to compute scattering coefficients from the former. In our numerical studies, we use two methods: matrix-product states (MPS) in Sect. 2.3 and exact diagonalization in Sect. 2.4.

2.1 Input-output formalism

In a scattering experiment, both the input and the output excitations evolve freely in the far past and far future, respectively. This allows us to solve scattering problems by means of the so-called input-output theory. It was introduced in [95] in a context of an atom in a cavity interacting with a an electromagnetic bath and was extended to waveguide QED with *a point-like scatterer* in [96] for *one and two photons* and in [122] for more photons. In this thesis, we have applied this method to one- and two-photon scattering. For the sake of clarity, as in [96], in this section we choose a two-level system as scatterer in order to illustrate the method. In Sect. 5.3, we will apply the method to the one- and two-photon scattering from a $\mathrm{V}^{(N)}$ atom.

2.1.1 Model: approximations and chirality

We use some typical approximations and assumptions. First, we consider that the qubit-waveguide interaction is point-like, happening at $x = 0$. Second, the interaction Hamiltonian between the photon and the two-level system is treated within the rotating-wave approximation (RWA), already introduced in Sect. 1.1 (see Eqs. (1.6) and (1.7)). The coupling between the two-level atom and the photon field is momentum independent. The Hamiltonian (1.1) reads

$$\begin{aligned} H = &\int_0^{\infty} dk\ \omega_k a^\dagger_{+,k} a_{+,k} + \int_{-\infty}^{0} dk\ \omega_k a^\dagger_{-,k} a_{-,k} \\ &+ \Delta\sigma^+\sigma^- + g_+ \int_0^{\infty} dk\ (\sigma^+ a_{+,k} + \sigma^- a^\dagger_{+,k}) + g_- \int_{-\infty}^{0} dk\ (\sigma^+ a_{-,k} + \sigma^- a^\dagger_{-,k}). \end{aligned} \tag{2.1}$$

Here $\sigma^\pm$ are the ladder operators of the qubit, already introduced in Sect. 1.1 ($\sigma^+ = |1\rangle\langle 0|$ and $\sigma^- = |0\rangle\langle 1|$), and $a_{s,k}$ is the bosonic annihilation operator for a photon with momentum k and direction $s = \pm$ for right- and left-moving photons respectively. The excitation energy of the two-level system is denoted as Δ and g_s is the coupling strength to the s modes. As said, g_s does not depend on the momentum of the photon modes. As we will justify in Sect. 2.1.3, this approximation is Markovian [95].

We linearize the dispersion relation around the energy of the incoming photons ω_0, $\omega_k \simeq \omega_0 + v_g|k \mp k_0|$ for right- and left-moving photons respectively. The momentum k_0 is such that $\omega_{\pm k_0} = \omega_0$ and $\pm v_g$ is the group velocity at $k = \pm k_0$. The zero of energy is at ω_0. In addition, we refer the momenta to $\pm k_0$ for right- and left-moving photons respectively. Therefore, we can rewrite the dispersion relation as $\omega_k = v_g|k|$. We can extend the integration range $(0, +\infty)$ to $(-\infty, +\infty)$, which is valid if the energies of the incident photons are close enough to the linearization point ω_0 [123]. With all this, the Hamiltonian (2.1) can be approximated by

$$\begin{aligned} H = &\int_{-\infty}^{\infty} dk\ (a^\dagger_{+,k} a_{+,k} - a^\dagger_{-,k} a_{-,k})\, v_g k \\ &+ \Delta\sigma^+\sigma^- + \sum_{s=\pm} g_s \int_{-\infty}^{\infty} dk\ (\sigma^+ a_{s,k} + \sigma^- a^\dagger_{s,k}). \end{aligned} \tag{2.2}$$

Unless we explicitly claim the opposite, we will assume all the integrals go from $-\infty$ to $+\infty$ in this section, so we will drop the integration limits.

Notice that this Hamiltonian contemplates the possibility of dissimilar couplings, $g_+ \neq g_-$, from the emitter to left- and right-moving photons. This is interesting in its own right, as the waveguide could be chiral and allow the propagation in only one direction. This case has been thoroughly studied in the literature [45], both theoretically [44, 124–126] and experimentally, using platforms such as photonic crystals interacting with quantum dots [43, 44], or nanofibers coupled to nanoparticles or atoms [57, 58]. Besides, chirality is interesting as a tool, as the scattering properties in the nonchiral case ($g_- = g_+ = g$) can be related to those of the fully chiral one ($g_- = 0$, $g_+ = g$) [96], which are easier to compute because the latter involves a single branch of photons. We will follow this approach, deriving first the scattering matrix for a chiral waveguide and explicitly providing the steps to generalize the result to the nonchiral case later on. As we consider just one kind of photons, we have one set of bosonic operators; therefore, we drop the subindex related to the direction: a_ω. Besides, if we take length units such that $v_g = 1$, the dispersion relation is $\omega_k = k$. In consequence, we can use either ω or k without distinction. We write all the expressions in terms of k.

2.1.2 Scattering matrix and input-output operators

We introduce the matrix elements of the scattering operators (1.12), as well as some operators that we will need. The N-photon scattering matrix in momentum space is defined as

$$S^{\mathrm{c}}_{p_1\ldots p_N,k_1\ldots k_N} = \langle p_1 \ldots p_N | S^{\mathrm{c}} | k_1 \ldots k_N \rangle \,. \tag{2.3}$$

This is nothing but the probability amplitude of going from an input state with N photons, with momenta $k_1, \ldots, k_N$, to an output state with N photons and momenta $p_1, \ldots, p_N$. The number of input and output photons is the same, since the model (2.2) is number conserving. The superscript "c" refers to the chiral case ($g_- = 0$). The states $|k_1 \ldots k_N\rangle$ and $|p_1 \ldots p_N\rangle$ denote the input and output states with frequencies or momenta $k_1, \ldots, k_N$ and $p_1, \ldots, p_N$, respectively. These states are free in the interaction picture and exist long before ($t_{\mathrm{in}} \to -\infty$) and long after ($t_{\mathrm{out}} \to +\infty$) the interaction takes place (see Sect. 1.2). From now on, we will not write explicitly the limits and assume that the times t_{in} and t_{out} are in the far past and future, respectively. We define the following auxiliary states

$$|(k_1 \ldots k_N)^+\rangle = e^{iHt_{\mathrm{in}}} e^{-iH_{\mathrm{ph}}t_{\mathrm{in}}} |k_1 \ldots k_N\rangle = \Omega_+ |k_1 \ldots k_N\rangle \,, \tag{2.4}$$

$$|(k_1 \ldots k_N)^-\rangle = e^{iHt_{\mathrm{out}}} e^{-iH_{\mathrm{ph}}t_{\mathrm{out}}} |k_1 \ldots k_N\rangle = \Omega_- |k_1 \ldots k_N\rangle \,. \tag{2.5}$$

The second equality of each equation defines the so-called Møller isometries $\Omega_\pm$. From this and the definition of S, Eq. (1.12), the scattering matrix (2.3) can be written as

$$S^{\mathrm{c}}_{p_1\ldots p_N,k_1\ldots k_N} = \langle (p_1 \ldots p_N)^- | (k_1 \ldots k_N)^+ \rangle \,. \tag{2.6}$$

We define the input-output operators

$$a_{\text{in}}(k) = \Omega_+ a_k \Omega_+^\dagger, \tag{2.7}$$

$$a_{\text{out}}(k) = \Omega_- a_k \Omega_-^\dagger. \tag{2.8}$$

These are bosonic operators, $[a_{\text{in}}(k), a_{\text{in}}^\dagger(p)] = [a_{\text{out}}(k), a_{\text{out}}^\dagger(p)] = \delta(k-p)$. They fulfill

$$a_{\text{in}}^\dagger(k_1)\dots a_{\text{in}}^\dagger(k_N)\left|\phi_0\right\rangle = \left|(k_1\dots k_N)^+\right\rangle, \tag{2.9}$$

$$a_{\text{out}}^\dagger(p_1)\dots a_{\text{out}}^\dagger(p_N)\left|\phi_0\right\rangle = \left|(p_1\dots p_N)^-\right\rangle, \tag{2.10}$$

where $\left|\phi_0\right\rangle = \left|\text{vac}\right\rangle\left|0\right\rangle$ is the ground state of the full model (2.2), being $\left|\text{vac}\right\rangle$ the photonic vacuum state ($a_k\left|\text{vac}\right\rangle = 0\ \forall k$) and $\left|0\right\rangle$ the ground state of the qubit ($\sigma^-\left|0\right\rangle = 0$). Using this and Eq. (2.6), we rewrite the scattering matrix

$$S^{\text{c}}_{p_1\dots p_N, k_1\dots k_N} = \langle\phi_0|a_{\text{out}}(p_1)\dots a_{\text{out}}(p_N)a_{\text{in}}^\dagger(k_1)\dots a_{\text{in}}^\dagger(k_N)|\phi_0\rangle\,. \tag{2.11}$$

Therefore, we can compute the scattering matrix by finding the relation between the output and the input operators. As we will see, we will need these operators in the time domain, $a_{\text{in}}(t) = 1/\sqrt{2\pi}\int dk\, a_{\text{in}}(k)e^{-ikt}$ and $a_{\text{out}}(t) = 1/\sqrt{2\pi}\int dk\, a_{\text{out}}(k)e^{-ikt}$. They fulfill [95, 96]

$$a_{\text{in}}(t) = \frac{1}{\sqrt{2\pi}}\int dk\ a_k(t_{\text{in}})e^{-ik(t-t_{\text{in}})}, \tag{2.12}$$

$$a_{\text{out}}(t) = \frac{1}{\sqrt{2\pi}}\int dk\ a_k(t_{\text{out}})e^{-ik(t-t_{\text{out}})}. \tag{2.13}$$

where $a_k(t) = e^{iHt}a_k e^{-iHt}$ is a_k in the Heisenberg picture at time t. Eqs. (2.12) and (2.13) will be useful later.

2.1.3 Equations of motion

We work in the Heisenberg picture, so we need to find the Heisenberg equations,

$$\frac{dO(t)}{dt} = i[H, O(t)], \tag{2.14}$$

for the atom and photon operators with the chiral model, Eq. (2.2) with $g_+ = g$ and $g_- = 0$. They read

$$i\frac{da_k(t)}{dt} = ka_k(t) + g\sigma^-(t), \tag{2.15}$$

$$i\frac{d\sigma^-(t)}{dt} = \Delta\sigma^-(t) - g\int dk\ \sigma_z(t)a_k(t), \tag{2.16}$$

where $\sigma_z = |1\rangle\langle 1| - |0\rangle\langle 0|$. We multiply Eq. (2.15) by e^{ikt} and formally integrate it from t_{in} to t

$$a_k(t) = a_k(t_{\text{in}})e^{-ik(t-t_{\text{in}})} - ig\int_{t_{\text{in}}}^{t} dt'\ \sigma^-(t')e^{-ik(t-t')}. \tag{2.17}$$

We define the following operator

$$\Phi(t) = \frac{1}{\sqrt{2\pi}}\int dk\ a_k(t) \tag{2.18}$$

Integrating Eq. (2.17) with respect to k and using Eq. (2.12)

$$\Phi(t) = a_{\text{in}}(t) - i\sqrt{\frac{\gamma}{2}}\sigma^-(t), \tag{2.19}$$

where $\gamma = \pi g^2$. Multiplying again Eq. (2.15) by e^{ikt}, but integrating now from t to t_{out}

$$a_k(t) = a_k(t_{\text{out}})e^{-ik(t-t_{\text{out}})} + ig\int_{t}^{t_{\text{out}}} dt'\ \sigma^-(t')e^{-ik(t-t')}. \tag{2.20}$$

Integrating this in k and using Eqs. (2.13) and (2.18)

$$\Phi(t) = a_{\text{out}}(t) + i\sqrt{\frac{\gamma}{2}}\sigma^-(t). \tag{2.21}$$

From Eqs. (2.19) and (2.21)

$$a_{\text{out}}(t) = a_{\text{in}}(t) - i\sqrt{2\gamma}\sigma^-(t). \tag{2.22}$$

This equation is Markovian, in the sense that the output photon field does not depend on the state of the scatterer at previous times. However, if we had consider g dependent on k, the second term would be an integral in time, breaking this picture. This is the reason why we called Markov approximation to the case in which g does not depend on k, as we anticipated in Sect. 2.1.1.

We need to know the dynamics of $\sigma^-(t)$. It is given by Eq. (2.16), but it is convenient to rewrite it in terms of the input-output operators. Using the definition of $\Phi(t)$, Eq. (2.18), and the relation between $\Phi(t)$ and $a_{\text{in}}(t)$, Eq. (2.19), we can rewrite Eq. (2.16) as

$$\frac{d\sigma^-(t)}{dt} = -(i\Delta + \gamma)\sigma^-(t) + i\sqrt{2\gamma}\sigma_z(t)a_{\text{in}}(t) \tag{2.23}$$

With this, we already have the necessary dynamical equations to compute the scattering matrix by means of the input-output formalism.

We can generalize this method to other scatterers. In such a case, Eq. (2.22) would change depending on the nature of the scatterer, and we would have to find a system of equations of motion analogous to Eq. (2.23) for other operators. *E.g.*, this method has been extended to two collocated two-level systems in [127]. As said in the introduction of the section, we applied the formalism to a generalized V atom [128] (see Sect. 5.3).

In what follows, we make use of Eqs. (2.22) and (2.23) to find the scattering-matrix elements.

2.1.4 One-photon scattering

The amplitude for the transition from an input state with momentum k into an outgoing state with momentum p, S^{c}_{pk}, is given by Eq. (2.11) for $N = 1$

$$S^{\mathrm{c}}_{pk} = \langle \phi_0 | a_{\mathrm{out}}(p) a^{\dagger}_{\mathrm{in}}(k) | \phi_0 \rangle \,. \tag{2.24}$$

Using Eq. (2.22)

$$S^{\mathrm{c}}_{pk} = \delta(p-k) - i\sqrt{2\gamma}\, \langle \phi_0 | \sigma^{-}(p) | k^{+} \rangle \,, \tag{2.25}$$

with

$$\langle \phi_0 | \sigma^{-}(p) | k^{+} \rangle = \int dt\, \frac{e^{ipt}}{\sqrt{2\pi}} \langle \phi_0 | \sigma^{-}(t) | k^{+} \rangle \,. \tag{2.26}$$

The dynamics of the matrix elements of $\sigma^{-}(t)$ is obtained by sandwiching Eq. (2.23) between $\langle \phi_0 |$ and $| k^{+} \rangle$

$$\frac{d}{dt} \langle \phi_0 | \sigma^{-}(t) | k^{+} \rangle = -(i\Delta + \gamma) \langle \phi_0 | \sigma^{-}(t) | k^{+} \rangle + i\sqrt{2\gamma}\, \langle \phi_0 | \sigma_z(t) a_{\mathrm{in}}(t) | k^{+} \rangle \,. \tag{2.27}$$

Let us compute the second term of the right hand side

$$\begin{aligned} \langle \phi_0 | \sigma_z(t) a_{\mathrm{in}}(t) | k^{+} \rangle &= \langle \phi_0 | e^{-iHt} \sigma_z a_{\mathrm{in}} e^{iHt} | k^{+} \rangle \\ &= \langle \phi_0 | \left(\left(|1\rangle \langle 1| - |0\rangle \langle 0| \right) \otimes \mathbb{I}_{\mathrm{ph}} \right) a_{\mathrm{in}} e^{iHt} | k^{+} \rangle \,, \end{aligned} \tag{2.28}$$

where $\mathbb{I}_{\mathrm{ph}}$ is the identity operator in the photon space. Obviously, $\langle \phi_0 | \left(|1\rangle \langle 1| \otimes \mathbb{I}_{\mathrm{ph}} \right) = 0$ and $\langle \phi_0 | \left(|0\rangle \langle 0| \otimes \mathbb{I}_{\mathrm{ph}} \right) = \langle \phi_0 |$. Thus

$$\langle \phi_0 | \sigma_z(t) a_{\mathrm{in}}(t) | k^{+} \rangle = - \langle \phi_0 | a_{\mathrm{in}}(t) | k^{+} \rangle \,. \tag{2.29}$$

Using Eq. (2.9) and the facts that $a_{\mathrm{in}}(t)$ is the Fourier transform of $a_{\mathrm{in}}(k)$ and that $a_{\mathrm{in}}(k)$ is a bosonic operator

$$\langle \phi_0 | \sigma_z(t) a_{\mathrm{in}}(t) | k^{+} \rangle = - \langle \phi_0 | a_{\mathrm{in}}(t) | k^{+} \rangle = - \frac{e^{-ikt}}{\sqrt{2\pi}} . \tag{2.30}$$

Introducing this in (2.27)

$$\frac{d}{dt}\left\langle\phi_0|\sigma^-(t)|k^+\right\rangle = -(i\Delta+\gamma)\left\langle\phi_0|\sigma^-(t)|k^+\right\rangle + i\sqrt{\frac{\gamma}{\pi}}e^{-ikt}. \tag{2.31}$$

This equation can be integrated

$$\left\langle\phi_0|\sigma^-(t)|k^+\right\rangle = \frac{e^{-ikt}}{\sqrt{2\pi}}s_k, \tag{2.32}$$

with

$$s_k = \frac{\sqrt{2\gamma}}{k-\Delta+i\gamma}. \tag{2.33}$$

Introducing this in Eq. (2.25),

$$S^{\mathrm{c}}_{pk} = t^{\mathrm{c}}_k\,\delta(k-p), \tag{2.34}$$

with

$$t^{\mathrm{c}}_k = \frac{k-\Delta-i\gamma}{k-\Delta+i\gamma}. \tag{2.35}$$

This is the transmission amplitude, so its square modulus gives the transmission probability. In this case, $|t^{\mathrm{c}}_k|^2 = 1$, since we are dealing with a lossless chiral model. Notice that the scattering matrix is proportional to a Dirac delta, which ensures energy conservation.

As mentioned at the end of the previous section, Eqs. (2.22) and (2.23) would be different for another kind of scatterer. In such a case, in order to compute the scattering matrix we would just have to sandwich another set of equations of motion analogous to Eq. (2.23) and solve the corresponding algebraic system of equations.

2.1.5 Two-photon scattering

We can also compute the two-photon chiral-scattering matrix

$$S^{\mathrm{c}}_{p_1p_2k_1k_2} = \left\langle\phi_0|a_{\mathrm{out}}(p_1)a_{\mathrm{out}}(p_2)a^\dagger_{\mathrm{in}}(k_1)a^\dagger_{\mathrm{in}}(k_2)|\phi_0\right\rangle. \tag{2.36}$$

Introducing the identity $\int dk\; a^\dagger_{\mathrm{in}}(k)\,|\phi_0\rangle\,\langle\phi_0|\,a_{\mathrm{in}}(k)$ between $a_{\mathrm{out}}(p_1)$ and $a_{\mathrm{out}}(p_2)$ and using Eqs. (2.22), (2.24), and (2.34), we obtain

$$\begin{aligned} S^{\mathrm{c}}_{p_1p_2k_1k_2} &= t^{\mathrm{c}}_{p_1}(\delta(p_1-k_1)\delta(p_2-k_2)+\delta(p_1-k_2)\delta(p_2-k_1)) \\ &\quad - it^{\mathrm{c}}_{p_1}\sqrt{2\gamma}\left\langle p_1^+|\sigma^-(p_2)|(k_1k_2)^+\right\rangle. \end{aligned} \tag{2.37}$$

Let us compute $\langle p_1^+|\sigma^-(p_2)|(k_1k_2)^+\rangle$. We can rewrite it in terms of a Fourier transform

$$\left\langle p_1^+|\sigma^-(p_2)|(k_1k_2)^+\right\rangle = \int dt\,\frac{e^{ip_2t}}{\sqrt{2\pi}}\left\langle\phi_0|a_{\mathrm{in}}(p_1)\sigma^-(t)a^\dagger_{\mathrm{in}}(k_1)a^\dagger_{\mathrm{in}}(k_2)|\mathrm{vac}\right\rangle.$$

We find the equations for the integrand from Eq. (2.23)

$$\begin{aligned}\frac{d}{dt}\left\langle p_1^+\middle|\sigma^-(t)\middle|(k_1k_2)^+\right\rangle = &-(i\Delta+\gamma)\left\langle p_1^+\middle|\sigma^-(t)\middle|(k_1k_2)^+\right\rangle \\ &+\sqrt{2\gamma}\left\langle p_1^+\middle|\sigma_z(t)a_{\mathrm{in}}(t)\middle|(k_1k_2)^+\right\rangle.\end{aligned} \tag{2.38}$$

We have to compute the second term of the right-hand side of the equality, which is inhomogeneous. Using the fact that the input operators are bosonic and Eq. (2.30), this term can be written as a transition amplitude between single-photon states

$$\left\langle p_1^+\middle|\sigma_z(t)a_{\mathrm{in}}(t)\middle|(k_1k_2)^+\right\rangle = \left\langle p_1^+\middle|\sigma_z(t)\middle|k_1^+\right\rangle\frac{e^{-ik_2t}}{\sqrt{2\pi}} + (k_1\leftrightarrow k_2). \tag{2.39}$$

In order to compute $\langle p^+|\sigma_z(t)|k^+\rangle$, we rewrite σ_z as $2\sigma^+\sigma^- - \mathbb{I}$. Then

$$\left\langle p^+\middle|\sigma_z(t)\middle|k^+\right\rangle = 2\left\langle p^+\middle|\sigma^+(t)\sigma^-(t)\middle|k^+\right\rangle - \delta(k-p). \tag{2.40}$$

We introduce the identity between $\sigma^+(t)$ and $\sigma^-(t)$. The only contribution comes from $|\phi_0\rangle\langle\phi_0|$. Using Eqs. (2.32) and (2.33)

$$\left\langle p^+\middle|\sigma_z(t)\middle|k^+\right\rangle = \frac{1}{\pi}e^{-i(k-p)t}s_p^*s_k - \delta(k-p). \tag{2.41}$$

Introducing this in Eq. (2.39)

$$\begin{aligned}\left\langle p_1^+\middle|\sigma_z(t)a_{\mathrm{in}}(t)\middle|(k_1k_2)^+\right\rangle = &\frac{1}{\sqrt{2\pi}}\frac{1}{\pi}e^{-i(k_1+k_2-p_1)t}s_{p_1}^*(s_{k_1}+s_{k_2}) \\ &-\frac{1}{\sqrt{2\pi}}e^{-ik_2t}\delta(k_1-p_1) - \frac{1}{\sqrt{2\pi}}e^{-ik_1t}\delta(k_2-p_1).\end{aligned} \tag{2.42}$$

Using this in Eq. (2.38), we can integrate that equation, obtaining

$$\begin{aligned}\left\langle p_1^+\middle|\sigma^-(t)\middle|(k_1k_2)^+\right\rangle = &-\frac{1}{\sqrt{2\pi}}\frac{1}{\pi}s_{k_1+k_2-p_1}s_{p_1}^*(s_{k_1}+s_{k_2})e^{-i(k_1+k_2-p_1)} \\ &+\frac{1}{\sqrt{2\pi}}\delta(k_2-p_1)s_{k_1}e^{-ik_1t} + \frac{1}{\sqrt{2\pi}}\delta(k_1-p_1)s_{k_2}e^{-ik_2t}.\end{aligned} \tag{2.43}$$

Coming back to the energy domain

$$\begin{aligned}\left\langle p_1^+\middle|\sigma^-(p_2)\middle|(k_1k_2)^+\right\rangle = &-\frac{1}{\pi}\delta(k_1+k_2-p_1-p_2)s_{p_2}s_{p_1}^*(s_{k_1}+s_{k_2}) \\ &+s_{k_1}\delta(k_2-p_1)\delta(k_1-p_2) + s_{k_2}\delta(k_1-p_1)\delta(k_2-p_2).\end{aligned} \tag{2.44}$$

Introducing this in Eq. (2.37) and using the relation $t_k^{\mathrm{c}}s_k^* = s_k$, which can be easily derived from Eqs. (2.33) and (2.35),

$$\begin{aligned}S^{\mathrm{c}}_{p_1p_2k_1k_2} = &\,t^{\mathrm{c}}_{k_1}t^{\mathrm{c}}_{k_2}(\delta(k_1-p_1)\delta(k_2-p_2)+\delta(k_1-p_2)\delta(k_2-p_1)) \\ &+i\,T^{\mathrm{c}}_{p_1p_2k_1k_2}\delta(k_1+k_2-p_1-p_2),\end{aligned} \tag{2.45}$$

with

$$T^{\mathrm{c}}_{p_1p_2k_1k_2} = \frac{1}{\pi}\sqrt{2\gamma} s_{p_1} s_{p_2}(s_{k_1} + s_{k_2}) \tag{2.46}$$

The first row of Eq. (2.45) describes the independent scattering of each photon. This term conserves the energy of each photon independently due to the Dirac deltas. The other term preserves the total energy, but it does not conserve the energy of both photons individually. It gives the effective photon-photon interaction induced by the scatterer, in this case a two-level system. As before, if we had considered another scatterer, we would have had to solve a different system of equations.

2.1.6 Scattering matrix in the nonchiral case

In this section, we explain how to compute the nonchiral scattering matrix from the fully chiral one. We define the following transformation

$$b_{\pm,k} = \frac{a_{+,k} \pm a_{-,-k}}{\sqrt{2}}. \tag{2.47}$$

Introducing this in the Hamiltonian (2.2)

$$H = \int_{-\infty}^{\infty} dk\ k(b^\dagger_{+,k} b_{+,k} + b^\dagger_{-,k} b_{-,k}) \tag{2.48}$$

$$+ \Delta\sigma^+\sigma^- + \sqrt{2}g \int dk\ (\sigma^+ b_{+,k} + \sigma^- b^\dagger_{+,k}) \tag{2.49}$$

The set of operators $\{b_{-,k}\}$ is decoupled, whereas the others $\{b_{+,k}\}$ are coupled with the two-level atom with coupling $g' = \sqrt{2}g$. This implies that the scattering matrix for $b_{+,k}$ is that of the chiral model, by changing g by g', and that for $b_{-,k}$ is given by the free evolution.

To compute the scattering matrix, we introduce input and output operators for $b_{s,k}$, $b_{s,\mathrm{in/out}}(k)$, fully analogously to what we did for a_k (see Eqs. (2.7) and (2.8)). They fulfill the bosonic commutation relations, $[b_{s,\mathrm{in(out)}}(p), b^\dagger_{s',\mathrm{in(out)}}(k)] = \delta_{ss'}\delta(k-p)$.

As we said above, the $b_{-,k}$ modes are decoupled, so its scattering matrix is trivial, that is

$$\begin{aligned} &\langle\phi_0| b_{-,\mathrm{out}}(p_1)\dots b_{-,\mathrm{out}}(p_N) b^\dagger_{-,\mathrm{in}}(k_1)\dots b^\dagger_{-,\mathrm{in}}(k_N)|\phi_0\rangle \\ &= \delta(p_1-k_1)\dots\delta(p_N-k_N) + \text{permutations}. \end{aligned} \tag{2.50}$$

However, $b_{+,k}$ does interact as if we had a chiral model by replacing g by $g' = \sqrt{2}g$, so its scattering matrix is the chiral one

$$\langle\phi_0| b_{+,\mathrm{out}}(p_1)\dots b_{+,\mathrm{out}}(p_N) b^\dagger_{+,\mathrm{in}}(k_1)\dots b^\dagger_{+,\mathrm{in}}(k_N)|\phi_0\rangle = S^{\mathrm{c}}_{p_1\dots p_N k_1\dots k_N}. \tag{2.51}$$

However, we are interested in the scattering matrix for the $a_{s,k}$ modes. We need to write $a_{s,k}$ in terms of $b_{s,k}$, Eq. (2.47),

$$a_{+,k} = \frac{b_{+,k} + b_{-,k}}{\sqrt{2}}, \tag{2.52}$$

$$a_{-,k} = \frac{b_{+,-k} - b_{-,-k}}{\sqrt{2}}. \tag{2.53}$$

We also define input-output operators for $a_{s,k}$, $a_{s,\mathrm{in/out}}(k)$. We compute now the single-photon S matrix. Without loss of generality, the input photon will be right moving, $a^\dagger_{+,\mathrm{in}}(k)\,|\phi_0\rangle$. The outgoing photon can be right- or left-moving. We first consider the right-moving case

$$\begin{aligned} S_{pk} &= \langle\phi_0|a_{+,\mathrm{out}}(p)a^\dagger_{+,\mathrm{in}}(k)|\phi_0\rangle \\ &= \frac{1}{2}\,\langle\phi_0|(b_{+,\mathrm{out}}(p) + b_{-,\mathrm{out}}(p))(b^\dagger_{+,\mathrm{in}}(k) + b^\dagger_{-,\mathrm{in}}(k))|\phi_0\rangle \\ &= \frac{1}{2}\,\Big(\langle\phi_0|b_{+,\mathrm{out}}(p)b^\dagger_{+,\mathrm{in}}(k)|\phi_0\rangle + \langle\phi_0|b_{-,\mathrm{out}}(p)b^\dagger_{-,\mathrm{in}}(k)|\phi_0\rangle\Big) \\ &= \frac{1}{2}(S^{\mathrm{c}}_{pk} + \delta(k-p)). \end{aligned} \tag{2.54}$$

We have applied the transformation given by Eqs. (2.52) and (2.53) (second line), the fact that $b_{s,\mathrm{in/out}}(k)$ are bosonic (third line), and Eqs. (2.50) and (2.51) in the last line. Notice this result does not depend on the kind of scatterer. Particularizing for the two-level system (Eqs. (2.34) and (2.35))

$$S_{pk} = t_k\delta(k-p), \tag{2.55}$$

being t_k the nonchiral-transmission amplitude

$$t_k = \frac{t^{\mathrm{c}}_k + 1}{2} = \frac{k-\Delta}{k-\Delta+i\gamma}. \tag{2.56}$$

In this expression, and in any other S-matrix element of the full model, $\gamma = \pi(g')^2 = 2\pi g^2$. Analogously, the scattering matrix for a left-moving output photon reads

$$S_{-pk} = \langle\phi_0|a_{-,\mathrm{out}}(p)a^\dagger_{+,\mathrm{in}}(k)|\phi_0\rangle = \frac{1}{2}(S^{\mathrm{c}}_{pk} - \delta(k-p)) = r_k\delta(k-p), \tag{2.57}$$

with r_k the reflection amplitude

$$r_k = \frac{t^{\mathrm{c}}_k - 1}{2} = \frac{-i\gamma}{k-\Delta+i\gamma}. \tag{2.58}$$

Comparing this to the transmission amplitude, Eq. (2.56), we see that $r_k + 1 = t_k$. It is well known that this system has full reflection, $|r_k|^2 = 1$, if the energy of the input photon matches the energy of the qubit, $k = \Delta$ [99, 100, 102, 129].

We now apply this program to the two-photon scattering matrix. In particular, we compute the two-photon S matrix for right-moving incident and outgoing photons ($p_1, p_2, k_1, k_2 > 0$):

$$\begin{aligned}
S_{p_1 p_2 k_1 k_2} =& \langle\phi_0| a_{+,\mathrm{out}}(p_1) a_{+,\mathrm{out}}(p_2) a^\dagger_{+,\mathrm{in}}(k_1) a^\dagger_{+,\mathrm{in}}(k_2)|\phi_0\rangle \\
=& \frac{1}{4}\Big(\langle\phi_0| b_{+,\mathrm{out}}(p_1) b_{+,\mathrm{out}}(p_2) b^\dagger_{+,\mathrm{in}}(k_1) b^\dagger_{+,\mathrm{in}}(k_2)|\phi_0\rangle \\
&+ \langle\phi_0| b_{+,\mathrm{out}}(p_1) b_{-,\mathrm{out}}(p_2) b^\dagger_{+,\mathrm{in}}(k_1) b^\dagger_{-,\mathrm{in}}(k_2)|\phi_0\rangle \\
&+ \langle\phi_0| b_{+,\mathrm{out}}(p_1) b_{-,\mathrm{out}}(p_2) b^\dagger_{-,\mathrm{in}}(k_1) b^\dagger_{+,\mathrm{in}}(k_2)|\phi_0\rangle \\
&+ \langle\phi_0| b_{-,\mathrm{out}}(p_1) b_{+,\mathrm{out}}(p_2) b^\dagger_{-,\mathrm{in}}(k_1) b^\dagger_{+,\mathrm{in}}(k_2)|\phi_0\rangle \\
&+ \langle\phi_0| b_{-,\mathrm{out}}(p_1) b_{+,\mathrm{out}}(p_2) b^\dagger_{+,\mathrm{in}}(k_1) b^\dagger_{-,\mathrm{in}}(k_2)|\phi_0\rangle \\
&+ \langle\phi_0| b_{-,\mathrm{out}}(p_1) b_{-,\mathrm{out}}(p_2) b^\dagger_{-,\mathrm{in}}(k_1) b^\dagger_{-,\mathrm{in}}(k_2)|\phi_0\rangle\Big) \\
=& \frac{1}{4}\left(S^{\mathrm{c}}_{p_1 p_2 k_1 k_2} + S^{\mathrm{c}}_{p_1 k_1}\delta(k_2 - p_2) + S^{\mathrm{c}}_{p_1 k_2}\delta(k_1 - p_2)\right. \\
&+ S^{\mathrm{c}}_{p_2 k_2}\delta(k_1 - p_1) + S^{\mathrm{c}}_{p_2 k_1}\delta(k_2 - p_1) \\
&\left.+ \delta(k_1 - p_1)\delta(k_2 - p_2) + \delta(k_1 - p_1)\delta(k_2 - p_2)\right), \qquad (2.59)
\end{aligned}$$

where we have used the transformation relating $a_{s,k}$ and $b_{s,k}$, see Eq. (2.47), and Eqs. (2.50) and (2.51). As before, we have shown that we can write the two-photon nonchiral scattering matrix in terms of the chiral one. Particularizing for the two-level system (Eqs. (2.34), (2.45), and (2.56))

$$\begin{aligned}
S_{p_1 p_2 k_1 k_2} =& t_{k_1} t_{k_2}(\delta(k_1 - p_1)\delta(k_2 - p_2) + \delta(k_1 - p_2)\delta(k_2 - p_1)) \\
&+ \frac{1}{4}\frac{i}{\pi}\sqrt{2\gamma} s_{p_1} s_{p_2}(s_{k_1} + s_{k_2})\delta(k_1 + k_2 - p_1 - p_2). \qquad (2.60)
\end{aligned}$$

This result is very similar to the chiral case (Eq. (2.45)): the first row describes the independent scattering of each photon and the second one gives the effective photon-photon interaction induced by the qubit. Notice that the interaction term is identical to the chiral one up to a constant factor 1/4. Following an analogous process, we find S matrix for the other output channels

$$\begin{aligned}
S_{-p_1 -p_2 k_1 k_2} =& r_{k_1} r_{k_2}(\delta(k_1 + p_1)\delta(k_2 + p_2) + \delta(k_1 + p_2)\delta(k_2 + p_1)) \\
&+ \frac{1}{4}\frac{i}{\pi}\sqrt{2\gamma} s_{-p_1} s_{-p_2}(s_{k_1} + s_{k_2})\delta(k_1 + k_2 + p_1 + p_2), \qquad (2.61) \\
S_{-p_1 p_2 k_1 k_2} =& r_{k_1} t_{k_2}\delta(k_1 + p_1)\delta(k_2 - p_2) + t_{k_1} r_{k_2}\delta(k_1 - p_2)\delta(k_2 + p_1) \\
&+ \frac{1}{4}\frac{i}{\pi}\sqrt{2\gamma} s_{-p_1} s_{p_2}(s_{k_1} + s_{k_2})\delta(k_1 + k_2 + p_1 - p_2), \qquad (2.62) \\
S_{p_1 -p_2 k_1 k_2} =& t_{k_1} r_{k_2}\delta(k_1 - p_1)\delta(k_2 + p_2) + r_{k_1} t_{k_2}\delta(k_1 + p_2)\delta(k_2 - p_1) \\
&+ \frac{1}{4}\frac{i}{\pi}\sqrt{2\gamma} s_{p_1} s_{-p_2}(s_{k_1} + s_{k_2})\delta(k_1 + k_2 - p_1 + p_2). \qquad (2.63)
\end{aligned}$$

In particular, we can write the nonlinear term in general as

$$T_{p_1p_2k_1k_2} = \frac{1}{4}T^{\mathrm{c}}_{|p_1||p_2||k_1||k_2|}. \tag{2.64}$$

In conclusion, we can compute the nonchiral S matrix provided we know the chiral one, which is easier to find.

2.2 Master equation

The input-output formalism needs the dynamics of the scatterer ($\sigma^-(t)$ in the example given above, see Eq. (2.22)). Considering we have a small system (the scatterer) coupled to a reservoir (the photonic media), we can apply the master-equation formalism [130] as an alternative to the Heisenberg equations explained in the previous section. This method, first developed by Belavin et al [131] and later explored by Kossakowski, Lindblad, Gorini, and others [132–134], allows us to derive an equation of motion for the reduced density matrix of the system ρ (the scatterer in our case). Assuming the Markov approximation and imposing complete positivity to the evolution, ρ evolves according to

$$\frac{d\rho}{dt} = -i[H_{\mathrm{sc}}, \rho] + \sum_l \gamma_l \left(V_l \rho V_l^\dagger - \frac{1}{2}\{V_l^\dagger V_l, \rho\} \right), \tag{2.65}$$

where H_{sc} is the Hamiltonian of the scatterer, $\gamma_l > 0\ \forall l$, and $\{V_l\}$ is a set of operators. Both γ_l and V_l depend on the whole system (scatterer+environment).

This formalism is useful when the external driving is classical. Besides, one can easily include both temperature and losses with this method.

In particular, we will derive the master equation for an external driving at fixed frequency ω, which allows us to solve the dynamics of the scatterer and find the scattering coefficients. In order to find the equation, we need to assume that the light-matter coupling is perturbative up to second order.

2.2.1 Transmission amplitude as a coherent expected value

We start by showing an intermediate result. We find an expression for the one-photon transmission amplitude t_k in terms of the input-output equations provided the system is excited by a coherent state with amplitude α and input frequency ω and momentum k

$$|\alpha_k\rangle = \mathrm{e}^{\alpha a^\dagger_{+,\mathrm{in}}(k) - \mathrm{H.c.}} |\phi_0\rangle, \tag{2.66}$$

being $|\phi_0\rangle$ the ground state of the whole system.

Let us compute the following expected value

$$\langle\alpha_k|a_{+,\text{out}}(t)|\alpha_k\rangle = e^{-|\alpha|^2/2}\sum_n \frac{\alpha^n}{n!}\langle\alpha_k|\, a_{+,\text{out}}(t)(a^\dagger_{+\text{in}}(k))^n\,|\phi_0\rangle$$

$$= \frac{\alpha}{\sqrt{2\pi}}\int dk' e^{-ik't}\,\langle\phi_0|a_{+,\text{out}}(k')a^\dagger_{+,\text{in}}(k)|\phi_0\rangle + \mathcal{O}(\alpha^2). \tag{2.67}$$

Using Eq. (2.55)

$$\langle\alpha_k a|a_{+,\text{out}}(t)|\alpha_k\rangle = \frac{\alpha e^{-ikt}}{\sqrt{2\pi}}t_k + \mathcal{O}(\alpha^2). \tag{2.68}$$

By means of an analogous computation

$$\langle\alpha_k|a_{+,\text{in}}(t)|\alpha_k\rangle = \frac{\alpha e^{-ikt}}{\sqrt{2\pi}} + \mathcal{O}(\alpha^2). \tag{2.69}$$

The limit $\alpha\to 0$ of the quotient between both expected values is

$$\lim_{\alpha\to 0}\frac{\langle\alpha_k|a_{+,\text{out}}(t)|\alpha_k\rangle}{\langle\alpha_k|a_{+,\text{in}}(t)|\alpha_k\rangle} = \lim_{\alpha\to 0}\frac{\alpha e^{-ikt}t_k/\sqrt{2\pi}+\mathcal{O}(\alpha^2)}{\alpha e^{-ikt}/\sqrt{2\pi}+\mathcal{O}(\alpha^2)} = t_k. \tag{2.70}$$

We have shown that the one-photon transmission amplitude can be written in terms of expected value of a coherent state $|\alpha_k\rangle$ when $\alpha\to 0$. From now on in this section, we assume that all the expectation values are in $|\alpha_k\rangle$: for any operator A, $\langle A\rangle = \langle\alpha_k|A|\alpha_k\rangle$.

2.2.2 Linear-response theory and input-output formalism

We write down an input-output relation analogous to (2.22) for a coherent driving. Eq. (2.22) can be generalized [95]

$$a_{+,\text{out}}(t) = a_{+,\text{in}}(t) - i\int\frac{d\omega}{\sqrt{2\pi}}\int dt'\; g(\omega)\mathrm{e}^{-i\omega(t-t')}G(t'), \tag{2.71}$$

where $g(\omega)$ now depends on ω, and $G(t)$ is the operator that couples the scatterer to the waveguide in the Heisenberg picture.

As shown in Eq. (2.70), t_k can be computed using a coherent driving at frequency ω in the limit of zero amplitude. Thus, we can use linear-response theory to compute $\langle G(t)\rangle$

$$\langle G(t)\rangle = \alpha\Xi(\omega)\mathrm{e}^{i\omega t} + \text{c.c.} \tag{2.72}$$

where $\Xi(\omega)$ is the so-called linear susceptibility. Taking the expected value of Eq. (2.71), replacing the latter in that equation, and taking the limit $\alpha\to 0$

$$\lim_{\alpha\to 0}\langle a_{+,\text{out}}(t)\rangle = \lim_{\alpha\to 0}\left(\langle a_{+,\text{in}}(t)\rangle - i\sqrt{2\pi}g(\omega)\alpha\Xi(\omega)\mathrm{e}^{-i\omega t}\right). \tag{2.73}$$

From this and Eq. (2.70)

$$t_k = 1 - i2\pi g(k)\Xi(k). \tag{2.74}$$

Therefore, in order to compute the transmission amplitude we need to obtain the linear susceptibility.

2.2.3 Quantum-optics master equation

We here explicitly write the master equation (2.65) for our system. Let $\{|i\rangle\}$ be the set of eigenstates of the scatterer, with $|0\rangle$ its ground state. We define Γ_{ij} as the decay rate between $|i\rangle$ and $|j\rangle$ due to the coupling to the environment. We can split this coupling as $\Gamma_{ij} = \Gamma^0_{ij} + \gamma_{ij}$, being Γ^0_{ij} the decay rate into the waveguide and γ_{ij} the contribution of other external modes, such as phonons, nonguided electromagnetic modes, etc. We assume the scatterer is under a coherent driving (2.66). Then, the quantum-optics master equation reads

$$\begin{aligned}\frac{d\rho}{dt} =& -i[H_{\mathrm{sc}},\rho] - i\alpha g(\omega) 2\cos(\omega t)[G(t),\rho]\\ &+ 2\sum_{ij}\Gamma_{ij}\Big(L_{ij}\rho L^\dagger_{ij} - \frac{1}{2}\{L^\dagger_{ij}L_{ij},\rho\}\Big),\end{aligned} \tag{2.75}$$

where $L_{ij} = |j\rangle\langle i|$ causes the transitions between $|i\rangle$ and $|j\rangle$ and the operator $\mathcal{D}$ is a diagonal matrix that induces dephasing.

As we will show, we can compute the susceptibility $\Xi(\omega)$ (2.72) and the transmission amplitude, using this equation.

2.2.4 Calculation of the susceptibility

In order to compute $\Xi(\omega)$ we split the master equation (2.75) as

$$\frac{d\rho}{dt} = \mathcal{L}_0\rho + \alpha\, 2\cos(\omega t)\,\mathcal{L}_1\rho \tag{2.76}$$

with the unperturbed

$$\mathcal{L}_0 = -i[H_{\mathrm{sc}},\rho] + 2\sum_{ij}\Gamma_{ij}\Big(L_{ij}\rho L^\dagger_{ij} - \frac{1}{2}\{L^\dagger_{ij}L_{ij},\rho\}\Big) + \mathcal{D}\rho\mathcal{D} - \frac{1}{2}\{\mathcal{D}^2,\rho\} \tag{2.77}$$

and perturbed part

$$\mathcal{L}_1\rho = -ig(\omega)[G(t),\rho]. \tag{2.78}$$

In absence of perturbation, $\mathcal{L}_1 = 0$ ($\alpha = 0$) the solution of the master equation can be written as

$$\rho_{ij}(t) = \rho_{ij}(0)\mathrm{e}^{-(i\Delta_{ij}+\Gamma_{ij})t}, \tag{2.79}$$

where Δ_{ij} is the energy gap between $|i\rangle$ and $|j\rangle$. With this at hand, we can use the linear-response theory and write, (see Ref. [135, Chap. 6]),

$$\begin{aligned}\Xi(\omega) &= \Xi_r(0) + i\omega \int_0^\infty dt\, \Xi_r(t)\, e^{i\omega t} \\ &= \sum_{ij} G_{ij}\rho_{ji}(0)\big(1 + i\omega \int_0^\infty dt\, e^{-(\Gamma_{ji}+i(\Delta_{ji}-\omega))t}\big) \\ &= \sum_{ij} G_{ij}\rho_{ji}(0)\frac{\Gamma_{ji}+i\Delta_{ji}}{\Gamma_{ji}+i(\Delta_{ji}-\omega)} \\ &\simeq \sum_{\Delta_{ji}\simeq\omega} G_{ij}\rho_{ji}(0)\frac{\Gamma_{ji}+i\Delta_{ji}}{\Gamma_{ji}+i(\Delta_{ji}-\omega)}\end{aligned} \tag{2.80}$$

Here, $G_{ij} = \langle i|G|j\rangle$. The function $\Xi_r(t)$ stands for the unperturbed evolution when the initial conditions are those computed with the stationary solution for the master equation: $\mathcal{L}_0 + \alpha\mathcal{L}_1$, *i.e.* the total master equation (2.75) with a constant perturbation (without the cosine modulation). The approximation in the last equality considers that the main contribution comes from the terms with frequencies Δ_{ji} closer to the driving frequency ω.

Finding the nondiagonal elements of ρ from the the quantum-optical master equation (2.75) with a constant perturbation instead of the cosine term, we can evaluate $\Xi(\omega)$, so the transmission amplitude t_k from Eq. (2.74).

We will use this method in Sect. 5.2, where we solve the single-photon scattering through a three-level system with cyclic level structure.

2.3 Matrix-Product States

Our model (1.1) can be thought as a many-body system in one dimension. One of the most powerful tools to deal with these systems is matrix-product states (MPS) [87–94]. In this section, we briefly review this technique. We apply this in Sections 3.2, 4.2, 5.1, 5.2, and 5.5.

A general many-body quantum state with N bodies in one dimension can be written as

$$|\Psi\rangle = \sum_{i_1,\ldots,i_N=1}^{d_1,\ldots,d_N} c_{i_1,\ldots,i_N}\, |i_1,\ldots,i_N\rangle\,, \tag{2.81}$$

where $\{c_{i_1,\ldots,i_N}\}$ is a set of complex numbers, $\{|i_n\rangle\}$ is an orthonormal b asis of the Hilbert space of the n-th site, and d_n is the Hilbert-space dimension of the corresponding site. The set of coefficients $c_{i_1,\ldots,i_N}$ can be stored in a matrix $C_{i_1,(i_2,\ldots,i_N)}$. Every matrix $n\times m$ admits a singular-value decomposition (SVD)

[136], that is, a matrix M can be written as

$$M = U\Sigma V^\dagger, \tag{2.82}$$

where U is a $n\times n$ unitary matrix, Σ is a $n\times m$ diagonal matrix with nonnegative entries, called singular values σ_i, and V is unitary $m \times m$. Applying this on C

$$C_{i_1,(i_2,\dots,i_N)} = \sum_{n_2=1}^{D_2} U_{i_1,n_2}\sigma_{n_2}V^*_{(i_2,\dots,i_N),n_2}, \tag{2.83}$$

with $D_2 = \min\{d_1, d_2d_3\dots d_N\}$. Now, we define $(A_1^{i_1})_{1,n_2} = U_{i_1,n_2}$ and $c'_{n_2,i_2,\dots,i_N} = \sigma_{n_2}V^*_{(i_2,\dots,i_N),n_2}$. Then, the state can be written as

$$|\Psi\rangle = \sum_{i_1,\dots,i_N=1}^{d_1,\dots,d_N}\sum_{n_2=1}^{D_2}(A_1^{i_1})_{1,n_2}c'_{n_2,i_2,\dots,i_N}|i_1,\dots,i_N\rangle. \tag{2.84}$$

As before, we store the set of coefficients $c'_{n_2,i_2,\dots,i_N}$ in a matrix $C'_{(n_2,i_2),(i_3,\dots,i_N)}$ and we take the SVD of C'

$$C'_{(n_2,i_2),(i_3,\dots,i_N)} = \sum_{n_3=1}^{D_3} U'_{(n_2,i_2),n_3}\sigma'_{n_3}V'^*_{(i_3,\dots,i_N),n_3}, \tag{2.85}$$

with $D_3 = \min\{D_2d_2, d_3d_4...d_N\}$. We define $(A_2^{i_2})_{n_2,n_3} = U_{(n_2,i_2),n_3}$ and $c''_{n_3,i_3,\dots,i_N} = \sigma'_{n_3}V'^*_{(i_3,\dots,i_N),n_3}$. Therefore,

$$|\Psi\rangle = \sum_{i_1,\dots,i_N=1}^{d_1,\dots,d_N}\sum_{n_2,n_3=1}^{D_2,D_3}(A_1^{i_1})_{1,n_2}(A_2^{i_2})_{n_2,n_3}c''_{n_3,i_3,\dots,i_N}|i_1,\dots,i_N\rangle. \tag{2.86}$$

Iterating this procedure

$$|\Psi\rangle = \sum_{i_1,\dots,i_N=1}^{d_1,\dots,d_N}\sum_{n_2,\dots,n_N=1}^{D_2,\dots,D_N}(A_1^{i_1})_{1,n_2}\dots(A_{N-1}^{i_{N-1}})_{n_{N-1},n_N}c^{(N-1)}_{n_N,i_N}|i_1,\dots,i_N\rangle. \tag{2.87}$$

Defining $(A_N^{i_N})_{n_N,1} = c^{(N-1)}_{n_N,i_N}$

$$|\Psi\rangle = \sum_{i_1,\dots,i_N=1}^{d_1,\dots,d_N}\sum_{n_2,\dots,n_N=1}^{D_2,\dots,D_N}(A_1^{i_1})_{1,n_2}(A_2^{i_2})_{n_2,n_3}\dots(A_{N-1}^{i_{N-1}})_{n_{N-1},n_N}(A_N^{i_N})_{n_N,1}|i_1,\dots,i_N\rangle. \tag{2.88}$$

Notice that the sums in $n_2,\dots,n_N$ are in fact products of the matrices $A_1^{i_1}$, $A_2^{i_2}$, etc., so we can rewrite the state as

$$|\Psi\rangle = \sum_{i_1,\dots,i_N=1}^{d_1,\dots,d_N} A_1^{i_1}\dots A_N^{i_N}|i_1,\dots,i_N\rangle. \tag{2.89}$$

We have shown that every $c_{i_1,\dots,i_N}$ can be written as a product of matrices $D_1 \times D_2, \dots, D_N \times D_{N+1}$, with $D_1 = D_{N+1}$. This is a matrix-product state [90]. In the example, $D_1 = 1$, but it can take other values; *e.g.*, when working with periodic boundary conditions. Taking this into account, the general form of an MPS reads

$$|\Psi\rangle = \sum_{i_1,\dots,i_N=1}^{d_1,\dots,d_N} \mathrm{Tr}(A_1^{i_1} \dots A_N^{i_N}) |i_1, \dots, i_N\rangle. \tag{2.90}$$

In other words, every coefficient $c_{i_1,\dots,i_N}$ can be expressed as

$$c_{i_1,\dots,i_N} = \mathrm{Tr}(A_1^{i_1} \dots A_N^{i_N}) = (A_1^{i_1})_{n_1,n_2} (A_2^{i_2})_{n_2,n_3} \dots (A_N^{i_N})_{n_N,n_1}, \tag{2.91}$$

where the repeated indices are summed. Generally, we take this convention from now on; otherwise, we will explicitly state it.

Let us discuss the meaning of the indices of $(A_m^{i_m})_{n_m,n_{m+1}}$. First, i_m is the physical index, since it gives the state of the m-th site. The others, n_m and n_{m+1}, are the so-called virtual indices, since they do not have a physical origin. However, as we will see in the following, they have a clear meaning.

2.3.1 MPS as an efficient description of one-dimensional many-body states

Now, we justify why the representation of many-body states in terms of MPS is efficient. For simplicity, let $d_m = d$ and $D_m = D$, $\forall m$. Therefore, Eq. (2.90) has dD^2N numbers to encode d^N coefficients. This means that, if we want to describe exactly the original state, D has to be exponentially large. However, as we will argue, we can truncate the bond dimensions D_m to $\chi_m \ll D_m$ under certain circumstances, such that the new state

$$|\Psi_\chi\rangle = \sum_{i_1,\dots,i_N=1}^{d_1,\dots,d_N} \sum_{n_1,n_2,\dots,n_N=1}^{\chi_1,\chi_2,\dots,\chi_N} (A_1^{i_1})_{n_1,n_2} \dots (A_N^{i_N})_{n_N,n_1} |i_1, \dots, i_N\rangle. \tag{2.92}$$

is arbitrarily close to the original one, Eq. (2.90). In order to justify this, we need to discuss a couple of concepts: the corner of the Hilbert space and entanglement.

It is widely accepted that the physical states live on a tiny subspace or *corner* of the Hilbert space. This can be justified: if we consider time evolution of a general state up to time t, with t polynomial in the number of bodies N, the evolved state samples an exponentially small volume in Hilbert space [137]. It is our task to figure out the corner of our problem. As we will see now, these states share a property: they are slightly entangled.

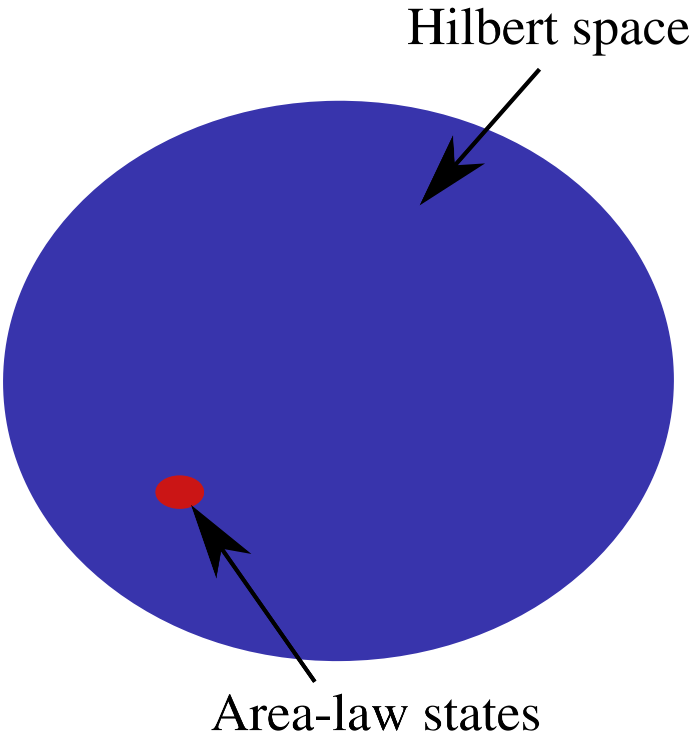

Figure 2.1: Graphical representation of the whole Hilbert space and the tiny subspace of states obeying the area law.

But, what is entanglement? A system consisting of two subsystems A and B is entangled if the state of the whole system is not a tensor product of two states belonging to each subsystem, *i.e.*, if it cannot be written in the following way

$$|\Psi\rangle = |\Phi_A\rangle|\xi_B\rangle. \tag{2.93}$$

This implies that each subsystem is not described by a pure state, but they are in mixed states, that is, density matrices. Entanglement is one of the most genuine quantum characteristics, since there does not exist an analogous concept in classical physics.

One of the most celebrated quantities to quantify entanglement is the Von Neumann entropy [138]

$$S_{\mathrm{VN}} = -\mathrm{Tr}(\rho \log \rho), \tag{2.94}$$

where ρ is the reduced density matrix corresponding to one of the subsystems (S_{VN} does not depend on the chosen subsystem provided the whole system is in a pure state). Let us consider a system living on a $\mathcal{D}$-dimensional physical space. We do a bipartition of the system into two subsystems A and B, with Hilbert spaces H_A and H_B. Let us define L as some typical length of the "surface" separating both subsystems[1]. The entanglement entropy S_{VN} between H_A and H_B for an arbitrary state $|\Psi\rangle$ scales with $L^{\mathcal{D}}$. However, ground states of gapped local Hamiltonians follow the so-called area law, which states that S_{VN} scales with $L^{\mathcal{D}-1}$. We show this graphically in Fig. 2.1. This law arose in the context of black holes [139], but it turned out to be a general law for quantum-field theories and condensed-matter physics [140].

Therefore, the ground state belongs to the subset of states with low entanglement. In this work, we consider few-photon states on the ground state, so we expect them to be slightly entangled. In other words, the low-energy sector is equivalent to the low-entanglement sector and this is our *corner*.

Let us argue why MPS are efficient to describe this corner. The coefficient D_m is the rank of the reduced density matrices corresponding to the sites $\{1, \ldots, m\}$ and $\{m+1, \ldots, N\}$ [90]. It gives a measurement of the entanglement: if it is one, the state is not entangled since both reduced density matrix are pure states, whereas if $D > 1$, the subsystems are not described by pure states and the system is entangled. It can be rigorously shown that D is a good entanglement measure, since it sets an upper bound for the Von Neumann entropy [90]. In consequence, we can efficiently parametrize states with low entanglement using MPS. This is formalized in [93], where the authors show that the distance between the most optimal MPS and the real ground state is exponentially small with the number of bodies N if D increases polynomially with N. In consequence, we can solve the problem with a polynomial complexity, instead of exponential.

There are previous methods related to MPS, such as the numerical renormalization group (NRG) [141] and the density-matrix renormalization group (DMRG) [142]. In fact, DMRG gives an MPS as ground state [88, 89]. DMRG studies reinforce our previous discussion, since they showed that the ground or even slightly excited states of 1D gapped Hamiltonians are slightly entangled [142]; in particular, given one of these states and a bipartition of the system, the singular values of the corresponding density matrices, which are good measures for entanglement, decay exponentially.

It is important to remark that MPS is best suited to 1D systems. This is related to the area law, since it means that entanglement is smaller when the spatial dimension decreases. In addition, notice that the construction of an MPS is adapted to the 1D geometry, since D_m measures the entanglement between the piece of the chain at the left of m (including m) and the rest. If we tried to apply this program to a higher-dimensional system, D_m would not have the same meaning and we could not truncate it drastically. Anyway,

---

[1] By surface we mean a $\mathcal{D}-1$-dimensional space contained in the whole $\mathcal{D}$-dimensional space.

there are similar methods suited to higher dimensions [93, 94], such as projected entangled-pair states (PEPS).

2.3.2 Diagrammatic representation: Norm and expected values

When one considers different operations with MPS, it is much easier to do diagrammatic representations. They are helpful to develop a deeper intuition on MPS and tensor networks in general. We will use both the diagrammatic representation and explicit formulas in this section.

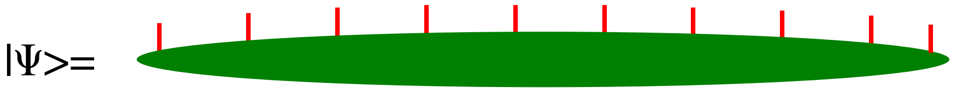

Figure 2.2: Diagrammatic representation of a state $|\Psi\rangle$. Each red leg corresponds to a physical index i_m.

A general coefficient $c_{i_1,\dots,i_N}$ can be graphically expressed as seen in Fig. 2.2. Besides, when written in terms of tensors $(A_m^{i_m})_{n_m,n_{m+1}}$, see Eq. (2.91), $c_{i_1,\dots,i_N}$ can be represented as a network, as seen in Fig. 2.3. There, the circles are the tensors A_m, the legs pointing up correspond to the physical indices i_m and the others are the virtual ones, n_m, n_{m+1}. We contract the joined indices, which in this case are n_m, n_{m+1}. We will follow this convention in all the graphical representations of MPS.

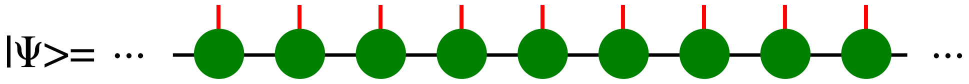

Figure 2.3: MPS diagrammatic representation of a state $|\Psi\rangle$. Each tensor is represented as a green circle with three legs: two horizontal (virtual) and one vertical (physical). The virtual legs (horizontal black lines) are contracted, since they are joined, whereas the physical ones (vertical red lines) are not.

We can compute the square of the norm

$$\begin{aligned}\langle\Psi|\Psi\rangle =& c^*_{i_1,\dots,i_N} c_{i_1,\dots,i_N}\\ =&(A_1^{i_1})^*_{n_1,n_2}(A_2^{i_2})^*_{n_2,n_3}\dots(A_N^{i_N})^*_{n_N,n_1}\\ &(A_1^{i_1})_{l_1,l_2}(A_2^{i_2})_{l_2,l_3}\dots(A_N^{i_N})_{l_N,l_1}.\end{aligned}\tag{2.95}$$

Here we also have to contract the physical indices, which we show graphically in Fig. (2.4). Notice that we can get $\langle\Psi|\Psi\rangle$ without computing all the coefficients $c_{i_1,\dots,i_N}$.

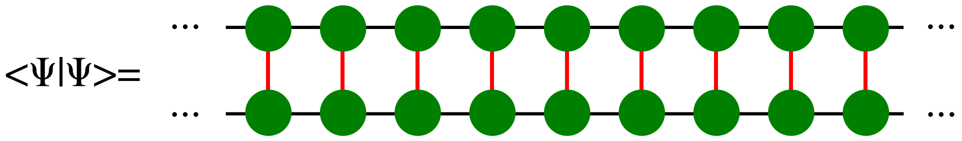

Figure 2.4: Diagrammatic representation of $\langle\Psi|\Psi\rangle$. Now, the physical indices are also contracted.

We also calculate expected values. Every operator can be written as a sum of products of local operators, that is, a sum of operators like

$$O = O_1 \otimes O_2 \otimes \cdots \otimes O_N, \tag{2.96}$$

where O_m is an operator acting on the m-th site. If $O_m^{i_m,j_m} = \langle i_m|O_m|j_m\rangle$ and $(E_m)_{i,j,k,l} = (A_m^{i_m})^*_{i,k} O_n^{i_m,j_m} (A_m^{j_m})_{j,l}$, where m is not summed, the expected value of such a product of local operators is

$$\begin{aligned}\langle O\rangle &= (A_1^{i_1})^*_{n_1,n_2} O_1^{i_1,j_1} (A_1^{j_1})_{l_1,l_2} (A_2^{i_2})^*_{n_2,n_3} O_2^{i_2,j_2} (A_2^{j_2})_{l_2,l_3} \\ &\quad \ldots (A_N^{i_N})^*_{n_N,n_1} O_N^{i_N,j_N} (A_N^{j_N})_{l_N,l_1} \\ &= (E_1)_{n_1,l_1,n_2,l_2} (E_2)_{n_2,l_2,n_3,l_3} \ldots (E_N)_{n_N,l_N,n_1,l_1}.\end{aligned} \tag{2.97}$$

As before, it is possible to compute the expected value of an operator without previously computing the coefficients $c_{i_1,\ldots,i_N}$, just via the tensors. The graphical representation is in Fig. 2.5. Note that each blue box corresponds to one of the O_m and has two physical indices, which are contracted with those of $|\Psi\rangle$ and $\langle\Psi|$. For some complicated operators, this scheme can be quite inefficient. In such a case, as we will explain later, we can write an operator in its matrix-product-operator representation, which we shall introduce later, so that the expected value can be obtained directly without writing the operator in a sum of operators like (2.96).

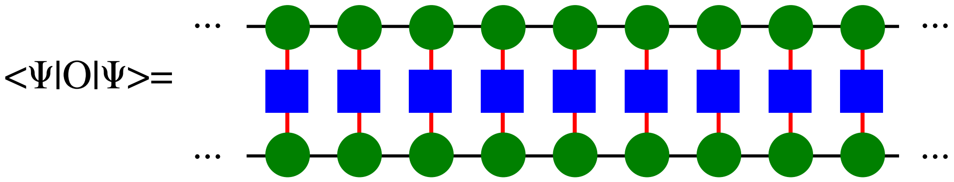

Figure 2.5: Graphical representation of $\langle\Psi|O|\Psi\rangle$. Each blue box represents the local operators O_1, O_2, etc.

2.3.3 Truncation procedure

One of the keys of the MPS technique is the truncation process. Given a state $|\Psi\rangle$ written as an MPS, given by Eq. (2.90), with bond dimensions χ_m, the truncation procedure consists of finding a new set of tensors with smaller values of the virtual indices $\chi'_m < \chi_m$. Mathematically, we have to minimize the distance between the initial state $|\Psi\rangle$ (with tensors A_m) and another MPS $|\Phi\rangle$ with smaller tensors B_m. That is, we want to minimize

$$F(|\Psi\rangle, |\Phi\rangle) = (\langle\Psi| - \langle\Phi|)(|\Psi\rangle - |\Phi\rangle) = 1 + \langle\Phi|\Phi\rangle - 2\mathrm{Re}(\langle\Psi|\Phi\rangle). \tag{2.98}$$

One has to compute $\langle\Phi|\Phi\rangle$ and $\langle\Psi|\Phi\rangle$, which can be done by standard MPS techniques, as explained in the previous section. Once we have these quantities, we can minimize the distance in an iterative way, *i.e.* we minimize the distance with respect to B_1, with all the tensors constant, after that, the tensors B_1, B_3, B_4, etc. remain constant and the function is minimized with respect to B_2, and so on. Let us define $v_m^{A(B)}$ as the vectorization of the tensor $A_m(B_m)$. As shown in App. A, minimizing F with respect to B_m is equivalent to minimize the following quadratic form

$$f_m(A_m, B_m) = 1 + (v_m^A)^\dagger M_1 v_m^B - 2\mathrm{Re}\left((v_m^A)^\dagger M_2 v_m^B\right), \tag{2.99}$$

where M_1 and M_2 are matrices introduced in App. A, which depend on the rest of the tensors. Notice that f_m is equal to F, but its variables are just the tensors linked to the m-th site. It achieves its minimum value when v_m^A and v_m^B fulfill the following system of linear equations, which is obtained after some tedious but straightforward algebra:

$$M_1 v_m^A = M_2^\dagger v_m^B. \tag{2.100}$$

By iterating this process, we find optimal tensors for every site. It is possible to sweep the lattice several times until some convergence criteria is fulfilled, *e.g.*, when the distance is smaller than a preset tolerance.

2.3.4 Time evolution: real and imaginary time

We explain here how to do time evolution with MPS. We restrict ourselves to time-independent Hamiltonians. The time-evolution operator relating the state at different times, $U(t)\,|\Psi\rangle = |\Psi(t)\rangle$, reads (remember that we are taking $\hbar = 1$):

$$U(t) = \exp(-iHt). \tag{2.101}$$

In many-body physics, the Hamiltonians are usually sums of local terms, that is

$$H = \sum_{i=1}^{N} h_i, \tag{2.102}$$

where h_i encapsulates the local Hamiltonian of the i-th site and the interactions between this site and a finite set of neighbors around it. Here, we just consider nearest-neighbor interaction, so h_i encodes the interaction between the sites i and $i+1$ [2].

Computing $U(t)$ exactly and applying it on an MPS is not convenient, because the result is not an MPS anymore. We need to take some approximations. First, we split the Hamiltonian: $H = H_O + H_E$, with $H_O = h_1 + h_3 + \ldots$, *i.e.* the Hamiltonian corresponding to the odd links and $H_E = h_2 + h_4 + \ldots$ that corresponding to the even ones. Both of them are sums of commuting Hamiltonians, $[h_n, h_{n+2}] = 0$. Assuming N even

$$\exp(-iH_O t) = \exp(-ih_1 t)\exp(-ih_3 t)\ldots\exp(-ih_{N-1}t), \tag{2.103}$$

$$\exp(-iH_E t) = \exp(-ih_2 t)\exp(-ih_4 t)\ldots\exp(-ih_N t). \tag{2.104}$$

We have to express $\exp(-i(H_E + H_O)t)$ in terms of exponentials of H_E and H_O. We use the Suzuki-Trotter decompositions [143]. The second-order one is

$$\exp\left(-i(H_E + H_O)\Delta t\right) = \exp(-iH_E\Delta t)\exp(-iH_O\Delta t) + \mathcal{O}(\Delta t^2). \tag{2.105}$$

There are improved versions [92], such as the third-order one, which is the one that we have used in this thesis

$$\begin{aligned}&\exp\left(-i(H_E + H_O)\Delta t\right)\\ &= \exp(-iH_E\Delta t/2)\exp(-iH_O\Delta t)\exp(-iH_E\Delta t/2) + \mathcal{O}(\Delta t^3).\end{aligned} \tag{2.106}$$

We compute $|\Psi(t)\rangle = U(t)|\Psi\rangle$ by applying n times $U(\Delta t)$ on $|\Psi\rangle$, with Δt such that $n\Delta t = t$. We plot the diagrammatic representation of a single step, $U(\Delta t)|\Psi\rangle$, in Fig. 2.6. We see that the algorithm consists of acting sequentially with a set of one- and two-body operators.

Applying $u_m(t) = e^{-ih_m t}$, a one- or two-body operator, on an MPS is a trivial task [90]. If $u_m(t)$ is a one-body operator, once applied on an MPS, the result is trivially an MPS. If $u_m(t)$ is a two-body operator (Fig. 2.7), the new state is not an MPS anymore, since it mixes the tensors corresponding to the sites m and $m+1$, and the new state has a tensor linked to the couple of sites $(m, m+1)$ ($B_{m,m+1}$ in Fig. 2.7). Iterating this process, we would get a state without a tensor-product structure, with an exponentially large amount of parameters. However, we recover the MPS structure after one step by doing a singular value decomposition (SVD) of the tensor $B_{m,m+1}$, getting a new couple of tensors A'_m and A'_{m+1}. The drawback is that χ_m, the dimension of

---

[2] h_N considers the interaction between N and 1 if periodic boundary conditions (pbc) are implemented, whereas it is just a free Hamiltonian for the site N if we consider free boundary conditions (fbc).

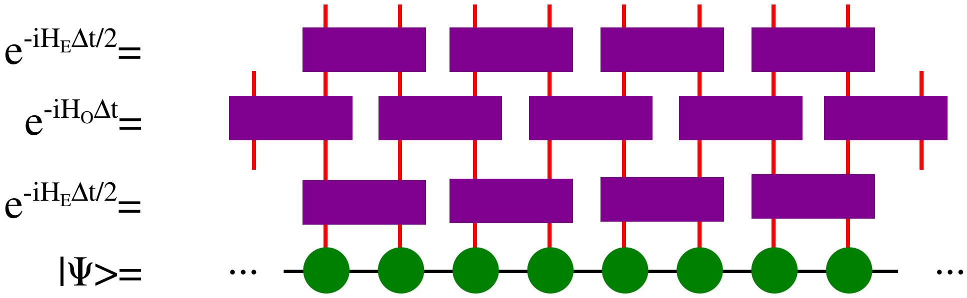

Figure 2.6: A single step of time evolution, applying the third-order Suzuki-Trotter expansion: $U(t) = e^{-iH_E\Delta_t/2}e^{-iH_O\Delta_t}e^{-iH_E\Delta_t/2}$. Notice that each term $e^{-ih_m t}$ (purple boxes) is a four-leg tensor, since it acts on two sites.

the link connecting m and $m+1$, increases. In order to control the value of χ_m, we apply the truncation procedure explained in the previous section after each step.

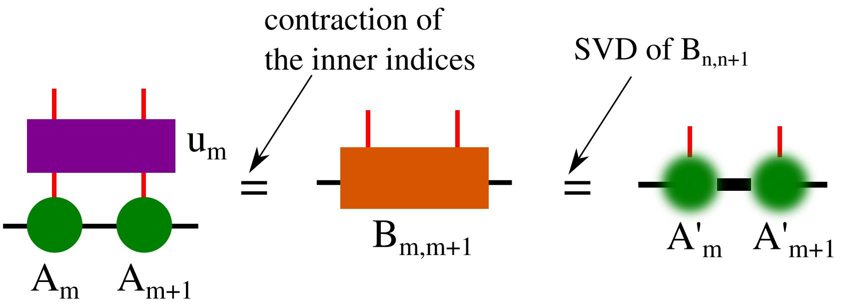

Figure 2.7: Steps of time evolution under MPS for two-body gates: (i) we apply u_m (purple box) on $|\Psi\rangle$, affecting just A_m and A_{m+1} (green circles), (ii) we contract the corresponding internal indices and get a new tensor $B_{m,m+1}$ associated to the sites m and $m+1$ (orange box), and (iii) we split $B_{m,m+1}$ by means of a SVD to get a new pair of tensors A'_m and A'_{m+1} (blurred green circles).

As a final remark, there exist other ways to implement the time evolution, *e.g.*, Runge Kutta and Arnoldi-like methods [92].

Imaginary evolution: computing the low-energy eigenstates

Evolution with imaginary time (with negative imaginary part) sends the initial state to the ground state, provided they are not orthogonal. Let us prove this. First, any state can be written as a sum of eigenstates of the Hamiltonian $\{|\phi_n\rangle\}$, whose eigenvalues $\{E_n\}$ are such that $E_0 < E_1 < E_2 \leq E_3 \leq \dots$ (we consider that there can be degenerate states, but the ground and the first-excited state are unique)

$$|\Psi(0)\rangle = \sum_n c_n |\phi_n\rangle. \tag{2.107}$$

Applying time evolution

$$|\Psi(t)\rangle = e^{-iHt}|\Psi(0)\rangle = \sum_n c_n e^{-iE_n t}|\phi_n\rangle. \tag{2.108}$$

If $t = -i\tau$, with $\tau \in \mathbb{R}^+$:

$$|\Psi(\tau)\rangle = \sum_n c_n e^{-E_n \tau}|\phi_n\rangle. \tag{2.109}$$

Since the time evolution is not unitary in this case, we define $|\varphi(\tau)\rangle$ by normalizing $|\Psi(\tau)\rangle$

$$|\varphi(\tau)\rangle = \frac{|\Psi(\tau)\rangle}{\sqrt{\langle\Psi(\tau)|\Psi(\tau)\rangle}} = \frac{\sum_n c_n e^{-E_n\tau}|\phi_n\rangle}{\sqrt{\sum_m |c_m|^2 e^{-2E_m\tau}}}. \tag{2.110}$$

Taking the limit $\tau \to \infty$

$$\lim_{\tau\to\infty} |\varphi(\tau)\rangle = \frac{c_0}{|c_0|}|\phi_0\rangle, \tag{2.111}$$

which is equal to the ground state. Once we know the ground state, we can compute excited states. For instance, the first-excited state can be found as the minimum-energy state orthogonal to the ground state. In other words, given the seed state (2.107), we have to substitute it by

$$|\Psi'(0)\rangle = |\Psi(0)\rangle - \langle\phi_0|\Psi(0)\rangle\,|\phi_0\rangle\,. \tag{2.112}$$

Applying imaginary-time evolution on $|\Psi'(0)\rangle$, defining $|\varphi'(\tau)\rangle$ analogously to $|\varphi(\tau)\rangle$ (Eq. (2.110)) and taking the long-time limit

$$\lim_{\tau\to\infty} |\varphi'(\tau)\rangle = \frac{c_1}{|c_1|}\,|\phi_1\rangle\,, \tag{2.113}$$

which is the first-excited state. We can iterate this process to find other excited states. In order to compute these states there are alternative routes, but they depend on the symmetries of the considered problem. We will illustrate this with a particular example in Sect. 3.2. These methods (both the orthogonalization one and the alternative routes we will introduce later) work if the gap between $|\phi_n\rangle$ and $|\phi_{n+1}\rangle$ is finite. Therefore, they are not valid for computing scattering states, since they belong to a continuum, to say an example.

In our case, our system will be initially (before generating the input photons) in the ground state, since experimental realizations of few-photon scattering problems usually work at low temperatures. However, as we will see, the knowledge of the low-energy states provides useful information on the scattering properties.

Finally, let us note that there are other methods to find the ground state. For instance, it is possible to minimize the expected value of the Hamiltonian [93].

2.3.5 Matrix-Product Operators (MPO)

We introduce here a representation of operators analogous to MPS. We can always write a general operator O as a product of tensors [144, 145]

$$O = \mathrm{Tr}(C_1^{i_1,j_1} C_2^{i_2,j_2} \dots C_L^{i_N,j_N}) |i_1 i_2 \dots i_N\rangle\langle j_1 j_2 \dots j_N|. \tag{2.114}$$

This is the so-called matrix-product-operator (MPO) representation. We show it graphically in Fig. 2.8.

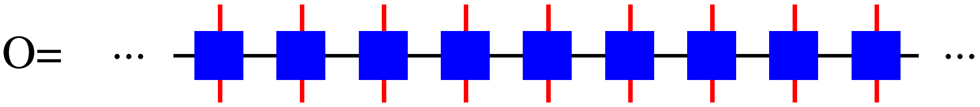

Figure 2.8: Diagram of an MPO. The blue squares represent the local tensors $(C_m^{i_m,j_m})_{n_m,n_{m+1}}$. There are two vertical lines per site, one for each physical index, i_m and j_m.

We can apply an operator written as an MPO on an MPS and the result is still an MPS. Let us show this by applying O on a general MPS $|\Psi\rangle$ (2.90)

$$O|\Psi\rangle = (C_1^{i_1,j_1})_{n_1,n_2}(A_1^{j_1})_{m_1,m_2} \dots (C_N^{i_N,j_N})_{n_N,n_1}(A_L^{j_N})_{m_N,m_1}|i_1 \dots i_N\rangle. \tag{2.115}$$

We define $(B_a^{i_a})_{[n_a,m_a],[n_{a+1},m_{a+1}]} = (C_a^{i_a,j_a})_{n_a,n_{a+1}}(A_a^{j_a})_{m_a,m_{a+1}}$. Considering $[n_a, m_a]$ and $[n_{a+1}, m_{a+1}]$ as single indices

$$O|\Psi\rangle = (B_1^{i_1})_{[n_1,m_1],[n_2,m_2]}(B_2^{i_2})_{[n_2,m_2],[n_3,m_3]} \dots (B_L^{i_L})_{[n_L,m_L],[n_1,m_1]}|i_1 i_2 \dots i_L\rangle, \tag{2.116}$$

we see $O\,|\Psi\rangle$ is an MPS. We illustrate this pictorially in Fig. 2.9. This result has several applications. For instance, we can compute an expected value $\langle\Psi|O|\Psi\rangle$, since $O\,|\Psi\rangle$ is also an MPS and the expected value turns out to be a scalar product between two MPS. We can also do time evolution. Let us integrate the Schrödinger equation by means of the Euler algorithm, $|\Psi(t+\Delta t)\rangle = -i\Delta t H\,|\Psi(t)\rangle$. If we know the MPO representation of H, $|\Psi(t+\Delta t)\rangle$ can be easily computed. This can be generalized to finer methods mentioned in the previous section, such as a Runge-Kutta or Arnoldi-like algorithms [92].

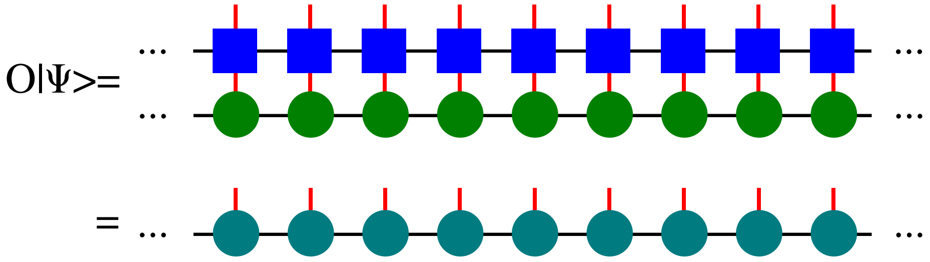

Figure 2.9: An operator O acting on a state $|\Psi\rangle$, using their MPO and MPS representations, respectively. Contracting the internal physical indices, we get a new MPS (turquoise circles).

We finally explain how to find the MPO representation of an operator O. In general, it is not trivial at all. It is feasible for some simple cases. For instance, a sum of one-body operators

$$O_1 = \sum_{m=1}^{N} X_m, \tag{2.117}$$

has a simple MPO representation. Defining $(X_m)_{i_m,j_m} = \langle i_m|X_m|j_m\rangle$, it is straightforward to show that the following matrices are valid [144]

$$C_m^{i_m,j_m} = \begin{pmatrix} \delta_{i_m,j_m} & 0 \\ (X_m)_{i_m,j_m} & \delta_{i_m,j_m} \end{pmatrix} \qquad m = 2,3,\dots,L-1, \tag{2.118}$$

whereas $C_1^{i_1,j_1} = ((X_1)_{i_1,j_1}, \delta_{i_1,j_1})$ and $C_L^{i_L,j_L} = (\delta_{i_L,j_L}, (X_L)_{i_L,j_L})^T$. We can also find the tensors for a particular case of a sum of two-body operators

$$O_2 = \sum_{m=1}^{N} X_m Y_{m+1}. \tag{2.119}$$

The following matrices represent this state [144]

$$C_m^{i_m,j_m} = \begin{pmatrix} \delta_{i_m,j_m} & 0 & 0 \\ (Y_m)_{i_m,j_m} & 0 & 0 \\ 0 & (X_m)_{i_m,j_m} & \delta_{i_m,j_m} \end{pmatrix} \qquad n = 2,3,\dots,N-1, \tag{2.120}$$

$C_1^{i_1,j_1} = (0, (X_1)_{i_1,j_1}, \delta_{i_1,j_1})$ and $C_L^{i_N,j_N} = (\delta_{i_N,j_N}, (Y_N)_{i_N,j_N}, 0)^T$. As before, $(Y_n)_{i_n,j_n}$ are the matrix elements of Y_n. In the following section, we will introduce an important application of this to write some instances of quantum states as MPS.

2.3.6 Writing states as MPS

We need to write the initial state as an MPS. Doing this for a general state is complicated, or even computationally impossible, since one has to take the

SVD of exponentially huge matrices. Luckily, there are some tools to write a state as an MPS in some simple cases. In this section, we consider some instances.

Product states

Let us consider first the simplest case, that is, product states, in which the n-th body is in the state

$$|\psi_n\rangle = \sum_{i_n=1}^{d_n} c_{i_n}^{n} |i_n\rangle , \tag{2.121}$$

so

$$|\Psi\rangle = \sum_{i_1,i_2,\ldots,i_N=1}^{d_1,d_2,\ldots,d_N} c_{i_1}^{1} c_{i_2}^{2} \ldots c_{i_N}^{N} |i_1, i_2, \ldots, i_N\rangle. \tag{2.122}$$

Comparing this with (2.89), we see that this already is a MPS with $D = 1$ for all the matrices and $A_m^{n_m} = c_{n_m}^{m}$. This allows us to use product states as seeds for imaginary-time evolution.

Case with several excitations

When working with scattering problems, the initial state is not generally a product state. Usually, the system is initially in its ground state and then one generates some input photons. In order to create a photon, it is necessary to apply

$$A_c = \sum_x c_x a_x^{\dagger}, \tag{2.123}$$

on the ground state. Since A_c is a sum of one-body operators, it accepts a simple MPO representation (see Eq. (2.118)). If we know the MPS representation of the ground state, which can be found by imaginary-time evolution, we can create a photon by applying the MPO representation of A_c on the ground state, and the new state is still an MPS, as discussed in Sect. 2.3.5 (see Fig. 2.9). If we want to simulate scattering with more photons, we just have to apply operators like A_c several times.

2.4 Exact diagonalization

If the dimension of the Hilbert space is not too large, we can exactly diagonalize the Hamiltonian (1.1). *E.g.*, if we consider an array with few cavities (less than 10, roughly) or if we can restrict ourselves to a tiny subspace of the Hilbert space.

This relies on finding a basis of the Hilbert space, $\{|\phi_n\rangle\}$, computing the matrix elements of the Hamiltonian, $H_{nm} = \langle\phi_n|H|\phi_m\rangle$, and ing such a matrix. Here, *exact* can be misleading, since we refer to some standard numerical algorithm for diagonalizing a matrix, such as QR algorithm, power method, etc.

In this work, generally, the complexity of the problems is too big, so we usually employ the approximate methods shown in the previous sections. However, we can solve the Hamiltonian (1.1) with exact diagonalization for some instances, *e.g.*, the single-particle dynamics of a tight-binding chain coupled to a two-level atom or impurity (see Sect. 3.3).

Chapter 3

Spectral Properties of H

The power of the new quantum mechanics in giving us a better understanding of events on an atomic scale is becoming increasingly evident. The structure of the helium atom, the existence of half-quantum numbers in band spectra, the continuous spatial distribution of photo-electrons, and the phenomenon of radioactive disintegration, to mention only a few examples, are achievements of the new theory which had baffled the old.

Arthur Compton, Foreword to the English edition of The Physical Principles of the Quantum Theory by W. Heisenberg (1930) [146].

Given a Hamiltonian H describing a physical system, its eigenstates $\{|\phi_n\rangle\}$ and energies (or frequencies, since we use a system of units where $\hbar = 1$) $\{\omega_n\}$ fully determine the physical properties of the system. For instance, if the system is isolated, the time evolution of a state $|\Psi(t)\rangle$ can be written in terms of them

$$|\Psi(t)\rangle = \sum_n c_n e^{-i\omega_n t} |\phi_n\rangle \,, \tag{3.1}$$

with c_n being the projections of the initial state on the n-th eigenstate, $c_n = \langle\phi_n|\Psi(0)\rangle$. Besides, if the system is in thermal equilibrium at temperature T, it is described by a density matrix ρ

$$\rho = \frac{1}{Z}\sum_n e^{-\omega_n/k_B T} |\phi_n\rangle \langle\phi_n| \,, \tag{3.2}$$

where $k_B \simeq 1.38\times 10^{-23}\, m^2\, kg\, s^{-1} K^{-1}$ is the Boltzmann constant and $Z = \sum_n e^{-\omega_n/k_B T}$ is the partition function.

Eigenvalues are also essential in scattering. For instance, the emission and absorption spectra of an atomic ensemble display peaks and extinctions at the energies of the atoms. In a waveguide QED context, the scattering spectrum can also reveal information on the energies of the scatterer. In particular, the reflection spectrum of a photon interacting with a two-level system exhibits a full-reflection resonance when the energy of the photon matches the energy splitting of the two-level system (see [99, 100, 102] and Eq. (2.58)).

Apart from the eigenstates of the isolated scatterers, additional bound states appear due to the interaction between the few-level systems and the photonic media [147–149], with photonic excitations that are confined to the vicinity of the scatterer. These bound states have been shown to be relevant, for instance, in two-photon scattering [103], where the scatterer can end up trapping one of the flying photons. They can also be applied to suppress the decoherence [150], or to enhance the quantum correlations [151–153]. Recently, the photonic bound states have been extended both to the multiparticle domain [154, 155] and to higher dimensional photonic media [156, 157]. They are also relevant experimentally, since a bound state has been found [54] in a circuit QED architecture [47–51]. There are other state-of-the-art technologies where these states can be potentially detected, *e.g.*, photonic crystals [40, 43, 45], cold atoms [73, 74], and diamond structures with color centers [71, 72].

All these examples highlight the relevance of $|\phi_n\rangle$ and ω_n in general and, specifically, for few-photon scattering in 1D systems. In some simple cases, computing the eigenstates and energies of a system can be easily done by means of exact diagonalization (see Sect. 2.4) or even analytically. However, it is usually a highly nontrivial task which can be performed using imaginary-time evolution with MPS (see Sect. 2.3.4). For that, one can find the ground state by considering any seed state that is not orthogonal to it (Eq. (2.107)), and applying imaginary-time evolution in the long-time limit (Eq. (2.111)). Doing the same with a properly chosen seed state orthogonal to all states with lower energy (Eq. (2.112)), we can find low-energy excited states (Eq. (2.113)).

In this chapter we discuss the single-particle eigenstates of H (1.1) under the RWA (analytically) (see Sect. 3.1) and the ground state and first excited states in the ultrastrong coupling regime numerically by means of MPS (see Sect. 3.2). After that, in Sect. 3.3 we study how the bound state influence the spontaneous decay of the two-level atom under the RWA.

3.1 Rotating-Wave Approximation

For our photonic medium, we choose the discrete version of the nonchiral waveguide (1.2) and for the scatterer we take a two-level system or qubit. With this, we rewrite the Hamiltonian of waveguide QED within the RWA, introduced in the introduction (see (1.7))

$$H=\epsilon\sum_x a_x^\dagger a_x - J\sum_x(a_x^\dagger a_{x+1}+\text{H.c.})+\Delta\sigma^+\sigma^-+g(\sigma^-a_{x_{\rm sc}}^\dagger+\sigma^+a_{x_{\rm sc}}). \quad (3.3)$$

The parameters and the operators were already introduced in Sect. 1.1. We fix the position of the scatterer at $x_{\rm sc}=0$. A scheme of the system and its cosine-shaped dispersion relation are shown in Fig. 3.1.

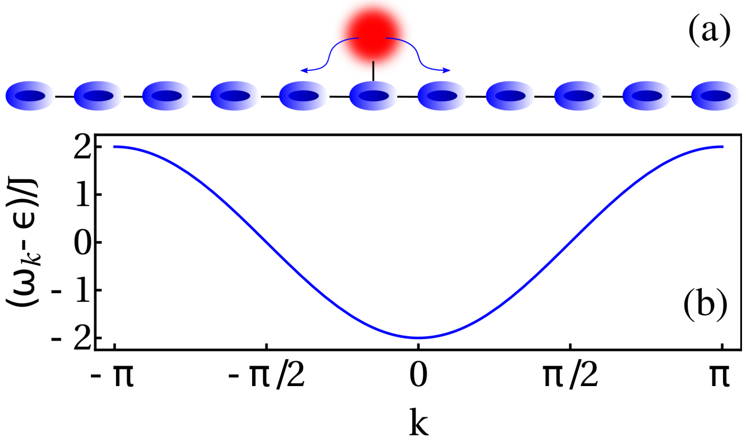

Figure 3.1: **(a) Scheme of the system.** In blue, the bosonic coupled-cavity array. The qubit is represented as a blurred red circle. **(b) Dispersion relation for the bosonic array**.

This Hamiltonian commutes with the number operator (1.9), $[H,N]=0$ (see Sect. 1.1). In consequence, the eigenstates of the Hamiltonian are also eigenstates of N and we can diagonalize H at subspaces with a well-defined number of excitations. We label the eigenstates and energies as $|\phi_n^m\rangle$ and ω_n^m, where m is the number of excitations. In this section, we restrict ourselves to $m=0$ and $m=1$.

The space with zero excitations is trivial. It has one state: the vacuum state of the photonic field $|\text{vac}\rangle$, with the qubit in its ground state $|0\rangle$

$$|\phi_0^0\rangle=|\text{vac}\rangle\,|0\rangle\,. \quad (3.4)$$

Applying the Hamiltonian (3.3) on $|\phi_0^0\rangle$, we trivially show that $\omega_0^0=0$.

In the one-excitation subspace, a complete basis is formed by the scattering eigenstates [102], which we will discuss later, and the bound (localized) states $|\phi_n^1\rangle$ [103, 158], which we introduce now. They read

$$|\phi_n^1\rangle=C_n\left(\sum_x e^{-\kappa_n|x|}a_x^\dagger+d_n\sigma^+\right)|\text{vac}\rangle\,|0\rangle\,, \quad (3.5)$$

The factor C_n is a normalization constant, $1/|\kappa_n|$ is the localization length, and d_n is the qubit amplitude.

First, we show that $|\phi^1_n\rangle$ is an eigenstate of H, that is, it fulfills

$$H\,|\phi^1_n\rangle = \omega^1_n\,|\phi^1_n\rangle\,. \tag{3.6}$$

Applying H on $|\phi^1_n\rangle$:

$$\begin{aligned}H\,|\phi^1_n\rangle = C_n\Bigg(&\epsilon\sum_x e^{-\kappa_n|x|}a^\dagger_x - J\sum_x(e^{-\kappa_n|x+1|}a^\dagger_x + e^{-\kappa_n|x|}a^\dagger_{x+1})\\ &+\Delta d_n\sigma^+ + g(d_n a^\dagger_0 + \sigma^+)\Bigg)\,|\text{vac}\rangle\,|0\rangle\,.\end{aligned} \tag{3.7}$$

In order to show that $|\phi^1_n\rangle$ is an eigenstate, we project Eq. (3.6) on $\langle\text{vac}|\,\langle 0|\,\sigma^-$ and $\langle\text{vac}|\,\langle 0|\,a_x$, taking into account the expressions of $|\phi^1_n\rangle$ and $H\,|\phi^1_n\rangle$, Eqs. (3.5) and (3.7)

$$\Delta d_n + g = d_n\omega^1_n, \tag{3.8}$$

$$\epsilon e^{-\kappa_n|x|} - J(e^{-\kappa_n|x+1|} + e^{-\kappa_n|x-1|}) + g d_n\delta_{x0} = e^{-\kappa_n|x|}\omega^1_n, \tag{3.9}$$

with δ_{xy} being the Kronecker delta. Evaluating (3.9) at $x \neq 0$

$$\omega^1_n = \epsilon - J(e^{-\kappa_n} + e^{\kappa_n}), \tag{3.10}$$

which shows that $|\phi^1_n\rangle$ is an eigenstate, provided we find solutions for κ_n fulfilling Eqs. (3.8) and (3.9) for $x = 0$. From (3.8)

$$d_n = \frac{g}{\omega^1_n - \Delta}. \tag{3.11}$$

Introducing this and the value of ω^1_n (3.10) into Eq. (3.9) for $x = 0$ and defining $\eta_n = e^{-\kappa_n}$

$$\eta_n^4 + \frac{\Delta-\epsilon}{J}\eta_n^3 + \left(\frac{g}{J}\right)^2\eta_n^2 - \frac{\Delta-\epsilon}{J}\eta_n - 1 = 0, \tag{3.12}$$

which is a fourth-degree algebraic equation for η_n. This equation has four solutions. However, we have two constrains: (i) $\text{Re}(\kappa_n) > 0$, so that the photonic population does not explode at $x \to \pm\infty$, and (ii) $\text{Im}(\kappa_n) = 0, \pi$, since the energies $\omega^1_n = \epsilon - J(e^{-\kappa_n} + e^{\kappa_n})$ are real. Numerical evidence shows that there are only two solutions for η_n compatible with these restrictions, so there are two bound states: $|\phi^1_0\rangle$ and $|\phi^1_1\rangle$. Once we know η_n and thus κ_n, we can compute the energy ω^1_n (3.10) and d_n (3.11). Lastly, the normalization factor C_n is

$$C_n = \left(\frac{1+e^{-2\kappa_n}}{1-e^{-2\kappa_n}} + |d_n|^2\right)^{-1/2}. \tag{3.13}$$

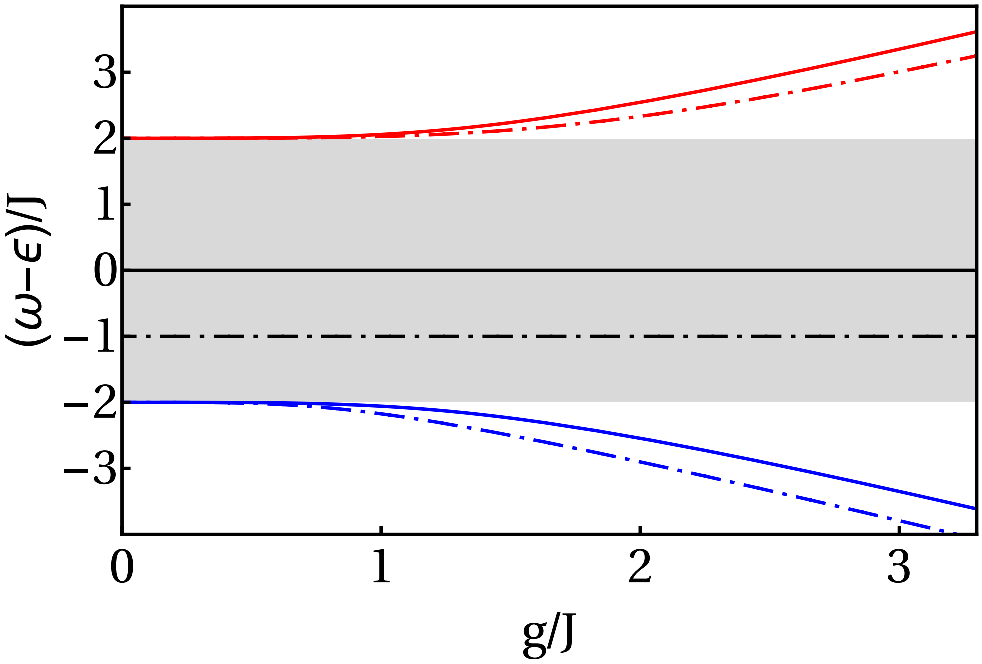

Figure 3.2: **Bound-state energies.** Bound-state energies $(\omega_\pm - \epsilon)/J$ for two cases: $(\Delta - \epsilon)/J = 0$ (solid lines) and $(\Delta - \epsilon)/J = -1$ (dotted-dashed lines). The red curves are for ω_+ and the blue ones for ω_-. As a reference, the values of $(\Delta - \epsilon)/J = 0$ and $(\Delta - \epsilon)/J = -1$ are represented by the solid and dotted-dashed black lines. The photonic band is shown by the shaded region.

These bound states are ubiquitous to the kind of models we study. In fact, as shown in [159], they exist if the band of states of the photonic model is finite; in our case $\omega_k \in (\epsilon - 2J, \epsilon + 2J)$.

We plot the bound-state energies ω_n^1 for $n = 0, 1$ as a function of the coupling constant g, as well as the band of propagating states in Fig. 3.2. We plot these energies with respect to the bare frequencies of the cavities ϵ and in units of the hopping constant J. We show two cases: (i) when the qubit energy Δ is at the middle of the band ($\Delta - \epsilon = 0$, solid lines) and (ii) when Δ is closer to the band bottom ($\Delta - \epsilon = -J$, dotted-dashed lines). The energies of the bound states lie outside of the band, thus they are localized (not propagating). Notice that, if $J \to \infty$, then $\omega_k \in (-\infty, \infty)$, so there cannot be bound states in this case. As $g \to 0$, $\omega_{0(1)}^1$ approaches the bottom (top) of the band. This means that, as the qubit and the photons decouple, the lower (upper) bound state become the photonic state with momentum $k = 0$ ($k = \pi$). If Δ is in the middle of the band, the energies of the bound states are symmetrically located. Otherwise, if the qubit energy is below the center, $\Delta - \epsilon < 0$, the difference between ω_+ and Δ is larger than that between Δ and ω_- ($|\omega_+ - \Delta| > |\omega_- - \Delta|$).

Therefore, the position of the Δ with respect to the band center originates an asymmetry between ω_1^1 and ω_0^1.

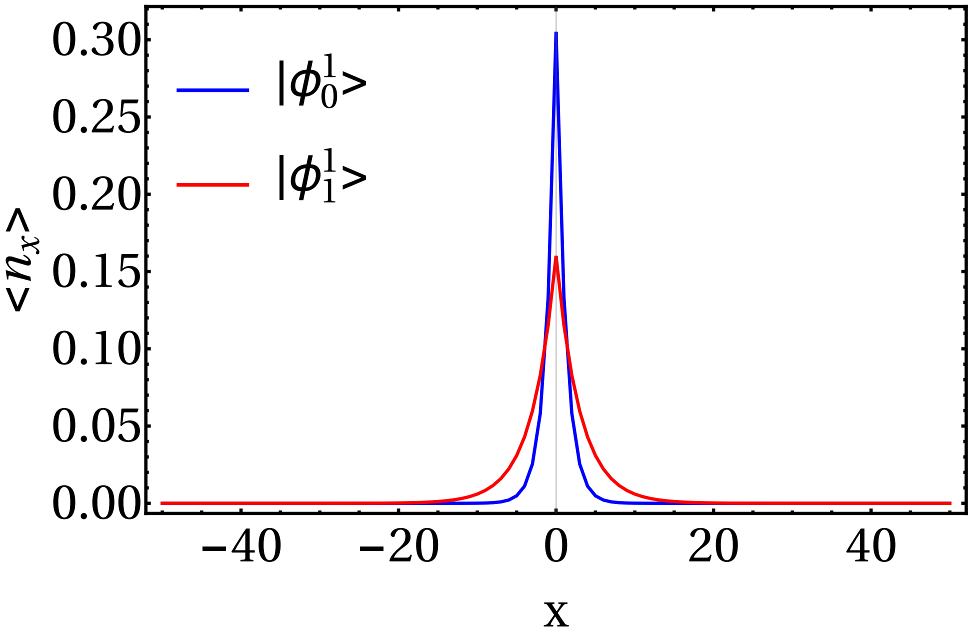

Figure 3.3: **Bound-state populations in RWA.** Bound-state photon population $\langle n_x \rangle$ plotted in red and blue lines for $|\phi_0^1\rangle$ and $|\phi_1^1\rangle$ respectively. The parameters are $(\Delta - \epsilon)/J = -1$ and $g/J = 1$.

We also plot the photon population of both bound states in Fig. 3.3, for a representative case of the qubit energy below the middle of the band, $(\Delta - \epsilon)/J = -1$, for $g/J = 1$. As seen, they are strongly localized around the qubit (in fact, exponentially localized; see Eq. (3.5)).

Let us now review the form of the single-particle scattering eigenstates of (3.3) and their physical implications. They read [102]

$$|\Psi_k\rangle = \Big[\sum_{x<0}(e^{ikx} + r_k e^{-ikx})a_x^\dagger + \sum_{x\geq 0} t_k e^{ikx} a_x^\dagger + d_k b^\dagger\Big]|0\rangle. \tag{3.14}$$

The coefficients t_k and r_k have a clear physical meaning: they are the transmission and reflection amplitudes for an incident plane wave, respectively. They are given by,

$$t_k = \frac{iv_k(\omega_k - \Delta)}{iv_k(\omega_k - \Delta) - g^2}\,, \tag{3.15}$$

$$r_k = t_k - 1\,, \tag{3.16}$$

$$d_k = \frac{g t_k}{\omega_k - \Delta}\,. \tag{3.17}$$

As we saw in the continuous version (see Sect. 2.1 and Eq. (2.55)), this system presents perfect reflection, $R_k \equiv |r_k|^2 = 1$, if the energy of the input photon is equal to Δ, see Eqs. (3.15) and (3.16). This is seen in Figs. 3.4(a) and (b), where R_k is plotted as a function of $(\omega_k - \epsilon)/J$ for several values of Δ and as a function of $(\omega_k - \epsilon)/J$ and $(\Delta - \epsilon)/J$, respectively. Considering the input photon as a single-photon-spectroscopy probe, we could be tempted to argue that, like in the scattering single-photon resonance, the average energy of the emitted photon by the spontaneous emission of a qubit should be the qubit

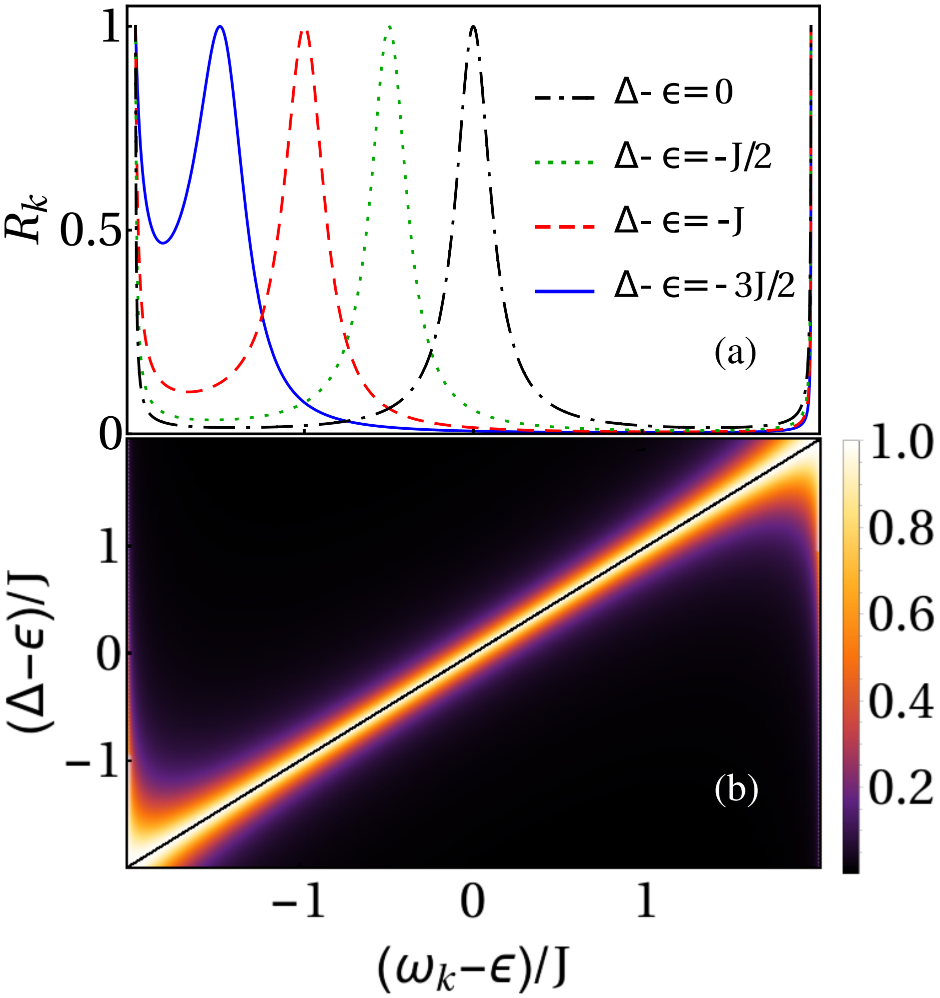

Figure 3.4: **Reflection probability.** (a) Reflection R_k as a function of $(\omega_k - \epsilon)/J$ for several values of Δ. (b) Reflection R_k as a function of both $(\omega_k - \epsilon)/J$ and $(\Delta - \epsilon)/J$ for $g = J/2$. The black line marks the condition $\Delta = \omega_k$, where $R_k = 1$ (maxima in panel (a)). Notice that $R_k = 1$ also at the band edges (Eq. (3.15)) and that both graphics share horizontal axis.

bare energy Δ. We will see in Sect. 3.3 that, due to the presence of bound states, this is not the case.

3.2 Spectral properties in ultrastrong waveguide QED

In the ultrastrong coupling regime (1.5), the Hamiltonian of the previous section (Eq. (3.3)) must be modified

$$H = \epsilon \sum_x a_x^\dagger a_x - J \sum_x (a_x^\dagger a_{x+1} + \text{H.c.}) + \Delta \sigma^+ \sigma^- + g(\sigma^+ + \sigma^-)(a_0^\dagger + a_0). \tag{3.18}$$

Due to the counter-rotating terms, $g(\sigma^+ a_0^\dagger + \sigma^- a_0)$, the Hamiltonian does not commute with the number operator, $[H, N] \neq 0$. This lack of symmetry makes the problem not analytically solvable neither for the ground state nor for the lowest excited states. We solve the problem of finding the bound states by using MPS with imaginary time evolution. However, we cannot compute the scattering ones, since the gap between them is 0 (see Sect. 2.3.4).

Even though this model does not preserve the number of excitations, it changes the excitations in pairs so it must conserve the parity. That is to say, the Hamiltonian commutes with the parity operator

$$\mathcal{P} = e^{i\pi N} = e^{i\pi\left(\sum_x a_x^\dagger a_x + \sigma^+ \sigma^-\right)}, \tag{3.19}$$

Let us show that $[H, \mathcal{P}] = 0$. The Hamiltonian in the rotating-wave approximation, Eq. (3.3), commutes with N, so it also does with $\mathcal{P}$. Therefore, we just need to show that $[\sigma^+ a_0^\dagger, \mathcal{P}] = 0$, since $[\sigma^- a_0, \mathcal{P}] = [\mathcal{P}, \sigma^+ a_0^\dagger]^\dagger$. Notice that

$$[\sigma^+ a_0^\dagger, \mathcal{P}] \left| n_{\text{ph}}, 1 \right\rangle = 0, \tag{3.20}$$

where $\left| n_{\text{ph}}, m \right\rangle$ is the state with n_{ph} in the central cavity and the qubit in the m-the state. Taking now $m = 0$

$$\begin{aligned} [\sigma^+ a_0^\dagger, \mathcal{P}] \left| n_{\text{ph}}, 0 \right\rangle &= (\sigma^+ a_0^\dagger e^{i\pi n_{\text{ph}}} \left| n_{\text{ph}}, 0 \right\rangle - \mathcal{P} \sqrt{n_{\text{ph}} + 1} \left| n_{\text{ph}} + 1, 1 \right\rangle) \\ &= (e^{i\pi n_{\text{ph}}} - e^{i\pi(n_{\text{ph}}+2)}) \left| n_{\text{ph}} + 1, 1 \right\rangle = 0, \end{aligned} \tag{3.21}$$

which ends the proof. In consequence, we denote as $|\phi_n^\pm\rangle$ the eigenstates with even/odd parity, with $\omega_n^\pm$ their corresponding energies.

We use imaginary-time evolution with MPS (Sect. 2.3.4) to find these eigenstates. We can write any state as

$$|\Psi\rangle = |\Psi_+\rangle + |\Psi_-\rangle, \tag{3.22}$$

with $\mathcal{P}\,|\Psi_\pm\rangle = \pm\,|\Psi_\pm\rangle$. These states fulfill

$$|\Psi_\pm\rangle = \frac{1}{2}(|\Psi\rangle \pm \mathcal{P}\,|\Psi\rangle). \tag{3.23}$$

Therefore, we use $|\Psi_\pm\rangle$ as the seed state for imaginary-time evolution in order to find the ground state and the first excited states for the even/odd subspaces.

Numerical evidence shows that the ground state of the full Hilbert space has even parity, $|\phi_0^+\rangle$, which happens in the Rabi model [160, 161]. We also compute the first excited state in the even subspace $|\phi_1^+\rangle$ taking $|\Psi_+\rangle$ as a seed and looking for the minimum-energy state orthonormal to $|\phi_0^+\rangle$.

In Fig. 3.5, we show our results for these eigenenergies. We see that ω_0^+ now does depend on g, whereas it was constant in the RWA. Besides, ω_0^- matches ω_0^1 in the low-coupling limit (see Fig. 3.2). This means that $|\phi_0^-\rangle$ has one excitation for $g \to 0$. The first excited state in the even subspace, $|\phi_1^+\rangle$, has two excitations in the limit $g \to 0$. Multiphoton bound states have been found in this system in the RWA [154, 155]. Notice that the gap $\omega_0^- - \omega_0^+$ decreases with g. We numerically find that this gap eventually vanishes as $g \to \infty$. Similar behavior has been found for other systems, such as the Rabi model, with a qubit coupled to an only cavity [161], or the Rabi-Hubbard model [85, 86], where the gap $\omega_0^- - \omega_0^+$ vanishes for finite g. Instead, the gap $\omega_1^+ - \omega_0^+$ remains finite in the limit $g \to \infty$. We see all these features in the eigenstates of the Rabi model (see again the inset of Fig. 3.5).

We plot the number of photonic excitations of these states in Fig. 3.6. As expected, they are sharply localized around the qubit ($x = 0$). The ground state now does have excitations, whereas the equivalent state in the RWA has no particles.

As we will formally set in Sect. 4.1, by applying momentum creation operators such as (2.123) on bound states, we can define a continuum or band of propagating photonic states. That is, we can define bands on the states $|\phi_n^\pm\rangle$, whose energies are $(\omega_k)_n^\pm = \omega_n^\pm + \omega_k$, with $\omega_k = \epsilon - 2J\cos k$, the dispersion relation of the model. We show two instances of these bands in Fig. 3.7. We can extract valuable information from this. In the RWA, we found two bound states in the one-particle sector, $|\phi_n^1\rangle$, just under and over the one-photon band defined on the ground state of the model (see Fig. 3.2). Whereas $|\phi_0^1\rangle$ is the RWA version of $|\phi_0^-\rangle$, we show now that there is not a state analogous to $|\phi_1^1\rangle$ in the ultrastrong coupling. The energy of this hypothetical state would emerge from the top edge of the band defined on the ground state (around 1.6 in the limit $g \to 0$ in Fig. 3.7). This energy would be embedded in a continuum of energies: the one-photon band defined on $|\phi_1^+\rangle$ (blue-shaded region in Fig. 3.7). Besides, both this state and the states belonging to that band would have odd parity. However, a bound state embedded in a continuum can exist

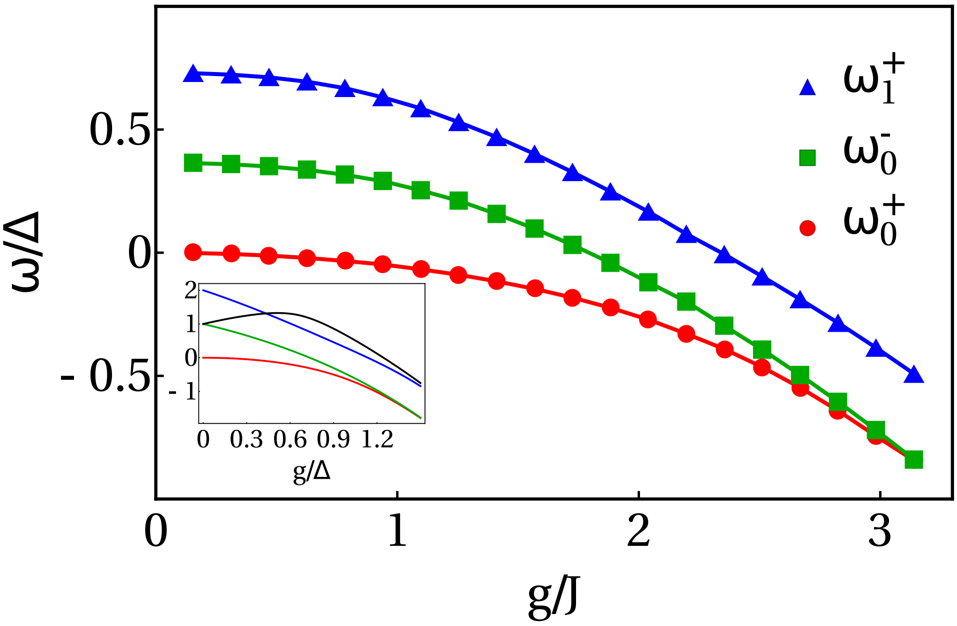

Figure 3.5: **Bound-state energies in the ultrastrong regime.** Energies ω_0^+, ω_0^-, and ω_1^+ in units of the qubit splitting Δ, as a function of g/J. The points are numerical results with MPS. We join the points to guide the eye. We fix the bare energies of the cavities $\epsilon/\Delta = 1$ and the hopping constant $J/\Delta = 1/\pi$. In the inset, we plot the energies of the Rabi model for the same parameters. The legend for the colors is the same as in the main figure. We also plot the first excited state in the odd subspace (black curve) to illustrate the crossing.

if, and only if, the state has a symmetry different from the states belonging to the continuum. In consequence, $|\phi_1^1\rangle$ *does not* exist in the ultrastrong regime. It seems a paradox, since this state does exist in RWA. The puzzle is solved by noting that in the ultrastrong regime this state becomes a resonance with a long lifetime, that diverges in the RWA limit. Finally, notice that the first excited state in the even space, $|\phi_1^+\rangle$, does exist in spite of being inside the band $(\omega_k)_0^+$. This is possible because this state is even, whereas this band has odd parity.

3.3 Example: Spontaneous decay under the presence of bound states

We will study later the influence of the bound states in scattering problems (see Sect. 5.1). Here, we study how they modify the spontaneous decay of an excited qubit under the rotating-wave approximation (Eq. (3.3)), results presented in [162].

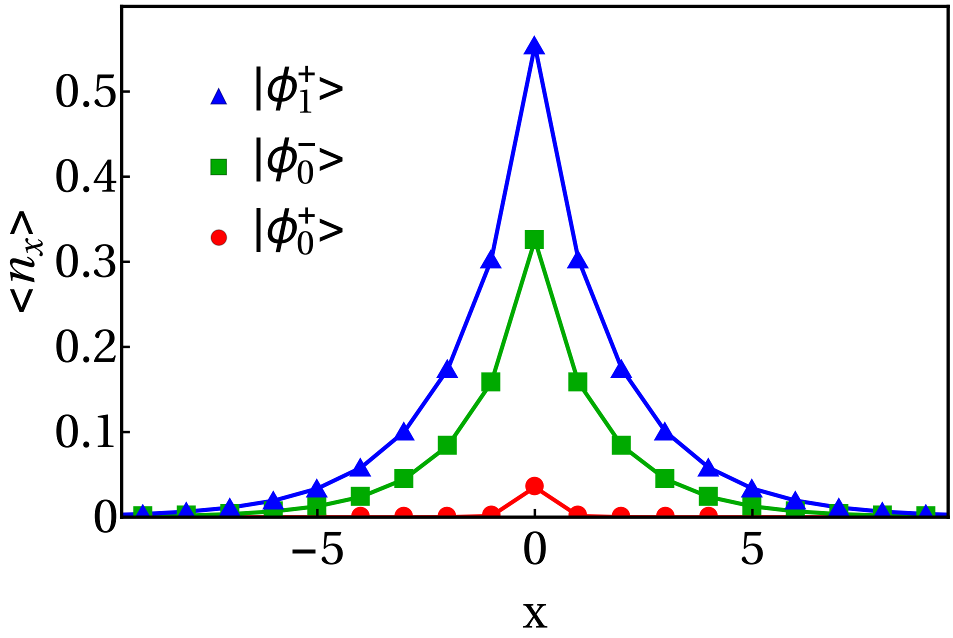

Figure 3.6: **Bound-state populations in ultrastrong.** Bound-state photon population $\langle n_x \rangle$ beyond the RWA plotted with red circles, green squares, and blue triangles for $|\phi_0^+\rangle$, $|\phi_1^-\rangle$, and $|\phi_1^+\rangle$, respectively. The parameters are those of Fig. 3.5.

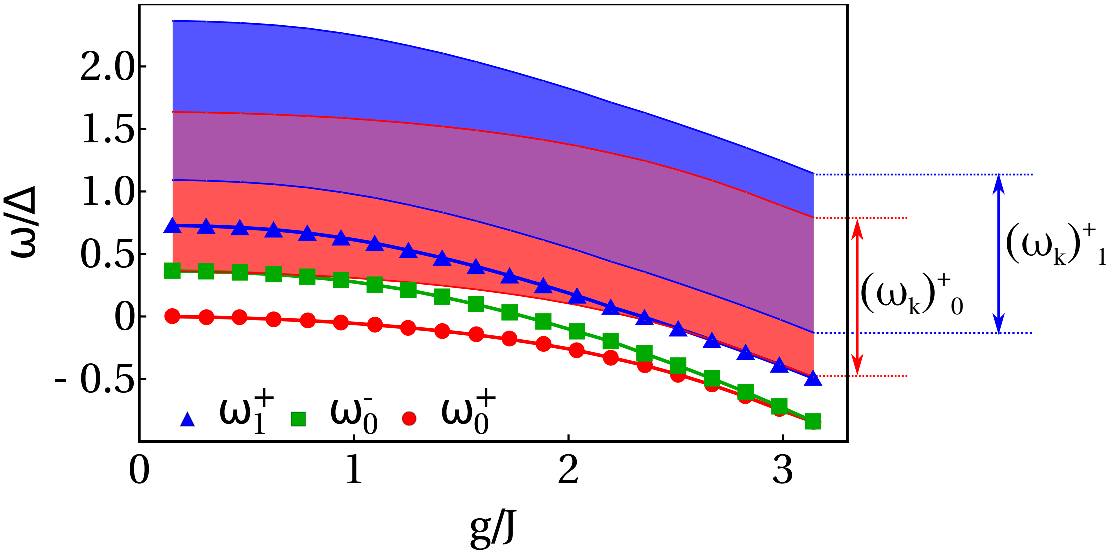

Figure 3.7: **One-photon bands on bound states.** We show the one-photon bands $(\omega_k)_0^+$ and $(\omega_k)_1^+$ in the red and blue shaded regions, respectively. The purple-shaded region renders the overlap between both bands. For completeness, we show again the energies ω_0^+, ω_0^-, and ω_1^+.

How the bound states modify the spontaneous decay has already been treated in the literature in two cases: when the energy of the excited state of the qubit is in the middle of the band [163] or when it is close to its inferior limit, so the superior limit of the band can be neglected [164]. Here, we solve it for *general* values of the parameters, which are (i) Δ with respect to the the band and (ii) the ratio between the qubit-photon coupling and the bandwidth.

In order to study the spontaneous decay, we consider that the two-level atom is excited at $t = 0$, $|\Psi(0)\rangle = \sigma^+|0\rangle$, and compute the time evolution of the state. Spanning this state at time t in bound and scattering eigenstates, Eqs. (3.5) and (3.14), respectively, it reads

$$|\Psi(t)\rangle = \int_{-\pi}^{\pi} \frac{dk}{2\pi}\, c_k e^{-i\omega_k t}|\Psi_k\rangle + c_1 e^{-i\omega_1^1 t}|\phi_1^1\rangle + c_0 e^{-i\omega_0^1 t}|\phi_0^1\rangle, \tag{3.24}$$

with

$$c_k = d_k^* = \frac{iv_k g}{iv_k(\omega_k - \Delta) + g^2}, \tag{3.25}$$

$$c_{1/0} = \left(\frac{1 + e^{-2\kappa_\pm}}{1 - e^{-2\kappa_\pm}} + \frac{g^2}{(\omega_{1/0}^1 - \Delta)^2}\right)^{-\frac{1}{2}} \frac{g}{\omega_{1/0}^1 - \Delta}. \tag{3.26}$$

In the following, we exploit these formulae to obtain our results.

3.3.1 Energy shift

The state given by Eq. (3.24) can be used to obtain the average value of the Hamiltonian (3.3). As it is a conserved quantity, it must be equal to the value at $t = 0$, which is Δ:

$$\langle H\rangle = \Delta = \int_{-\pi}^{\pi} \frac{dk}{2\pi}|c_k|^2\omega_k + |c_1|^2\omega_1^1 + |c_0|^2\omega_0^1\,. \tag{3.27}$$

The average energy for the propagating field is

$$\omega_{\rm ph} \equiv \frac{\int_{-\pi}^{\pi}\omega_k|c_k|^2 dk/2\pi}{\int_{-\pi}^{\pi}|c_k|^2 dk/2\pi} = \frac{\int_{-\pi}^{\pi}\omega_k|c_k|^2 dk/2\pi}{(1 - P_{\rm lig})}, \tag{3.28}$$

with $P_{\rm lig} \equiv |c_1|^2 + |c_0|^2$. Using Eq. (3.27), we can write $\omega_{\rm ph}$ in a more convenient way

$$\omega_{\rm ph} = \frac{\Delta - |c_1|^2\omega_1^1 - |c_0|^2\omega_0^1}{1 - P_{\rm lig}}, \tag{3.29}$$

which shows that the energy of the emitted photon is typically different from Δ because of the presence of the bound states. In short, the amount of energy going to the propagating states must compensate that going to the bound ones so that the total energy is conserved. This is the physical origin of the energy shift of the emitted photon.

This result confirms that the scattering and emission spectra are different, since the scattering resonance always occurs when the input energy is exactly Δ, see Eq. (3.15) and Fig. 3.4.

The energy of the emitted photon $(\omega_{\text{ph}}-\epsilon)/J$ is plotted as a function of $(\Delta-\epsilon)/J$ in Fig. 3.8(a) for several values of g. The closer Δ is to the band edges, the more ω_{ph} departs from Δ. In fact, if Δ is close to the bottom of the band, where the frequency shift is larger, the effect of the upper bound state is negligible $(|c_1|^2 \ll |c_0|^2)$, and vice versa. In conclusion, the frequency shift survives in waveguides without an upper cutoff. The shift increases monotonically with g. Eventually, as $g/J \to \infty$, the emitted energy coincides with the middle of the band for all Δ. Notice that, when the qubit energy is in the middle of the band, *i.e.* when $\Delta = \epsilon$, the following relation holds: $|c_1|^2(\omega_1^1 - \Delta) = |c_0|^2(\Delta - \omega_0^1)$. Inserting this in Eq. (3.29), we conclude that the emitted energy is equal to the qubit one in this case, $\omega_{\text{ph}} = \Delta$. This is related to the symmetry of the energy of the bound states (see Fig. 3.2).

We also study the energy distribution of the emitted photon $|c_k|^2$. We plot it as a function of $(\omega_k - \epsilon)/J$ and $(\Delta - \epsilon)/J$ for the representative cases of $g = J/5$ and $g = J/2$ (Figs. 3.8(b) and (c), respectively). If the coupling is small enough (left panel), the energy distribution is well peaked around $\omega_k = \Delta$. However, as g increases (right panel), $|c_k|^2$ reaches its maximum for $\omega_k \neq \Delta$, being the difference larger the closer Δ is to one of the band edges. This deviation of the maximum away from Δ implies a frequency shift of the emitted photon, as already seen in Eq. (3.29) and Fig. 3.8(a). The reason is simple. In the spontaneous emission some energy is released into the bound states, with a mean energy that does not generally match the qubit energy. Therefore, the coupling into flying photons must compensate for this imbalance. However, due to the fact that bound and scattering states are orthogonal, the former do not play any role in the latter. It is worthy to emphasize that this mechanism is rather general. In any photonic system supporting single-particle bound states, the frequency of the flying photon arising from spontaneous emission will present a spectral shift with respect to the bare frequency of the qubit Δ.

We also characterize the emission probability into propagating modes

$$P_{\text{emission}} = 1 - P_{\text{lig}} = 1 - |c_1|^2 - |c_0|^2 \tag{3.30}$$

in Fig. 3.9. Two effects are observed. First, the emission into bound states is negligible ($P_{\text{emission}} \simeq 1$) in the range $g/J \ll 1$. Increasing this ratio, P_{emission}

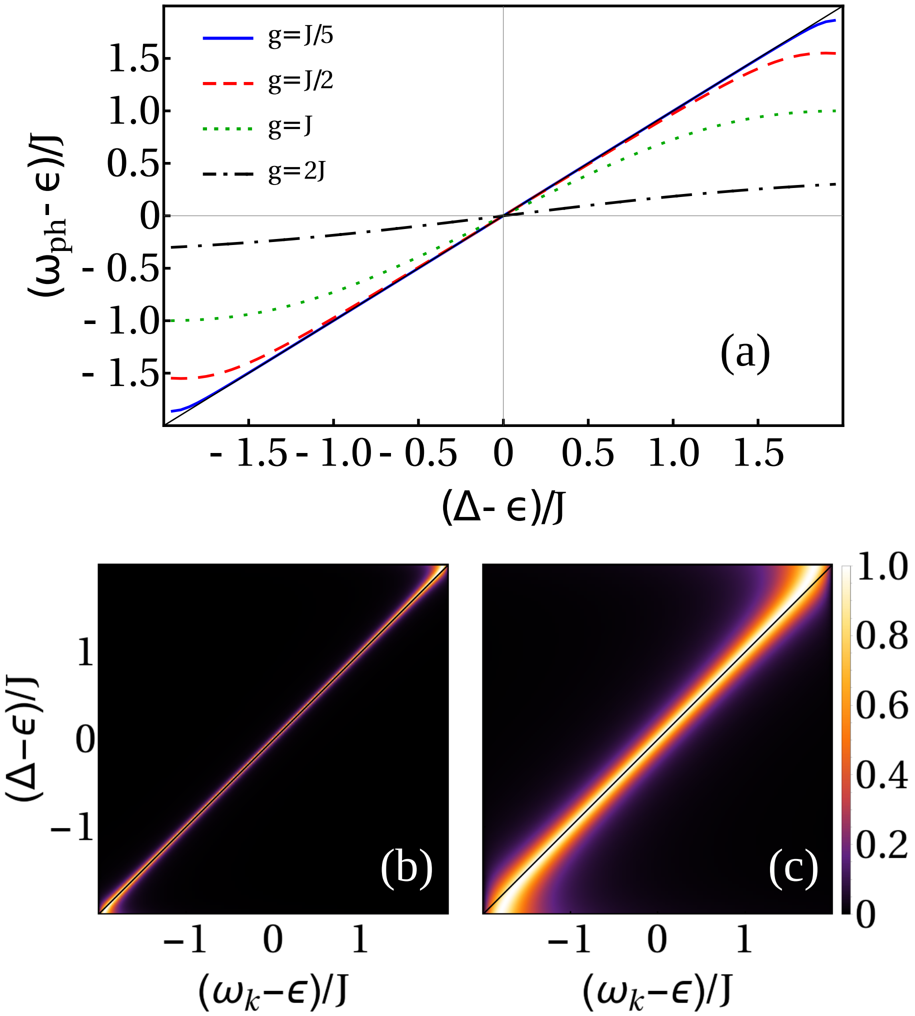

Figure 3.8: **Emitted energy.** **(a)** Average energy of the emitted photon $(\omega_{\mathrm{ph}}-\epsilon)/J$ as a function of $(\Delta-\epsilon)/J$ for $g = J/5, J/2, J, 2J$. For reference, the straight line renders the diagonal $\omega_{\mathrm{ph}} = \Delta$. In **(b)** and **(c)**, we plot $|c_k|^2$ as a function of both $(\omega_k-\epsilon)/J$ and $(\Delta-\epsilon)/J$, for $g = J/5$ and $g = J/2$, respectively. The black line renders $\Delta = \omega_k$. For each Δ, we normalize c_k such that $\max_k(|c_k|^2) = 1$.

decreases. Besides, the closer Δ is to the band gap, the smaller P_{emission} is. Anyway, the emission probability is appreciable for really large values of the ratio g/J: for instance $g/J \simeq 2.5$ yields $P_{\mathrm{emission}} \simeq 0.25$ for the values of Δ considered in Fig. 3.9.

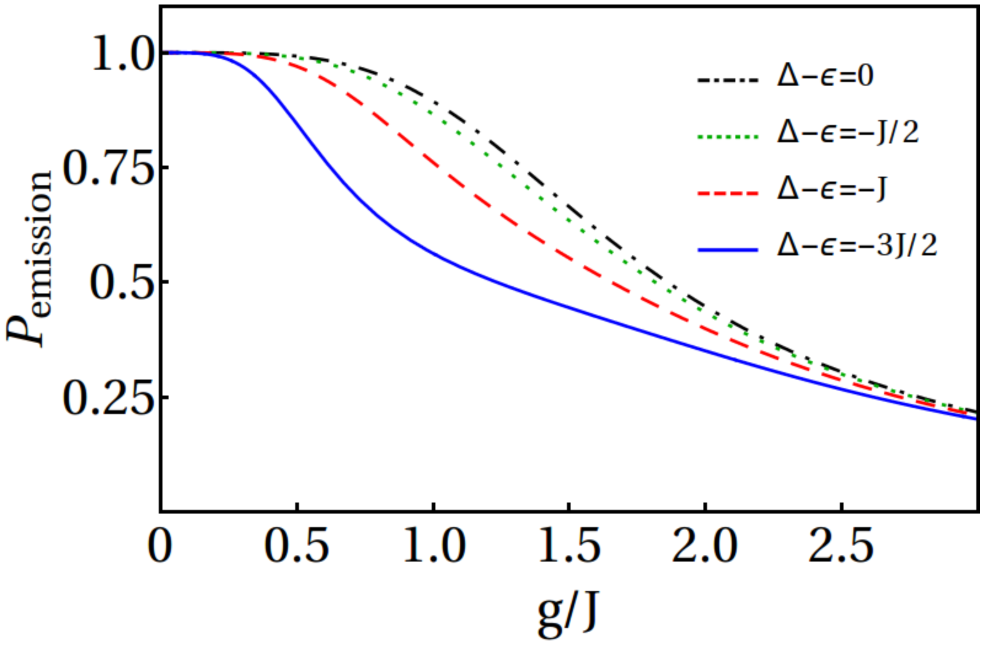

Figure 3.9: **Probability of photon emission.** Probability of emitting a flying photon, $P_{\text{emission}} = 1 - P_{\text{lig}} = 1 - |c_1|^2 - |c_0|^2$, as a function of g/J for $\Delta - \epsilon = -3J/2, -J, -J/2, 0$ from bottom to top (solid blue, dashed red, dotted green, and dotted-dashed black, respectively).

3.3.2 Emitted field

We now study the spatial profile of the emitted field. We compute the amplitudes in position space, $\phi_x(t) \equiv \langle 0|a_x|\Psi(t)\rangle$ (see App. B.1). The photon probability distribution $|\phi_x(t)|^2$ is shown in Fig. 3.10, at time $t = 75/J$ and $g = J/5$, for two values of the detuning: $\Delta - \epsilon = 0$ (blue solid) and $\Delta - \epsilon = -J$ (red dashed). The vertical solid black lines represent $x = \pm x_{\text{max}} \equiv \pm v_{\text{max}} t$, defined in terms of the maximum group velocity $v_{\text{max}} = v_{k=\pi/2} = 2J$.

The probability $|\phi_x|^2$ is mostly confined for x such that $|x| < x_{\text{max}}$. Therefore, even though the original model is nonrelativistic, we can define a causal cone from v_{max}. For $|x| > x_{\text{max}}$, this probability is not zero but it decays exponentially, as expected for the free-field scalar *propagator*, see [165, Sect. 4.5] and [166, Sect. 2]. If Δ is in the middle of the band, the emitted photon has a momentum distribution peaked around $k = \pi/2$, where $v_k = v_{\text{max}}$. If $\Delta \neq \epsilon$, the velocity of the emitted photon is not peaked around v_{max} so the maximum of $|\phi_x|^2$ is below x_{max} (see the dashed red curve of Fig. 3.10, where $\Delta - \epsilon = -J$). Lastly, notice that the emitted photon would be well peaked around $|x_{\text{max}}|$ in position space if the dispersion relation were linear, independently of the value of Δ.

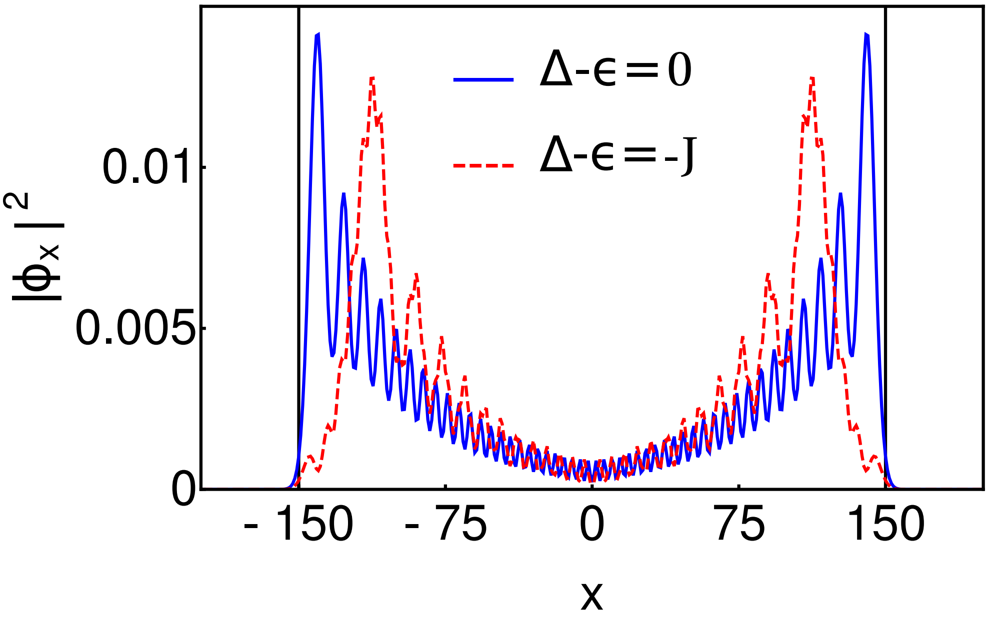

Figure 3.10: **Field distribution.** $|\phi_x|^2$ as a function of x at time $t = 75/J$ for $\Delta - \epsilon = 0$ (solid blue) and $\Delta - \epsilon = -J$ (dashed red) for coupling $g = J/5$. The black solid vertical lines render the propagation limit $|x| = x_{\max} = v_{\max} t$, with $v_{\max} = v_{k=\pi/2} = 2J$.

3.3.3 Qubit dynamics

We finish with a detailed study of the qubit dynamics. From Eq. (3.24), we extract the time dependence of the amplitude of its excited state $\sigma^+|0\rangle$

$$c_{\mathrm{e}}(t) = \langle 0|\sigma^-|\Psi(t)\rangle = c_{\mathrm{e}}^{\mathrm{s}}(t) + c_{\mathrm{e}}^{\mathrm{b}}(t)\,, \tag{3.31}$$

with $c_{\mathrm{e}}^{\mathrm{b}}(t) = \sum_{\alpha=0,1} |c_\alpha|^2 e^{-i\omega_\alpha^1 t}$ and $c_{\mathrm{e}}^{\mathrm{s}}(t) = \int_{-\pi}^{\pi} dk |c_k|^2 e^{-i\omega_k t}/2\pi$ the contributions from the bound and scattering states respectively, see Eqs. (3.5) and (3.14).

First, we focus on $c_{\mathrm{e}}^{\mathrm{s}}(t)$:

$$c_{\mathrm{e}}^{\mathrm{s}}(t) = e^{-i\epsilon t} \frac{4g^2}{\pi J^2} \int_{-1}^{1} dy\; F(y) e^{i2yJt}, \tag{3.32}$$

with

$$F(y) = \frac{\sqrt{1-y^2}}{4(1-y^2)\left((\Delta-\epsilon)/J + 2y\right)^2 + (g/J)^4}. \tag{3.33}$$

The behavior of $c_{\mathrm{e}}^{\mathrm{s}}(t)$ is determined by the kernel $F(y)$, which is related to the density of photonic states as a function of the dimensionless energy $y = \cos k$. This kernel is plotted in Fig. 3.11(a). At sufficiently long times, the oscillating

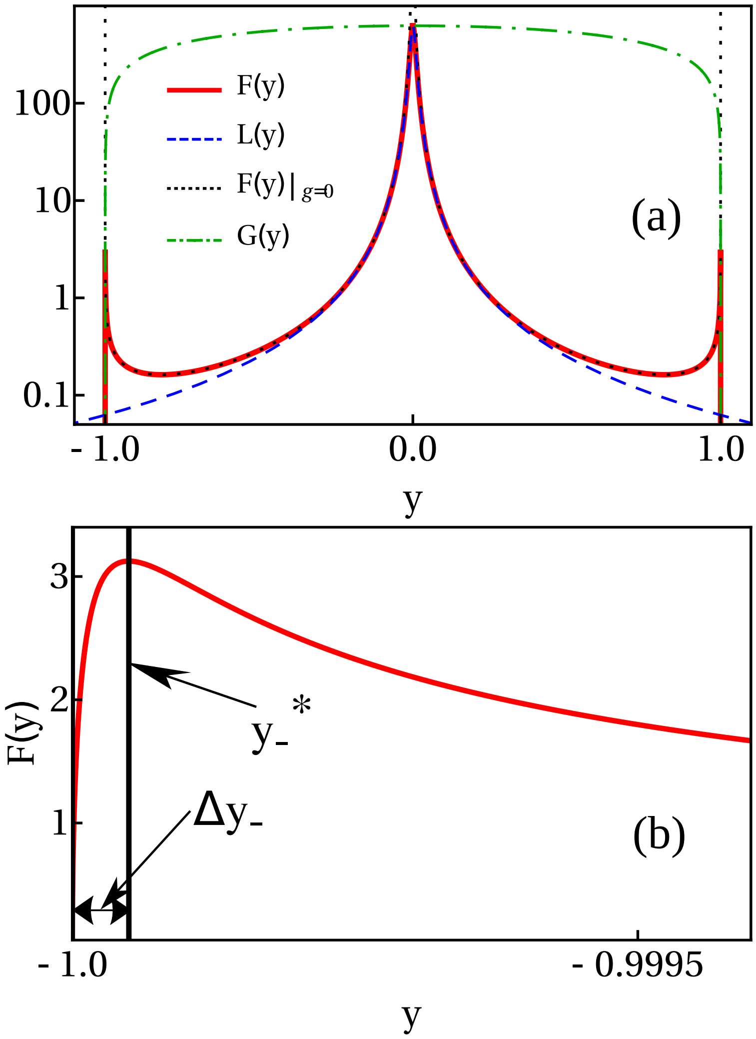

Figure 3.11: **Integrand for $c_{\rm e}^{\rm s}(t)$.** (a) Kernel $F(y)$ in logarithmic scale for $g = J/5$ (red, solid), Lorentzian approximation (blue, dashed), $F(y)$ for $g = 0$ (black, dotted), and $G(y)$ (Eq. (B.12), black, dotted-dashed). We fix $\Delta = \epsilon$. In (b), we zoom in $F(y)$ around $y \gtrapprox -1$, with the same parameters as those used in (a). The kernel $F(y)$ reaches a maximum at $y = y_-^*$ and $\Delta y_- = y_-^* + 1$. Notice that the scale is not logarithmic in this case.

term in the integral (3.32), e^{i2yJt}, cancels out any smooth contribution of $F(y)$. Therefore, the asymptotic relaxation dynamics is governed by the sharpest peaks and the singularities of $F(y)$. There are three main contributions: (i) a Lorentzian peak, associated to a pole of $F(y)$ in the complex plane, (ii) two peaks appearing at $y_\pm^*$, with $y_\pm^*$ close to ± 1 (see Fig. 3.11(b), where we zoom in $F(y)$ around $y = -1$), and (iii) the singular points at $y = \pm 1$, where the first derivative of $F(y)$ is discontinuous. All these features are clearly seen Figs. 3.11(a) and (b).

The Lorentzian peak in $F(y)$ gives an exponential decay $c_{\rm e}^{\rm s}(t) \sim e^{-(i\varphi+1/2\tau_0)t}$. This is equivalent to an excited atom emitting photons into the free space. This contribution is both the fastest and the main one for short-enough times, $t < \tau_0$, since it comes from the widest peak in $F(y)$, see Fig. 3.11(a). We compare the (numerical) exact results for τ_0 and $\delta\varphi \equiv \varphi - \Delta$, computed by integrating Eq. (3.32), with those obtained with the Lorentzian approximation of $F(y)$ in Fig. 3.12. We also compare the results to those obtained with Fermi's Golden Rule: $\tau_0^{\rm FGR} = J \sin k_\Delta / g^2$, with k_Δ such that $\omega_{k_\Delta} = \Delta$, and $\varphi^{\rm FGR} = \Delta$. Fermi's Golden Rule describes accurately the exact results when Δ is around the middle of the band, but corrections are necessary when Δ gets closer to the band edges or when the coupling g increases. Notice that the two-level-atom energy appears in the phase of the exponential up to a correction: $\varphi = \Delta + \delta\varphi$. This is reminiscent of the Lamb effect. However, this energy shift is different from that of the emitted photon (compare Fig. 3.8 to Figs. 3.12 (c) and (d)), even though both converge to Δ in the limit $g/J \to 0$. In fact, as we have said, there is another characteristic energy of the system with a different behavior: the single-photon reflection resonance, which occurs precisely at Δ (see Fig. 3.4 and Eq. (3.16)).

At later times, $t \gg \tau_0$, the singular parts of $F(y)$ are relevant. Singularities give nonexponential decays [159, 167]. In particular, the contribution of the peaks of $F(y)$ at $y_\pm^*$, with $y_\pm^* \simeq \pm 1$, starts to dominate. Let us define the widths of these peaks at $y_\pm^*$ as $\Delta y_\pm \equiv |y_\pm^* \mp 1|$ (see Fig. 3.11(b)). For short-enough times, when e^{i2Jyt} can be considered to be constant for $y \in (-1, -1+\Delta y_-)$ and $y \in (1-\Delta y_+, 1)$, the kernel $F(y)$ can be approximated by setting $g = 0$ (black dotted curve in Fig. 3.11(a)). At $g = 0$, the kernel diverges as $1/\sqrt{1-y^2}$ when $y \to \pm 1$. This kind of singularity gives an algebraic decay $t^{-1/2}$ for $c_{\rm e}^{\rm s}(t)$. For long-enough times, when e^{i2Jty} cannot be taken as a constant, we have to consider the full kernel, with the actual value of g. Therefore, the mentioned divergences are rounded off and the algebraic decay is modified by exponential factors. In other words, these peaks provide a contribution $c_{\rm e}^{\rm s}(t) = t^{-1/2}(a_- e^{-i2Jt} e^{-t/2\tau_{1,-}} + a_+ e^{i2Jt} e^{-t/2\tau_{1,+}})$, with $\tau_{1,\pm} = (4J\Delta y_\pm)^{-1}$. We show the values of the constants $a_\pm$ and the details on the computation in App. B.2.

Eventually, these exponential contributions vanish. The only surviving contribution comes from the singularities at the band edges. There, $F(y)$ is not differentiable and gives a nonexponential (power-law) contribution for all times to $c_{\rm e}^{\rm s}(t)$, which dominates for $t \gg \tau_0, \tau_{1,\pm}$. We show in App. B.2 that this contribution goes as $c_{\rm e}^{\rm s}(t) \sim t^{-3/2} \cos(2Jt - 3\pi/4)$. This transition between

$t^{-1/2}$ and $t^{-3/2}$ decay was already discussed in [164], but they did not see the oscillating factors, since they took the two-level-system energy really close to the lower part of the band, neglecting the contribution of the upper bound state. As mentioned, this decay with $t^{-3/2}$ originates from a discontinuity in the derivative of the density of photonic states and is quite common in impurity decay problems [168], both for continuous systems [169, 170] and for discrete ones [171–173].

The contribution of the bound states $c_{\mathrm{e}}^{\mathrm{b}}(t)$ is much simpler: it gives an oscillatory term which persists for infinitely long times: $P_{\mathrm{e}}^{\mathrm{b}}(t) \equiv |c_{\mathrm{e}}^{\mathrm{b}}(t)|^2 = |c_1|^4 + |c_0|^4 + 2|c_1 c_0|^2 \cos((\omega_1^1 - \omega_0^1)t)$, [159, 163].

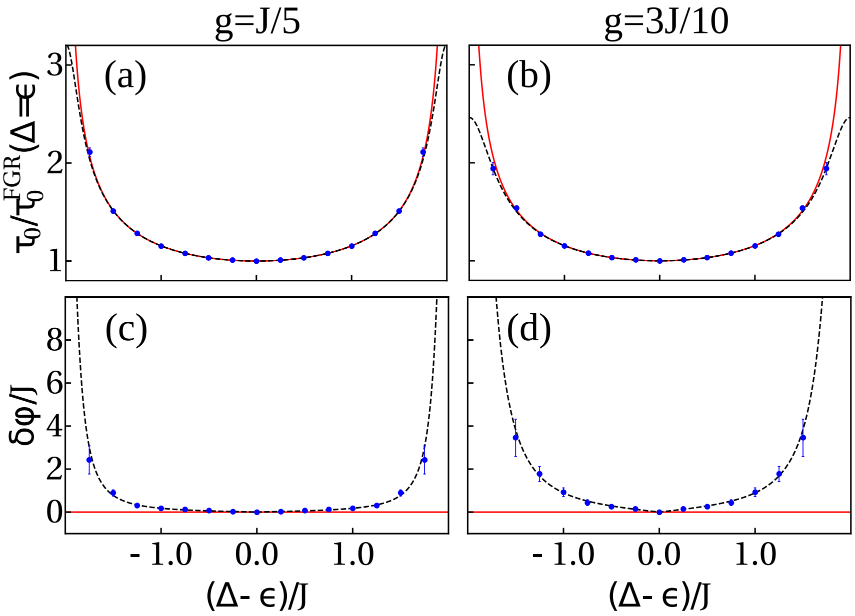

Figure 3.12: **Exponential decay.** **(a), (b)** $\tau_0/\tau_0^{\mathrm{FGR}}(\Delta - \epsilon = 0)$ and **(c), (d)** $\delta\varphi/J$ as a function of the position of the qubit energy with respect to the band for $\epsilon = \Delta$. The coupling is $g = J/5$ (left panels) and $g = 3J/10$ (right panels). We divide τ_0 by the decay time given by the Fermi's Golden Rule at the middle of the band, $\tau_0^{\mathrm{FGR}}(\Delta - \epsilon = 0)$. The red solid curve and the black dashed one correspond to the Fermi's Golden Rule and to the single-pole approximation, respectively. The blue points are computed numerically; we fit the exact dynamics computed with (3.32) to an exponential for $t < \tau_0$.

We sum up all this information in Fig. 3.13, where we plot the qubit dynamics for $\Delta - \epsilon = 0$ and $g = J/5$ (same parameters as in Fig. 3.11), using logarithmic scale. For the sake of clarity, we average the oscillations coming from the different contributions: $a_- e^{-i2Jt} + a_+ e^{i2Jt}$ (arising from the peaks around $y_\pm^*$), $\cos(2Jt - 3\pi/4)$ (from the singularities at $y = \pm 1$), and $\cos((\omega_+ - \omega_-)t)$ (from $c_{\mathrm{e}}^{\mathrm{b}}(t)$). The population $P_{\mathrm{e}}(t) = |c_{\mathrm{e}}(t)|^2$ is drawn as a black, dotted curve.

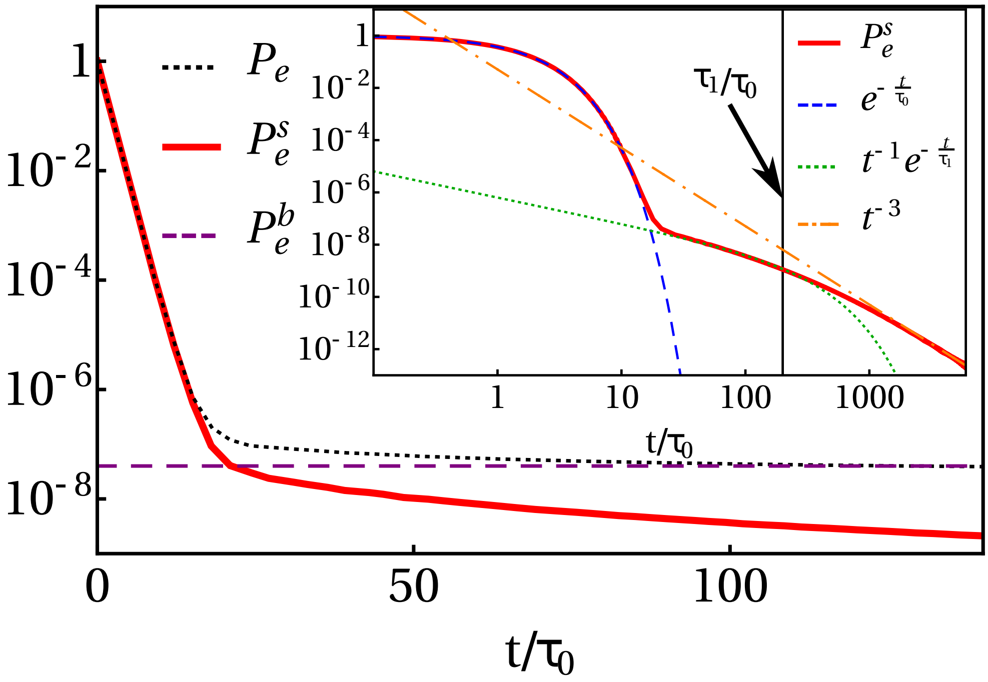

Figure 3.13: **Qubit dynamics.** $P_\mathrm{e}(t)$ (black, dotted), $P_\mathrm{e}^\mathrm{s}(t)$ (red, solid), and $P_\mathrm{e}^\mathrm{b}(t)$ (purple, dashed) for $\Delta - \epsilon = 0$ and $g = J/5$ in logarithmic scale. In the inset we show $P_\mathrm{e}^\mathrm{s}(t)$ in log-log scale with the three contributions: the exponential decay (blue, dashed), the power-law with t^{-1} (green, dotted), and the decay with t^{-3} (orange, dotted-dashed). For the sake of clarity, we average the fast oscillations in the occupations.

It first decays as e^{-t/τ_0}. In addition, the bound-state term dominates over the remaining contributions from the scattering states. Therefore, after a transient period, $P_\mathrm{e}(t)$ achieves the stationary regime of $P_\mathrm{e}^\mathrm{b}(t)$ (purple, dashed curve; remind that we are not showing the oscillations). We also show $P_\mathrm{e}^\mathrm{s}(t) = |c_\mathrm{e}^\mathrm{s}(t)|^2$ in the red solid curve. After the initial exponential decay with e^{-t/τ_0}, where $P_\mathrm{e}^\mathrm{s}(t) \simeq P_\mathrm{e}(t)$, it decays sub-exponentially. In order to see the different contributions to this sub-exponential decay more clearly, we plot it in the inset in log-log scale. After the mentioned exponential decay with e^{-t/τ_0}, it follows a decay with $t^{-1}e^{-\tau_1}$ for $\tau_0 \ll t \simeq \tau_1$ (as $\Delta - \epsilon = 0$, $\tau_1 \equiv \tau_{1,+} = \tau_{1,-}$; in particular $\tau_1 \simeq 200\tau_0$ for the chosen parameters). Eventually, as $t \gg \tau_1$, $P_\mathrm{e}^\mathrm{s}(t)$ goes with t^{-3}. The agreement between the analytical predictions (blue dashed curve for e^{-t/τ_0}, green dotted curve for $t^{-1}e^{-t/\tau_1}$ and orange dotted-dashed curve for t^{-3}) and the exact (numerical) integration is clear in the figure.

Finally, even though we have focused on the case with Δ in the middle of the band, the mathematical analysis shown in App. B.2 is general, so another choice of parameters will give the same qualitative behavior.

Effect of losses

All the previous results in this chapter have considered a lossless system. Here we incorporate losses to the model. We add an imaginary part both to the qubit energy and the cavity energy, $\tilde{\Delta} = \Delta - i\gamma_{\mathrm{e}}/2$ and $\tilde{\epsilon} = \epsilon - i\gamma_{\mathrm{c}}/2$.

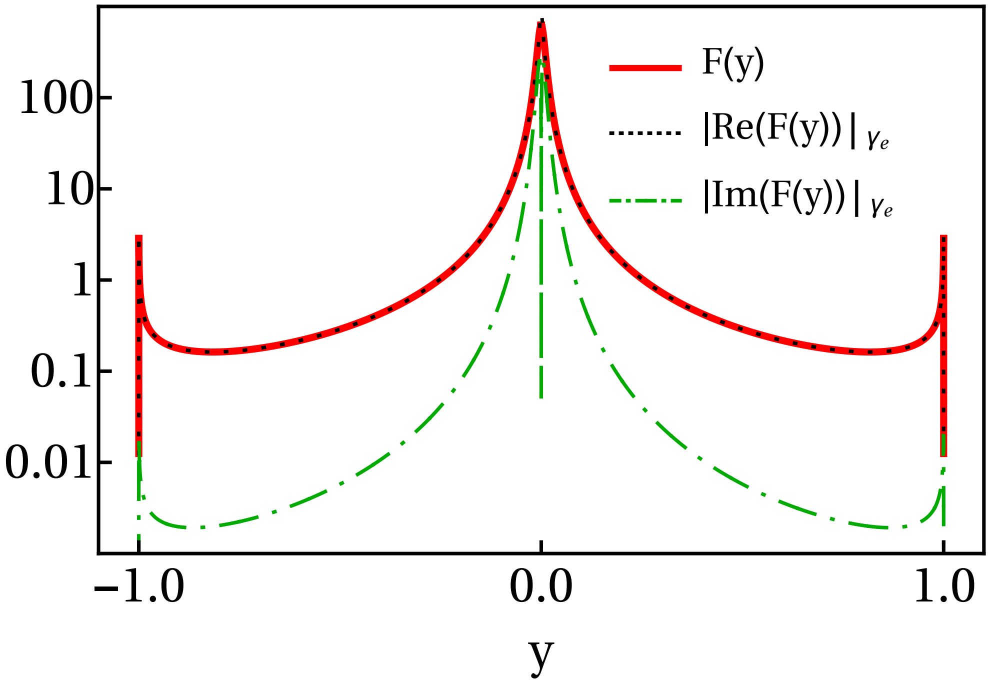

Figure 3.14: **Integrand for $c_{\mathrm{e}}^{\mathrm{s}}(t)$ with an imaginary part in Δ.** Kernel $F(y)$ in logarithmic scale for $\gamma_{\mathrm{e}} = 0$ (red, solid), as well as its real and imaginary part for $\gamma_{\mathrm{e}} = g/10$. The other parameters are those of Fig. 3.11.

The dynamics is still given by Eqs. (3.32) and (3.33) by changing Δ and ϵ by $\tilde{\Delta}$ and $\tilde{\epsilon}$, respectively. We take $\gamma_{\mathrm{e/c}}/g \sim 0 - 0.15$. Considering losses in the qubit, the integrand $F(y)$ resembles the one for the lossless case (compare Figs. 3.14 to 3.11), apart from the fact that now it is a complex function; the same happens if instead we add losses to the cavities. Therefore, we can repeat the analysis done for the lossless case.

We illustrate the modifications with $\gamma_{\mathrm{e}} \neq 0$ in Fig. 3.15. Initially, the population still decays exponentially, but the decay rate is a sum of the previous one, $1/\tau_0$, and γ_{e}: the amplitude reads $c_{\mathrm{sc}}(t) \propto e^{-(i\varphi + 1/2\tau_0 + \gamma_{\mathrm{e}}/2)t}$ (see Fig. 3.15(a)). The power law with t^{-1}, $c_{\mathrm{e}}^{\mathrm{s}}(t) = t^{-1/2}(a_- e^{-i2Jt} e^{-t/2\tau_{1,-}} + a_+ e^{i2Jt} e^{-t/2\tau_{1,+}})$, is preserved. The coefficients $a_\pm$, whose expressions are shown in App. B.2, get modified $10^{-5}\%$ at most for the chosen values of γ_{e}. Lastly, the asymptotic decay with t^{-3} does not depend on Δ (see App. B.2). The robustness of the power-law tails is seen in Fig. 3.15(b).

If we instead consider lossy cavities, $\gamma_{\mathrm{c}} \neq 0$, there is a global factor $e^{-\gamma_{\mathrm{c}} t/2}$ multiplying $c_{\mathrm{sc}}(t)$ (see Eq. (3.32)). When integrating $F(y)$, the imaginary part in ϵ adds an increasing exponential $e^{\gamma_{\mathrm{c}} t/2}$ to $c_{\mathrm{sc}}(t)$, contrarily to Δ (see the denominator of $F(y)$, Eq. (3.33); Δ and ϵ have opposite signs). This increasing exponential cancels out with the global factor $e^{-\gamma_{\mathrm{c}} t/2}$. Therefore, no modifications are seen in the initial exponential regime (see Fig. 3.16(a)). The global factor $e^{-\gamma_{\mathrm{c}} t/2}$ suppresses the power laws in the long-time limit. If the characteristic time of the losses $1/\gamma_{\mathrm{c}}$ is larger than $\tau_{1,\pm}$, we can see the power-law tails for intermediate times (see Fig. 3.16(b)).

To finish, some features, such as the spectroscopic shifts in the spontaneously emitted photons, can be detectable by tuning up and down the frequency of the qubit with respect to the band edge. For probing the dynamics, we suggest using a more sophisticated protocol that (i) places the qubit energy at the right frequency, (ii) then excites it, and after a finite time t (iii) detunes the qubit and probes dispersively its excited state population. All these ideas can be implemented in state-of-the-art setups with superconducting cavities and transmon qubits [54] and also with quantum dots in photonic crystals [40, 43, 45].

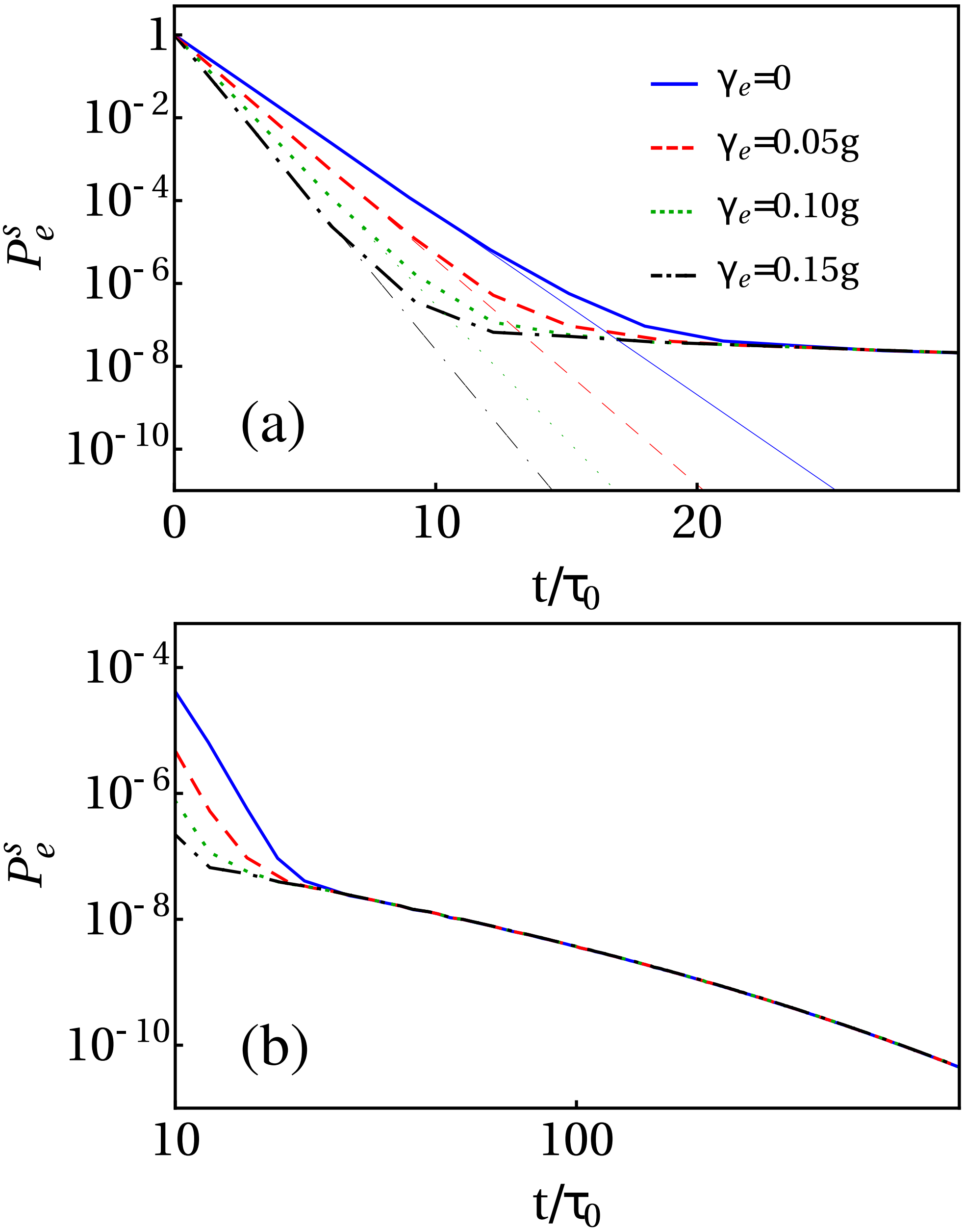

Figure 3.15: **Qubit dynamics for $\gamma_\mathrm{e} \neq 0$.** (a) $P_\mathrm{e}^\mathrm{s}(t)$ in logarithmic scale for several values of γ_e. The thicker lines are the exact results, whereas the thinner ones are the analytical prediction for the exponential regime: $P_\mathrm{e}^\mathrm{s}(t) \propto e^{-(1/\tau_0+\gamma_\mathrm{e})t}$. (b) The same in log-log scale and in the long-time regime. The values of γ_e are those of panel (a).

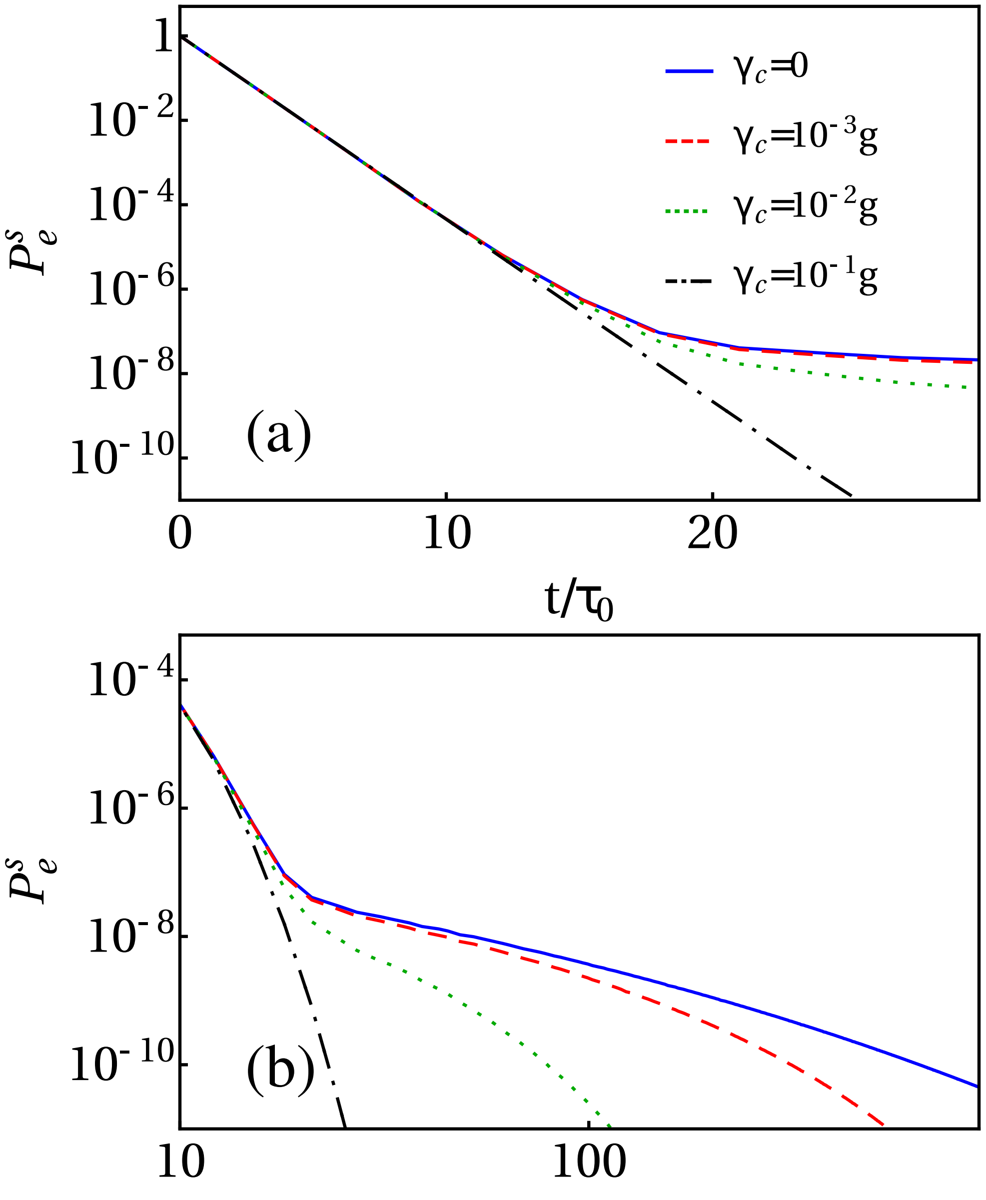

Figure 3.16: **Qubit dynamics for $\gamma_c \neq 0$.** (a) $P_e^s(t)$ in logarithmic scale for several values of γ_c. (b) The same in log-log scale and in the long-time regime. The values of γ_c are those of panel (a). The power laws survive for intermediate times for moderate values of γ_c, but they disappear if γ_c is too large (black curve).

Chapter 4

S Matrix: Analytical Properties

The scientist is also a composer... You could think of science as discovering one particular thing - a supernova or whatever. You could also think of it as discovering this whole new way of seeing the world.

Lisa Randall in an interview with Samuel P. Jacobs [174].

In scattering theory, the S operator (Eq. (1.12)) is the most relevant mathematical object, since it determines the output state given a general input (Eq. (1.11)). Therefore, it is worthy to study the mathematical properties of S. In fact, there are some recent papers in which several analytical characteristics of S are determined [122, 175].

Besides the mathematical properties of S are interest per se, they can give information on the allowed and forbidden scattering channels. *E.g.*, if $S_{p_1 p_2, k} = 0$ for all p_1, p_2, and k, the channel with two-photon generation from one and only one input photon is forbidden. Besides, the scattering matrix has to be compatible with the symmetries of the system. For instance, it has to guarantee the energy conservation.

It is the goal of this chapter to find out the mathematical structure of the S matrix in waveguide QED. In particular, in Sect. 4.1 we derive the general structure for S imposed by causality, which in turn is not a fundamental property, but it emerges from the Hamiltonian (1.1); besides, we consider there can be inelastic one-photon scattering. We study the properties of S if the scattering is linear in Sect. 4.2.

4.1 Causality

Causality is expected to hold in every circumstance. The causality principle states that two space-like-separated experiments, such that no signal traveling at the speed of light can connect them, must provide uncorrelated results [176]. In quantum field theory (QFT), strict causality imposes that two operators $A(x,t)$ and $B(y,t')$ acting on two space-like-separated points (x,t) and (y,t'), must commute,

$$[A(x,t), B(y,t')] = 0 \text{ if } |x-y| - c|t-t'| > 0, \tag{4.1}$$

where c is the speed of light (we restrict ourselves to 1+1 dimensions). Another consequence of causality in QFT appears in the study of scattering events or collisions: scattering matrices describing causally disconnected events must "cluster", or decompose into a product of independent scattering matrices [177]. In fact, all acceptable QFT interactions must result in S matrices fulfilling such a decomposition [178].

Nonrelativistic quantum mechanics is an effective theory which allows signals to propagate arbitrarily fast, but which may give rise to different forms of emergent approximate causality. The typical examples are low-energy models in solid state, where quasiparticle excitations have a maximum group velocity. In this case, there exists an approximate light cone, outside of which the correlations between operators are exponentially suppressed. Lieb and Robinson rigorously demonstrated this emergent causality for spin-models on lattices with bounded interactions that decay rapidly with the distance [179]. Lieb-Robinson bounds not only imply causality in the information-theoretical sense [180], but lead to important results in the static properties of many-body Hamiltonians, such as the clustering of correlations, locality in the dynamics of lattices of harmonic oscillators, and the area law in gapped models [181–183].

In this section, we demonstrate the existence and explore the consequences of emergent causality in the nonrelativistic framework of waveguide QED. These models do not satisfy Lorentz or translational invariance, they are typically dispersive, and the photon-matter interaction may become highly nonperturbative. These results were published in [184].

The main result in this section is the structure of the N-photon S matrix in waveguide QED, rigorously deduced from emergent causality constraints. Our result builds on the general Hamiltonian of waveguide QED (1.1), when the interaction Hamiltonian is given by (1.4). We do not take any approximations such as the RWA or the Markovian limit. To derive the S-matrix decomposition we are assisted by several intermediate and important results, of which we remark (i) the freedom of wave packets far away from the scatterer,

(ii) Lieb-Robinson-like independence relations and approximate light-cones for propagating wave packets, (iii) a characterization of the ground-state properties, and (iv) a proper definition and derivation of scattering input and output states.

We illustrate our results with two representative examples. The first one is a numerical study of scattering in the ultrastrong coupling limit (see [118, 185] and Sect. 5.1), where we demonstrate the cluster decomposition and the nature of the ground state predicted by our intermediate results. The second is an analytical study of a nondispersive medium interacting with a general scatterer, which admits exact calculations. Here we find the structure of the S matrix from general principles, including the inelastic processes. We recover the nontrivial form computed by Xu and Fan for a particular case in [175] and find the natural generalization of the standard cluster decomposition.

4.1.1 Localized wave packets

In order to talk about causality, we introduce a set of localized wave packets, that is, they have a well-defined position. As we will see below, approximate localization becomes essential in the discussion, allowing us to distinguish the order in which photons interact with the scatterer.

Let us introduce the creation operator $\psi_{\bar{k}\bar{x}}(t)^\dagger$ for a wave packet as

$$\psi_{\bar{k}\bar{x}}(t-t_0)^\dagger = \int e^{ik\bar{x}-i\omega_k(t-t_0)}\varphi_{\bar{k}}(k)a_k^\dagger\, dk. \tag{4.2}$$

The wave function $\varphi_{\bar{k}}(k) \in \mathcal{L}^2$ is normalized and centered around the average momentum $\bar{k}$. The exponential factor $e^{ik\bar{x}}$ ensures the wave packet is centered around $\bar{x}$ in position space at time $t = t_0$.

Our results are general but we will implement our calculations using wave packets with either Gaussian

$$\varphi_{\bar{k}}(k) = \frac{1}{\sqrt[4]{2\pi}\sqrt{\sigma_k}} \exp\left[-(k-\bar{k})^2/4\sigma_k^2\right], \tag{4.3}$$

or Lorentzian envelopes

$$\varphi_{\bar{k}}(k) = \sqrt{\frac{\sigma_k}{\pi}}\frac{1}{k-\bar{k}+i\sigma}. \tag{4.4}$$

These wave functions are only approximately localized in the sense that the probability of finding a photon decays exponentially far away from the center $\bar{x}$. The width σ_k in momentum space implies a localization length in position space $\sigma \propto 1/\sigma_k$.

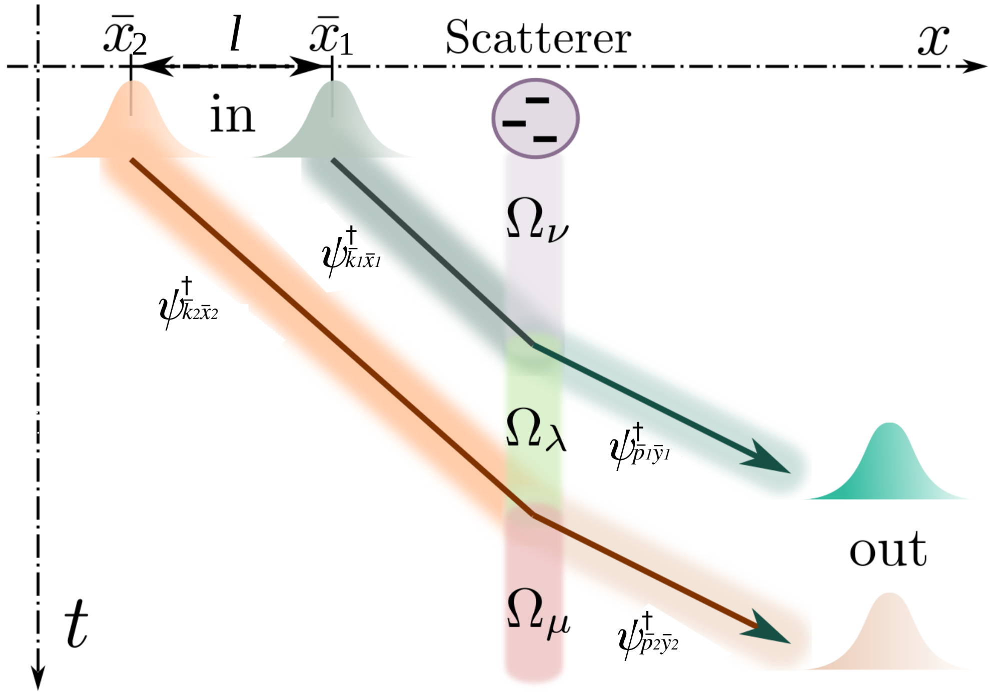

Figure 4.1: Two incoming photons with average momenta $\bar{k}_1$ and $\bar{k}_2$, initially centered around distant points $\bar{x}_1$ and $\bar{x}_2$ ($l \to \infty$), scatter against a general quantum object. The whole system can have several bound states (localized and not propagating). In the figure, the scatterer-field is initially in one of those bound states $|\Omega_\nu\rangle$ (gray region). If the first incoming photon leaves the scattering region in another localized eigenstate $|\Omega_\lambda\rangle$ the second photon *meets* the interaction region in a different state that the found by the first wave packet. If this occurs (see main text of the section) the scattering matrix cannot be just a product, it must differentiate the order in which both events happen.

Fig. 4.1 illustrates the collision of two localized wave packets against a quantum impurity in a chiral medium. The average momentum of the wave packets $\bar{k}_1$ or $\bar{k}_2$ determines the group velocity at which the photons move $v_g(k) = \partial_k \omega_k$. The wave packets may be distorted due both to the dispersive nature of the medium and the interaction with the scatterer.

4.1.2 Sufficient conditions for having a well-defined scattering theory

In the typical scattering geometry, the interaction occurs in a finite region. Besides, one usually assume that asymptotically far away from that region the field is a linear combination of free-particle states (generated via creation operators on the noninteracting vacuum) even in the presence of the scatterer-waveguide interaction.

A sufficient condition for this is that both the ground state and any non-propagating excited state accessible by scattering $|\Omega_\mu\rangle$ are indistinguishable from the vacuum state $|\mathrm{vac}\rangle$ far away from the scatterer. Mathematically this occurs when

$$\lim_{\bar{x}\to\pm\infty} \langle \Omega_\mu | O(\bar{x}, \Delta x) | \Omega_\mu \rangle = \langle \mathrm{vac} | O(\bar{\mathrm{x}}, \Delta) | \mathrm{vac} \rangle \,, \tag{4.5}$$

where $O(\bar{x}, \Delta x)$ is an operator with compact support in the finite interval $\bar{x} - \Delta x/2 < x < \bar{x} + \Delta x/2$ and the vacuum state $|\mathrm{vac}\rangle$ is such that $a_k \,|\mathrm{vac}\rangle = 0$ $\forall k$.

Given a general Hamiltonian (1.1), we do not generally know whether the condition (4.5) is satisfied. Thus, we must assume the existence of scattering states. In this work, we provide a further evidence of the validity of this assumptions by demonstrating a limited version of Eq. (4.5) (see App. C.1) for the ground state of Hamiltonian (1.1), which reads

$$\langle \Omega_0 | \psi^\dagger_{\bar{k}\bar{x}} \psi_{\bar{k}\bar{x}} | \Omega_0 \rangle \leq \mathcal{O}(|\bar{x}|^{-n}), \;\; |\bar{x}| \to \infty \tag{4.6}$$

provided that (i) for all k, $|g_k/\omega_k| < \infty$ and (ii) that the correlators $\langle \Omega_0 | a_k^\dagger a_p | \Omega_0 \rangle$ are n-differentiable functions.

This result is insufficient for the most general case. As we saw in Chapter 3, the waveguide-QED Hamiltonian (1.1) may support excited eigenstates which are localized around the scattering center [103, 118, 154, 155] and which may be visited during the scattering. In this section, we will refer to these states as *ground states*. Besides, depending on its level structure, the scatterer can support several ground states; *e.g.*, a Λ atom has two stable states.

We have been unable to find a general proof that (4.5) is satisfied (and thus that input and output states can be defined) for nonpropagating excited states that appear in these systems. To overcome this problem we assume a plausible *first condition*: the Hamiltonian (1.1) has a finite set of ground states, $\{|\Omega_\mu\rangle\}$, which are localized in the sense of Eq. (4.5). Notice that with this assumption (1.1) has a well defined scattering theory (see. App. C.2.3). This condition allows the expression of the elements of S (see Eq. (1.12)) in the momentum basis:

$$(S_{\mathbf{pk}})_{\mu\nu} = \langle\Omega_\mu| \prod_i a_{p_i} S \prod_j a^\dagger_{k_j} |\Omega_\nu\rangle \,. \tag{4.7}$$

Another useful quantity is the scattering *amplitude*. For example, the single-photon amplitude is defined as:

$$A \equiv \langle\Omega_\mu|\psi^{\mathrm{out}}(t_+) S \psi^{\mathrm{in}}(t_-)^\dagger|\Omega_\nu\rangle \tag{4.8}$$

with $\psi^{\mathrm{in}}(t_-)^\dagger = \psi_{\bar{k}\bar{x}}(t_-)^\dagger$ and an analogous definition for $\psi^{\mathrm{out}}(t_+)$, where the average position of the input wave packet $\bar{x}$ is well separated from the scatterer.

In this section, we assume a *second condition*: the N-photon scattering process conserves the number of flying photons in the input and output states. We only provide results for the sector of the scattering matrix that conserves the number of excitations, excluding us from considering other scattering channels, such as downconversion processes. Notice, however, that a large number of systems fulfills this condition. For instance, the unbiased spin-boson model (where $H_{\mathrm{sc}} \propto \sigma_z$ and $G = \sigma_x$) exactly conserves the number of excitations within the rotating-wave approximation, which is valid when the coupling strength is much smaller than the photon energy (see Chap. 1 and Eq. 1.7). As we will see in Sect. 5.1, even in the ultrastrong coupling regime, the scattering process conserves the number of flying excitations within numerical uncertainties (see also Refs. [118, 119, 185]).

4.1.3 Approximate causality

We are describing waveguide QED using nonrelativistic models for which strict causality (4.1) does not apply. However, as a foundational result we have been able to prove that the waveguide-QED model (1.1) supports an approximate form of causality. This form states that there exists an approximate light cone, defined by the maximum group velocity, $c = \max(\partial_k\omega_k)$. Two wave-packet operators which are outside their respective cones and far away from the scatterer approximately commute.

To be precise we define the distance $d(x-y,t-t') = |\bar{x}-\bar{y}| - c|t-t'|$ and prove in App. C.2 that

$$\|[\psi_{\bar{k}\bar{x}}(t), \psi_{\bar{p}\bar{y}}(t')^\dagger]\| = \mathcal{O}\left(\frac{1}{|D|^n}\right) + \mathcal{O}\left(\frac{1}{|D_0|^{n-1}}\right) \tag{4.9}$$

holds for the full model, with $D \equiv d(x-y,t-t')$ being the distance between the packets and $D_0 \equiv \min\{d(\bar{x},t), d(\bar{x},t_0), d(\bar{y},t), d(\bar{y},t_0)\}$ being the minimum distance between them and the scatterer. The power n stands because we use that the dispersion relation is n-times differentiable. A sketch of the proof is as follows. First, we prove (4.9) for free fields, *i.e.* for wave packets moving under the photonic part of the Hamiltonian. In the Heisenberg picture, the phases $ik(\bar{x}-\bar{y}) - i\omega_k(t-t')$ can be bounded by the distance $d(x-y,t-t')$. Using the Riemann-Lebesgue lemma ($\int \mathrm{e}^{ikz} f(k)\, dk \to 0$, as $z \to \infty$) we find the power law decay, $|D|^{-n}$. Causality is thereby linked to the cancellation or averaging of fast oscillations in the unitary dynamics. Applying a similar technique to the interaction term in (1.1) (see Eq. (1.4)) allows us to prove that the wave packets evolve freely when they are sufficiently far away from the *influence* of the scatterer, producing the second algebraic decay term $|D_0|^{1-n}$. Next, we prove that the evolution of the wave packets for the full model is equal to that for the free model, provided the packets are far away from the scattering region. Therefore, the result for the commutator (4.9) also holds for the full Hamiltonian.

This result is analogous to Lieb-Robinson-type bounds that were initially developed for a lattice of locally interacting spins [179], and which were later generalized to finite-dimensional models, harmonic and anharmonic oscillators, master equations, and spin-boson lattices [181, 182, 186–190]. It is important to remark that the approximate causality in Eq. (4.9) is not obtained for the free theory, but for the *full* waveguide-QED model. As a consequence, we can use this to derive important results on the photon-scatterer interaction.

4.1.4 Causality and the scattering matrix

Causality imposes restrictions on the S matrix [178]. *E.g.*, the cluster decomposition that we summarize here. For now, let us consider the case of a unique ground state and split the S matrix into a free part S^0 and an interacting part T, both in momentum space

$$S_{\mathbf{pk}} = S^0_{\mathbf{pk}} + iT_{\mathbf{pk}}. \tag{4.10}$$

The free part S^0 is the component of S necessary to describe scattering processes when the input photons are far away. The interacting part T accounts for processes in which two or more photons coincide and interact simultaneously with the scatterer. Causality is then invoked to argue that they cannot influence each other if the input events are space-like separated. Thus, T does not contribute to the scattering amplitude as wave packets fall apart $|\bar{x}_i - \bar{x}_j| \to \infty$. This, together with energy conservation, imposes the constraint $iT_{\mathbf{pk}} = iC_{\mathbf{pk}}\delta(E_{\mathbf{p}} - E_{\mathbf{k}})$ [176]. In QFT (typically) momentum conservation is fulfilled, which implies that the free part S^0 is

$$S^0_{\mathbf{pk}} = \frac{1}{N!}\prod_{n=1}^{N} S_{p_n k_n} + \text{permutations}[k_n \leftrightarrow k_m, p_n \leftrightarrow p_m], \tag{4.11}$$

with $S_{p_n k_n} \propto \delta(\omega_{p_n} - \omega_{k_n})$ the one-photon S matrix. This is nothing but the cluster decomposition. Fourier transforming $S^0_{\mathbf{pk}}$, this structure also holds in real space

$$S^0_{\mathbf{yx}} = \frac{1}{N!}\prod_{n=1}^{N} S_{y_n x_n} + \text{permutations}[x_n \leftrightarrow x_m, y_n \leftrightarrow y_m]. \tag{4.12}$$

This shall be relevant in the following section, where we will work in position space.

4.1.5 Generalized cluster decomposition

Our goal is to explain how approximate causality (4.9) implies a cluster decomposition for the S matrix. We will also show that S^0 do not have the structure given by Eq. (4.11) if one-photon inelastic processes are allowed.

To understand how causality fixes the form of S^0 we refer to our Fig. 4.1 where two well separated wave packets interact with a scatterer. The scattering amplitude is,

$$A = \langle \Omega_\mu | \prod_{m=1}^{2} \psi^{\text{out}}_{\bar{p}_m \bar{y}_m}(t_+) \prod_{n=1}^{2} \psi^{\text{in}}_{\bar{k}_n \bar{x}_n}(t_-)^\dagger |\Omega_\nu\rangle \,.$$

Note that for a sufficiently large separation of the incident wave packets, the output state of the first packet must be causally disconnected from that of the second input. This implies that the input operator for the first wave packet must commute with the output operator for the second packet (see Eq. (4.9)). However, the second output and the first input will not commute in general. Therefore, we can approximate, at any degree of accuracy, the above amplitude as,

$$A \simeq \langle \Omega_\mu | \, \psi^{\text{out}}_{\bar{p}_2 \bar{y}_2}(t_+) \psi^{\text{in}}_{\bar{k}_2 \bar{y}_2}(t_-)^\dagger \, \psi^{\text{out}}_{\bar{p}_1 \bar{x}_1}(t_+) \psi^{\text{in}}_{\bar{k}_1 \bar{x}_1}(t_-)^\dagger \, |\Omega_\nu\rangle \,. \tag{4.13}$$

Let us know insert the identity between the operators $\psi^{\text{in}}_{\bar{k}_2\bar{x}_2}(t_-)^\dagger$ and $\psi^{\text{out}}_{\bar{p}_1\bar{y}_1}(t_+)$. Recalling the conditions discussed in Sect. 4.1.2, namely the localized nature for the ground states together with the fact that there is not particle creation, just $\{|\Omega_\lambda\rangle\langle\Omega_\lambda|\}_{\lambda=0}^{M-1}$ will contribute to the identity. The final result is:

$$A = \sum_{\lambda=0}^{M-1} A_{1,\nu\to\lambda} A_{2,\lambda\to\mu}, \tag{4.14}$$

with $A_{1,\nu\to\lambda} = \langle\Omega_\lambda|\,\psi^{\text{out}}_{\bar{p}_1\bar{y}_1}(t_+)\psi^{\text{in}}_{\bar{k}_1\bar{x}_1}(t_-)^\dagger\,|\Omega_\nu\rangle$, that is, $A_{1,\nu\to\lambda}$ is the probability amplitude of generating the transition $|\Omega_\nu\rangle \to |\Omega_\lambda\rangle$, while the wave packet for the first photon goes from $\psi^{\text{in}}_{\bar{k}_1\bar{x}_1}(t_-)$ to $\psi^{\text{out}}_{\bar{p}_1\bar{x}_1}(t_+)$. The definition and interpretation of $A_{2,\lambda\to\mu}$ are fully analogous.

We can generalize this expression to N photons, with initial average positions $\bar{x}_1 > \bar{x}_2 > \ldots > \bar{x}_N$ and asymptotic ground states $\lambda_N := \nu$ and $\lambda_0 := \mu$

$$A = \sum_{\lambda_1,\ldots,\lambda_{N-1}=0}^{M-1} \prod_{n=1}^{N} A_{n,\lambda_{N+1-n}\to\lambda_{N-n}}, \tag{4.15}$$

with

$$A_{n,\lambda_{N+1-n}\to\lambda_{N-n}} = \langle\Omega_{\lambda_{N-n}}|\,\psi^{\text{out}}_{\bar{p}_n\bar{y}_n}(t_+)\psi^{\text{in}}_{\bar{k}_n\bar{x}_n}(t_-)^\dagger\,|\Omega_{\lambda_{N+1-n}}\rangle\,. \tag{4.16}$$

The sketched constructive demonstration (we give a complete demonstration in App. C.3) has confirmed that causality imposes that the amplitude can be built from single-photon events whenever these events are well separated. Inelastic processes, which leave the scatterer in an excited state, yield the sum over intermediate states. If the ground state of the scatterer is unique, the amplitude is the product $A = \Pi_n A_n$. In this case, the S matrix in momentum space recovers the typical structure in QFT (see Eq. (4.11)). However, when inelastic-scattering events occur, the sum in (4.15) leads to a particular structure for the free part of the scattering matrix S^0 that we discuss now.

We now find the structure for S^0 in position space compatible with the amplitude (4.15). For the sake of simplicity, we work with chiral waveguides and a monotonousły growing group velocity, $\partial_k\omega_k \geq 0$. Therefore, we can order the events using step functions, eliminating unphysical contributions (*e.g.*, the wave packet $\psi_{\bar{k}_2\bar{x}_2}$ arriving before than $\psi_{\bar{k}_1\bar{x}_1}$, see Fig. 4.1). Some algebra (see Appendix C.4) yields that S^0 has the following structure

$$(S^0_{\mathbf{yx}})_{\mu\nu} = \sum_{\lambda_1\ldots\lambda_{N-1}=0}^{M-1} \prod_{n=1}^{N} (S_{y_n x_n})_{\lambda_{n-1}\lambda_n} \prod_{m=1}^{N-1} \theta(y_{m+1} - y_m)$$
$$+ \text{permutations}[x_n \leftrightarrow x_m, y_n \leftrightarrow y_m]. \tag{4.17}$$

The sum over intermediate states and the Heaviside functions are a direct consequence of causality, since they order the different wave packets and keep track of the state of the scatterer for each arrival. Nevertheless, if the ground state is unique ($M = 1$), the step functions cancel out and we recover the structure described by (4.12). However, strikingly, for $M > 1$ this S matrix cannot be written as a product of one-photon scattering matrices, up to permutations, due to the Heaviside functions. In order to shed light on this, it is convenient to move to momentum space. Although $(S^0_{\mathbf{pk}})_{\mu\nu}$ cannot be analytically calculated for a general dispersion relation, a mathematical expression can be found for a linear one. This calculation will be presented in Sect. 4.1.6 The final result is that $(S^0_{\mathbf{pk}})_{\mu\nu}$ cannot be written as a product of one-photon S-matrices. This has been recently pointed out in the particular example of a Λ atom by Xu and Fan [175].

4.1.6 Applications

The set of previous theorems and conditions create a framework that describes many useful problems and experiments in waveguide QED. We are now going to illustrate two particular problems which are amenable to numerical and analytical treatment, and which highlight the main features of all the results.

The first problem consists of a two-level system *ultrastrongly* coupled to a photonic crystal. The scattering dynamics has to be computed numerically. The simulations fully conform to our framework, showing the fast decay of photon-qubit dressing with the distance, the independence of space-like separated wave packets, and the decomposition of the two-photon scattering amplitude as a product (for the chosen parameters, the one-photon scattering is elastic).

The second problem consists of a general scatterer with several ground states that is coupled to a *nondispersive* medium and it serves to illustrate the breakdown of the S matrix decomposition as a product of one-photon scattering matrices in momentum space.

Ultrastrong scattering

Let us consider the Hamiltonian studied in Sect. 3.2 (see Eq. (3.18)): a system described by the discrete photonic Hamiltonian (Eq. (1.2)) ultrastrongly coupled to a two-level atom (Eq. (1.5)).

We computed the low-energy states of this model in Sect. 3.2 and saw that they are confined in a small region around the qubit (see Fig. 3.6). This result confirms our theoretical predictions from Eq. (4.6) and implies that the minimum-energy state $|\Omega_0\rangle$ can be approximated by the vacuum far away from the qubit.

According to the previous result, we can generate free wave packets, such as input and output states of Eqs. (C.33) and (C.34)) by inserting photons far away from the scatterer. We study the evolution of input states which consist of a pair of photons, see Eq. (C.33), with $|\Omega_\nu\rangle = |\Omega_0\rangle$. Both wave packets will be Gaussians, Eq. (4.3), with average momentum $\bar{k}$ and width in momentum space σ_k.

We study the scattering dynamics using MPS (see Sect. 2.3). We will provide more details on the simulations in Sect. 5.1, where we study the one-photon scattering in this coupling regime. Here, we demonstrate numerically that the correlations between the output photons vanish as the separation l between the input wave packet (see Fig. 4.1) increases. We get the two-photon wave function in momentum space $\phi_{p_1,p_2}(t) = \langle\Omega_0| a_{p_1} a_{p_2} |\Psi(t)\rangle$ to compute the fluorescence F at the far future t_+, which is the number of output photons whose energy and momentum differ from the input wave packets. More precisely

$$F = \int dp_1 dp_2 \, |\phi_{p_1,p_2}(t_+)|^2, \tag{4.18}$$

with p_1 and p_2 such that $\omega_{p_1} + \omega_{p_2} = 2(\omega_{\bar{k}} \pm \sigma_\omega)$ and $\omega_{p_1}, \omega_{p_2} \notin (\omega_{\bar{k}} - \sigma_\omega, \omega_{\bar{k}} + \sigma_\omega)$, being σ_ω the width of the input wave packets in energy space.

Fig. 4.2(g) shows F as function of the distance between the incident wave packets. When the wave packets are close enough the fluorescence maximizes and the output wave function shows a nontrivial structure, with $\phi_{p_1,p_2}(t_+) \neq 0$ even though $|p_1| \neq \bar{k}$ or $|p_2| \neq \bar{k}$ (see panels (a) and (c)). The wave function has also a rich structure in position space, with antibunching in the reflection component and bunching in the transmission one (see panels (b) and (d)). This structure was already found in the RWA [101]. For long distances, the fluorescence F vanishes (see panels (e) and (f)). In these cases, the output state is clearly uncorrelated: in position space, it consists of two well-defined wave packets and $\phi_{p_1,p_2}(t_+)$ goes to zero if $|p_1| \neq \bar{k}$ or $|p_2| \neq \bar{k}$. All this is a consequence of the cluster decomposition, see Eq. (4.15) and Theorem 6 in App. C.3.

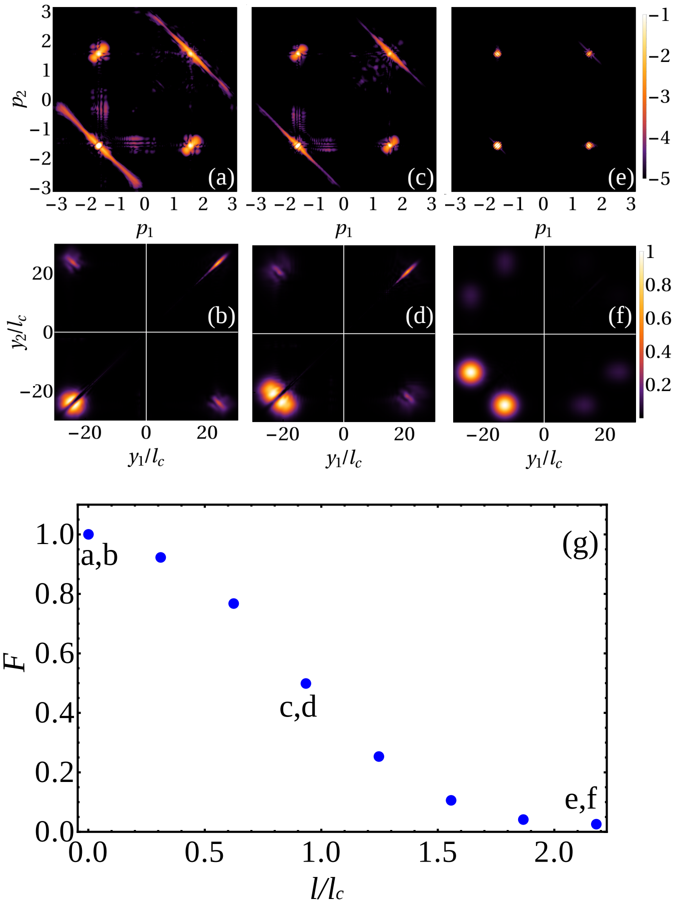

Figure 4.2: Output wave function in momentum/position space, (a/b), (c/d), and (e/f) for several values of the distance between the input photons and (g) fluorescence F for the two-photon output state as a function of the distance l between the two input wave packets. The values of the distances of the panels (a)-(f) are indicated in panel (g). We choose $g/\Delta = 0.3$. The values for the other parameters coincide with those of Fig. 3.6. Both incoming photons are on resonance with the qubit, $\omega_k = \Delta$. The distance l is in units of $l_c \simeq 1.719/\sigma_k$, with l_c such that we can resolve the incident packets if and only if $l > l_c$.

Inelastic scattering and linear dispersion relation: the cluster decomposition revisited

We set $\omega_k = c|k|$ in H_0. The scatterer and interaction are described by

$$H_{\text{sc}} = \sum_{\nu=0}^{M-1} E_\nu \left|\Omega_\nu\right\rangle \left\langle\Omega_\nu\right| + \sum_{J=0}^{M'-1} \tilde{E}_J \left|J\right\rangle \left\langle J\right|, \tag{4.19}$$

$$H_{\text{int}} = \sum_{J=0}^{M'-1} \sum_{\nu=0}^{M-1} g_{J,\nu} (\left|J\right\rangle \left\langle\Omega_\nu\right| a_0 + \text{H.c.}), \tag{4.20}$$

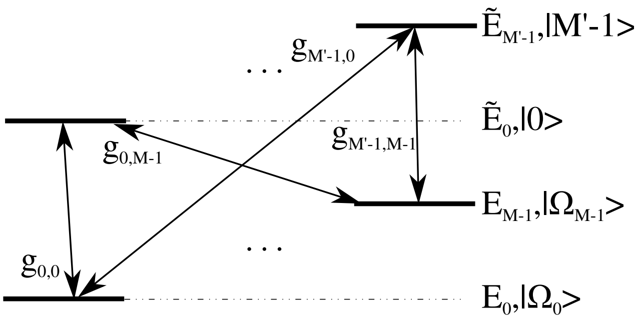

Figure 4.3: Level structure of the scatterer described by the Hamiltonian (4.19), interacting with a waveguide via (4.20). The photons induce transitions between the set of states $\{|J\rangle\}$ and the ground states $\{|\Omega_\nu\rangle\}$ with coupling strengths $g_{J,\nu}$.

where $\{|\Omega_\nu\rangle\}$ and $\{|J\rangle\}$ are the ground and decaying states of the scatterer, respectively, $\{E_\nu\}$ and $\{\tilde{E}_J\}$ are their energies, M and M' is the number of ground and excited states, respectively, and $g_{J,\nu}$ is the coupling strength corresponding to the transition $|\Omega_\nu\rangle \leftrightarrow |J\rangle$ (see Fig. 4.3). This is a prototypical situation in waveguide QED. *E.g.*, if there are two ground states, $M = 2$, and the decaying state is unique, $M' = 1$, the scatterer is a Λ atom. From now on, we work in units such that $c = 1$. We assume chiral waveguides: the scatterer only couples to $k > 0$, which simplifies the final expressions, so we can start from Eq. (4.17). Before writing down the two-photon S^0 matrix in momentum space, we need the one-photon scattering matrix. Imposing energy conservation, it has to be

$$(S_{pk})_{\mu\nu} = t_{\mu\nu}(k)\delta(p + E_\mu - k - E_\nu), \tag{4.21}$$

with k and p the incident and outgoing momenta, respectively, and $|\Omega_\nu\rangle$ and $|\Omega_\mu\rangle$ the initial and final ground states. The factor $t_{\mu\nu}(k)$ is the so-called transmission amplitude. The Dirac delta guarantees energy conservation. Then, the two-photon S^0 matrix, Eq. (4.17), in momentum space is

$$\begin{aligned}(S^0_{\mathbf{pk}})_{\mu\nu} &= \frac{1}{(2\pi)^2}\iint (S^0_{\mathbf{yx}})_{\mu\nu} e^{-i\mathbf{p}^T\mathbf{y}+i\mathbf{x}^T\mathbf{k}} d^2\mathbf{y}\, d^2\mathbf{x} \qquad (4.22)\\ &= \frac{i}{2\pi}\sum_{n,m=1}^{2}\sum_{\lambda=0}^{M-1}\frac{t_{\mu\lambda}(k_n)t_{\lambda\nu}(k_{n'})}{p_m + E_\mu - k_n - E_\lambda + i0^+}\\ &\times \delta(p_1 + p_2 + E_\mu - k_1 - k_2 - E_\nu).\end{aligned}$$

Here, $n' \neq n$, *e.g.*, $n' = 2$ if $n = 1$. The details on the computation are in Appendix C.5. This structure has recently been found by Xu and Fan for a Λ atom ($M = 2$, $M' = 1$) within the RWA and Markovian approximations [175]. At first sight (4.22) may look striking. The matrix S^0 is not the product of two Dirac-delta functions conserving the single-photon energy, as discussed in Sect. 4.1.4. The mathematical origin of the structure can be traced back to its form in position space, Eq. (4.17). The Heaviside functions set the order in which the different wave packets impinge on the scatterer. The product of Dirac-delta functions is recovered if $M = 1$ (see App. C.5). Besides, Eq. (4.22) is also remarkable because it presents the natural generalization of the cluster decomposition for the S matrix (cf. Eqs. (4.10) and (4.11)) when inelastic processes occur in the scattering.

A consequence of (4.22) is that S^0 contributes to the fluorescence F, Eq. (4.18). This seems to contradict our previous arguments, since S^0 is built from causally disconnected one-photon events (they do not overlap in the scatterer). To solve the apparent paradox we recall that (4.22) is a matrix element in momentum space (delocalized photons). For wave packets (4.2), the scattering amplitude is the integral of these wave packets with (4.22). In doing so we find that the fluorescence decays to zero as the separation grows, thus solving the puzzle.

In what follows the fluorescence decay is discussed within the *full* S matrix, *i.e.* we consider the contributions to F from S^0 and T (see Eq. (4.10)). Energy conservation imposes that $(T_{p_1p_2k_1k_2})_{\mu\nu} = (C_{p_1p_2k_1k_2})_{\mu\nu}\, \delta(p_1 + p_2 + E_\mu - k_1 - k_2 - E_\nu)$. Since the contribution of T vanishes as the photon-photon separation increases, C must be sufficiently smooth, at least smoother than a Dirac delta [176]. Then, we assume that $(C_{p_1p_2k_1k_2})_{\mu\nu}$ has simple poles with imaginary parts $\{\gamma_n^C\}$. Similarly, we expect that divergences of $t_{\mu\nu}(k)$ come from simple poles with imaginary parts $\{\gamma_n^t\}$. As far as we know, this structure has been found for all S matrices in waveguide QED [96, 127, 128, 175].

Let us write down the input state in momentum space

$$|\Psi_{\text{in}}\rangle = \int dk_1 dk_2\ \phi_1(k_1)\phi_2(k_2) e^{ik_2 l} a^\dagger_{k_1} a^\dagger_{k_2} |\Omega_\nu\rangle\,. \tag{4.23}$$

The functions $\phi_1(k)$ and $\phi_2(k)$ are localized far away the scattering region in position space. The exponential factor $e^{ik_2 l}$ ensures the separation between both wave packets is l. The output state reads

$$|\Psi_{\text{out}}\rangle = S\,|\Psi_{\text{in}}\rangle = \sum_\mu \int dp_1 dp_2\ \phi_\mu^{\text{out}}(p_1, p_2) a^\dagger_{p_1} a^\dagger_{p_2} |\Omega_\mu\rangle\,. \tag{4.24}$$

The two-photon wave function $\phi_\mu^{\text{out}}(p_1,p_2)$ reads

$$\begin{aligned}\phi_\mu^{\text{out}}(p_1,p_2) \propto \sum_{n=1}^{2}\sum_{m=1}^{2}\int dk_n \Bigg(&\frac{i}{2\pi}\sum_\lambda \frac{t_{\mu\lambda}(k_n)t_{\lambda\nu}(p_1+p_2+E_\mu-k_n-E_\nu)}{p_m+E_\mu-k_n-E_\lambda+i0^+} \\ &+i(\tilde{C}_{p_1p_2k_n})_{\mu\nu}\Bigg) \\ &\Big(\phi_1(k_n)e^{i(p_1+p_2+E_\mu-k_n-E_\nu)l}\phi_2(p_1+p_2+E_\mu-k_n-E_\nu) \\ &+\phi_1(p_1+p_2+E_\mu-k_n-E_\nu)e^{ik_nl}\phi_2(k_n)\Big)\,, \end{aligned} \tag{4.25}$$

being $(\tilde{C}_{p_1p_2k_n})_{\mu\nu} = \int dk_{\bar{n}}(C_{p_1p_2k_nk_{\bar{n}}})_{\mu\nu}\delta(p_1+p_2+E_\mu-k_n-k_{\bar{n}}-E_\nu)$, with $\bar{n}\neq n$. Even though this expression is cumbersome, we can clearly identify the contribution of S^0 and T. We solve this integral by means of the residue theorem. Each pole γ_n^t and γ_n^C, together with the exponentials e^{ik_nl} and $e^{i(p_1+p_2+E_\mu-k_n-E_\lambda)l}$, gives an exponentially decaying term, $e^{-|\gamma_n^t|l}$ or $e^{-|\gamma_n^C|l}$. We choose Lorentzian envelopes for the wave packets. They have a pole at $\bar{k}-i\sigma_k$ (see Eq. (4.4)). In consequence, the wave packets will give a term proportional to $e^{-\sigma_k l}$. Lastly, the imaginary part of the pole of the first term vanishes, $\sim i0^+$, so it gives a nondecaying term, $e^{-0^+l}=1$. The real part of this denominator imposes the single-photon-energy conservation. Thus, it results in the amplitude for the single-photon events, $\sum_\lambda A_{1,\nu\to\lambda}A_{2,\lambda\to\mu}$. Therefore, both S^0 and T contain fluorescent terms that vanish as the separation between the wave packets grows. The technical details are in App. C.6.

As a final application, our results show that the poles of the one- and two-photon scattering matrices $\{\gamma_n^t\}$ and $\{\gamma_n^C\}$ can be found by measuring the decay of F with the distance.

These results represent a significant evolution beyond the field-theoretical methods [38] that have been so successfully adapted to the study of waveguide QED. Developing an extensive set of theorems shown in the appendices, we have completed a program that derives the properties of the N-photon S matrix from the emergent causal structure of a nonrelativistic photonic system. This, together with the fact that the ground states of the Hamiltonian are trivial far away from the scatterer and the asymptotic independence of input and output wave packets, allows us to build a consistent scattering theory. Among the consequences of this framework, we have explained how the existence of Raman (inelastic) processes modifies the usual form of the cluster decomposition, producing a structure that includes the particular example developed in [175].

Our formal results also provide insight in the outcome of simulations for problems where no analytical derivation is possible, such as a qubit ultrastrongly coupled to a waveguide (see [118, 185] and Sect. 5.1). As a second example, we have considered a nondispersive medium $\omega_k = c|k|$, where we found the general form for the scattering matrix in momentum space (independent of the scatterer and the coupling to the waveguide), which has been recently calculated for a Λ atom [175] as a particular case. On top of that, we have clarified how fluorescence decays in a general scattering experiment.

Throughout the previous discussion we have focused our attention on scattering processes which conserves the number of photons (see Sect. 4.1.2). However, this is just a convenient restriction that can be lifted. One may incorporate more scattering channels for the photons using extra indices to keep track of the photon-annihilation and creation processes, which results in a slightly more involved version of Theorem 6. In particular, we can incorporate photon-creation events (see [191] and Sect. 5.2). Finally, our program can be extended to treat other systems, deriving a cluster decomposition for the scattering of spin waves in quantum-magnetism models or for fermionic excitations in many-body systems.

4.2 Linear vs nonlinear scattering

Once we have determined the structure of the scattering matrix in general, we analyze now the particular structure of S in linear systems, as well as the physical implications. Besides, we study how this linear behavior emerges in nonlinear systems, as they tend to be linear. The results exposed in this section were published in [185].

In quantum physics, *linear systems* are those whose Heisenberg equations form a linear set in the operators which describe the problem. In waveguide QED (see Hamiltonian (1.1)) this happens whenever the scatterers are *harmonic oscillators* (the waveguide itself is linear), both within the RWA and the non-RWA coupling regimes. In this case, H_{sc} in (1.1) is

$$H_{\text{sc}} = \sum_{i=1}^{M} \Delta_i b_i^\dagger b_i, \tag{4.26}$$

where M is the number of scatterers (in this case, oscillators), $\{b_i\}$ is a set of bosonic operators

$$[b_i, b_j^\dagger] = \delta_{ij}, \tag{4.27}$$

and Δ_i is the frequency of each oscillator. The interaction term may be the dipole-field Hamiltonian, even beyond the RWA,

$$H_{\text{int}} = \sum_{i=1}^{M} g_i (b_i + b_i^\dagger)(a_{x_i} + a_{x_i}^\dagger). \tag{4.28}$$

Here, g_i is the coupling strength of the i-th oscillator and x_i is its position in the waveguide.

4.2.1 Analytical properties of the S matrix with harmonic oscillators as scatterers

Once we have defined linear scattering, we present the first result of the section.

Theorem 1 *If the system is linear, that is, if the Heisenberg equations form a linear set, the only nonvanishing elements of the one-photon scattering matrix are*

$$S_{pk} = t_k \delta_{p,k} + r_k \delta_{p,-k} \, . \tag{4.29}$$

The theorem is expressed for systems with discrete values for the momenta. For continuous versions, the Kronecker deltas must be replaced by Dirac deltas.

The apparent simplicity of Theorem 1 requires some discussion. First, it implies that neither photon creation nor annihilation are possible. Second, Eq. (4.29) fixes the actual form for the output states,

$$|\Psi_{\text{out}}\rangle = \sum_{k>0} \tilde{\varphi}_k^{\text{in}} (t_k \, a_k^\dagger + r_k \, a_{-k}^\dagger) \, |\phi_0\rangle \ , \tag{4.30}$$

with $|\phi_0\rangle$ being the ground state. Therefore, in models with linear scattering, the only processes for one incoming photon are the reflection and transmission of the photon without changing its input energy (momentum). Notice that this is a nontrivial feature, since the Hamiltonian (1.1) is not number conserving: $[H, N] \neq 0$ if H_{sc} and H_{int} are given by (4.26) and (4.28) respectively, so the ground state $|\phi_0\rangle$ has not got a well-defined number of excitations. However, a single photon scatters by reflecting and transmitting without changing its energy and without creating additional excitations in the system. This result mathematically relies on the Bogolioubov transformation and physically on the fact that (1.1) is a *free* model in the quantum field theory language. The proof of this theorem is given in Appendix D.1.

The single-photon result, Theorem 1 can be generalized to the multiphoton case:

Theorem 2 *If the system is linear the N-photon scattering matrix is given by:*

$$\langle p_1, p_2, ..., p_N | S | k_1, k_2, ..., k_{N'} \rangle = \delta_{NN'} \sum_{n_1 \neq n_2 \neq ... \neq n_N} \langle p_1 | S | k_{n_1} \rangle ... \langle p_N | S | k_{n_N} \rangle \, . \tag{4.31}$$

The theorem says that in linear systems the scattering matrix is a product of single-photon scattering matrices. Consequently, no particle creation, Raman process, or photon-photon interactions are possible. The proof, detailed in Appendix D.2, is based on the single-photon result (see Theorem 1 of this section) together with Wick's theorem. We study the consequences of both theorems in the following sections.

4.2.2 The classical limit: Recovering the standard linear optics concept

Theorems 1 and 2 of this section dictate the scattering in linear systems. So far, it is not completely clear whether the definition for linear systems in quantum mechanics, together with the results in section 4.2.1, correspond to what linear optics means: that the properties of the scattered currents are independent of the input intensity (the number of input photons in our case). Here we show that linear systems satisfy this intensity independence and we will also comment on the classical limit for linear systems.

We consider a monochromatic coherent state as the N-photon input state,

$$|\Psi_{\text{in}}\rangle = |\alpha_k\rangle = \mathrm{e}^{-|\alpha_k|^2/2} \sum_{n=0}^{\infty} \frac{\alpha_k^n (a_k^\dagger)^n}{n!} |\phi_0\rangle \; . \tag{4.32}$$

Applying Theorems 1 and 2, the output state can be written as

$$|\Psi_{\text{out}}\rangle = e^{-|\alpha_k|^2/2} \sum_{n=0}^{\infty} \frac{\alpha_k^n (t_k a_k^\dagger + r_k a_{-k}^\dagger)^n}{n!} |\phi_0\rangle = |t_k \alpha_k\rangle \otimes |r_k \alpha_{-k}\rangle \; . \tag{4.33}$$

The second equality follows after some algebra. Just notice that:

$$\begin{aligned}\sum_{n=0}^{\infty} \frac{\alpha_k^n (a_k^\dagger(t_{\text{out}}))^n}{n!} &= \sum_{n=0}^{\infty} \sum_{m=0}^{n} \frac{1}{m!\,(n-m)!} (t_k \alpha_k a_k^\dagger)^m (r_k \alpha_k a_{-k}^\dagger)^{n-m} \\ &= \sum_{n=0}^{\infty} \frac{(t_k \alpha_k a_k^\dagger)^n}{n!} \sum_{n'=0}^{\infty} \frac{(r_k \alpha_k a_{-k}^\dagger)^{n'}}{n'!} .\end{aligned} \tag{4.34}$$

Equation (4.33) is a satisfactory result. The transmission and reflection coefficients t_k and r_k are independent of α_k. Recalling that $\langle \alpha_k | a_k^\dagger a_k | \alpha_k \rangle = |\alpha_k|^2$, this means that the scattering is independent from the *input intensity.* We note that linear systems transform coherent states onto coherent states. Therefore, harmonic oscillators neither change the statistics nor generate entanglement between the reflected and transmitted fields. Coherent states can be considered classical inputs in the limit $\alpha_k \to \infty$, thus linear systems do not generate *quantumness*. Finally, the last expression for $|\Psi_{\text{out}}\rangle$ in (4.33) has the *classical* interpretation in terms of transmitted $|t_k \alpha_k|^2$ and reflected $|r_k \alpha_k|^2$ currents ($|t_k|^2 + |r_k|^2 = 1$).

4.2.3 From nonlinear to linear

We study now the emergence of the linear behavior predicted by our theorems. We propose a scatterer which interpolates between linear and nonlinear scattering and quantify the nonlinearity. In particular, we consider M qubits placed for simplicity at the same point of the waveguide, $x_i = 0$ for all i

$$H_{\text{sc}} = \Delta \sum_{i=1}^{M} \sigma_i^+ \sigma_i^- \tag{4.35}$$

with the same qubit energy Δ. Also for simplicity, let us assume that the couplings g_i are also the same, $g = g_i \; \forall i$. Then

$$H_{\text{int}} = g \sum_{i=1}^{M} (\sigma_i^- + \sigma_i^+)(a_0 + a_0^\dagger). \tag{4.36}$$

We introduce the operator,

$$b \equiv \frac{1}{\sqrt{M}} \sum_{i=1}^{M} \sigma_i^- \;, \tag{4.37}$$

which creates Dicke states [192]. For the photonic part we take the tight-binding Hamiltonian (1.2), since we will solve the problem numerically by using MPS (see Sect. 2.3). Then, writing (4.35) and (4.36) in terms of b (4.37), the full Hamiltonian (1.1) reads

$$H_{\text{tot}} = \epsilon \sum_x a_x^\dagger a_x - J \sum_x (a_x^\dagger a_{x+1} + \text{H.c.}) + \Delta b^\dagger b + g\sqrt{M}(b^\dagger + b)(a_0^\dagger + a_0) \;. \tag{4.38}$$

We fix $\epsilon = \Delta = 1$ and $J = 1/\pi$ for all the numerical results. We see that the effective coupling is $g\sqrt{M}$ in terms of the b operator defined by (4.37). Besides, it is crucial to observe that [193]

$$[b, b^\dagger] = 1 - \frac{1}{M} \sum_j \sigma_j^+ \sigma_j^- \tag{4.39}$$

In the limit $\langle \sum_j \sigma_j^+ \sigma_j^- \rangle / M \ll 1$ (weak probe compared to the number of qubits) the operator b ($b^\dagger$) approximates an annihilation (creation) bosonic operator. Therefore, a large number of qubits is expected to behave as a harmonic oscillator.

We are interested in the nonlinear optical properties of a collection of qubits. The nonlinearities can be manifested in different observables. The theoretical results in section 4.2.1 say nothing about the nonlinear regime. In the following, we will compute some natural quantities as the reflection and transmission probabilities or photon-photon correlation. We will evaluate *how nonlinear the response is* as a function of the number of incoming photons and qubits. Throughout the following sections the RWA is assumed.

4.2.4 N photons vs M qubits: Total reflection spectrum

The combination of energy and number conservation implies that the output states for *one-photon* scattering through M qubits in the RWA are also given by Eq. (4.30) (like in linear systems).

For linear systems, which follow Eq. (4.31), the N-photon S matrix is a product of one-photon S matrices. Thus, if a qubit were a linear scatterer, N photons should be perfectly reflected at resonance (recall that there is perfect reflection if $\omega_{\text{in}} = \Delta$; see Fig. 3.4 and Eq. (3.16)). But a qubit is intrinsically *nonlinear*, since it cannot totally reflect more than one photon at the same time [101, 194]. Therefore, perfect reflection of N-photon ($N > 1$) input states is not expected to occur with one qubit. If we want to overpass this saturation effect, we may increase the number of qubits. In the limit $N/M \ll 1$, with N photons and M the number of qubits, the linear regime should be recovered, *i.e.* perfect reflection should happen (see Sect. 4.2.3).

Equipped with the MPS technique (see Sect. 2.3), we can study the linear-nonlinear transition as a function of the ratio N/M. In doing so, we provide quantitative meaning to the inequality $N/M \ll 1$.

The simulation of the scattering process follows four steps. First of all, we initialize the system in the ground state, which reads

$$|\phi_0\rangle = |\text{vac}\rangle \bigotimes_{j=1}^{N} |0\rangle_j \,, \tag{4.40}$$

that is, the photons are in the vacuum state and all the qubits are de-excited. Since $|\phi_0\rangle$ is a product state, it can be trivially written as an MPS (see Sect. 2.3.6). Second, we generate the input state. It comprises the ground state plus N incoming photons. We apply N creation operators written as MPO's (see Sect. 2.3.5) on the ground state, as explained in Sect. 2.3.6. Specifically, we create Gaussian wave packets, centered at x_0 with spacial width σ, moving towards the qubit with average momentum k_{in} (and corresponding frequency

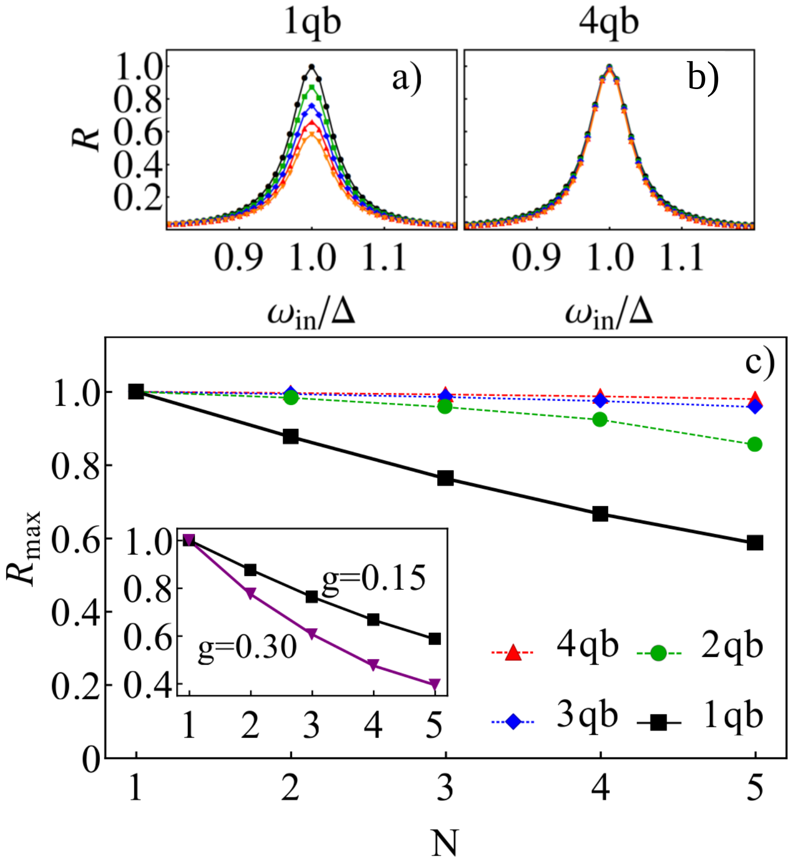

Figure 4.4: **Nonlinearities in the reflection probability.** We fix the parameters to $\epsilon = 1$, $J = 1/\pi$ and $\Delta = \epsilon = 1$. The input state, Eq. (4.41), has incident momentum $k_{\rm in} = \pi/2$ and width in position space $\sigma = 2$. a) R for $M = 1$ and $N = 1 - 5$ (black circles, green squares, blue diamonds, red triangles and orange inverted triangles, respectively); b) The same as in a) but with $M = 4$; c) $R_{\max}$ for $g\sqrt{M} = 0.15$, with $M = 1 - 5$ qubits (black squares/solid line, green circles/dashed line, blue diamonds/dotted line and red triangles/dotted-dashed line, respectively). In the inset we show the maximum of the reflection factor $R_{\max}$ as a function of N for $M = 1$, with $g = 0.15$ (black squares) and $g = 0.30$ (purple inverted triangles).

$\omega_{\rm in}$),

$$|\Psi(t_{\rm in})\rangle = (a^\dagger_\varphi)^N\,|{\rm vac}\rangle \equiv \Big(\sum_x \varphi_x\, a^\dagger_x\Big)^N\,|\phi_0\rangle\,, \tag{4.41}$$

with $\varphi_x \propto \exp[-(x-x_0)^2/2\sigma^2 + ik_{\rm in}]$. After that, we consider the time evolution, explained in Sect. 2.3.4. Once we know $|\Psi(t)\rangle$, we analyze the state, especially in the long-time limit, computing mean values, correlations, etc. (see Sect. 2.3.2).

Examples of useful quantities to characterize the scattering processes are (i) the average local number of photons $\langle n_x(t)\rangle = \langle\Psi(t)|\, a_x^\dagger a_x \,|\Psi(t)\rangle$, (ii) its equivalent in Fourier space $\langle n_k(t)\rangle$, and (iii) the N-photon wave function $\phi^t_{x_1,\ldots,x_N} = \langle\phi_0|a_{x_1}\ldots a_{x_N}|\Psi(t)\rangle$. We can get information on the scattering amplitude, for instance by computing the N-photon reflection factor for M qubits as $R_k = \langle n_{-k}(t_{\text{out}})\rangle \,/\, \langle n_k(t_{\text{in}})\rangle$.

We compute R_k from $N = 1$ to $N = 5$ input photons, with an incoming momentum centered at the resonant value $k_{\text{in}} = \pi/2$ ($\omega_{k_{\text{in}}} = \Delta$). This average momentum is chosen because it gives perfect one-photon reflection. The scatterer is composed by M collocated qubits. We plot the reflection spectrum in Figs. 4.4(a) and (b) respectively. The spectral width scales with the one-photon effective coupling $g\sqrt{M}$ (4.38), which is maintained constant in the calculations. As seen, the maximum reflection, which is $R_{\text{max}} = 1$ for $N = 1$ (see Fig. 3.4 and [99, 100, 102]), decreases as soon as $N > 1$. The effect is better observed in the one-qubit case, see Fig. 4.4(a). As argued before, by increasing the number of qubits we recover full reflection $R_{\text{max}} \simeq 1$. The dependence for R_{max} as a function of N/M is better represented in panel 4.4(c). The maximum of R_k decreases much faster with N for $M = 1$ than for $M > 1$. For $M = 4$, R_{max} hardly gets modified as a function of the number of photons in the considered range of N. Following [127] and [195], there is virtually total reflection for $N = 2$ and $M = 2$ if the photon energies individually match with those of the qubits. We see a slight deviation of this result because we are taking a nonmonochromatic input state and the component of the incident wave function for $k_1, k_2 \neq k_{\text{in}}$ is nonnegligible. Notice that R_{max} does not only depend on N and M, but also on the coupling, see the inset in 4.4(c). Therefore, the nonlinear characteristics do not only depend on the material (qubits) but on their coupling to the field too.

4.2.5 Two photons vs M qubits: Spatial photon-photon correlations in reflection

In this section, we compute the photon-photon correlations created by the scattering process for two-photon input states as a function of the number of qubits M. For further comparison and understanding, we begin by discussing the linear case, where the scatterer is a harmonic oscillator, $H_{\text{sc}} = \Delta b^\dagger b$, placed at $x = x_{\text{sc}}$. We have already discussed in this section that the scattering does not generate correlations if the scatterer is linear (see Theorem 2). The two-photon wave function factorizes: $|\phi^{t_{\text{out}}}_{x_1,x_2}|^2 = |\phi^{t_{\text{out}}}_{x_1}|^2 |\phi^{t_{\text{out}}}_{x_2}|^2$ (up to symmetrization if needed) and, in particular, the two photons must be bunched both in reflection and transmission: $|\phi^{t_{\text{out}}}_{x,x}|^2 = |\phi^{t_{\text{out}}}_{x}|^4$. In the nonlinear case, however, the reflected field by one qubit is totally antibunched [101, 194, 196], $|\phi^{t_{\text{out}}}_{x,x}|^2 = 0$

for $x < x_{\mathrm{sc}}$. Thus, antibunching can be used as a witness for nonlinearities. With these antecedents, we provide below answers to the following questions. How does this depend on the number of qubits? Is it possible to interpolate between the highly nonlinear case of one qubit and the linear case of a harmonic oscillator by adding qubits? If so, how many qubits are necessary to see linear behavior? As many as for the reflection factor, more, or less?

In Fig. 4.5(d), we plot the reflected part of $|\phi^{t_{\mathrm{out}}}_{x_1,x_2}|^2$ as a function of $x_1 - x_2$, fixing $(x_1+x_2)/2$ such that the reflection component is maximum. The effective coupling $g\sqrt{M}$ is kept constant for all the values of the number of qubits M and equals the coupling g for the case of the harmonic oscillator. We remind that $|\phi^{t_{\mathrm{out}}}_{x_1,x_2}|^2$ is proportional to the probability of having both photons separated by a distance $|x_1 - x_2|$. Therefore, $|\phi^{t_{\mathrm{out}}}_{x_1,x_1}|^2$ is the probability of seeing both photons at the same point. For $M = 1$, the numerical results (Fig. 4.5(d)) show $|\phi^{t_{\mathrm{out}}}_{xx}|^2 \simeq 0$, recovering the well-known photon antibunching in reflection (see [101, 194, 196] and Fig. 4.2). This effect is due to the fact that the qubit is saturated when a photon impinges on it, so it is not able to absorb a second photon; in consequence, the qubit cannot reflect both photons at the same time and the probability of seeing two photons in reflection at the same point vanishes. Surprisingly, photon antibunching and thus nonlinearity can still be resolved by increasing M, even for $M = 20$ [1]. The full contour for $|\phi_{x_1,x_2}|^2$ is shown in 4.5(a), (b), and (c) for one and two qubits and one harmonic oscillator respectively. Apart from the antibunched characteristics in the reflected signal, we can also appreciate that one qubit cannot reflect as much as two qubits, as we discussed in Sect. 4.2.4 (see Fig. 4.4). The transmitted photons are always bunched. The components around $(x_1 + x_2)/2 \simeq 0$ and $|x_1 - x_2| \simeq 200$ correspond to one photon being transmitted and the other reflected.

Once the physics has been discussed, let us finish with a brief note on how to solve the two-photon scattering against M qubits placed at the same point and within the RWA. We start by reminding that the RWA implies the conservation of the number of excitations. Therefore, in the two-excitation manifold and regarding the qubits, it suffices to consider the following states: $\{|0\rangle, |1\rangle \equiv b^\dagger |0\rangle, |2\rangle \equiv \frac{(b^\dagger)^2|0\rangle}{\sqrt{2(1-1/M)}}\}$ (see Eq. (4.37)). In consequence, if $N = 2$, the M qubits can be formally replaced by a three-level system with states given as above. As expected (see Sect. 4.2.3), in the limit $M \to \infty$, $|2\rangle = \frac{(b^\dagger)^2|0\rangle}{\sqrt{2}}$, as in the harmonic oscillator case.

---

[1] We note here that for the particular set of values $N = 2$ and $M = 2$ that, if $\omega_1 = \Delta_1$ and $\omega_2 = \Delta_2$ photons are bunched [127, 195] as it would be linear scattering. However, our initial wave packet is not monochromatic

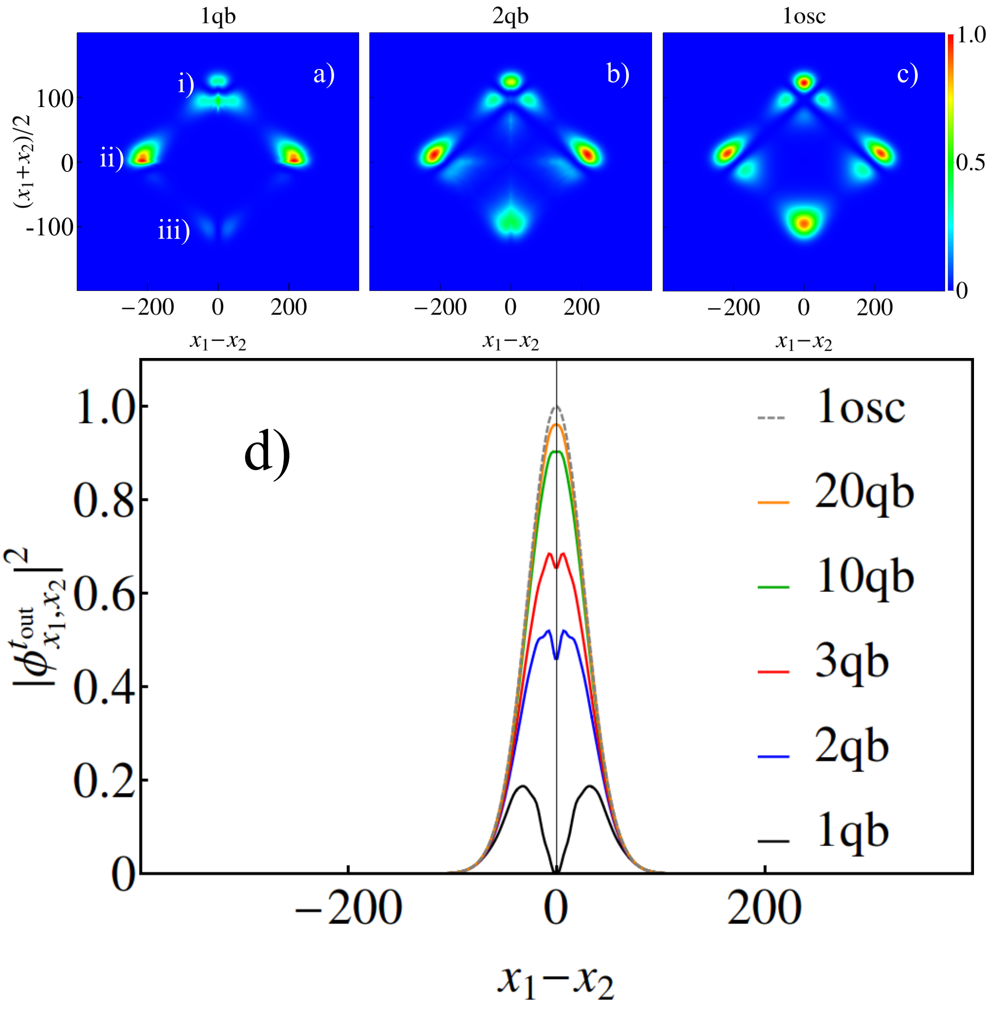

Figure 4.5: **Nonlinearities in the two-photon wave function.** $|\phi^{t_{\rm out}}_{x_1,x_2}|^2$ for $g\sqrt{M} = 0.10$, with a) $M = 1$, b) $M = 2$ qubits and c) a harmonic oscillator. $|\phi^{t_{\rm out}}_{x_1,x_2}|^2$ is normalized in each panel such that its maximum is set to 1. In the contours, i) corresponds to the transmitted-transmitted component, ii) to the transmitted-reflected one, and, finally iii) to the reflected-reflected part. d) $|\phi^{t_{out}}_{x_1,x_2}|^2$ fixing $(x_1 + x_2)/2$ for $g\sqrt{M} = 0.10$, with $M = 1, 2, 3, 10, 20$ qubits (solid, from bottom to top) and harmonic oscillator (dashed). Here, we normalize such that $|\phi^{t_{out}}_{x_1,x_1}|^2 = 1$ for the harmonic oscillator. The parameters ϵ, J, and Δ are those of Fig. 4.4. The average incident momentum is $k_{\rm in} = \pi/2$ and the width in position space is $\sigma = 20$.

Chapter 5

Nonlinear Photonics at Minimum Power

Nothing in life is to be feared, it is only to be understood. Now is the time to understand more, so that we may fear less.

Maria Salomea Skłodowska-Curie, as quoted in [197].

Typically, materials respond linearly to the electromagnetic (EM) field. Intense fields are usually demanded for accessing the nonlinear response [98, 198]. Therefore, a long standing challenge in science and technology is to develop devices containing giant nonlinear properties at small powers. The final goal is to shrink the required power into the few-photon limit [82–84]. In doing so, the material dipoles must interact more strongly with the driving photons than with the environment, which defines the *strong light-matter coupling* regime. Thus, quantum optical systems presenting strong light-matter interaction are excellent candidates for building nonlinear optical materials operating at tiny powers.

An ideal platform for having strong light-dipole coupling together with the possibility of generating and measuring few-photon currents is waveguide QED. As there are only two propagation directions (left and right), interference effects are much larger than in higher-dimensional systems. Besides, the coupling to the few-level systems is enhanced by the reduced dimensionality (Purcell effect). As mentioned in the introduction, several platforms can serve for the study (see Chapter 1). With this kind of systems, different nonlinear effects may be observed and used, such as photon-photon correlations [101, 122, 127, 128, 175, 194–196, 199–211], nonclassical light generation [212], lasing [213], optical transistors [214–216], quantum routers [217–219], or efficient photodetectors [220, 221].

Given the light-matter coupling g (see Eq. (1.5)), we can define a decay rate in a spontaneous-decay situation $\gamma \propto g^2/v$, where v is the group velocity (see for instance Eq. (2.19) and the subsequent text). We can also define decay rates into lossy modes γ', such as nonguided photons, phonons, etc. These magnitudes allow us to define different coupling regimes: (i) if $\gamma < \gamma'$, we are in the weak coupling regime; (ii) if $\gamma \gg \gamma'$ but γ is much smaller than the typical energy scales of the system (level splitting of the scatterers, etc.), we are in the strong-coupling regime, but the rotating-wave approximation is still valid (see Sect. 1.1); and (iii) when γ is much larger than both γ' and the energy scales of the systems, which is the so-called ultrastrong coupling (see Sect. 3.2). Novel physical effects have been predicted in this regime [111–117]. For instance, it has a great potential for nonlinear applications.

In this chapter, we solve several scattering problems in waveguide QED with nonlinear behavior.

5.1 One-photon scattering from one qubit in ultrastrong coupling regime

From the theoretical viewpoint, the scattering of multiphoton wave packets in waveguide QED is a complex problem even within the RWA [96, 101, 103, 127, 128, 207, 222], but the one-photon scattering is trivial [99, 100, 102], as seen in Sect. 3.1. However, beyond the RWA, computing the scattering of even one flying photon is difficult, as subspaces with different photon numbers mix in the dynamics. This converts the problem into a many-body one for which only partial solutions exist for models that consider linear (unbounded) dispersion relations and, typically, either in the perturbative regime ($g/\omega < 0.2$) or in the localization phase, ($g/\omega > 1$).

In this section, we solve numerically the scattering of a flying photon from a two-level system in the ultrastrong-coupling regime. This was published in [118].

5.1.1 Model and simulation

We model the photonic medium as an array of coupled cavities, described by (1.2). We take the full dipole-field interaction Hamiltonian, see (1.6). A scheme of the system is shown in Sect. 3.1, Fig. 3.1(a). For the sake of clarity, we rewrite here the Hamiltonian

$$H = \epsilon \sum_x a_x^\dagger a_x - J \sum_x (a_x^\dagger a_{x+1} + \text{H.c.}) + \Delta \sigma^+ \sigma^- + g(\sigma^+ + \sigma^-)(a_0 + a_0^\dagger). \quad (5.1)$$

We choose the same parameters as in Sect. 3.2: $\epsilon/\Delta = 1$, and $J/\Delta = 1/\pi$. Notice that the level splitting of the qubit is in the middle of the band: $\Delta = \epsilon$, where the curvature of the dispersion relation minimizes. Actually, in the low-coupling limit, when the linear approximation for ω_k is justified, $\omega_{k=0} = 0$, which makes this choice of parameters ideal for simulating scattering in free space. Anyway, this is not the goal of this section and the results we find here do not qualitatively change if we modify these parameters. From now on, we will express the energies in units of Δ. Notice that the number of particles is not conserved, so not even the ground state is trivial (Sect. 3.2). We solve (5.1) numerically using the MPS technique.

The simulation of the scattering process follows four steps: (i) we compute the ground state and other bound states by means of imaginary-time evolution (see Sect. 2.3.4), as described in Sect. 3.2 (see Figs. 3.5 and 3.6); (ii) we generate the input state, which comprises the ground state plus one incoming photon; (iii) we apply a creation operator written as an MPO (see Sect. 2.3.5) on the ground state, as explained in Sect. 2.3.6; in particular, we create a one-photon Gaussian wave packet, centered at x_0 with spacial width σ, moving towards the qubit with average momentum k_{in} (and corresponding frequency ω_{in}),

$$|\Psi(0)\rangle = a^\dagger_\varphi \,|\phi_0^+\rangle \equiv \sum_x \varphi_x \, a^\dagger_x \,|\phi_0^+\rangle \,, \tag{5.2}$$

with $\varphi_x \propto \exp[-(x-x_0)^2/2\sigma^2 + ik_{\text{in}}]$ and $|\phi_0^+\rangle$ the ground state of the model (see Sect. 3.2); and finally (iv) we compute the time evolution, as explained in Sect. 2.3.4. Once we know $|\Psi(t)\rangle$, we analyze the state, especially in the long-time limit, computing mean values, correlations, etc. (see Sect. 2.3.2). Examples of useful quantities to characterize the scattering are (i) the average local number of photons $\langle n_x(t)\rangle = \langle\Psi(t)|\, a^\dagger_x a_x \,|\Psi(t)\rangle$, (ii) its equivalent in Fourier space $\langle n_k(t)\rangle$, (iii) the qubit population $P(t) = \langle\Psi(t)|\sigma^+\sigma^-|\Psi(t)\rangle$, (iv) and the one-photon dynamics on top of the ground state $\varphi_x(t) = \langle\phi_0^+|a_x|\Psi(t)\rangle$. From the spatial Fourier transform of the latter we can extract the transmission amplitude as $t_k = \varphi_k(t_{\text{f}})/\varphi_k^{\text{free}}(t_{\text{f}})$, where t_{f} is a time long enough so that the scattering process has concluded, and φ_k^{free} is the photon amplitude when the qubit and the incoming photon do not interact. These quantities suffice for analyzing scattering amplitudes since, in all considered cases, the computed amplitude for generation of more than one propagating photon is negligible.

Figure 5.1 shows both $\langle n_x(t)\rangle$ and $\langle n_k(t)\rangle$ for two representative cases, corresponding to different values of the incident momentum k_{in}, and $g = 0.7$. For this value of g, at which the RWA is not valid, the GS comprises a photon cloud around the qubit, as seen in both $\langle n_x(t=0)\rangle$ (at $x \approx 0$) and $\langle n_k(t=0)\rangle$ (which presents a finite value around $k = 0$). As time evolves, we observe the typical scattering evolution. After a time span of free propagation ($t \lesssim 100$), an

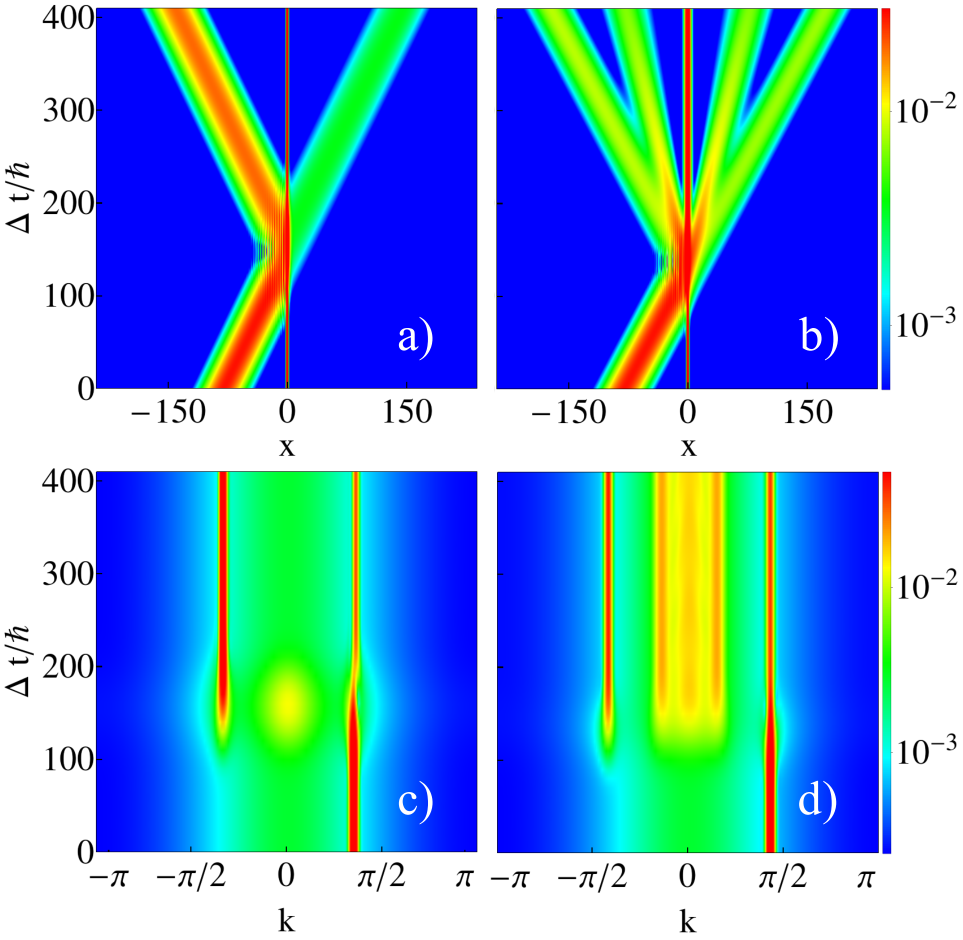

Figure 5.1: **Time evolution.** Evolution of $\langle n_x \rangle$ (upper panels) and $\langle n_k \rangle$ (lower panels) for $\omega_{in} = 0.70$ (left panels) and $\omega_{in} = 0.85$ (right panels). In both cases, at $t = 0$ an initial wave packet is set centered at $x_0 = -80$ and the coupling is $g = 0.7$. For $\omega_{in} = 0.70$ the scattering is elastic, while for $\omega_{in} = 0.85$ there is an inelastic scattering channeling too.

interaction period starts where both reflected and transmitted photon beams develop. Finally, at larger times ($t \gtrsim 300$), the scattered photon propagates freely.

5.1.2 Elastic spectrum

There are always reflected and transmitted *elastic* beams, which has the same energy as the incident one. Remarkably, as shown in the Fig. 5.1(b,d), for some parameters, there are also inelastic (Raman) processes where both reflected and transmitted wave packets propagate with a different frequency to the incident

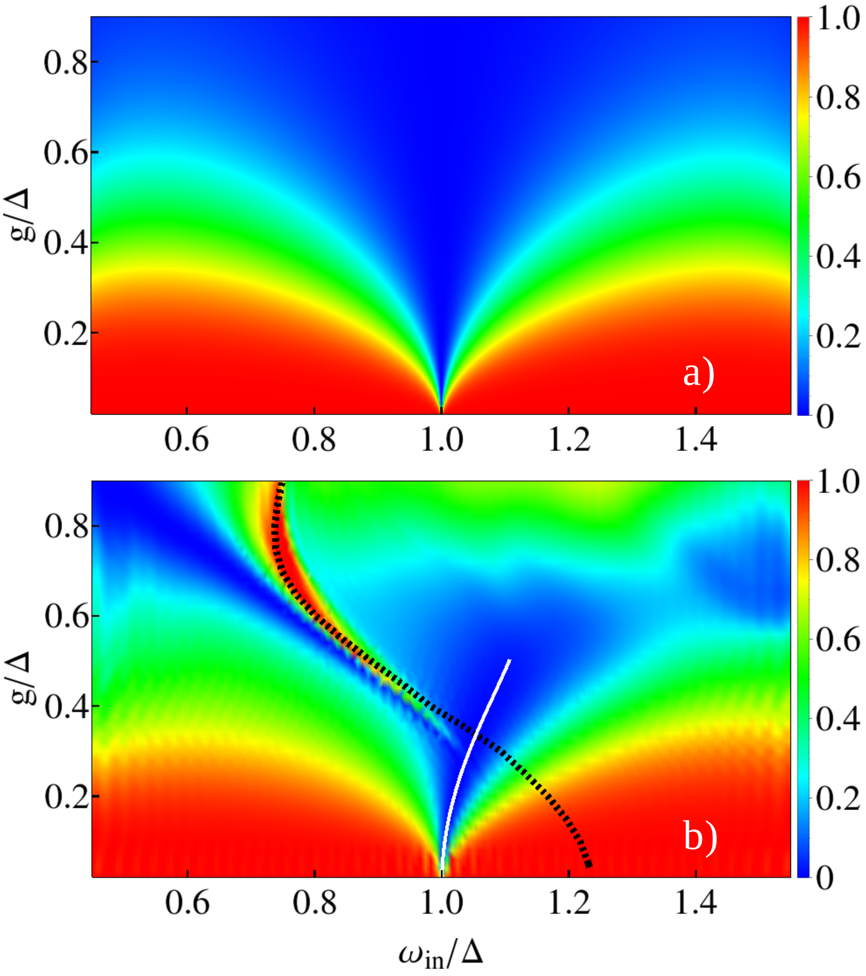

Figure 5.2: **Transmission as a function of both incident photon frequency ω_{in} and g.** *(a)* Transmittance within the RWA *(b)* Elastic Transmittance in the full model. The black line marks the estimated frequency for the Fano resonance while the white line gives the estimated spectral position for the transmittance minimum (see text).

one and thus a different speed, since the dispersion relation ω_k is nonlinear. Notice also that, in this case, after the scattering event the photon cloud around the qubit has changed, being now broader in real space (thus narrower in momentum space).

We analyze first the elastic spectrum and discuss the inelastic one in the following subsection. Fig. 5.2 renders the transmission into the *elastic* channel, as a function of both $\omega_{\rm in}$ and g. The top panel is obtained within the RWA, while the lower panel is computed using the full Hamiltonian.

For sufficiently small g ($g \lesssim 0.3$), the elastic transmission spectra is, both within the RWA and for the full model, characterized by a deep transmission minimum, with a spectral width that increases with g. The main difference is that, while within the RWA the minimum always occurs at $\omega_{\text{in}} = \Delta$ (see Fig. 3.4), in the full model the transmission minimum blueshifts with g. This is the so-called Bloch-Siegert effect, already observed in a circuit-QED system formed by a qubit and a resonator [106]. Our shift is also reminiscent of the frequency renormalization in the spin-boson model [115, 223], which is a continuum model without band edges. However, the renormalization group flow predicts a redshift of the effective frequency of the qubit. Here, the waveguide presents a natural cutoff at high energies, which prevents a direct application of the renormalization group. Nevertheless, the counter-rotating terms can be taken into account (see App. E), leading to an analytical condition for the spectral position of the transmission minimum, which is rendered in 5.2(b) (white line).

For larger g ($g > 0.3$), an asymmetric Fano-like resonance develops in the elastic transmission spectra. This feature combines a deep minimum and a strong transmission maximum, with a line width that increases monotonically with g. Fano resonances are the hallmark of long-lived states entering the scattering dynamics. In this case, its origin can be traced back to the energy ω' of a leaky bound state we found in the system, whose energy is plotted in Fig. 5.3 (see Fig. 3.5). This state was not computed with MPS, but by means of the exact diagonalization of a seven-cavity chain (see Sect. 2.4). As seen in the inset of Fig. 5.3, contrarily to the truly bound states, the excitations of this state do not decay to 0 that fast. Therefore, in the extended chain, this state can couple to propagating ones, appearing in the scattering spectrum. As seen in Fig. 5.2, the resonance energy of the Fano-like line matches with the energy of this leaky state ω' (black like in Fig. 5.2). Under the RWA, the leaky bound state becomes a real bound state with 3 excitations. Therefore, this state is not accessible to the propagation of one photon in the RWA due to the conservation of the number of particles. Counter-rotating terms mix the one and three excitation sectors, opening the way to the appearance of this novel long-lived transmission resonance.

Notice that for $g \gtrsim 0.7$ a new regime seems to appear where the transmission is largely enhanced for a wide frequency range. This is reminiscent of the decoupling between light and matter predicted when $g \gtrsim 1$ in cavity-QED [117]. The terms responsible of that decoupling are proportional to $(a_0 + a_0^\dagger)^2$. This term appears due to the fact that one must replace the linear momentum of the electrons $m_e\mathbf{v}$ by $m_e\mathbf{v} + e\mathbf{A}$ in the kinetic energy, where m_e and e are the electron mass and charge respectively, $\mathbf{v}$ its velocity, and $\mathbf{A}$ the magnetic vector potential. However, we do not incorporate these terms to the Hamilto-

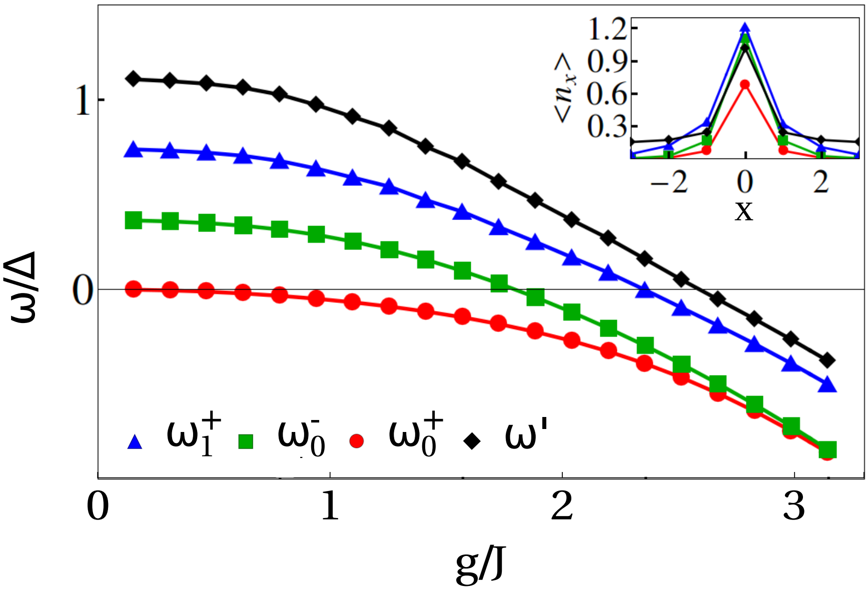

Figure 5.3: **Leaky bound state.** Energy of the leaky bound state ω' (black curve), together with the bound-state energies ω_0^+, ω_0^-, and ω_1^+ (see Fig. 3.5). In the inset, we plot the number of particles for $g = 0.7$. As seen, the profile for the leaky state does not decay so quickly, because it is not a truly bound state.

nian because they are expected to play a role only for values of g larger than those considered here. The analysis of the transmission spectra at such high g values, in the so-called "deep ultrastrong regime", is an interesting problem that is, however, beyond the aim of this section.

5.1.3 Inelastic spectrum

As seen in Figs. 5.1(b) and (d), we also have inelastic scattering. This is a nonlinear process in the sense of Eq. (4.29). Fig. 5.4 renders the transmitted flux at frequencies different to the incoming one, as a function of ω_{in}. The Fourier analysis reveals that the frequency of the output flying photon ω_{out} is linked to ω_{in} through

$$\omega_0^+ + \omega_{\text{in}} = \omega_1^+ + \omega_{\text{out}}, \tag{5.3}$$

where ω_1^+ is the energy of the state $|\phi_1^+\rangle$ (see Fig. 3.5 in Sect. 3.2). Therefore, this inelastic process corresponds to a Raman scattering [97, 98] that leaves the system in an excited bound state that, if counter-rotating terms were not present, would fully reside in the sector $N_{ext} = 2$. Within the RWA this sector is not accessible for one-photon propagating in the ground state, so this Raman process is a genuine ultrastrong feature.

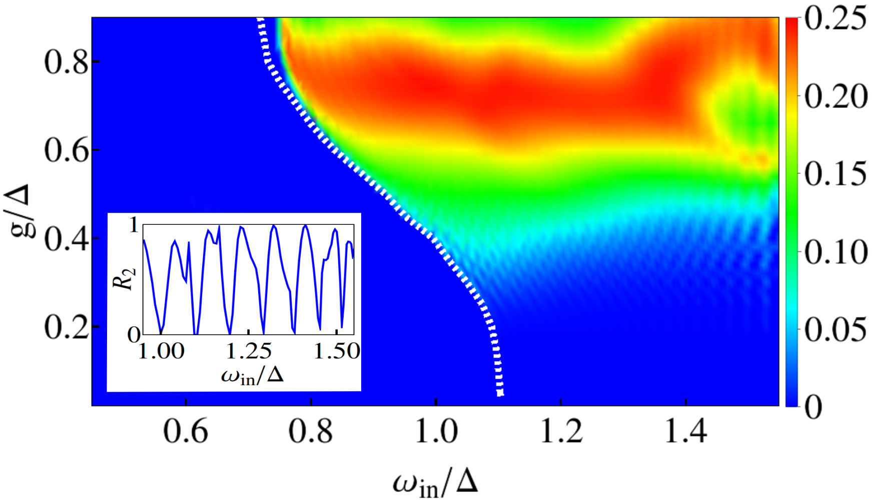

Figure 5.4: **Inelastic transmittance.** Transmittance in the full model in the inelastic channel as a function of both incident photon frequency ω_{in} and g. The white line is estimated boundary for the region where the photon frequency conversion occurs. The inset presents, for $g = 0.8$, the inelastic reflection spectra when the waveguide is terminated at position $\Delta x = 20$, showing that 100% efficient Raman process is possible using one incoming photon.

The Raman process is not energetically possible for all the values of ω_{in}, since it has to fulfill Eq. (5.3). This is seen in Fig. 3.7. Taking into account that ω_{out} necessarily belongs to the band defined on $|\phi_1^+\rangle$ (blue-shaded region; see discussion in the last paragraph of Sect. 3.2), the input frequency ω_{in} has to be in the region where the bands on $|\phi_0^+\rangle$ and $|\phi_1^+\rangle$ overlap (purple-shaded region). The minimum frequency at which the Raman process may occur is $\min[\omega_{\text{out}}] = \omega_1^+ - \omega_0^+ + \epsilon - 2J$. The dependence with g of this quantity is represented in figure 5.4 (white line), marking the boundary for existence the inelastic transmission.

The computed inelastic transmittance never exceeds 0.25. This turns out to be a fundamental upper bound: the maximization of the current in the inelastic channel, P_{ine}, subject to the conditions of current conservation ($1-|r|^2-|t|^2 = P_{\text{ine}}$), and continuity of the photonic wave function ($1 + r = t$), readily gives $\max[P_{\text{ine}}] = 0.5$. As a point-like qubit cannot differentiate between left and right, P_{ine} is equally divided in both directions. This argument is analogous to that leading to the maximum possible absorption by point-like scatterers [220]. Full absorption can be achieved in that case if a mirror is placed in the waveguide (the so called "one-port coherent perfect absorption" [224]). Exploiting this analogy, we have considered the case where the waveguide is terminated at the transmission side of the qubit. In this case, "one-port coherent perfect

Raman scattering", implying both photon frequency conversion and excitation of the dressed qubit, is possible with unit probability *at the one-photon level*, as shown in the inset of Fig. 5.4.

Both Fano and Raman processes described above are robust under moderate dissipation. Using a solvable model, that mimics dissipation by coupling the qubit to an auxiliary open waveguide, we have estimated that both processes should be visible at, at least, the dissipation levels present in some actual realizations in waveguide QED, such as superconducting circuits. Details on both the estimation and the model used can be found in App. F.

It is interesting to analyze whether this Raman process may also occur in other systems. There are other proposals in waveguide QED giving Raman or inelastic scattering [225, 226], but all of them require more complex systems. Under the RWA, a two-level atom has an inelastic scattering channel, but this process requires from two input photons [103, 158]. Besides, by virtue of Theorem 1 in Sect. 4.2.1, inelastic scattering is impossible if the scatterer is a linear system, such as a harmonic oscillator. Therefore, the system analyzed in this section represents the minimal setup for observing inelastic scattering with a single photon.

5.1.4 Qubit dynamics

We saw in Sect. 3.3 that the bound states influence the spontaneous-decay dynamics of a qubit in the RWA. Here we see that the qubit dynamics is influenced by the bound states in the ultrastrong regime under single-photon scattering. Figure 5.5 shows the time evolution of $\Delta P(t) = P(t) - P_0^+$, where $P(t)$ is the evolution of the population of the two-level system and P_0^+ this population in the ground state of the model $|\phi_0^+\rangle$. We send an incoming photon with a representative value of the input energy $\omega_{in} = 0.9$ (see Figs. 5.2 and 5.4) for several values of the coupling g. For $g < 0.3$, the qubit dynamics is governed by the passing wave packet and the exponential de-excitation of the qubit. For $0.3 < g < 0.55$, ΔP shows a slow decay characterized by multiexponential relaxations, associated to the resonant excitation of both the leaky bound state related to the Fano resonance. For higher g ($g = 0.55$), the Raman excitation is possible and ΔP is finite at long times.

A final comment is in order. Using energy and parity conservation, another scattering event would be possible: three outgoing photons with energies $\omega_{\text{out},1}$, $\omega_{\text{out},2}$, and $\omega_{\text{out},3}$, leaving the system in the ground state again, provided the energies fulfill

$$\omega_{\text{in}} = \omega_{\text{out},1} + \omega_{\text{out},2} + \omega_{\text{out},3}. \tag{5.4}$$

However, numerical evidence says this process does not occur. There are two

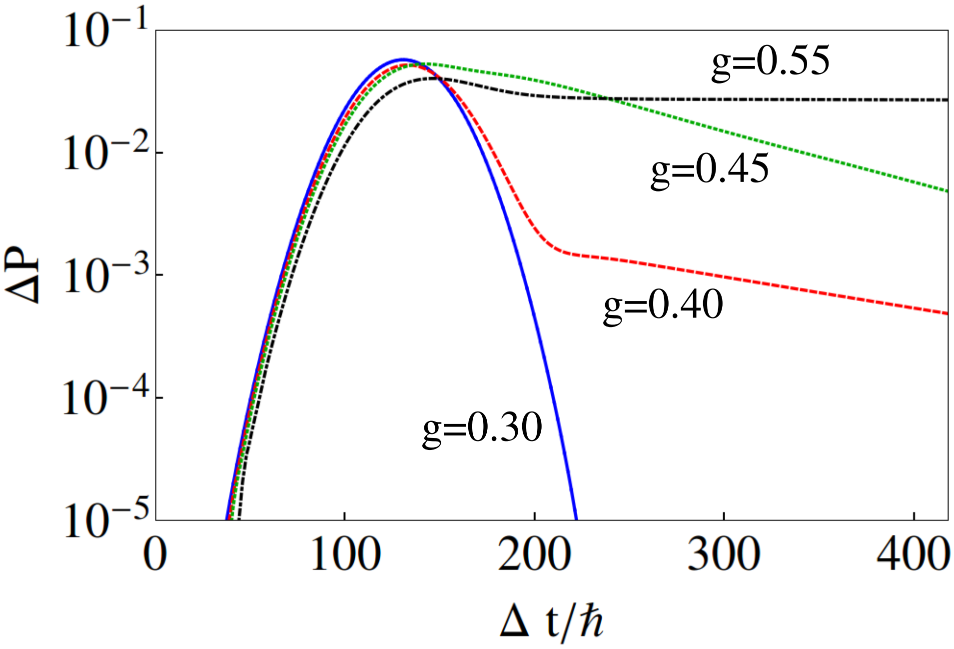

Figure 5.5: **Qubit dynamics.** Time evolution for the population of the qubit excited state, with respect to that in the ground state, for $\omega_{in} = 0.9$ and several values of the photon-qubit coupling g. The wave packet width is $\sigma = 20$, for which $|\delta\omega_{in}/4J| \simeq 0.04 \ll 1$. While for $g = 0.3$ (solid) the dynamics corresponds to a fast decay back to the ground state, multirelaxation long-lived process occur for $g = 0.4$ (dashed) and 0.45 (dotted). At $g = 0.55$ (dashed-dotted) Raman scattering is energetically possible and the qubit ends up in an excited stationary state.

options: (i) the process does happen, but the probability is too low due to the fact that this would involve the simultaneous interaction between several excitations or (ii) the process does not occur due to some hidden symmetry that suppresses this scattering channel. We have not been able to find out which one is the correct answer. In any case, this process is not relevant.

5.2 Photon generation

An optical process that may strongly benefit from an enhanced light-matter interaction is photon downconversion, where a light beam of a given frequency is split into two beams whose frequencies add up to the original one. Downconversion is routinely used for the generation of entangled photons and of light at convenient frequencies. This is already done in atomic and molecular systems and it could also be useful for energy harvesting, by using photons of high energy to excite more suitable transitions in a photovoltaic material.

Photon down and upconversion (the inverse process) are currently realized in bulk optics with the help of nonlinear noncentrosymmetric materials [98]. However, only a small part of the incident power is converted into a correlated two-photon output field [227–229]; due to the smallness of the fine structure constant, the typical performance of this process in crystals such as BBOs is very small, with only about one in every 10^{12} photons being downconverted [98].

In a few-photon-waveguide-QED context, downconversion consists in two-photon generation from one and only one incident photon. In the following, we propose a cyclic three-level system (C3LS) as a two-photon generator from one and only one photon. These results were published in [191].

The mechanism is rather simple. A photon impinges on a cyclic three-level system (C3LS) and resonantly populates the level $|2\rangle$, as schematically represented in Fig. 5.6(a). Additionally to the direct relaxation of $|2\rangle$ to the ground state, the cascade $|2\rangle \rightarrow |1\rangle \rightarrow |0\rangle$ allows the relaxation to be accompanied by the emission of two photons [198]. This mechanism was proposed for chiral waveguides [230]. Here we generalize the results for nonchiral waveguides, compare numerical and analytical calculations, include losses, analyze the entanglement of the output field, and suggest a possible experimental realization.

5.2.1 Model and implementation

We consider a cyclic three-level quantum system (C3LS) strongly coupled to a one-dimensional waveguide where photons can travel freely. We neglect thermal fluctuations and losses in the waveguide and, for the moment, in the C3LS. The Hamiltonian of the scatterer is

$$H_{\mathrm{sc}} = \sum_{j=0}^{2} \Delta_j \left|j\right\rangle \left\langle j\right| . \tag{5.5}$$

We will tackle the problem with the master-equation approach and by using MPS. For now, we focus on the former. As this method is based on the input-output formalism (see Sect. 2.2), we split the bosonic operators into right and left modes, $a_{+,k}$ and $a_{-,k}$, respectively. The interaction term reads

$$H_{\mathrm{int}} = G \int dk\, g(k)(a_{+,k} + a_{-,k}) + \mathrm{H.c.}, \tag{5.6}$$

where G us a generalized ladder operator that induces transitions in the C3LS

$$G = \sum_{i,j=0}^{2} G_{ij} \left|i\right\rangle \left\langle j\right| . \tag{5.7}$$

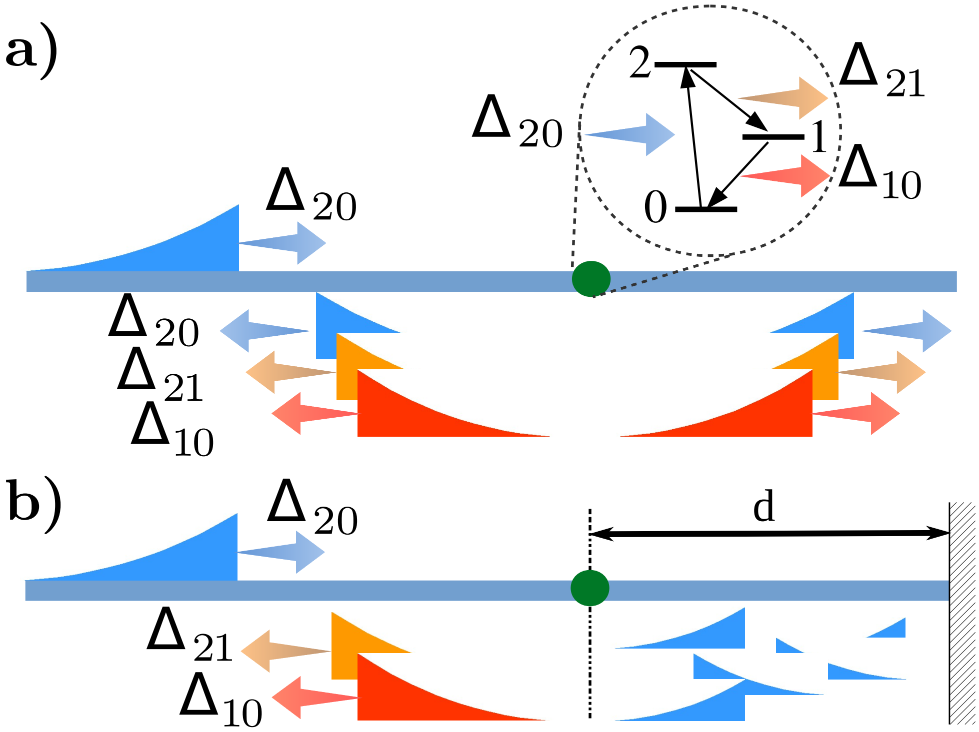

Figure 5.6: Downconversion setup. (a) A single incoming photon interacts with a three-level system. Part of it is elastically transmitted/reflected (Δ_{20}, blue) and part is downconverted into a pair of photons with frequencies Δ_{21} and Δ_{10} (orange and red). (b) Placing a mirror right after the scatterer at a suitable distance d, downconversion can become deterministic: all reflected photons have downconverted frequencies.

Here, G_{ij} is the coupling strength of the transition $|i\rangle \leftrightarrow |j\rangle$. For our purpose, we need G_{10}, G_{20}, and G_{21} different from 0 (see Fig. 5.6(a)). $g(k)$ is the momentum-dependent coupling. As we will see, the analytical results do not depend on the functional form of $g(k)$, but in the values it takes at the resonance energies Δ_1, Δ_2, and $\Delta_2 - \Delta_1$. Therefore, we do not consider a model in particular in the analytical computations. We will specify the model in the numerical computations in Sect. 5.2.2.

An important point is that a C3LS cannot be realized in systems that (i) are so small compared to the waveguide that the dipolar interaction dominates (like atoms) or (ii) whose quantum states are labeled by a spatial parity tag. The reason is that in those cases at least two of the three states in the C3LS must have the same parity, but the dipole interaction only couples states with different parity. However, effective C3LSs may appear in extended quantum systems, where couplings beyond the dipolar term must be considered. Imple-

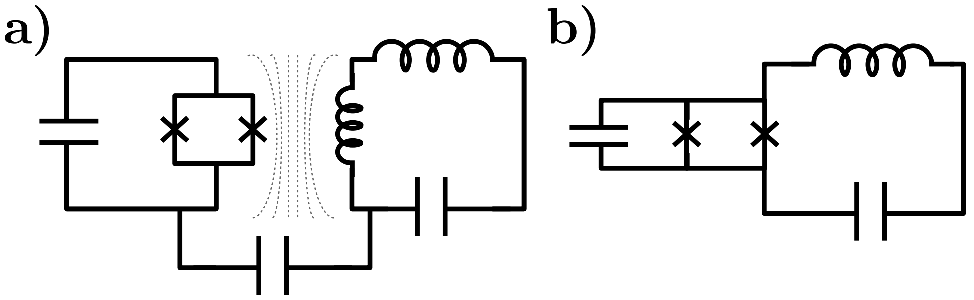

Figure 5.7: (a) A transmon can be both inductively and capacitively coupled to an LC resonator. Coupling strength can be increased by either increasing the SQUID area or (b) by sharing a conductor segment, in the spirit of Ref. [212] and similar proposals.

mentations of C3LS are some asymmetric molecules [231] and flux qubits made of superconducting circuits [227, 228]. Nevertheless, this last system leads to three quite dissimilar excitation energies. In order to obtain two downconverted photons of similar (and possibly equal) frequencies, we consider an alternative design for an effective C3LS in the microwave range using a transmon (a charge superconducting qubit shunted by a big capacitor).

Typically, inductive coupling between the transmon and the transmission line is negligible. The reason is that the transmon design is basically that of a one-dimensional electric dipole, without support for currents. In addition, the SQUID that controls the transmon frequency is usually small and shielded away from any coupling with the transmission line. Inductive couplings between transmons have been however demonstrated [232, 233]. We make use of similar ideas to envision a different coupling architecture that allows us to break the parity symmetry in the transmon setup.

Our starting point is a setup such as the one in Fig. 5.7(a), where the transmon SQUID is no longer screened and the superconducting island couples both capacitively and inductively to the resonator. The circuit Lagrangian (with inductive and capacitive coupling) is

$$\begin{aligned}\mathcal{L} = \int dx\; c(\partial_t\phi(x,t))^2 - \frac{1}{l}(\partial_x\phi(x,t))^2 \\ + \frac{1}{2C_\Sigma}(q-\mathcal{Q})^2 - E_J\cos(2\pi\Phi/\Phi_0)\cos\varphi\,.\end{aligned} \tag{5.8}$$

The first line accounts for the transmission line Lagrangian while the transmon and its coupling is written in the second line. Here, $\phi(x,t)$ is the (quantum) flux field, that in the interaction picture reads,

$$\phi(x,t) = \sqrt{\frac{Z_0}{4\pi}} \int_0^\infty d\omega \, \frac{1}{\sqrt{\omega}} \Big(a_{+,\omega} \mathrm{e}^{-i\omega(t-x/v)} \\ + a_{-,\omega} \mathrm{e}^{-i\omega(t+x/v)} + \text{H.c.} \Big) \,, \tag{5.9}$$

with v being the velocity of the field and $Z_0 = \sqrt{l/c}$ being the line impedance, where c (l) is the capacitance (inductance) per unit length. The superconducting Josephson energy is E_J and C_Σ is the capacitance. Charge and phase are quantized via $[\mathrm{e}^{i\varphi}, q] = 2e\, \mathrm{e}^{i\varphi}$. The transmon is driven and coupled to the line via the charge $\mathcal{Q}$ and the flux Φ ($\Phi_0 = h/2e$ is the flux quantum):

$$\mathcal{Q} = 2e\, n_g + c\, \partial_t \phi(x,t) \tag{5.10}$$

$$\Phi = \lambda\, \partial_x \phi(x,t) + \frac{\Phi_0}{2\pi} \varphi_{\text{ext}} \,. \tag{5.11}$$

We have introduced the coupling factor λ that accounts for the effective field induced by the transmon's SQUID after taking into account the screening. Inserting the latter in (5.8) and expanding the cosine up to first order in the quantum fluctuations $\partial_x \phi$ around $\partial_x \phi = 0$, we get the coupling Hamiltonian,

$$H_{\text{coupling}} = \frac{c}{C_\Sigma}\, q \partial_t \phi - \lambda d \frac{\pi}{\Phi_0} E_J \sin(\varphi_{\text{ext}}) \cos(\varphi)\, \partial_x \phi. \tag{5.12}$$

We still need to show that (5.12) provides the cyclic-coupling structure. We numerically diagonalize $H_{\text{transmon}} = \frac{1}{2C_\Sigma} q^2 - E_J \cos\varphi$ in the charge basis, retaining the first three levels $H_{\text{transmon}} = \sum_{j=0}^{2} \Omega_j |j\rangle\langle j|$. In the basis of these three eigenstates, we can compute the different coupling constants G_{ij} in H_{int} (see Eq. (5.6)). In Figure 5.8 we plot the contributions due to the charge operator q in (5.12). As already explained in the literature, $\langle i|q|i+1\rangle \neq 0$ but $\langle 0|q|2\rangle = 0$ [234]. A nonzero G_{20} value is obtained through the inductive coupling. Fig. 5.8 also renders the dependence of $\langle 0|\cos(\varphi)|2\rangle \neq 0$ on E_C/E_J (notice that $\langle i|\cos(\varphi)|i+1\rangle = 0$ since $\cos(\varphi)$ is an even operator and $|i\rangle$ and $|i+1\rangle$ have opposed parity). Therefore, by combining inductive and capacitive (electric and magnetic) coupling the transmon has a cyclic structure. Throughout the main text we set $E_C/E_J = 1/20$, which is a typical experimental value for transmons. This ratio, together with the density of states of the line, fixes the ratio $\Gamma_{10}^{(0)}/\Gamma_{21}^{(0)}$, with $\Gamma_{ij}^{(0)} \equiv 2\pi g^2(\Delta_{ij}) G_{ij}^2$, being the rates between quantum levels induced by coupling to the waveguide photons, and $\Delta_{ij} = \Delta_i - \Delta_j$. Standard experimental values of the rates are of the order of $10^{-3}\Delta_{10}$. Finally, we fix λ and C_Σ such that the two-photon generation is optimal (see below).

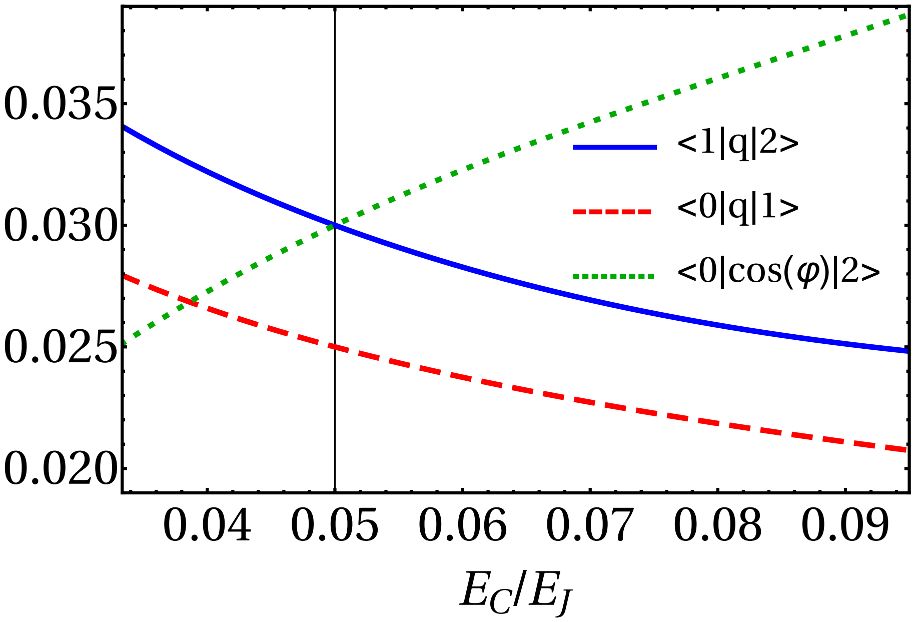

Figure 5.8: Nonzero charge $\langle i|q|j\rangle$ and flux $\langle i|\cos\varphi|j\rangle$ matrix elements contributing to the coupling operator G (see Eq. (5.12)). The vertical line marks the parameters chosen in our simulations with $E_C/E_J = 1/20$.

5.2.2 Numerical results

We numerically compute the time evolution of a one-photon wave packet by means of MPS (see Sect. 2.3), as we did in Sect. 5.1. We use the discrete photonic Hamiltonian (1.2), but the results do not depend on the model, as stated in Sect. 5.2.1. Our simulations assume that the incident photon was generated via spontaneous emission in an auxiliary qubit. This photon has an exponentially decaying profile in real space (see App. G.4). We emphasize that the physical mechanisms and the consequences of this section are given in terms of the different spontaneous emitted rates, both radiative and nonradiative, of the scatterer.

In Fig. 5.9 we plot the spectrum for the one-photon transmittance and reflectance when the input frequency is ω

$$|t^{(1)}(\omega)|^2 = \lim_{t\to\infty} |\langle\phi_0|a_{+,\omega}e^{-iHt}|\Psi_{\text{in}}\rangle / \langle\phi_0|a_{+,\omega}|\Psi_{\text{in}}\rangle|^2, \tag{5.13}$$

$$|r^{(1)}(\omega)|^2 = \lim_{t\to\infty} |\langle\phi_0|a_{-,\omega}e^{-iHt}|\Psi_{\text{in}}\rangle / \langle\phi_0|a_{+,\omega}|\Psi_{\text{in}}\rangle|^2, \tag{5.14}$$

and the probability of emitting two photons $P^{(2)}(\omega)$. The latter is given by

$$P^{(2)}(\omega) = \lim_{t\to\infty} \frac{\left|\sum_{s,s'=\pm}\sum'_{\omega_1\omega_2}\langle\phi_0|a_{s,\omega_1}a_{s',\omega_2}e^{-iHt}|\Psi_{\text{in}}\rangle\right|^2}{2|\langle\phi_0|a_{+,\omega}|\Psi_{\text{in}}\rangle|^2}. \tag{5.15}$$

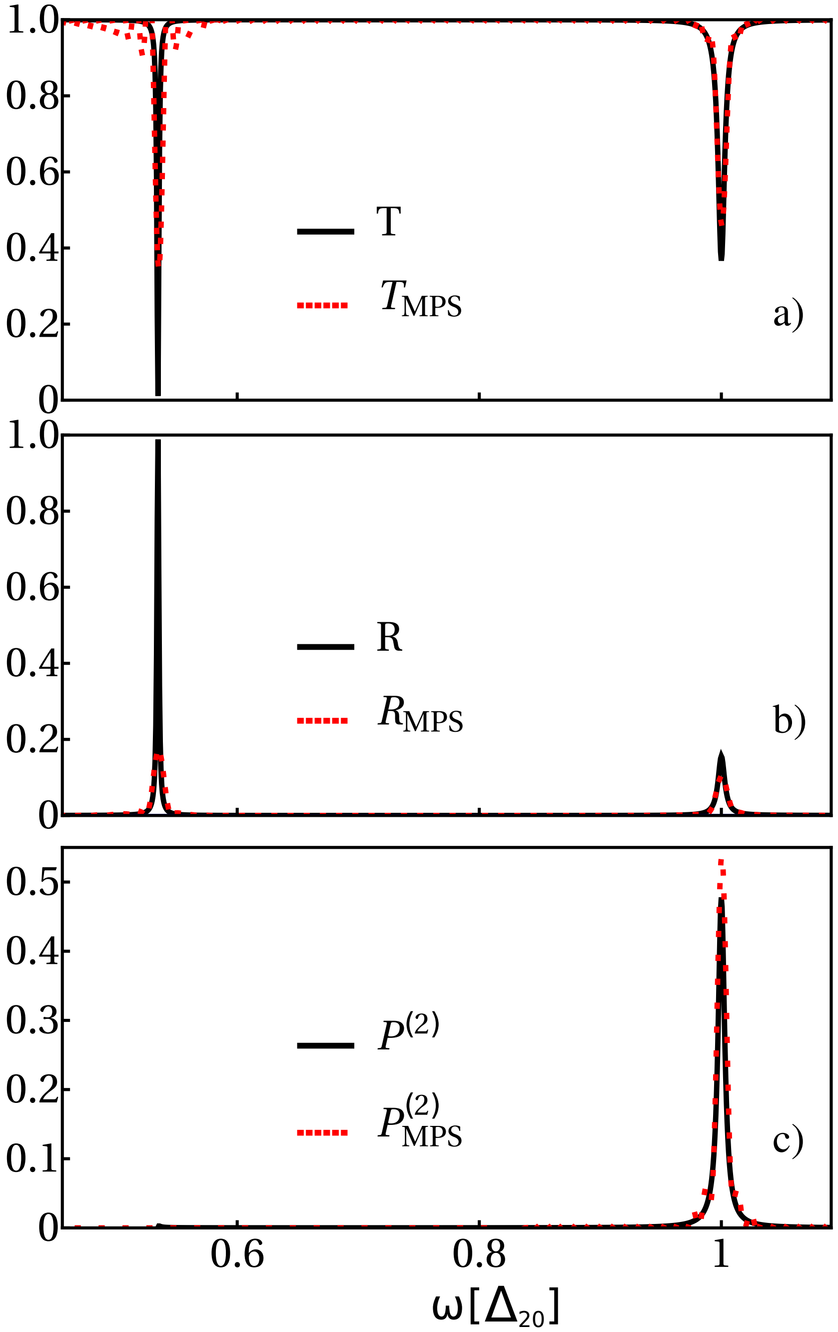

Figure 5.9: Scattering coefficients in a cyclic three-level system, as a function of the incident frequency ω. One-photon transmission (panel (a)), reflectance (panel(b)) and probability of two-photon generation $P^{(2)}(\omega)$ (panel(c)). We show both analytical (solid lines) and numerical results obtained with MPS (dotted lines). The parameters are $\Delta_{10} = 0.53$, $\Delta_{20} = 1$, $\Gamma^{(0)}_{10} = 10^{-3}$, $\Gamma^{(0)}_{20} = 1.4 \times 10^{-3}$ and $\Gamma^{(0)}_{21} = 2.2 \times 10^{-3}$. We remind that $\Gamma^{(0)}_{ij} = 2\pi g^2(\Delta_{ij})G^2_{ij}$.

The summation $\sum'_{\omega_1\omega_2}$ is performed over the values of ω_1 and ω_2 such that they fulfill energy conservation: $\omega_1+\omega_2=\omega$. The first transmission dip occurs when the photon energy is centered around $\omega=\Delta_{10}$. In this spectral region the $|0\rangle \rightarrow |1\rangle$ transition is the only one available. Thus, the C3LS behaves as an effective two-level system and the photon is fully reflected at resonance (see Fig. 3.4). Consequently, $P^{(2)}(\omega)=0$ in this frequency range (see Fig. 5.9(c)). In the second transmission dip, located at $\omega=\Delta_{20}$, the transmittance presents a finite minimum value, that is close to 0.5. Figures 5.9(b) and (c) show a remarkable 50% downconversion efficiency of the incoming photon into just two (and only two) outgoing photons, with only a very small amount of light reflected.

For the shake of completeness and to emphasize the fact that we have access to the time domain too, we plot the 3CLS level population in Fig. 5.10(a). We see that the second excited state gets populated first, since our incident photon is resonant with the transition $|0\rangle \leftrightarrow |2\rangle$. After the transient period, both levels decay to the ground state. We also plot the particles in energy space, $\langle n^{(+)}_{\omega}\rangle = \langle a^{\dagger}_{+,\omega}a_{+,\omega}\rangle$ and $\langle n^{(-)}_{\omega}\rangle = \langle a^{\dagger}_{-,\omega}a_{-,\omega}\rangle$, right- and left-moving respectively, in Figs. 5.10 (b) and (c). In doing so, we can visualize the two-photon generation in time domain. At the beginning, the photon spectral population presents a single peak around the incident energy of the right-moving photons. After the interaction has occurred, a peak has appeared in the population of left-moving photons at Δ_{20}, corresponding to the single-photon reflection (see Fig. 5.10 (c)). In addition, two peaks emerge after the scattering for both forward and backward traveling photons centered at Δ_{21} and Δ_{10}, associated to the generation of the two-photon state.

In order to characterize the two-photon wave function emerging from the downconversion process we compute the two-point wave function, both in position space $\phi^{\text{out}}_{x_1x_2} = \langle\phi_0|a_{x_1}a_{x_2}|\Psi(t_{\text{out}})\rangle$, and in energy space for right-moving photons $\tilde{\phi}^{\text{out}}_{\omega_1\omega_2} = \langle\Omega|a_{+,\omega_1}a_{+,\omega_2}|\Psi(t_{\text{out}})\rangle$. As shown in Fig. 5.11, both photons are emitted spatially in a symmetric way with respect to the position of the scatterer ($x=0$). In energy space, $\tilde{\phi}^{\text{out}}_{\omega_1\omega_2}$ is centered around $(\omega_1,\omega_2)=(\Delta_{10},\Delta_{21})$ and $(\Delta_{21},\Delta_{10})$ (white dotted lines), as expected from emission from a doubly resonant process. However, and similarly to the phenomena of resonance fluorescence, $\tilde{\phi}^{\text{out}}_{\omega_1\omega_2}$ is nonzero all along the isoenergetic curve $\omega_1+\omega_2=\omega$ (white solid line in Fig. 5.11(b)).

The emitted photons are entangled. The corresponding von Neumann entropy S_{VN} can be computed after normalizing the two-photon wave function, such that $\sum_{x_1x_2}|\phi^{\text{out}}_{x_1x_2}|^2=1$, and finding its Schmidt decomposition, $\phi^{\text{out}}_{x_1x_2}=\sum_m \lambda_m \varphi_{x_1,m}\chi_{x_2,m}$, being $\{\lambda_m\}$ the singular values. Then $S_{\text{VN}} = -\sum_m \lambda_m^2 \ln(\lambda_m^2)$ [235]. In the case shown in Fig. 5.11 we get $S_{\text{VN}}=1.44$.

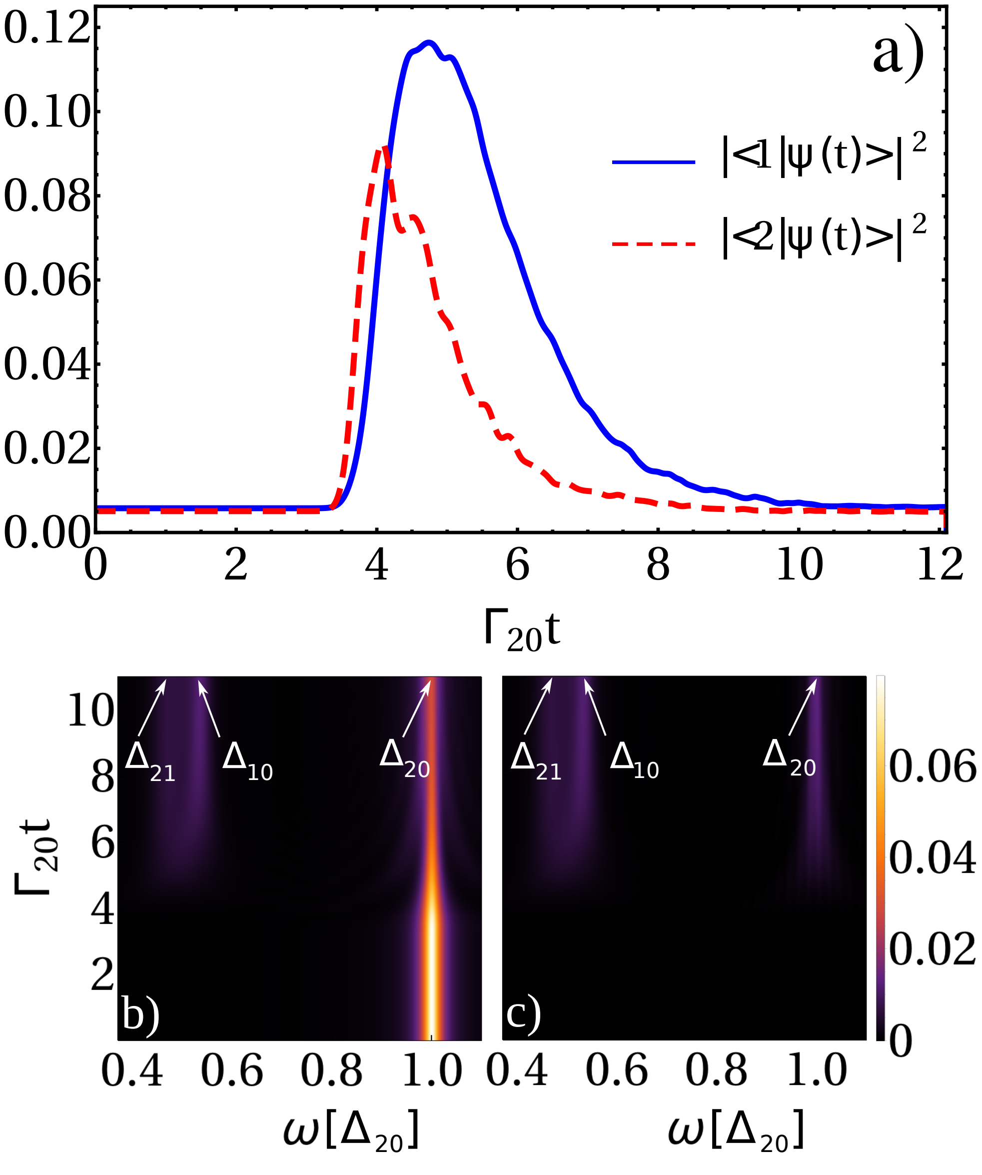

Figure 5.10: a) Population of the first (blue solid line) and second (red dashed line) excited states as a function of time. Photon occupation in energy space for b) right-moving, $\langle n_\omega^{(\mathrm{r})}\rangle$, and c) left-moving photons, $\langle n_\omega^{(\mathrm{l})}\rangle$, respectively, as a function of time. The energies are those of Fig. 5.2. Just for improve the visibility of the figure, we take larger values for the decay rates: $\Gamma_{10}^{(0)} = 0.021$, $\Gamma_{20}^{(0)} = 0.028$ and $\Gamma_{21}^{(0)} = 0.043$.

For a better understanding, we plot the contribution of each mode to S_{VN} in Fig. 5.12(a). The entropy is dominated by the first two singular values, but the contribution from the other Schmidt modes is nonnegligible. In order to quantify how the entropy is recovered from a given number of singular values,

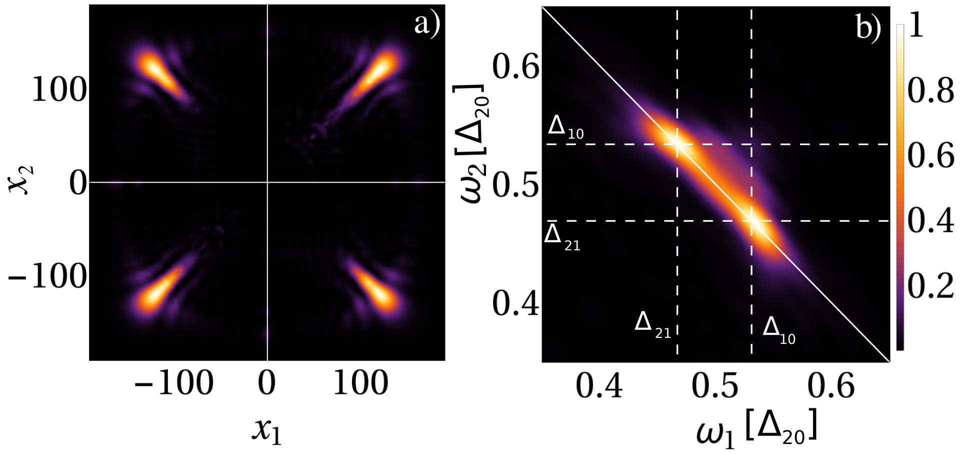

Figure 5.11: Square modulus of the two-photon wave function both in a) position, $|\phi^{\mathrm{out}}_{x_1x_2}|^2$ and b) energy space, $|\tilde{\phi}^{\mathrm{out}}_{\omega_1\omega_2}|^2$. The positions x_1 and x_2 are in units of v/Γ_{20}, with v the group velocity of the waveguide. The isoenergetic line, $\omega_1+\omega_2=\omega$, is shown in the bottom panel (white line). We normalize both wave functions such that $\max(|\phi^{\mathrm{out}}_{x_1x_2}|^2)=\max(|\tilde{\phi}^{\mathrm{out}}_{\omega_1\omega_2}|^2)=1$. The parameters are those of Fig. 5.10.

we define the entanglement entropy of the first m Schmidt modes

$$S_{\mathrm{VN},m} := -\sum_{n=1}^{m} \lambda_n^2 \ln(\lambda_n^2)\,, \tag{5.16}$$

and show $S_{\mathrm{VN},m}/S_{\mathrm{VN}}$ in the inset of Fig. 5.12.

Another measure of how the wave function can be represented by a fixed number of modes is the fidelity, *i.e.* the overlap between the actual two-photon state, $|\Psi_2\rangle = 1/\sqrt{2}\sum_{x_1,x_2}\phi^{\mathrm{out}}_{x_1,x_2}a^\dagger_{x_1}a^\dagger_{x_2}|\Omega\rangle$ and the state reconstructed with m modes:

$$|\Psi_{2,m}\rangle = \frac{1}{\sqrt{2}}\sum_{x_1,x_2}\phi^{\mathrm{out,m}}_{x_1,x_2}a^\dagger_{x_1}a^\dagger_{x_2}|\Omega\rangle, \tag{5.17}$$

being $\phi^{\mathrm{out,m}}_{x_1,x_2}$ the two-photon wave function reconstructed with the first m Schmidt modes, $\phi^{\mathrm{out,m}}_{x_1,x_2}=\sum_{n=1}^{m}\lambda_n\tilde{\varphi}_{x_1,n}\tilde{\chi}_{x_2,n}$. In Fig. 5.12(a) (inset) we check that the overlap qualitatively behaves as $S_{\mathrm{VN,m}}$.

Lastly, we can visualize how the two-photon wave function is reconstructed by adding modes. In Figs. 5.12(b), (c), and (d) we plot $|\tilde{\phi}^{\mathrm{out,m}}_{\omega_1,\omega_2}|^2$ for $m=1$, 2 and 3 respectively, whereas we plot $|\tilde{\phi}^{\mathrm{out}}_{\omega_1,\omega_2}|$ in panel (e). The white lines, as in Fig. 5.11, mark the isoenergertic condition. While the wave-function reconstruction with $m=1$ does not reproduce the bimodal aspect of the state, already with $m=2$ the double-peaked structure is well defined.

We have not discussed how to optimize the two-photon entanglement. Since the two-photon wave packet is created in the $2 \to 1 \to 0$ transition we can benefit from the studies on the spontaneous emission in cascaded systems and argue, as explained in [236], that maximally entangled states are expected in the regime $\Gamma_{21}/\Gamma_{10} \to 0$. In our model, this ratio is fixed by the relation E_C/E_J. However, another type of 3CLS or further engineering in the transmon, can tune this ratio and provide a way of generating different amounts of entanglement.

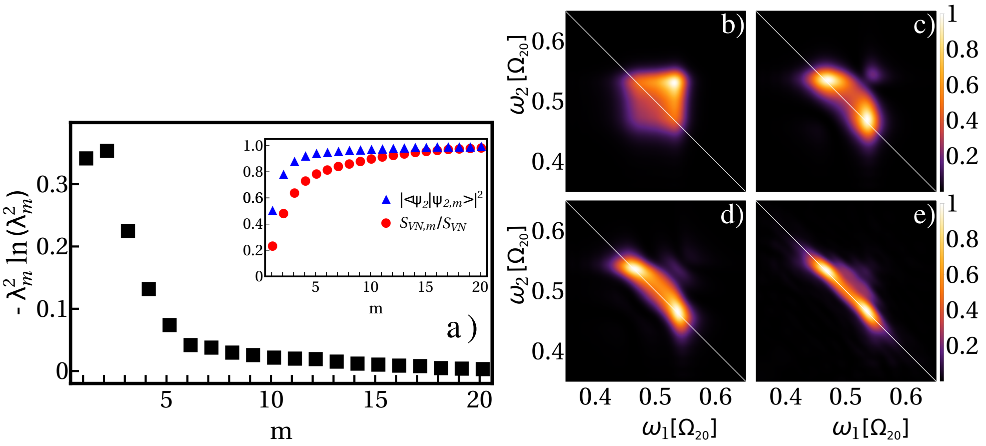

Figure 5.12: a) Contribution of each Schmidt mode to S_{VN}, $-\lambda_m^2 \ln(\lambda_m^2)$ as a function of m. In the inset, we plot the entropy of $|\Psi_{2,m}\rangle$ over the whole entropy, $S_{\mathrm{VN},m}/S_{\mathrm{VN}}$ (red circles) and the overlap between $|\Psi_2\rangle$ and $|\Psi_{2,m}\rangle$ (blue triangles) as a function of m. $|\tilde{\phi}^{\mathrm{out,m}}_{\omega_1,\omega_2}|^2$ for b) $m = 1$, c) $m = 2$, d) $m = 3$ and e) $m = L$ which is the exact result, cf. Fig. 5.11b) L is the number of modes, which matches with the number of points in the discretized waveguide; see Appendix 2.3). The parameters are those of Fig. 5.10.

5.2.3 Analytical calculations

The system considered is not analytically solvable. However, under fair assumptions we are able to provide rather general expressions for the downconversion efficiency. First, we remind that we have numerically tested that no more than two photons are generated in the dynamics. Therefore, the two-photon generation probability can be computed by energy conservation as

$$P^{(2)}(\omega) = 1 - |t^{(1)}(\omega)|^2 - |r^{(1)}(\omega)|^2 - A(\omega)\,. \tag{5.18}$$

Here, $t^{(1)}(\omega)$ and $r^{(1)}(\omega)$ are the one-photon transmittance and reflection respectively. The last term is the energy "absorbed" by the lossy channels, $A(\omega)$.

Besides, the 3CLS is assumed punctual. Thus the photonic wave function is continuous in the scatterer position, implying $r^{(1)}(\omega) = t^{(1)}(\omega) - 1$ [237].

In the following, we find the scattering coefficients $t^{(1)}(\omega)$, $r^{(1)}(\omega)$, and $A(\omega)$ by means of the master-equation approach introduced in Sect. 2.2. We first rewrite the master equation (2.75) introducing the Hamiltonian of the scatterer (5.5)

$$\begin{aligned}\frac{d\rho}{dt} =& - i[\sum_{j=0}^{2} \Delta_j \left|j\right\rangle \left\langle j\right| , \rho] - i\, \alpha g(\omega) 2\cos(\omega t)[G(t), \rho] \\ &+ 2 \sum_{\Delta_{ij}>0} \Gamma_{ij} \left(L_{ij} \rho L_{ij}^\dagger - \frac{1}{2}\{L_{ij}^\dagger L_{ij}, \rho\}\right) \\ &+ \mathcal{D}\rho\mathcal{D} - \frac{1}{2}\{\mathcal{D}^2, \rho\}\,, \end{aligned} \tag{5.19}$$

where $g(\omega)$ appears in Eq. (5.6) and G, now expressed in the Heisenberg picture, is introduced in Eq. (5.7). Let us recall the meaning of each term. The first one is the Von Neumann Equation; it would give the evolution of the C3LS if it were isolated. The second, stands for a classical driving. The second line contains the Lindblad terms describing both the hopping to the line and dissipative channels. There, $L_{ij} = |j\rangle\langle i|$ causes the transition between the states $|i\rangle$ and $|j\rangle$ with a rate Γ_{ij}. Additionally to the transition rates induced by coupling to the waveguide photons, this formulation allows us to consider the transitions γ_{ij} induced by coupling to other baths (as phonons or other components of the EM field). In this case, the total transition rate is $\Gamma_{ij} = \Gamma_{ij}^{(0)} + \gamma_{ij}$. The third line represents a Lindblad term that takes into account pure dephasing, with $\mathcal{D}$ being diagonal matrices in the basis of the scatterer. The dephasing rates, which are quantified by the diagonal elements of $\mathcal{D}$, simply modify the nonradiative losses γ_{ij} in the calculation for $t^{(1)}(\omega)$.

Following the steps shown in Sect. 2.2, and reproduced for this system in App. G.1, we get the expression for the transmission

$$\begin{aligned} t^{(1)}(\omega) =& 1 - \frac{i\Gamma_{10}^{(0)}}{(\omega - \Omega_{10}) + i(\Delta_{10} + \Gamma_{10}^{\phi})} \\ &- \frac{i\Gamma_{20}^{(0)}}{(\omega - \Delta_{20}) + i(\Gamma_{21} + \Gamma_{20} + \Gamma_{20}^{\phi})}. \end{aligned} \tag{5.20}$$

with $\Gamma_{ij}^{\phi} = \frac{1}{2}(\mathcal{D}_{ii} - \mathcal{D}_{jj})^2$ being the dephasing rates for the ρ_{ij} elements. Finally, the energy that leaves the waveguide can be approximated by (see also App. G.2),

$$A(\omega) \simeq 2\, \gamma_{20}\, |r^{(1)}(\omega)|^2 / \Gamma_{20}, \tag{5.21}$$

where this equation is valid around the transition $|2\rangle \to |0\rangle$, $\omega \simeq \Delta_{20}$. The validity of this analytical formalism is shown in Fig. 5.9, where the different scattering coefficients computed with this approximation are compared to the numerical results for the "lossless" case $\gamma_{ij} = 0$.

Some final comments are in order. In the presented theory, the main approximation is to assume that the 3CLS-line coupling strength is sufficiently small. This allows the use of the master equation (5.19) for computing the scatterer dynamics. This is a good assumption in (almost) every experiment so far. Apart from this approximation the theory is rather general, independent of the actual values for dephasing, nonradiative losses or spectral function for the waveguide.

Equation (5.18) can be used to search the optimal parameters for downconversion. The first observation is that losses are detrimental, always reducing $P^{(2)}(\omega)$. Even in absence of losses ($\gamma_{ij} = 0$), the two-photon generation can be considered as a loss mechanism *for the one-photon channel*, which implies that the fraction of energy downconverted is at most $\max P^{(2)}(\omega) = \frac{1}{2}$ (occurring when $r(\omega) = -\frac{1}{2}$). This is equivalent to the effect we already seen in the inelastic channel for one photon impinging into a qubit in the ultrastrong coupling regime in Sect. 5.1 (see Fig. 5.4). This bound can be exceeded by breaking the left-right symmetry in the waveguide by, *e.g.*, placing a mirror next to the C3LS, as sketched in Fig. 5.6(b).

Both reflectance and absorption can be calculated in this configuration by summing all multiple-scattering processes that the waveguide photon has with both the C3LS and the mirror [1]. The sum can be done analytically, see App. G.3, resulting in:

$$P^{(2)}(\omega) = 1 - \left| \frac{r^{(1)}(\omega) - \left(1 + 2r^{(1)}(\omega)\right)\Phi(\omega)}{1 + r^{(1)}(\omega)\Phi(\omega)} \right|^2 - \left| \frac{1 - \Phi(\omega)}{1 + r^{(1)}(\omega)\Phi(\omega)} \right|^2 A(\omega), \tag{5.22}$$

where $\Phi(\omega) = \mathrm{e}^{2ik(\omega)d}$, d is the distance between the mirror and the C3LS, Fig. 5.6(b), and $k(\omega)$ is the photon wave vector at frequency ω.

As drawn in Fig. 5.13, the maximum downconversion efficiency predicted by Eq. (5.22) occurs at resonance ($\omega = \Delta_{20}$), and for $\Gamma_{21}^{(0)}/\Gamma_{20}^{(0)} \simeq 2$ and $kd = \pi/2$, and can be approximated by:

$$\max P_2 = 1 - \frac{\gamma_{20} + \Gamma_{20}^{\phi}}{\Gamma_{20}} \tag{5.23}$$

---

[1] Eventually, we set $r_M = -1$, *i.e.* we neglect losses in the mirror, which is a good experimental assumption.

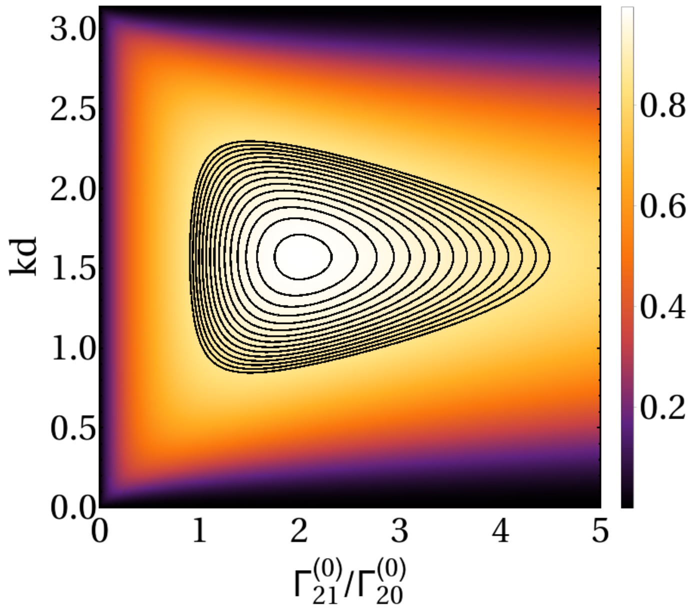

Figure 5.13: $P^{(2)}(\omega = \Omega_{20})$ as a function of the atom-mirror distance kd, See Fig. 5.6, and the ratio $\Gamma_{12}^{(0)}/\Gamma_{02}^{(0)}$. Losses are taken into account. In the figure, a conservative ratio $(\gamma_{20} + \Gamma_{20}^{\phi})/\Gamma_{20}^{(0)} = 0.01$ is used. The rest of the parameters are the same as in Fig. 5.2. Black lines mark isoefficiency curves, starting at 0.85 and finishing at 0.98.

So, remarkably, downconversion may be perfect in the considered configuration if losses are negligible. Equation (5.23) provides a simple expression for the maximum efficiency as a function of the ratio between the rates for absorption and coupling into waveguide photons. This ratio is a key figure of merit in Waveguide QED and values as small as 10^{-2} have already reported for effective two-level systems in both superconducting circuits [40] and photonic crystals [43]. Thus, two-photon generation with one and only one photon with an efficiency larger than 0.99 is doable using an appropriate C3LS.

Summarizing, we have shown that two photons can be efficiently generated by sending one and only one photon through a cyclic three-level atom in a realistic scenario. Remarkably, the downconversion process can in principle occur with unit probability, being only limited by energy leakage to other continuum of modes rather than to the waveguide and/or dephasing in the three-level system. Based on reported experimental data, we have estimated that a nearly perfect two-photon generator operating at the single-photon level is feasible in architectures based on either photonic crystals or superconducting circuits. Together with single atomic mirrors [99, 100, 102], single-photon lasing [213], single-photon Raman scattering [118] (see Sect. 5.1), and photon generation [191] (see Sect. 5.2), this result contributes to the toolbox of pho-

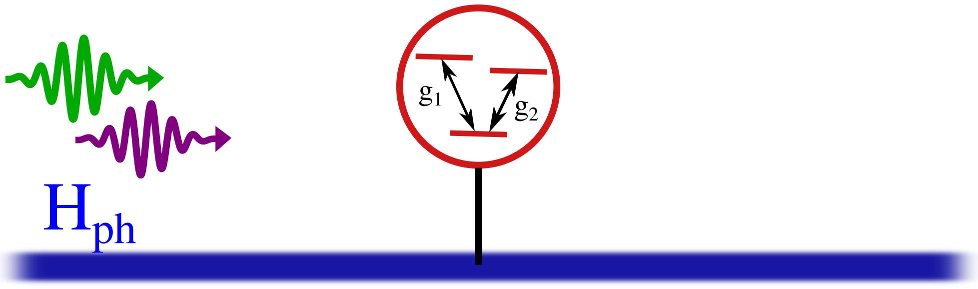

Figure 5.14: V-like three-level system coupled to a 1D waveguide. We will consider one- and two-photon propagation.

tonics with minimum power, where tasks usually associated to high intensities are performed at the one-photon level.

5.3 One- and two-photon scattering from a $\mathrm{V}^{(N)}$ atom

Generally, one-dimensional few-photon scattering exhibits nonlinear phenomena, as we have seen in the previous sections of this chapter. In particular, local scatterers usually have a nonlinear response to two-photon scattering [96, 104, 127, 185, 195] (see Sect. 4.2). Here, we compute the one- and two-photon S matrix from a $\mathrm{V}^{(N)}$ atom, a generalization of a three-level V-like atom (see Fig. 5.14). As we will see, this scatterer is nonlinear in the sense that the response depends on the number of input photons. These results were published in [128].

A $\mathrm{V}^{(N)}$ atom consists of a unique stable state and N excited states, with dipole transitions between the stable state and the rest, whereas the excited states are uncoupled (see Fig. 5.15). It is a generalization of a two-level system ($N = 1$) and a V atom ($N = 2$), which can be either an actual atom or an effective one, e.g., made with inductively coupled transmons [233] or with a charge qubit [238]. Beyond these cases, the $\mathrm{V}^{(N)}$-level structure describes many atomic spectra. For instance, the ground state $|0\rangle$ can represent one hyperfine state whose excitation is constrained to a subset of atomic states $\{|i\rangle\}_{i=1}^{N}$ due to different selection rules, depending on the polarization properties of the incoming light. Also, a $\mathrm{V}^{(N)}$ atom can describe N different two-level systems influenced by a blockade mechanism that prevents the simultaneous excitation of two or more absorbers (see Fig. 5.15b), a feature characteristic of Rydberg atoms used in various quantum information and quantum simulation tasks [239–241].

We compare the scattering properties in the case with $N = 2$ excited

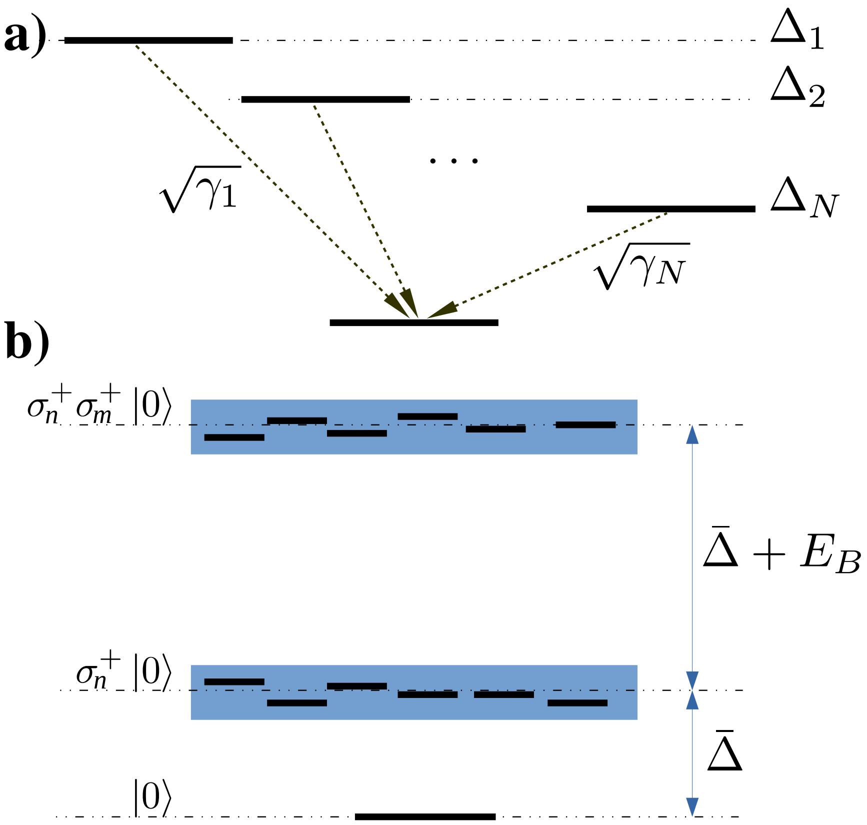

Figure 5.15: (a) Energy levels in a $\mathrm{V}^{(N)}$-atom. We study a point-like scatterer interacting with a continuum of propagating modes. The quantum impurity has N excited levels with energies Δ_i, $i = 1 \dots N$ and decay rates γ_i, which we use to parameterize the light-matter interaction. (b) The previous level structure can be a good approximation for N two-level systems presenting a blockade mechanism [239–241], where the excited states $|i\rangle = \sigma_i^+ |0\rangle$ of the respective atoms or qubits have a strong repulsive interaction, $E_B \gg \gamma_i$, thus preventing simultaneous multiple excitations.

levels with those for two independent collocated qubits. The single-photon scattering matrix from a V atom is equal to that of two qubits, due to the fact that the level structure in the single-excitation subspace is identical for both scatterers (see Fig. 5.17a) and Fig. 5.17b)). In particular, in both situations, the single-photon scattering presents the so-called coupled-resonator-induced transparency (CRIT). In this phenomenon, akin to electromagnetically induced transparency (EIT) [242], perfect photon transmission occurs due to Fano-type interference between virtual transitions to the coupled levels in the resonators [243]. However, we show that there are significant differences between the two-photon resonance fluorescence arising from scattering by a $\mathrm{V}^{(N)}$ atom and that from scattering by two collocated qubits. For instance, scattering by a $\mathrm{V}^{(N)}$ atom can present two-photon CRIT and lack of nonlinearity, a quite unusual phenomenon, which, for instance, does not occur in a waveguide-QED scenario with two collocated qubits.

5.3.1 Model

Consider a nonchiral waveguide interacting with a point-like $\mathrm{V}^{(N)}$ atom. We solve the problem by means of the input-output formalism (see Sect. 2.1), so we must assume a linear dispersion relation, the rotating-wave approximation (see Sect. 1.1 and Eq. (1.7)), and enlarge the integration ranges in momentum space from $(0, +\infty)$ to $(-\infty, +\infty)$. Therefore, we take the Hamiltonian (2.2) and choose units such that the group velocity is $v_g = 1$. Modifying appropriately the scatterer and interaction terms, the Hamiltonian now reads

$$\begin{aligned} H = & \int dk\; k(a^\dagger_{+,k} a_{+,k} - a^\dagger_{-,k} a_{-,k}) \\ & + \sum_{n=1}^{N} \Delta_n \sigma_n^+ \sigma_n^- + \sum_{s=\pm} \sum_{n=1}^{N} dk\; g_{sn} \int (\sigma_n^+ a_{s,k} + \sigma_n^- a^\dagger_{s,k}), \end{aligned} \tag{5.24}$$

where Δ_n is the energy gap between $|0\rangle$ and $|n\rangle$, being $\{|n\rangle\}_{n=1}^N$ the set of excited states of the atom, g_{sn} is the coupling strength for the transition $|0\rangle \leftrightarrow |n\rangle$ and the s modes, and $\sigma_n^+ = |n\rangle \langle 0| \otimes \mathbb{I}_{\mathrm{ph}}$ and $\sigma_n^- = |0\rangle \langle n| \otimes \mathbb{I}_{\mathrm{ph}}$ are the ladder operators for the generalized V atom, with $\mathbb{I}_{\mathrm{ph}}$ being the identity operator in the photonic space.

5.3.2 Input-output equations

As mentioned, we compute the one- and two-photon S matrix by means of the input-output formalism, so we mimic the steps followed in Sect. 2.1, adapting each step to the $\mathrm{V}^{(N)}$ atom.

We consider first the chiral model, $g_{+n} = g_n \neq 0$ and $g_{-n} = 0$, and consider a single set of modes $\{a_k\}$. We need the Heisenberg equations for a_k and σ_n^-, which we derive from (5.24)

$$i\frac{da_k(t)}{dt} = ka_k(t) + \sum_{n=1}^{N} g_n \sigma_n^-(t), \tag{5.25}$$

$$i\frac{d\sigma_n^-(t)}{dt} = \Delta_n \sigma_n^-(t) + \sum_{m=1}^{N} \int dk\, g_m\, c_{mn}(t) a_k(t), \tag{5.26}$$

with the operators c_{mn} being

$$c_{mn} = \delta_{mn}\ |0\rangle\langle 0| \otimes \mathbb{I}_{\text{ph}} - \sigma_m^+ \sigma_n^-. \tag{5.27}$$

Following the steps from (2.17) to (2.22) in Sect. 2.1 and replacing the two-level-system Heisenberg equations, Eqs. (2.15) and (2.16), by those derived for the $\mathrm{V}^{(N)}$ atom, Eqs. (5.25) and (5.26), we obtain the relation between $a_{\text{out}}(t)$ and $a_{\text{in}}(t)$ analogous to (2.22)

$$a_{\text{out}}(t) = a_{\text{in}}(t) - i\sum_{n=1}^{N} \sqrt{2\gamma_n}\, \sigma_n^-(t), \tag{5.28}$$

where $\gamma_n = \pi g_n^2$ is the spontaneous emission rate of the n-th transition $|n\rangle \to |0\rangle$ coupled to the chiral waveguide. We can also compute $\Phi(t)$, Eq. (2.18), for this model, following the steps explained between Eqs. (2.17) and (2.19), replacing Eq. (2.15) by (5.25), getting

$$\Phi(t) = a_{\text{in}}(t) - i\sum_{n=1}^{N} \sqrt{\frac{\gamma_n}{2}} \sigma_n^-(t). \tag{5.29}$$

Using this expression, the definition of $\Phi(t)$, Eq. (2.18), and (5.26), we can derive the equation of motion for $\sigma_n^-(t)$ in terms of $a_{\text{in}}(t)$

$$i\frac{d\sigma_n^-(t)}{dt} = \sum_{m=1}^{N} A_{nm}\, \sigma_m^-(t) + \sum_{m=1}^{N} \sqrt{2\gamma_m}\, c_{mn}(t)\, a_{\text{in}}(t), \tag{5.30}$$

with the matrix $A_{nm} = \Delta_n \delta_{nm} - i\sqrt{\gamma_n \gamma_m}$. The system of equations formed by Eqs. (5.28) and (5.30) is analogous to (2.22) and (2.23), so it allows us to find the S matrix for the $\mathrm{V}^{(N)}$ atom. Notice that we recover both (2.22) and (2.23) taking the limit $N = 1$ (two-level system) in Eqs. (5.28) and (5.30).

5.3.3 Single-photon scattering

We derive here the single-photon S matrix for a chiral waveguide, $S_{pk}^{\text{c}} = \langle \phi_0 | a_{\text{out}}(p) a_{\text{in}}^\dagger(k) | \phi_0 \rangle$. Adapting the steps between Eqs. (2.24) and (2.34) to a

$\mathrm{V}^{(N)}$ atom, which we detail in App. H.1, we get

$$S^{\mathrm{c}}_{pk} = t^{\mathrm{c}}_k\, \delta(k-p), \tag{5.31}$$

$$t^{\mathrm{c}}_k = 1 - i \sum_{n=1}^{N} \sqrt{2\gamma_n}\, s^n_k, \tag{5.32}$$

with

$$s^n_k = \sum_{m=1}^{N} \sqrt{2\gamma_m}\, [(k-A)^{-1}]_{nm}. \tag{5.33}$$

The limit of a qubit ($N = 1$) can be trivially recovered. In this case, A is not a matrix, but just a number and

$$s_k = \frac{\sqrt{2\gamma}}{k - \Delta + i\gamma}, \tag{5.34}$$

$$t^{\mathrm{c}}_k = 1 - i\sqrt{2\gamma}s_k = \frac{k - \Delta - i\gamma}{k - \Delta + i\gamma}, \tag{5.35}$$

which match the results shown in Sect. 2.1, see Eqs. (2.33) and (2.35).

As explained in Sect. 2.1.6, the scattering coefficients in the nonchiral case can be obtained from the chiral ones. The nonchiral transmission coefficient is $t_k = (t^{\mathrm{c}}_k + 1)/2$ (see first equality of Eq. (2.56)). With this, we obtain the expression for one-photon scattering matrix of the $\mathrm{V}^{(N)}$ atom:

$$t_k = 1 - i \sum_{n=1}^{N} \sqrt{\frac{\gamma_n}{2}} s^n_k, \tag{5.36}$$

while the reflection coefficient is $r_k = t_k - 1$ [237]. For $N = 2$ (V atom), these results coincide with those published in previous works [244, 245]. It is worthy to remind that γ_n is $2\pi g_n^2$ instead of πg_n^2 in all the S-matrix elements in the nonchiral case, as we explained in Sect. 2.1.6. Finally, it is easy to check that the transmission amplitude for two collocated qubits is also given by (5.36) for $N = 2$ [127], that is, the one-photon scattering does not distinguish between a V atom and two collocated two-level systems.

5.3.4 Two-photon scattering

We compute now the chiral two-photon S matrix

$$S^{\mathrm{c}}_{p_1 p_2 k_1 k_2} = \langle \phi_0 | a_{\mathrm{out}}(p_1) a_{\mathrm{out}}(p_2) a^\dagger_{\mathrm{in}}(k_1) a^\dagger_{\mathrm{in}}(k_2) | \phi_0 \rangle \,. \tag{5.37}$$

We mimic the steps followed between (2.36) and (2.44), changing what has to be changed for the $\mathrm{V}^{(N)}$ atom. The details can be found in App. H.2.

As for the two-level system, the two-photon S^{c} matrix is the sum of a linear contribution (product of t_k^{c} coefficients, given by (5.32)) and a nonlinear one,

$$\begin{aligned} S^{\mathrm{c}}_{p_1p_2k_1k_2} &= t^{\mathrm{c}}_{p_1}t^{\mathrm{c}}_{p_2}[\delta(p_1-k_1)\delta(p_2-k_2)+(k_1\leftrightarrow k_2)] \\ &\quad + iT^{\mathrm{c}}_{p_1p_2k_1k_2}\delta(p_1+p_2-k_1-k_2), \end{aligned} \tag{5.38}$$

The nonlinear term T^{c} is responsible for the fluorescence spectrum, where the individual energy of each photon is not conserved but the total energy is. It reads

$$\begin{aligned} T^{\mathrm{c}}_{p_1p_2k_1k_2} &= \frac{t^{\mathrm{c}}_{p_1}}{2\pi}\sum_{n=1}^{N}\sqrt{2\gamma_n}s^n_{p_2}\sum_{m=1}^{N}(s^m_{p_1})^*(s^m_{k_1}+s^m_{k_2}) \\ &\quad + \frac{t^{\mathrm{c}}_{p_1}}{2\pi}\sum_{n=1}^{N}s^n_{p_2}(s^n_{k_1}+s^n_{k_2})\sum_{m=1}^{N}\sqrt{2\gamma_m}(s^m_{p_1})^*. \end{aligned} \tag{5.39}$$

This particular expression will be useful later on. However, it is not evident that it is symmetric under the exchange $p_1 \leftrightarrow p_2$ or $k_1 \leftrightarrow k_2$, as it should be. After some manipulations, described in Appendix H.2, we arrive to an expression where these exchange symmetries are clearly visible:

$$\begin{aligned} T^{\mathrm{c}}_{p_1p_2k_1k_2} &= \frac{2}{\pi}\frac{1}{(1+i\alpha_{p_1})(1+i\alpha_{p_2})}\times \\ &\times\left(\frac{\alpha_{p_2}\beta_{p_1k_1}+\alpha_{p_1}\beta_{p_2k_1}}{1+i\alpha_{k_1}}+\frac{\alpha_{p_2}\beta_{p_1k_2}+\alpha_{p_1}\beta_{p_2k_2}}{1+i\alpha_{k_2}}\right), \end{aligned} \tag{5.40}$$

with

$$\alpha_k = \sum_{n=1}^{N}\frac{\gamma_n}{k-\Delta_n},\ \beta_{kp} = \sum_{n=1}^{N}\frac{\gamma_n}{(k-\Delta_n)(p-\Delta_n)}. \tag{5.41}$$

As a check, notice that Eq. (5.38) satisfies the general structure that the two-photon scattering matrix should have according to the cluster-decomposition principle when the ground state of the scatterer is unique (see Eq. (4.10) and Sect. 4.1): a term that indicates conservation of the energy of the individual photons (containing two delta functions) and another term that only conserves total energy (the term with a single delta function). Also, taking $N = 1$ in Eq. (5.39), we recover the two-level-system result, see Eq. (2.46).

All formulas above have been derived for the chiral case. The result for a nonchiral medium with left- and right-moving photons can be obtained from the chiral one, as we explained in Sect. 2.1.6. The relation between the chiral and nonchiral nonlinear terms is that of the two-level system, see Eq. (2.64),

$$T_{p_1p_2k_1k_2} = \frac{1}{4}T^{\mathrm{c}}_{|p_1||p_2|k_1k_2}, \tag{5.42}$$

with the prescription that when computing the nonchiral T the decay rates used in the expression for T^{c} should be those $\gamma_n = 2\pi g_n^2$, as explained at the end of the previous section.

Chiral scattering matrix from a V atom ($N = 2$)

Even though in general the previous expressions must be numerically computed, the case of a V atom ($N = 2$) admits a simple analytical expression. We find $T^{\mathrm{c}}_{p_1p_2k_1k_2} = T^{\mathrm{c1}}_{p_1p_2k_1k_2} + T^{\mathrm{c2}}_{p_1p_2k_1k_2}$, with

$$T^{\mathrm{c1}}_{p_1p_2k_1k_2} = \frac{\sqrt{2}}{\pi} \sum_{n=1}^{2} \sqrt{\gamma_n}\, s^n_{p_1} s^n_{p_2} \left(s^n_{k_1} + s^n_{k_2}\right), \tag{5.43}$$

$$T^{\mathrm{c2}}_{p_1p_2k_1k_2} = \frac{1}{\sqrt{2}\pi} \sum_{n=1}^{2} s^n_{p_1} s^{\bar{n}}_{p_2} \sum_{m=1}^{2} \sqrt{\gamma_{\bar{m}}} \left(s^m_{k_1} + s^m_{k_2}\right), \tag{5.44}$$

where we have defined $\bar{n} = 2$ if $n = 1$, and $\bar{n} = 1$ if $n = 2$, and

$$s^n_k = \sqrt{2\gamma_n} \frac{k - \Delta_{\bar{n}}}{(k - \Delta_1 + i\gamma_1)(k - \Delta_2 + i\gamma_2) + \gamma_1\gamma_2} \tag{5.45}$$

For completeness, let us recall that the two-photon scattering matrix for the case of two collocated qubits can be written in a similar way, with the same $T^{\mathrm{c1}}_{p_1p_2k_1k_2}$ but with a expression for $T^{\mathrm{c2}}_{p_1p_2k_1k_2}$ given by [127]:

$$\begin{aligned} T^{\mathrm{c2}}_{p_1p_2k_1k_2} = &- \frac{i}{\sqrt{2}\pi} \sum_{n=1}^{2} s^n_{p_1} s^n_{p_2} \sum_{m=1}^{2} \sqrt{\gamma_{\bar{m}}} \left(s^m_{k_1} + s^m_{k_2}\right) \\ &\times \frac{\sqrt{\gamma_1\gamma_2}}{k_1 + k_2 - \Delta_1 - \Delta_2 + i\gamma_1 + i\gamma_2}. \end{aligned} \tag{5.46}$$

In the following subsections, we deal with various applications of the scattering formulas in the nonchiral case, where $g_{-n} = g_{+n}$ in (5.24). We begin by comparing a V atom ($N = 2$) with two collocated qubits. We will show that, while the one-photon scattering cannot distinguish between these two experimental setups (see Eq. (5.36) and the subsequent discussion), remarkable differences appear in their two-photon scattering. We will also show that a V$^{(N)}$-level scheme exhibits CRIT in the two-photon scattering spectrum, i.e., for some values of the incoming photon energies the two-photon transmission is perfect and all nonlinear phenomena cancel out due to destructive interference.

5.3.5 Two-photon fluorescence

We use the previous expressions to analyze how much information can be extracted from a two-photon spectroscopy. For this, we concentrate on the

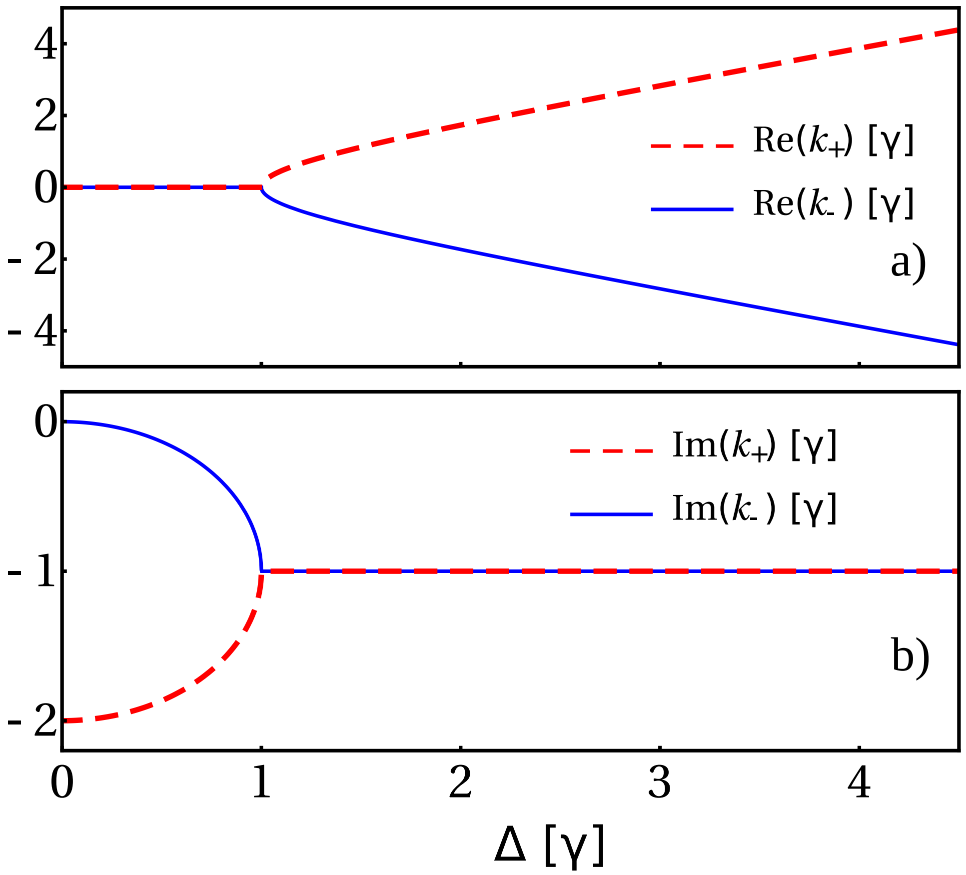

Figure 5.16: Real and Imaginary part of the single-particle poles of the scattering matrix as a function of $\Delta \equiv \Delta_1 = -\Delta_2$. These results apply to both scattering by a V atom and by two collocated qubits. We have assumed that $\gamma_1 = \gamma_2 = \gamma$.

$N = 2$ case (a V atom) and, for simplicity, consider that both excitations have the same spontaneous emission rate, $\gamma_1 = \gamma_2 = \gamma = 1$, which thus sets the unit of energy. Without loss of generality, we assume $\Delta \equiv \Delta_1 = -\Delta_2$, which means that we have chosen the zero of energy to be located at $(\Delta_1 + \Delta_2)/2$.

Let us recall that the one-photon transmission, see Eq. (5.36), vanishes when the photon energy matches an excitation energy in the scatterer [99, 100, 102]. A two-photon transmission spectroscopy may provide extra information, beyond revealing the excitation energies. If any, this effect should be contained in the nonlinear part of the scattering matrix $T_{p_1 p_2 k_1 k_2}$. In order to analyze the two-photon scattering by a V atom it is convenient to compare it with that by two collocated qubits, already discussed in Ref. [127]. Notice that the *one*-photon scattering is identical in these cases because they present the same single-excitation manifold (see level structure in Fig. 5.17, panels a) and b)).

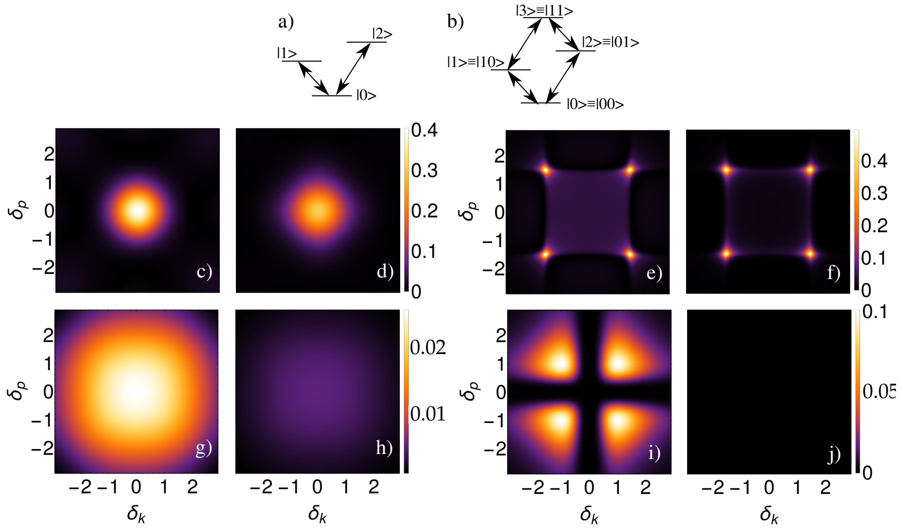

Figure 5.17: a) V-atom level structure and b) two-qubit level structure. Intensity for resonance fluorescence: $|T_{p_1p_2k_1k_2}|^2$ in units of $1/\gamma^2$ for a V atom (panels c), e), g), and i)) and two collocated qubits (panels d), f), h), and j)). In all cases $\gamma_1 = \gamma_2 = \gamma$ and $\Delta_1 = -\Delta_2 \equiv \Delta$. We define $\delta E \equiv k_1 + k_2$. In panels c) and d), $\Delta = 1.5\gamma$ and $\delta E = 3\gamma$. In panels e) and f), $\Delta = 0.5\gamma$ and $\delta E = 3\gamma$. In panels g) and h), $\Delta = 0$ and $\delta E = 3\gamma$, and in panels i) and j) $\Delta = \gamma$ and $\delta E = 0$.

The analysis of the results is facilitated by the knowledge of the poles of $T_{p_1p_2k_1k_2}$. For both the V atom and the two collocated qubits, $T_{p_1p_2k_1k_2}$ presents poles at the same spectral positions as the one-particle scattering amplitudes s_k^n, Eqs. (5.43), (5.44) and (5.46). There are two kinds of one-particle poles, corresponding to scattering through the states $|\pm\rangle = \frac{1}{\sqrt{2}}(|1\rangle \pm |2\rangle)$ (see panels a) and b) in Figure 5.17), which form a basis spanning the two single-excitation states of the scatterer. The spectral position of these poles as a function of Δ is shown in Fig. 5.16. Two regimes can be differentiated: when $\Delta > \gamma$, the two excitations essentially behave as independent ones. They are spectrally located at approximately $\pm\Delta$ and present an amplitude decay rate that coincides with the "bare" rate, γ. For $\Delta < \gamma$, the two excitations hybridize leading to a super-radiant and a sub-radiant state, both of them spectrally located at the average frequency of the two bare excitations. Additionally, the scattering from two qubits gives rise to a "collective" two-photon pole at $k_1+k_2 = \Delta_1+\Delta_2+i(\gamma_1+\gamma_2)$ [127], which is not present in the case of scattering from a V atom.

A representative set of results is shown in Fig. 5.17, where we plot $|T_{p_1p_2k_1k_2}|^2$ as a function of both $\delta_k = (k_1 - k_2)/2$ and $\delta_p = (p_1 - p_2)/2$. Each panel considers different total frequencies of the incident photons, $\delta E = k_1 + k_2$, and excitation energies, $\pm\Delta$. Left panels show the results for the V atom, while the right panels render the ones for the two collocated qubits. In all panels, the 4-fold rotational symmetry of $|T_{p_1p_2k_1k_2}|^2$ arises from a combination of the indistinguishability of the photons (which makes $S_{p_1p_2k_1k_2}$ invariant under the interchange $k_1 \leftrightarrow k_2$ or $p_1 \leftrightarrow p_2$) and time-reversal symmetry (which makes $S_{p_1p_2k_1k_2} = S_{k_1k_2p_1p_2}$ [246]).

Let us first discuss the case where the two incoming photons cannot be in resonance with both single-particle states, this is, when $|k_1+k_2-\Delta_1-\Delta_2| > 0$. An analysis of this case shows that the fluorescence $|T_{p_1p_2k_1k_2}|^2$ is maximum when *one* of the incoming photons and *one* of the outgoing photons are resonant with one of the one-photon transitions. Depending on the difference between the bare excitation energies, we can differentiate two situations. The first one is when the excitation levels are essentially uncoupled: $\Delta > \gamma$. This instance is represented in panels c) and d) of Fig. 5.17. Resonances occur at photon energies $\approx \pm\Delta$, and decay with a rate γ (see Fig. 5.16). In terms of δ_k and δ_p this implies that $|T_{p_1p_2k_1k_2}|^2$ is maximum for $\delta_p = \pm\delta_k = \pm(\delta E - 2\Delta)/2$, (which in the case represented in the figure implies $\delta_p = \delta_k = 0$). The second situation appears when the excitation energies strongly couple, i.e. when $\Delta < \gamma$. Now, both single-photon transitions occur at zero energy, and thus the two-photon resonance appears at $\delta_p = \pm\delta_k = \pm\delta E/2$. One of the transitions is super-radiant, while the other one is sub-radiant and shows up as a narrow peak in the intensity for resonance fluorescence (panels e) and f) of Fig. 5.17). As $\Delta \to 0$, the spectral width of the sub-radiant state narrows but, additionally, its coupling to the incoming photons vanishes when $\gamma_1 = \gamma_2$. In the limit $\Delta = 0$ (shown in panels g) and h) of Fig. 5.17) $|-\rangle$ is a dark state and the V atom is exactly mapped into a single qubit, with a single excited state given by $|+\rangle$ and a modified spontaneous emission rate 2γ. The fluorescence is only due to the super-radiant state and, correspondingly, the maximum fluorescence is now much smaller than when the sub-radiant state dominates. The two qubits are mapped to a three-level atom, with excited states $|+\rangle$ and $|11\rangle$, and cascaded transitions with equal excitation energies. The existence of the two-photon state in the case of two collocated qubits diminishes the photon-photon interaction with respect to that of the V atom.

This analysis shows that in the nonresonant case the difference between the fluorescence of the V atom and the pair of qubits is quantitative. The nonlinearity is higher for the V atom, because it is more sensitive to saturation effects than the pair of qubits.

A different situation arises when both incoming photons may be in resonance with the two one-photon transitions, i.e., when $k_1 + k_2 = 0$. Then, the two qubits can simultaneously scatter two photons and the nonlinear contribution to the scattering matrix vanishes [127] (see panel j)). In contrast, the

V atom does not present the doubly excited state $|11\rangle$ and the fluorescence cannot be quenched with this mechanism. As seen in panel i) of Fig. 5.17, the intensity of resonance fluorescence is maximum when the energy of each incoming photon equals those of the excitations in the V atom.

Notice, however, that fluorescence quenching, $T_{p_1 p_2 k_1 k_2} = 0$, also appears in the scattering by the V atom, when $\delta_k = 0$ and $\delta_p = 0$. We explain this effect in the following subsection.

In all the previous discussion we have considered two collocated qubits without a direct interaction between them. However, the presence of dipole-dipole interaction can be straightforwardly taken into account as two interacting qubits can be mapped to a new pair of independent qubits with modified energies and coupling constants. Thus, any pair of interacting collocated qubits has a corresponding V atom with the same effective energies and coupling constants.

5.3.6 Two-photon CRIT interference

The coupling of one propagating photon to two or more resonant transitions can produce situations where the transmission is perfect, a phenomenon denoted as coupled-resonator-induced transparency [243]. According to Eq. (5.36), perfect one-photon transmission occurs whenever the input frequency matches the condition:

$$\sum_{n=1}^{N} \sqrt{\gamma_j} s_k^n = 0 \tag{5.47}$$

This condition can be recast into a $(N-1)$-degree polynomial in k, with $N-1$ roots, $k_{\mathrm{CRIT}}^{N,n}$ $(n = 1, \ldots, N-1)$. For the $N = 2$ case, the condition for transparency is:

$$k_{\mathrm{CRIT}}^{2,1} = \frac{\gamma_2 \Delta_1 + \gamma_1 \Delta_2}{\gamma_1 + \gamma_2}. \tag{5.48}$$

This is seen in Fig. 5.18, where we plot the one-photon transmission probability $|t_k|^2$ as a function of k for $N = 2$ and $\Delta_2 - \Delta_1 = \gamma$. The transmission probability vanishes when the photon is in resonance with either of the one-excitation transitions Δ_1 and Δ_2 and it depicts transparency ($|t_k|^2 = 1$) when $k = k_{\mathrm{CRIT}}^{2,1}$.

The computed two-photon scattering matrix allows the study of the conditions which lead to the vanishing of the nonlinear term $T_{p_1 p_2 k_1 k_2}$, which is responsible for both fluorescence and photon-photon interaction. Previous studies have found fluorescence quenching for the two-photon power spectrum in a V atom ($N = 2$) illuminated with *classical* light [247], and also in the case

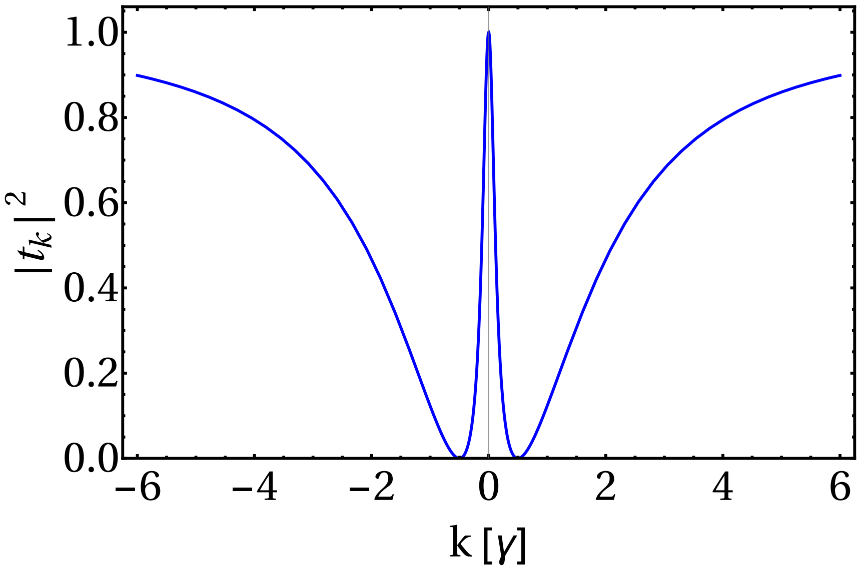

Figure 5.18: One-photon transmission $|t_k|^2$ (Eq. (5.32)). The transmission vanishes when $k = \Delta_n$ and goes to 1 when $k = k^{2,1}_{\mathrm{CRIT}}$ (Eq. (5.48)).

of a driven λ system when the incoming photons satisfy the one-photon CRIT condition [248].

For the case of a V$^{(N)}$ atom, it is easy to show that $T_{p_1p_2k_1k_2} = 0$ whenever each incoming photon satisfies a one-photon CRIT condition. For this, we first consider that the *outgoing* photons satisfy $p_1 = k^{N,j}_{\mathrm{CRIT}}$ and $p_2 = k^{N,l}_{\mathrm{CRIT}}$. Introducing the CRIT condition (Eq. (5.47)) in Eq. (5.39), we obtain $T_{p_1p_2k_1k_2} = 0$, for any pair of incoming photons and that particular channel for outgoing photons. As time-reversal symmetry implies $T_{p_1p_2k_1k_2} = T_{k_1k_2p_1p_2}$, we obtain that $T_{p_1p_2k_1k_2} = 0$ whenever the incoming photons satisfy the single-photon CRIT conditions, for any value of the outgoing photon energies. Notice that this derivation also applies to the driven λ atom since, in the system eigenbasis $|\pm\rangle$, it can be mapped to a V atom. This fluorescence quenching is shown in Fig. 5.19, where we represent $|T_{p_1p_2k_1k_2}|^2$, for both $N = 2$ and $N = 3$, when one input photon frequency is taken at $k^{N,1}_{\mathrm{CRIT}}$, while the frequency of the other incoming photon frequency varies. We already saw this effect in Fig. 5.17, panel i). In that case, the CRIT condition for the input photons is fulfilled for $k_1 = k_2$, so $T_{p_1p_2k_1k_2} = 0$ for $\delta_k = 0$. In the same way, $T_{p_1p_2k_1k_2}$ also vanishes when the output energies satisfy $\delta_p = 0$.

If one of the photons is not at a CRIT condition, photon-photon interactions emerge, being maximal when the individual energies of the outgoing photons coincide with those of the incoming ones (dashed lines in Fig. 5.19), as explained in the previous subsection.

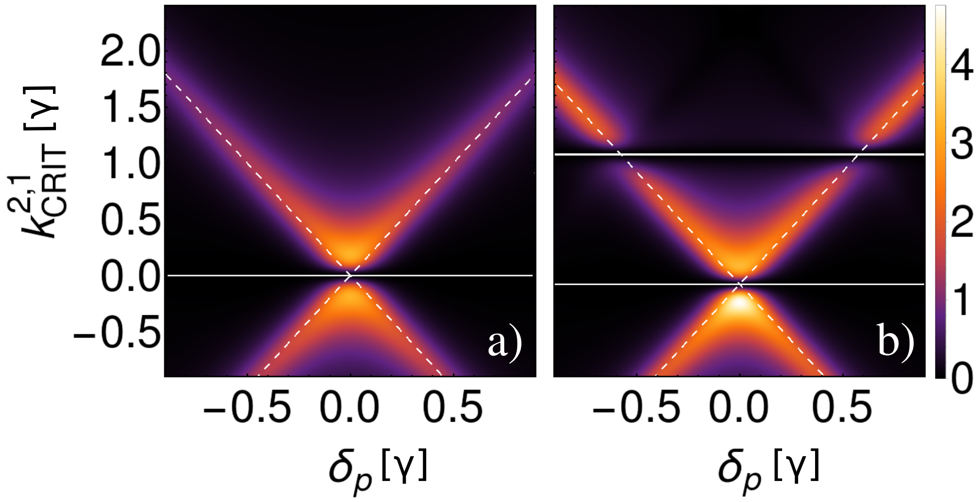

Figure 5.19: Intensity for resonance fluorescence: $|T_{p_1 p_2 k_1 k_2}|^2$ in units of $1/\gamma^2$, with fixed $k_1 = k^{2,1}_{\mathrm{CRIT}}$, vs $k_2 - k^{2,1}_{\mathrm{CRIT}}$ and δ_p, for $N = 2$ (panel a) and $N = 3$ (panel b). We fix $\gamma_j = \gamma$ and $\Delta_{j+1} - \Delta_j = \gamma$. The solid white lines represent $k_2 = k^{2,1}_{\mathrm{CRIT}}$ in the left panel, and $k_2 = k^{3,1}_{\mathrm{CRIT}}$ (bottom) and $k_2 = k^{3,2}_{\mathrm{CRIT}}$ (top) in the right panel. The dashed white lines render the condition for the individual conservation of both photon energies, $p_1 = k_1$ and $p_2 = k_2$, or vice versa.

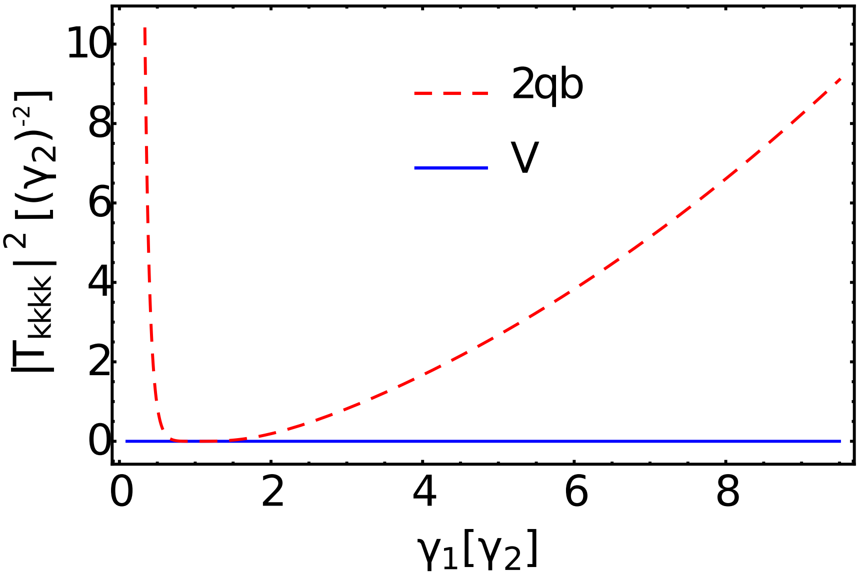

Figure 5.20: Intensity for resonance fluorescence: $|T_{kkkk}|^2$, with fixed $k = k^{2,1}_{\mathrm{CRIT}}$, as a function of γ_1, for both a V atom (blue, solid curve) and two qubits (red, dashed). We have taken $\Delta = \gamma_2$. Notice that fluorescence quenching only occurs at $\gamma_1 = \gamma_2$ for the two qubits, but it always vanishes at the two-photon CRIT condition for the V atom.

Notice that the statement that fluorescence is quenched in a two-photon scattering process whenever both incident photons satisfy a CRIT condition, which occurs for a $\mathrm{V}^{(N)}$ atom, does not necessarily apply to all possible scatterers. A counterexample is the case of two collocated qubits. There, fluorescence quenching occurs when the total energy of the incoming photons is equal to the sum of the excitation energies ($k_1 + k_2 = \Delta_1 + \Delta_2$), but only when both qubits couple equally to the waveguide ($\gamma_1 = \gamma_2$) [127]. As shown in Fig. 5.20, if these couplings are unequal, the two qubits present a nonvanishing resonance fluorescence when the incoming photons are at individual CRIT conditions, $k = k_{\mathrm{CRIT}}^{2,1}$. The chosen output frequencies are also k, but this is irrelevant, as other choices would only change the intensity of the fluorescence, but not the overall dependence on γ_1/γ_2. In contrast, in the V case, the fluorescence is not generally quenched when the total energy of the incoming photons is equal to the sum of the excitation energies. But, when each of the two incoming (or outgoing) photons is at one-photon CRIT conditions, both of them are transmitted with unit amplitude and the fluorescence is quenched, even for dissimilar couplings of the excitations to the waveguide (see Fig. 5.20).

Summarizing, in this section we have presented the one- and two-photon scattering theory for a $\mathrm{V}^{(N)}$ atom coupled to either a chiral or a nonchiral waveguide. We have highlighted that a two-photon spectroscopy can characterize different level structures that would be indistinguishable in a one-photon experiment. Besides, we have introduced the concept of two-photon CRIT. We have shown that in the $\mathrm{V}^{(N)}$-atom structure the two-photon resonance fluorescence is completely quenched when each photon is at single-photon CRIT condition. This can be understood as the quantum version for the phenomenon of fluorescence quenching which occurs when driving a V atom with classical light [247]. These effects can be seen in the laboratory with state-of-the-art technologies in systems like atoms with a V-level structure, or collections of Rydberg atoms where a blockade mechanism prevents simultaneous multiexcitation.

5.4 Analysis of quantum phase gates with two-photon scattering

Now, we sketch an application of scattering in waveguide QED to quantum computation. There are proposals to do quantum computing with quantum optics [249, 250] and with waveguide QED in particular [251]. Actually, some protocols have already been implemented: quantum teleportation between a flying photon and a solid-state spin qubit [252], generation of entanglement between spin qubits mediated by flying photons [253] or quantum-state transfer between quantum dots [254], to say a few.

We propose a momentum-based two-qubit phase gate in a waveguide-QED scenario. The photonic medium is a chiral waveguide interacting with a local impurity, such as a two-level system, two collocated two-level systems, or a V atom; actually, this work was the motivation to compute the S matrix of the generalized V atom (see Sect. 5.3). It was recently proven that a quantum phase gate cannot be realized in this system if the input photons are monochromatic [200]. Therefore, we need nonmonochromatic photons. We find that the gate is feasible in such a case. Unfortunately, the efficiency of the process is too low for all the scatterers considered, so our proposal is not a promising implementation.

A clarification is in order. In general, throughout this thesis qubit refers to a quantum system with two levels. However, here, by qubit we mean two states forming the logical basis of the unit of quantum information. This basis will be formed by photonic states. Therefore, in this section, when the scatterer is also a qubit, we refer to it as two-level system to avoid any confusion.

5.4.1 Two-qubit phase gate

In quantum information, a two-qubit phase gate is represented by the following unitary transformation

$$|00\rangle \to |00\rangle\,, \tag{5.49}$$

$$|10\rangle \to e^{i\phi_a}\,|10\rangle\,, \tag{5.50}$$

$$|01\rangle \to e^{i\phi_b}\,|01\rangle\,, \tag{5.51}$$

$$|11\rangle \to e^{i(\phi_a+\phi_b+\delta)}\,|11\rangle\,, \tag{5.52}$$

with ϕ_a, ϕ_b, and δ being phases. This gate for $\delta = \pi$ and a particular set of one-qubit protocols form a set of universal quantum gates [17].

Let us suppose we have a general separable two-qubit input state

$$\begin{aligned} |\psi_{\text{in}}\rangle &= \mathcal{N}(|0\rangle + c_a\,|1\rangle) \otimes (|0\rangle + c_b\,|1\rangle) \\ &= \mathcal{N}(|00\rangle + c_a\,|10\rangle + c_b\,|01\rangle + c_a c_b\,|11\rangle), \end{aligned} \tag{5.53}$$

with $c_a, c_b \in \mathbb{C}$ and $\mathcal{N} = \sqrt{1 + |c_a|^2 + |c_b|^2 + |c_a c_b|^2}$ a normalization constant. The output state after applying the phase gate (Eqs. (5.49)-(5.52)) reads

$$|\psi_{\text{out}}\rangle = \mathcal{N}(|00\rangle + c_a e^{i\phi_a}\,|10\rangle + c_b e^{i\phi_b}\,|01\rangle + c_a c_b e^{i(\phi_a+\phi_b+\delta)}\,|11\rangle). \tag{5.54}$$

Comparing this to (5.53), which is a general separable state, we see that $|\psi_{\text{out}}\rangle$ is entangled provided $\delta \neq 0 \pmod{2\pi}$. We can quantify the amount of entanglement generated by this quantum gate by means of the Von Neumann

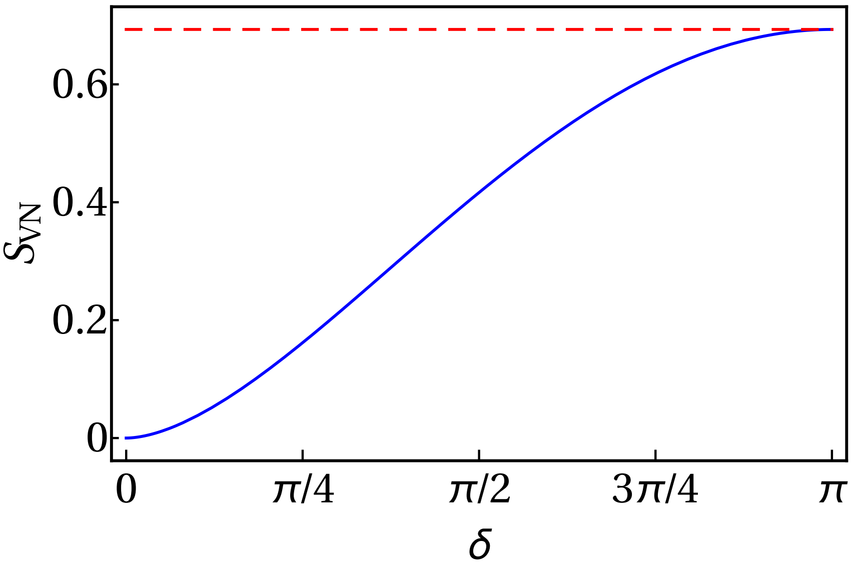

Figure 5.21: Entanglement entropy S_{VN}, see Eq. (5.55), as a function of the phase δ for $c_a = c_b = 1$. The red dashed line renders the maximum possible value for S_{VN}: $(S_{\mathrm{VN}})_{\max} = \log 2$.

entropy (2.94), which reads

$$S_{\mathrm{VN}} = \log 2 - \frac{1}{2}\left[(1+f)\log(1+f) + (1-f)\log(1-f)\right]. \tag{5.55}$$

We leave the computation and the expression of f to App. I.1 (see Eq. (I.3)), and directly represent the results for S_{VN} in Fig. 5.21. As expected, there is no entanglement if $\delta = 0$. In fact, the entropy is an increasing function of δ in the interval $[0, \pi]$. In particular, if $c_a = c_b = 1$ and $\delta = \pi$, then $S_{\mathrm{VN}} = \log 2$, which is the maximum possible value for the qubit-qubit entropy (see again Fig. 5.21).

5.4.2 Implementation in waveguide QED

Here, we make our proposal to realize this gate with waveguide QED. There have been other proposals to implement a quantum phase gate in the literature with waveguide QED [255] and it has already been realized in several quantum-optics setups [256, 257].

We propose a two-qubit phase gate *à la Knill-Laflamme-Millburn* [258]. The physical system is formed by four chiral waveguides, as seen in Fig. 5.22, with sets of annihilation operators $\{a_{1,k}\}$, $\{a_{2,k}\}$, $\{b_{1,k}\}$, and $\{b_{2,k}\}$. The two logical qubits are:

$$\text{1st qubit}: \qquad |0\rangle = a^\dagger_{1,k}\,|\text{vac}\rangle\,, \quad |1\rangle = b^\dagger_{1,k}\,|\text{vac}\rangle\,. \tag{5.56}$$

$$\text{2nd qubit}: \qquad |0\rangle = a^\dagger_{2,k}\,|\text{vac}\rangle\,, \quad |1\rangle = b^\dagger_{2,k}\,|\text{vac}\rangle\,, \tag{5.57}$$

with k the momentum for the input photons.

Now we describe how the two-qubit states get modified. Let us start by $|00\rangle$. Notice that the photons traveling through a_1 and a_2 evolve freely. Therefore, $|00\rangle$ is not modified: $|00\rangle \to |00\rangle$.

The horizontal gray lines are beam splitters:

$$b^\dagger_{1,k}\,|\text{vac}\rangle \to \frac{1}{\sqrt{2}}(b^\dagger_{1,k} + b^\dagger_{2,k})\,|\text{vac}\rangle\,, \tag{5.58}$$

$$b^\dagger_{2,k}\,|\text{vac}\rangle \to \frac{1}{\sqrt{2}}(b^\dagger_{1,k} - b^\dagger_{2,k})\,|\text{vac}\rangle\,. \tag{5.59}$$

The yellow boxes are local scatterers (a two-level system, a V atom, etc.). As the waveguides are chiral, the one-photon scattering along the waveguides b_1 or b_2 induces a phase $\phi_k = \arg(t^{\rm c}_k)$, where $t^{\rm c}_k$ is the chiral transmission amplitude (we do not include any label for the waveguide because both scatterers are identical). Under two-photon scattering through b_1 or b_2 and ignoring the contributions to other output channels (the scattering might generate pairs of photons with different momenta), the induced phase is $2\phi_k + \delta_k$. Considering this and the beam splitters, the gate is characterized by the following transformations

$$|00\rangle \to |00\rangle\,, \tag{5.60}$$

$$|10\rangle \to e^{i\phi_k}\,|10\rangle\,, \tag{5.61}$$

$$|01\rangle \to e^{i\phi_k}\,|01\rangle\,, \tag{5.62}$$

$$|11\rangle \to e^{i(2\phi_k+\delta_k)}\,|11\rangle\,, \tag{5.63}$$

so this implements a two-qubit phase gate (cf. (5.49)-(5.63)). We need $\delta_k \neq 0$ to implement the gate, that is, the response of the system must be *nonlinear* in the number of incoming photons.

5.4.3 The necessity of wave packets

As shown in [200], the analytical structure for the two-photon scattering matrix from a point-like scatterer with a unique ground state (see for instance Eq. (2.45)) implies that $\delta_k = 0$ for monochromatic input photons. This is rather counter-intuitive. The two-photon scattering matrix is nonlinear unless the scatterer is linear, which means that two-photon scattering is generally different

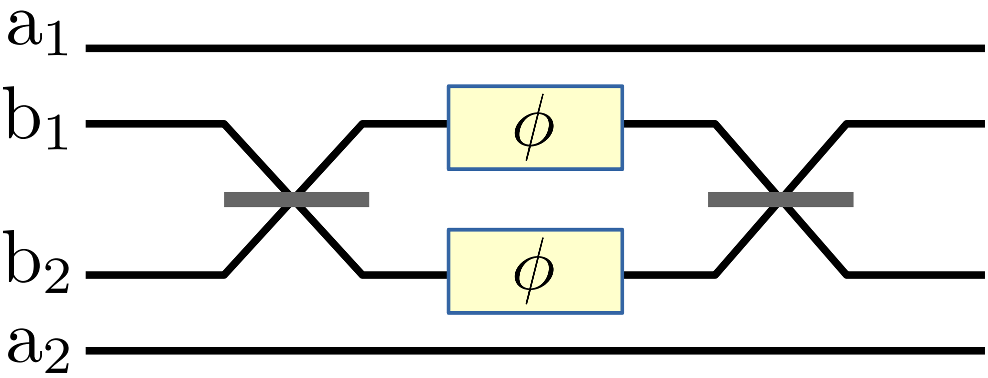

Figure 5.22: Scheme of the phase gate. The horizontal gray segments are the beam splitters. The yellow boxes are the point-like scatterers, which induce the one- and two-photon phases.

from one-photon scattering. However, the origin of nonlinear effects can be traced back to saturation of the scatterer, which occurs when the incident photons are localized wave packets. In consequence, we propose to relax the monochromaticity to overcome this problem, considering wave packets instead of plane waves:

$$c^\dagger(\bar{k}) = \int dk\, \varphi_{\bar{k}}(k) c_k^\dagger, \tag{5.64}$$

with $\varphi_{\bar{k}}(k)$ such that $\int dk\, |\varphi_{\bar{k}}(k)|^2 = 1$ and $\int dk\, k|\varphi_{\bar{k}}(k)|^2 = \bar{k}$.

We consider Gaussian and Lorentzian wave packets with width σ_k (see Eqs. (4.3) and (4.4)). In this case, the action of the gate given by Eqs (5.60)-(5.63) must be replaced by

$$|00\rangle \to |00\rangle\,, \tag{5.65}$$

$$|10\rangle \to |t(\bar{k},\sigma_k)|e^{i\phi(\bar{k},\sigma_k)}\,|10\rangle\,, \tag{5.66}$$

$$|01\rangle \to |t(\bar{k},\sigma_k)|e^{i\phi(\bar{k},\sigma_k)}\,|01\rangle\,, \tag{5.67}$$

$$|11\rangle \to |S(\bar{k},\sigma_k)|e^{i(2\phi(\bar{k},\sigma_k)+\delta(\bar{k},\sigma_k))}\,|11\rangle\,, \tag{5.68}$$

with $t(\bar{k},\sigma_k)$ and $S(\bar{k},\sigma_k)$ being the integrated one- and two-photon scattering amplitudes

$$t(\bar{k},\sigma_k) = \int dk\; t_k^{\mathrm{c}}|\varphi_{\bar{k}}(k)|^2, \tag{5.69}$$

$$S(\bar{k},\sigma_k) = \frac{1}{2}\int dp_1 dp_2 dk_1 dk_2\; S^{\mathrm{c}}_{p_1p_2k_1k_2}\, \varphi^*_{\bar{k}}(p_1)\varphi^*_{\bar{k}}(p_2)\varphi_{\bar{k}}(k_1)\varphi_{\bar{k}}(k_2). \tag{5.70}$$

The phases are calculated as the arguments of the amplitudes:

$$\phi(\bar{k},\sigma_k) = \arg(t(\bar{k},\sigma_k)), \tag{5.71}$$

$$\delta(\bar{k},\sigma_k) = \arg(S(\bar{k},\sigma_k)) - 2\phi(\bar{k},\sigma_k). \tag{5.72}$$

Notice that Eqs. (5.65)-(5.68) are equal to Eqs. (5.60)-(5.63) if $|t(\bar{k},\sigma_k)|^2 = 1$ and $|S(\bar{k},\sigma_k)|^2 = 1$. Therefore, we compute $|t(\bar{k},\sigma_k)|^2$ and $|S(\bar{k},\sigma_k)|^2$ to quantify how efficient the process and we refer to them as *efficiencies.* We also calculate the phase shift of the gate $\delta(\bar{k},\sigma_k)$ (see Eqs. (5.60)-(5.63)). As said in the introduction of this section, we compute these numbers for a two-level system, two collocated two-level systems, and a V atom.

5.4.4 Phase shift and efficiency

Here, we compute the phase shift $\delta(\bar{k},\sigma_k)$ as a function of the width in momentum space σ_k and the mean momentum $\bar{k}$ of the input photons for different scatterers, as well as the efficiencies of the process. We will consider a two-level system (see Eqs. (2.33), (2.35), (2.45), and (2.46)), a V atom (see Eqs. (5.32), (5.33), (5.38), and (5.39)), and two collocated two-level systems (see Eqs. (5.46)).

We start with the two-level system. We consider Lorentzian wave packets (Eq. (4.4)). From the one- and two-photon scattering matrices, given by Eqs. (2.34) and (2.45) respectively, we can compute the amplitudes (5.69) and (5.70). Going to the complex plane and applying the residue theorem, the calculation is straightforward. We obtain:

$$t(\bar{k},\sigma_k) = \frac{i(\sigma_k-\gamma)+\bar{k}-\Delta}{i(\gamma+\sigma_k)+\bar{k}-\Delta}, \tag{5.73}$$

$$S(\bar{k},\sigma_k) = (t(\bar{k},\sigma_k))^2 + \frac{8i\gamma^2\sigma_k}{(i(\gamma+\sigma_k)+\bar{k}-\Delta)^2(i(\gamma+3\sigma_k)+\bar{k}-\Delta)}. \tag{5.74}$$

Notice that $S(\bar{k},\sigma_k) = (t(\bar{k},\sigma_k))^2$ for $\sigma_k = 0$, so $\delta(\bar{k},\sigma_k) = 0$. This is consistent with the fact that the gate cannot be implemented with monochromatic photons [200]. We plot the modulus of the phase shift in units of π, $|\delta(\bar{k},\sigma_k)|/\pi$, in Fig. 5.23(a). It is different from 0 around the resonance $\bar{k} = \Delta$ when σ_k is large enough. In fact, $\delta(\bar{k},\sigma_k) = \pi$ for $\bar{k} = \Delta$, which is the needed value for doing a universal quantum computer (see Sect. 5.4.1). This is seen in Fig. 5.23(b), where we plot a cut of the phase shift as well as the efficiencies $|t(\bar{k},\sigma_k)|^2$ and $|S(\bar{k},\sigma_k)|^2$ for $\bar{k} = \Delta$. The phase shift suffers a sharp transition from 0 to π at $\sigma_k^- = \gamma\,(4-\sqrt{13})/3$ and it goes again to 0 at $\sigma_k^+ = \gamma\,(4+\sqrt{13})/3$, which are the points where the two-photon efficiency $|S(\Delta,\sigma)|^2$ drops to 0 (this can be shown analytically from Eqs. (5.73) and (5.74)). Therefore, the gate is feasible with nonmonochromatic wave packets. However, we are far from the ideal case, since the efficiencies are clearly smaller than 1. For instance, if we want to apply sequentially this gate, after a few iterations the efficiencies will drop to 0 rapidly.

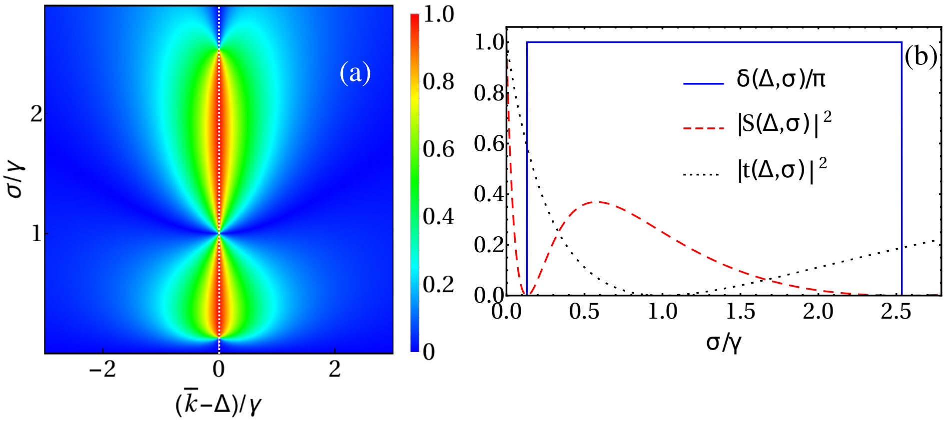

Figure 5.23: (a) Phase shift $|\delta(\bar{k},\sigma_k)|/\pi$ as a function of both $\bar{k}$ and σ_k. If $\sigma_k \to 0$ or $\bar{k}$ is off resonance, $\delta(\bar{k},\sigma_k) \to 0$. However, close to resonance and for $(4-\sqrt{13})/4 < \sigma_k/\gamma < (4+\sqrt{13})/4$, the phase shift is significant, being maximum, $|\delta(\Delta,\sigma_k)| = \pi$, for $\bar{k} = \Delta$ and $\sigma_k \in (\gamma\,(4-\sqrt{13})/4, \gamma\,(4+\sqrt{13})/4)$. In panel (b), we plot the phase shift as a function of σ_k, fixing $\bar{k} = \Delta$. We see the sharp transitions between 0 and π. We also plot the efficiencies: $|t(\Delta,\sigma_k)|^2$ and $|S(\Delta,\sigma_k)|^2$. As said in the main text, they are too low.

We also consider Gaussian wave packets (Eq. (4.3)). In such a case, we numerically integrate Eqs. (5.69) and (5.70). The qualitative behavior is identical to the Lorentzian case: at resonance $\bar{k} = \Delta$, the phase shift jumps from 0 to π for some value of σ_k. We compare the efficiency $|S(\Delta,\sigma_k)|^2$ to the Lorentzian case in Fig. 5.24. As seen, $|S(\Delta,\sigma_k)|^2$ is clearly larger for the Gaussian wave packets (Fig. 5.24(a)), so Gaussians are better for implementing the gate. In any case, we are still far from perfect efficiency.

We compute now the efficiencies and phase shift for the V atom (see (5.32), (5.33), Eqs. (5.38), and (5.39)) and the two collocated two-level atoms (see also Eqs. (5.43) and (5.46)).

The coupling strength is the same for both levels or two-level systems, $\gamma = \gamma_1 = \gamma_2$; their energies Δ_1 and Δ_2 are in principle different. Here we present the results when the incident photon is at resonance with Δ_1. Let us start by considering Lorentzian wave packets (Eq. (4.4)). As before, the computations are done by going to the complex plane and applying the residue theorem. The final expressions are presented in App. I.2. We plot the two-photon efficiency $|S(\bar{k} = \Delta_1,\sigma_k)|^2$ for both systems in Fig. 5.25 and we compare the results to

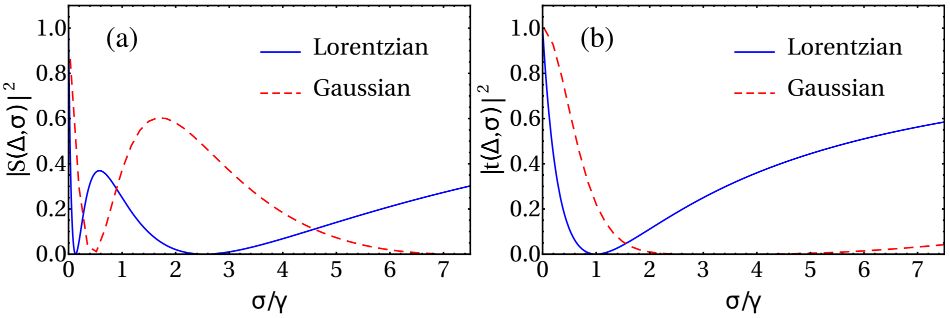

Figure 5.24: Efficiencies (a) $|S(\Delta,\sigma_k)|^2$ and (b) $|t(\Delta,\sigma_k)|^2$ as a function of σ for Lorentzian (blue solid line) and Gaussian (red dashed line) input wave packets. As seen, the efficiency is larger for the Gaussian. Notice that $S(\Delta,\sigma_k)$ also vanishes for two values of σ_k in the Gaussian case: these points give the jumps of the phase shift between 0 and π, as seen in Fig. 5.23(b) for the Lorentzians.

that for a two-level atom. If there is no detuning, ($\Delta_1 - \Delta_2 = 0$, panel (a)), the efficiency given by the two collocated two-level systems is much smaller than the others. The interpretation is clear. As argued in Sect. 4.2, the saturation effects enhance the nonlinearities, whereas two collocated two-level atoms are able to absorb two incoming photons without saturating (see Fig. 4.4). The V atom behaves as the two-level system up to a shift in σ_k/γ (see panel 5.25(a)), since a V atom is equivalent to a two-level system for this election of parameters, replacing γ by 2γ. We recover the two-level-system result if $|\Delta_1 - \Delta_2|$ is very large for both scatterers (panel (d), $\Delta_1 - \Delta_2 = 10\gamma$). For intermediate values of the detuning, the efficiency is always smaller than that given by a two-level system in both cases (Figs. 5.25(b) and (c)).

In conclusion, we have shown the gate is feasible by relaxing the monochromaticity condition, which is the experimentally realistic situation. Besides, we are able to achieve the optimal value for the phase shift $\delta(\bar{k},\sigma_k) = \pi$. Unfortunately, the efficiencies are far from being ideal for all the scatterers considered in this section: a two-level atom, a V atom, and two collocated two-level atoms. Therefore, this setup is not a candidate for implementing efficient quantum phase gates. Anyway, hopefully, once we have shown $|t(\bar{k},\sigma_k)|^2$ and $|S(\bar{k},\sigma_k)|^2$ can be different from 0, there might be other scatterers which give arbitrarily high values for these efficiencies.

5.5 Interqubit distance effects

We incorporate a new ingredient here, the interqubit distance. Qubit-qubit interactions mediated by the electromagnetic field decay with the distance in two and three dimensions [259]. One dimension is special: the field-wavefront

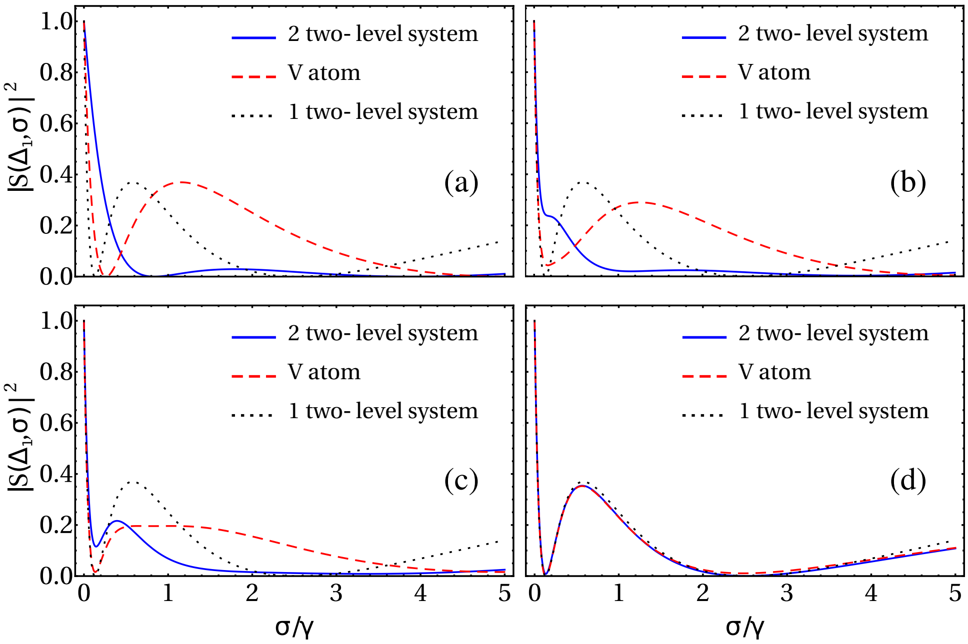

Figure 5.25: Efficiency $|S(\bar{k} = \Delta_1, \sigma_k)|^2$ of two collocated two-level systems (blue solid lines) and a V atom (red dashed lines), fixing $\bar{k} = \Delta_1$ and $\gamma = \gamma_1 = \gamma_2$. We consider different values of the detuning: (a) $\Delta_1 - \Delta_2 = 0$, (b) $\Delta_1 - \Delta_2 = \gamma$, (b) $\Delta_1 - \Delta_2 = 2\gamma$, and (d) $\Delta_1 - \Delta_2 = 10\gamma$. We compare the results to the two-level system (black dotted lines).

area does not grow with distance and, thus, the interaction does not decay but it is periodically modulated instead. The period depends on the level splitting of the qubits and the dispersion relation in the waveguide. This and other distance effects have been theoretically investigated in a multitude of arrangements [104, 207, 216, 237, 260–266]; the periodicity of the coupling in particular has been experimentally demonstrated quite recently [49].

Under the Markovian approximation, the induced qubit-qubit interaction is considered instantaneous. This implies that the photon scattering by several qubits would be the same for interqubit distances $d \equiv x_{i'} - x_i$, related by

$$d' = d + \frac{\pi}{k_{\text{in}}} q, \tag{5.75}$$

where q is an integer.

In order to illustrate nonMarkovian effects related to a finite interqubit distance, let us consider the situation of $N = 2$ input photons and three qubits separated by some nearest-neighbor distance d. With the MPS tool, we solve the problem exactly for any interqubit distance. Thus, we do not make any approximation like the small distance or the Markovian one. We take

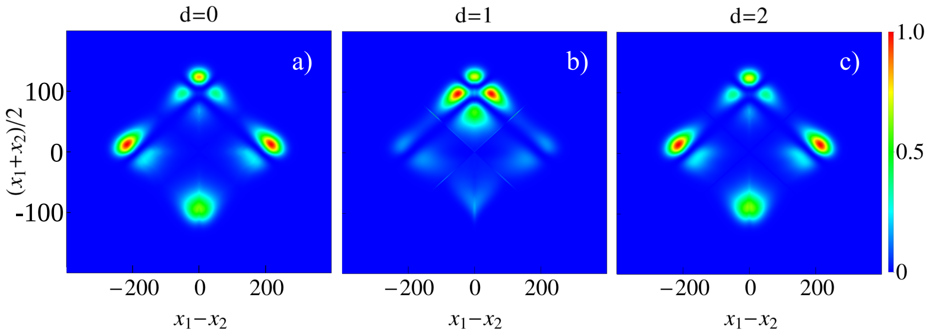

Figure 5.26: **Two-photon wave function for different qubit-qubit distances.** $|\phi^{t_{\rm out}}_{x_1,x_2}|^2$ for two incident photons and three qubits with inter-qubit distance d. i), ii) and iii) mean the same as in Fig. 4.5. The incoming photons are characterized by $\sigma = 20$ and $k_{\rm in} = \pi/2$. We take $d = 0, 1, 2$, (left, middle and right columns respectively), so the first and the third cases should be equivalent according to the Markov approximation because of (5.75). We consider the RWA Hamiltonian and take $g\sqrt{3} = 0.10$.

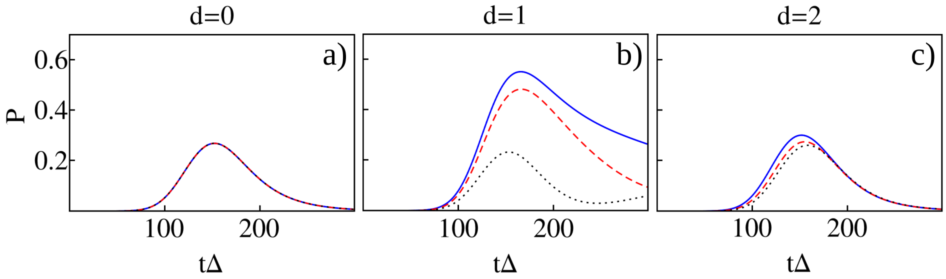

Figure 5.27: **Qubit populations for different qubit-qubit distances.** Qubit population of the first (solid blue), the second (dashed red) and the third qubit (dotted black). The parameters are those of figure 5.26.

the RWA and both input photons are at resonance with the two-level atoms ($k_{\rm in} = \pi/2$). We plot both the square modulus of the two-photon wave function $|\phi^{t_{\rm out}}_{x_1,x_2}|^2$ and the qubit populations $P_i = \langle\Psi|\sigma_i^+\sigma_i^-|\Psi\rangle$ in Figs. 5.26 and 5.27, respectively. Regarding the photons, the characteristics are the same at zero distance and $d = 2$, which are equivalent in the Markov approximation due to (5.75) (recall that we are considering $k_{\rm in} = \pi/2$). However, the wave function is drastically modified when this condition is not fulfilled (Fig. 5.26(b), $d = 1$). The inherent nonMarkovian properties of our exact simulation can be appreciated by comparing the qubit population in Figs. 5.27(a) and (c). If $d \neq 0$, the qubit at the left is excited first, then the central qubit and finally the one to the right. Anyway, up to these shifts in time, the profiles of both panels are qualitatively identical. However, for a nonequivalent distance, the dynamics differs significantly (see Fig. 5.27(b), with $d = 1$).

The contours for $|\phi^{t_{\text{out}}}_{x_1,x_2}|^2$ for $d = 0$ and $d = 2$ are closer to the linear scattering result than that for $d = 1$ case (see Figs. 4.5(c) and 5.26(a), (b), and (c)). This enhancement of nonlinear properties with the distance can be understood as follows. At distances $\frac{\pi}{k_{\text{in}}} q$ (equivalent to zero distance according to Eq. (5.75)), following the Markov approximation, only qubit states generated by the ladder operator $b^\dagger$ in Eq. (4.37) are visited during the dynamics. For two-photon input states, the nonlinearities die out as $1/M$ (see Sect. 4.2.5). For distances not fulfilling this condition of equivalent, more qubit states (satisfying the number conservation imposed by the RWA) can play a role. The fact that more qubit modes participate in the dynamics for $d = 1$ is apparent from Fig. 5.27(b). Notice that, clearly, more frequencies are involved in the evolution of P, since the profiles are much more complicated. Importantly enough, $d = 1$ corresponds to a distance where the coherent interaction between the qubits are maximized, while the correlations in the qubit decays are minimized. This is named as subradiant case. As we can observe, the qubit decay (after excitation) is slower in this case.

Chapter 6

Conclusions

> *You look at science (or at least talk of it) as some sort of demoralizing invention of man, something apart from real life, and which must be cautiously guarded and kept separate from everyday existence. But science and everyday life cannot and should not be separated.*
>
> Rosalind Franklin, in a letter to her father [267].

In this thesis, we have covered different aspects of the growing field of waveguide QED. In Chapter 1, we have introduced the kind of models we consider and some general aspects on scattering theory. We have reviewed some previously known methods to solve scattering in waveguide QED in Chapter 2, besides we have explained how to apply matrix-product states (MPS) to this field. We have studied the spectral properties of these models in different regimes of coupling (RWA and ultrastrong) and the effect of the bound states on a spontaneous-decay situation in Chapter 3. Some analytical properties of the scattering matrix have been determined in Chapter 4. We have studied nonlinear processes in scattering in waveguide QED in Chapter 5. In the following, we briefly summarize the results of the thesis and present the conclusions.

6.1 Methods: MPS vs. other techniques

We have reviewed some methods for solving waveguide-QED problems in Chapter 2, such as the input-output formalism (Sect. 2.1), its combination with the master equation (Sect. 2.2) or exact diagonalization (Sect. 2.4). Besides, we have explained how to apply MPS to these problems (Sect. 2.3).

This is the first time MPS are used in this context. This technique allows us to determine the dynamics of the system, having access to the evolution of different observables, such as the number of photons in position or momentum space (see Figs. 5.1 and 5.10(b-c)) or the population of the scatterer (see Figs. 5.5, 5.10(a), and 5.27). In this sense, MPS gives more information than the previously known methods, which just describe the long-time asymptotic behavior. Besides, one can naturally go beyond the RWA, which is not trivial with the other techniques. In fact, the ultrastrong coupling had not been studied previously in a waveguide-QED context to the best of our knowledge. This technique also provides the low-energy eigenstates of the model. In addition, we can easily simulate N-photon scattering with $N = 3, 4 \ldots$, which is extremely difficult with other tools. However, other methods, such as the input-output formalism, allow us to compute the two-photon scattering matrix in momentum space, which would require from a prohibitive amount of computational resources with MPS. Therefore, we think MPS is a useful numerical tool for scattering in waveguide QED that complements the information given by the other tools.

6.2 Eigenstates of H

We have studied the eigenstates of the Hamiltonian in Chapter 3. We have reviewed the already known scattering and bound states in RWA in Sect. 3.1. Besides, we have characterized some low-energy bound states in the ultrastrong regime (see Sect. 3.2).

We have seen that the bound states are essential for understanding the underlying mechanisms of few-photon waveguide QED. In particular, in Chapter 3, we have studied the spontaneous decay of a two-level atom under the RWA, where the one-photon bound states play an important role in the dynamics of the qubit (see Sect. 3.3). In posterior chapters, we have seen that these states strongly influence the scattering (see Sect. 5.1).

6.3 Analytical properties of S: More than mathematics

We have studied some analytical properties of the S matrix in Chapter 4. In Sect. 4.1, we have shown that approximate causality holds for our nonrelativistic models, which in turns implies a particular structure for the free part of the S matrix. In Sect. 4.2, we have found the scattering matrix for linear scattering and we support our results with numerical simulations with MPS to see how this linear behavior emerges.

Besides that the analytical properties of S are relevant per se, they give valuable information. For instance, looking at the expression of the free part of the scattering matrix S^0 imposed by causality if inelastic single-photon processes are allowed (see Eq. (4.17)), we see that it induces photon-photon correlations, which does not happen if inelastic events are forbidden (see Eq. (4.12)). Contrarily, if the scatterers are linear, neither photon-photon correlations nor particle annihilation or creation occur (see Theorems 1 and 2 of Sect. 4.2). In conclusion, the scope of the study of the mathematical structure of S goes beyond the fundamental aspects, since it allows us to predict effects measurable in the laboratory.

6.4 Nonlinear photonics with few photons

We have studied several nonlinear effects in waveguide QED in Chapter 5: (i) One-photon scattering from one qubit in the ultrastrong coupling regime, which gives new features, such as an inelastic spectrum (Sect. 5.1), (ii) two-photon generation with one and only one input photon (Sect. 5.2), (iii) one- and two-photon scattering from a $\mathrm{V}^{(N)}$ atom, where the photon-photon correlations can be suppressed for some values of the input parameters, (iv) the potential realization of a two-qubit quantum gate, which requires from a nonlinear phase (see Sect. 5.4), and (v) the effect of interqubit distance in two-photon scattering (see Sect. 5.5), where we see nonMarkovian effects.

The efficiency of these nonlinear processes overcomes the values usually found in nonlinear classical optics. In fact, we have shown that it is possible to induce deterministic frequency conversion (see Sect. 5.1 and Fig. 5.4) and two-photon generation (see Sect. 5.2 and Fig. 5.10(c)). We can also switch on and off the generation of photon-photon correlations in two-photon scattering from a $\mathrm{V}^{(N)}$ atom (see Sect. 5.3 and Fig. 5.19).

All these phenomena allow us to manipulate quantum states, which can have applications in quantum-information science. For instance, if we encode the information in the frequency of the photons, the Raman scattering in the ultrastrong permits to process this information. The scattering from the $\mathrm{V}^{(N)}$ atom can generate and suppress the photon-photon entanglement, which is an essential resource for quantum computation. We have exemplified these potential applications by proposing a protocol for a potential two-qubit phase gate in Sect. 5.4.

Chapter 7

Conclusiones

En esta tesis hemos tratado varios problems del emergente campo de la electrodinámica cuántica en guías de onda. En el capítulo 1 hemos introducido el tipo de modelos que tratamos de resolver y algunos aspectos generales de teoría de scattering. Hemos revisado algunos métodos ya conocidos para resolver scattering en electrodinámica cuántica en guías de onda en el capítulo 2, además de que hemos explicado cómo aplicar MPS a este campo. Hemos estudiado las propiedades espectrales de estos modelos en varios regímenes de acoplo (RWA y ultrafuerte) y el efecto de los estados ligados en una situación de decaimiento espontáneo en el capítulo 3. Algunas propiedades analíticas de la matriz de scattering se han determinado en el capítulo 4. Hemos estudiado procesos no lineales en scattering en electrodinámica cuántica en guías de onda en el capítulo 5. En lo que sigue a continuación, resumimos brevemente los resultados de la tesis y presentamos las conclusiones.

7.1 Métodos: MPS frente a otras técnicas

Hemos revisado algunos métodos para resolver problemas de electrodinámica cuántica en guías de onda en el capítulo 2, tales como el formalismo input-output (sección 2.1), su combinación con ecuaciones maestras (sección 2.2) o diagonalización exacta (sección 2.4). Además, hemos explicado cómo aplicar MPS a estos problemas (sección 2.3).

Esta es la primrea vez en la que se usan MPS en este contexto. Esta técnica nos permite determinar la dinámica del sistema, teniendo acceso a la evolución de varios observables, como el número de fotones en los espacios de posición o de momentos (ver figuras 5.1 y 5.10(b-c)) o la población de las impurezas (ver figuras 5.5, 5.10(a) y 5.27). En este sentido, MPS da más información que otros métodos previamente conocidos, que solo describen el comportamiento asintótico a tiempos largos. Además, se puede ir de forma natural más allá de la RWA, lo cual no es trivial con las otras técnicas. De hecho, el acoplo ultrafuerte no se había estudiado previamente en un contexto de electrodinámica cuántica en guías de onda hasta donde nosotros sabemos. Esta técnica también proporciona los autoestados de baja energía del modelo. Además,podemos simular con facilidad scattering de N fotones con $N = 3, 4 \ldots$, lo cual es extremadamente difícil con otras herramientas. Por contra, otros métodos, tales como el formalismo input-output, nos permiten calcular la matriz de scattering de dos fotones en el espacio de momentos, lo cual requeriría de una cantidad prohibitiva de recursos computacionales con MPS. Por tanto, concluimos que MPS es una herramienta numérica útil para scattering en electrodinámica cuántica en guías de onda que complementa la información que dan otras técnicas.

7.2 Autoestados de H

Hemos estudiado los autoestados del hamiltoniano en el capítulo 3. Hemos revisado los ya conocidos estados de scattering y ligados en RWA en la sección 3.1. Además, hemos caracterizado varios estados ligados de baja en energía en el régimen ultafuerte (ver sección 3.2).

Hemos visto que los estados ligados son esenciales para comprender los mecanismos subyacentes de electrodinámica cuántica en guías con pocos fotones. En particular, en el capítulo 3 hemos estudiado el decaimiento espontáneo de un átomo de dos niveles bajo la RWA, donde los estados ligados de una excitación juegan un papel importante en la dinámica del qubit (ver sección 3.3). En capítulos posteriores, hemos visto que estos estados influyen fuertemente en el scattering (ver sección 5.1).

7.3 Propiedades analíticas de S: No solo matemáticas

Hemos estudiado algunas propiedades analíticas de la matriz S en el capítulo 4. En la sección 4.1 hemos demostrado que se cumple la causalidad de forma aproximada para nuestros modelos no relativistas, que a su vez implica una estructura particular para la parte libre de la matriz S. En la sección 4.2 hemos encontrado la matriz de scattering para sistemas lineales y hemos apoyado nuestros resultados en simulaciones numéricas con MPS para ver cómo este comportamiento lineal emerge.

Aparte del hecho de que las propiedades analíticas de S son relevantes per se, dan una valiosa información práctica. Por ejemplo, mirando la expresión de la parte libre de la matriz de scattering, S^0, impuesta por causalidad en el caso en el que es posible tener procesos inelásticos de scattering de un fotón (ver ecuación (4.17)), vemos que esta induce correlaciones entre los fotones, lo cual no ocurre si estos procesos inelásticos están prohibidos (ver ecuación (4.12)). Por contra, si los scatterers son lineales, no hay ni correlaciones entre fotones ni generación o aniquilación de partículas (ver los teoremas 1 y 2 de la sección 4.2). En resumen, estudiar la estructura matemática de S va más allá de los aspectos fundamentales, ya que nos permite predecir efectos medibles en el laboratorio.

7.4 Fotónica no lineal con pocos fotones

Hemos estudiado varios efectos no lineales en electrodinámica cuántica en guías de onda en el capítulo 5: (i) scattering de un fotón interaccionando con un qubit en el régimen de acoplo ultrafuerte, el cual presenta nueva fenomenología respecto a la RWA, como por ejemplo un espectro inelástico (sección 5.1), (ii) generación de dos fotones a partir de un único fotón de entrada (sección 5.2), (iii) scattering de uno y dos fotones interaccionando con un átomo $\mathrm{V}^{(N)}$, donde las correlaciones entre fotones se pueden suprimir para ciertos valores de los parámetros, (iv) la potencial realización de una puerta cuántica de fase de dos qubits, lo cual requiere de una fase no lineal (ver sección 5.4) y (v) el efecto de la distancia entre qubits en scattering de dos fotones (ver sección 5.5).

La eficiencia de estos procesos no lineales supera los valores típicamente encontrados en óptica clásica no lineal. De hecho, hemos demostrado que es posible inducir de forma determinista conversión de frecuencia (ver sección. 5.1 y figura 5.4) y generación de dos fotones (ver sección 5.2 y figura 5.10(c)). También podemos controlar la generación de correlaciones entre fotones en el scattering de dos fotones a través de un átomo $\mathrm{V}^{(N)}$ (ver sección 5.3 y figura 5.19).

En todos estos fenómenos estamos manipulando estados cuánticos, lo cual puede tener aplicaciones en información cuántica. Por ejemplo, si codificamos la información en la frecuencia de los fotones, el scattering Raman en el ultrafuerte permite procesar esta información. El scattering a través del átomo $\mathrm{V}^{(N)}$ puede generar y suprimir el entrelazamiento entre fotones, el cual es un recurso fundamnetal en computación cuántica. Hemos ejemplificado estas potenciales aplicaciones proponiendo un protocolo para una puerta de fase de dos qubits en la sección 5.4.

Appendix A

Details about the truncation of MPS

In this appendix we explain the details on the procedure to approximate one MPS by another one with smaller value of the bond dimension.

The problem consists of minimizing iteratively a function which is a sum of scalar products (2.98). During this section, we consider the generic scalar product $\langle \xi | \chi \rangle$, whose MPS tensors are $A(\xi)$ and $A(\zeta)$ respectively. First of all, since the whole function is minimized with respect to the tensors linked to a given site, we are going to write a scalar product between MPS in the following way:

$$\langle \xi | \zeta \rangle = (v_n^{\xi})^{\dagger} M v_n^{\zeta}, \tag{A.1}$$

where v_n^{ξ} and v_n^{ζ} are the vectorizations of $A(\xi)^n$ and $A(\zeta)^n$ respectively. Using the MPS representation, this scalar product is:

$$\begin{aligned} \langle \xi | \zeta \rangle =& (A(\xi)_1^{i_1})^*_{k_1,k_2} (A(\xi)_2^{i_2})^*_{k_2,k_3} \dots (A(\xi)_L^{i_L})^*_{k_L,k_1} \\ & (A(\zeta)_1^{i_1})_{l_1,l_2} (A(\zeta)_2^{i_2})_{l_2,l_3} \dots (A(\zeta)_L^{i_L})_{l_L,l_1}. \end{aligned} \tag{A.2}$$

We rewrite it in the following way:

$$\langle \xi | \zeta \rangle = (A_L)_{k_1,l_1,k_n,l_n} (A(\xi)_n^{i_n})^*_{k_n,k_{n+1}} (A(\zeta)_n)^{i_n}_{l_n,l_{n+1}} (A_R)_{k_{n+1},l_{n+1},k_1,l_1}, \tag{A.3}$$

where A_L and A_R are:

$$\begin{aligned}(A_L)_{k_1,l_1,k_n,l_n} &= (A(\xi)_1^{i_1})^*_{k_1,k_2}(A(\zeta)_1^{i_1})_{l_1,l_2}\cdots \\ &\quad (A(\xi)_{n-1}^{i_{n-1}})^*_{k_{n-1},k_n}(A(\zeta)_{n-1}^{i_{n-1}})_{l_{n-1},l_n} \qquad \text{(A.4)}\\ (A_R)_{k_{n+1},l_{n+1},k_1,l_1} &= (A(\xi)_{n+1}^{i_{n+1}})^*_{k_{n+1},k_{n+2}}(A(\zeta)_{n+1}^{i_{n+1}})_{l_{n+1},l_{n+2}}\cdots \\ &\quad (A(\xi)_L^{i_L})^*_{k_L,k_1}(A(\zeta)_L^{i_L})_{l_L,l_1}. \qquad \text{(A.5)}\end{aligned}$$

Now, another tensor C is introduced:

$$C_{k_{n+1},l_{n+1},k_n,l_n} = (A_R)_{k_{n+1},l_{n+1},k_1,l_1}(A_L)_{k_1,l_1,k_n,l_n}. \tag{A.6}$$

Then, the scalar product becomes:

$$\langle\xi|\zeta\rangle = (A(\xi)^{i_n})^*_{k_n,k_{n+1}}C_{k_{n+1},l_{n+1},k_n,l_n}A(\zeta)^{i_n}_{l_n,l_{n+1}}. \tag{A.7}$$

It is convenient to introduce a Kronecker delta:

$$\langle\xi|\zeta\rangle = (A(\xi)^{i_n})^*_{k_n,k_{n+1}}C_{k_{n+1},l_{n+1},k_n,l_n}\delta_{i_n,j_n}A(\zeta)^{j_n}_{l_n,l_{n+1}}. \tag{A.8}$$

Another auxiliary tensor is defined as:

$$D_{k_n,i_n,k_{n+1},l_n,j_n,l_{n+1}} = C_{k_{n+1},l_{n+1},k_n,l_n}\delta_{i_n,j_n}. \tag{A.9}$$

Then:

$$\langle\xi|\zeta\rangle = (A(\xi)_n^{i_n})^*_{k_n,k_{n+1}}D_{k_n,i_n,k_{n+1},l_n,j_n,l_{n+1}}(A(\zeta)_n^{j_n})_{l_n,l_{n+1}}. \tag{A.10}$$

Finally, we can define the vectorizations $A(\xi)_n$ by joining all the indices:

$$(v_n^{\xi})_{[k_n,i_n,k_{n+1}]} = (A(\xi)_n^{i_n})^*_{k_n,k_{n+1}}, \tag{A.11}$$

and the same for v_n^{ζ}. Here, $[k_n, i_n, k_{n+1}]$ is again a single index, in such a way that we construct a vector from a tensor with three indices (the same for v_n^{ζ}). In the same way, we define a matrix M by joining the indices of the tensor D in two sets:

$$M_{[k_n,i_n,k_{n+1}],[,l_n,j_n,l_{n+1}]} = D_{k_n,i_n,k_{n+1},l_n,j_n,l_{n+1}}. \tag{A.12}$$

Then, the scalar product is:

$$\langle\xi|\zeta\rangle = (v_n^{\xi})^*_{[k_n,i_n,k_{n+1}]}M_{[k_n,i_n,k_{n+1}],[,l_n,j_n,l_{n+1}]}(v_n^{\zeta})_{[,l_n,j_n,l_{n+1}]}, \tag{A.13}$$

or, in vectorial notation:

$$\langle\xi|\zeta\rangle = (v_n^{\xi})^{\dagger}Mv_n^{\zeta}. \tag{A.14}$$

Therefore, we have obtained (2.99), as well as how to build M.

Appendix B

Influence of the bound states on the spontaneous decay

B.1 Emitted field

The emitted field $\phi_x(t) = \langle 0|a_x|\Psi(t)\rangle$ can be computed spanning $|\Psi(t)\rangle$ in energy eigenstates (3.24):

$$\begin{aligned}\phi_x(t) = \frac{1}{2\pi}\int_{-\pi}^{\pi} dk\, c_k e^{-i\omega_k t}\langle 0|a_x|\Psi_k\rangle \\ + c_+ e^{-i\omega_+ t}\langle 0|a_x|\Psi_+\rangle + c_- e^{-i\omega_- t}\langle 0|a_x|\Psi_-\rangle.\end{aligned} \tag{B.1}$$

In order to compute the amplitude $\langle 0|a_x|\Psi_k\rangle$ we take the expression of $|\Psi_k\rangle$, Eq. (3.14), for $k > 0$:

$$\langle 0|a_x|\Psi_k\rangle = \begin{cases} e^{ikx} + r_k e^{-ikx} & x < 0, \\ t_k e^{ikx} & x \geq 0. \end{cases} \tag{B.2}$$

If $k < 0$:

$$\langle 0|a_x|\Psi_k\rangle = \begin{cases} t_k e^{ikx} & x < 0, \\ e^{ikx} + r_k e^{-ikx} & x \geq 0. \end{cases} \tag{B.3}$$

The amplitudes $\langle 0|a_x|\Psi_\pm\rangle$ are computed by projecting on $|\Psi_\pm\rangle$ (Eq. (3.5)):

$$\langle 0|a_x|\Psi_\pm\rangle = N_\pm e^{-\kappa_\pm |x|}. \tag{B.4}$$

B.2 Impurity dynamics: analyzing the integrand

B.2.1 Exponential decay

In order to extract the first exponential decay, we can approximate $F(y)$ by $L(y) = a_p/(y - y_p)$, being y_p the pole corresponding to the peak of $F(y)$, with $-1 < \mathrm{Re}(y_p) < 1$ and $\mathrm{Im}(y_p) > 0$, and a_p the residue of $F(y)$ at $y = y_p$. The value of y_p is found numerically, equating the denominator of $F(y)$ to 0 (see Eq. (3.33)). The residue a_p is computed by definition. We extend the integration domain to $\pm\infty$. Then, applying the residue theorem

$$c_{\mathrm{e}}^{\mathrm{s}}(t) = i8a_p(g/J)^2 e^{-i\epsilon t} e^{i2y_pJt}, \tag{B.5}$$

By computing this numerically, we obtain the decay rate $\tau_0 = (4J\ \mathrm{Im}(y_p))^{-1}$ and the phase $\varphi = \epsilon - 2J\ \mathrm{Re}(y_p)$, as shown in Fig. 3.12 in the main text.

B.2.2 Sub-exponential regime: $t^{-1/2}$

The kernel $F(y)$ has a sharp behavior around $y_{\pm}^*$. In fact, it diverges when $y \to \pm 1$ if $g = 0$. In order to take into account this contribution, we can approximate $F(y)$ by $F(y)|_{g=0}$ (see blue, dashed curve of Fig. 3.11(a))

$$c_{\mathrm{e}}^{\mathrm{s}}(t) \simeq \frac{4g^2 e^{-i\epsilon t}}{\pi J^2} \int_{-1}^{1} dy \frac{e^{i2yJt}}{4\sqrt{1-y^2}((\Delta-\epsilon)/J+2y)^2}. \tag{B.6}$$

If $2\Delta y_{\pm} Jt \ll 1$, with $\Delta y_{\pm} = |y_{\pm}^* \mp 1|$, the oscillatory term e^{i2yJt} will not be sensitive to the difference between $F(y)$ and $F(y)|_{g=0}$ when y is close to the edges. As we are concerned in the contribution around ± 1, we can approximate the integral as:

$$\begin{aligned} c_{\mathrm{e}}^{\mathrm{s}}(t) \simeq \frac{4g^2 e^{-i\epsilon t}}{\sqrt{2}\pi J^2} \bigg(& \frac{J^2}{(\Delta-\epsilon-2J)^2} \int_{-1}^{\infty} dy \frac{e^{i2yJt}}{4\sqrt{1+y}} \\ & + \frac{J^2}{(\Delta-\epsilon+2J)^2} \int_{-\infty}^{1} dy \frac{e^{i2yJt}}{4\sqrt{1-y}} \bigg). \end{aligned} \tag{B.7}$$

These integrals are analytical

$$c_{\mathrm{e}}^{\mathrm{s}}(t) \simeq \frac{g^2 e^{-i\epsilon t}}{2\sqrt{2\pi Jt}} \left(\frac{e^{-i2Jt}}{(\Delta-\epsilon-2J)^2} + \frac{e^{i2Jt}}{(\Delta-\epsilon+2J)^2} \right). \tag{B.8}$$

In consequence, $P_{\mathrm{e}}^{\mathrm{s}}(t)$ decays with $(Jt)^{-1}$ after the initial exponential decay if $\tau_0 \ll t \ll \tau_{1,\pm}$, with $\tau_{1,\pm} = (4J\Delta y_{\pm})^{-1}$. We can rewrite the last expression by adding the decaying exponentials with $\tau_{1,\pm}$:

$$c_{\mathrm{e}}^{\mathrm{s}}(t) \simeq \frac{g^2 e^{-i\epsilon t}}{2\sqrt{2\pi J t}} \left(\frac{e^{-i2Jt}}{(\Delta-\epsilon-2J)^2} e^{-t/2\tau_{1,-}} + \frac{e^{i2Jt}}{(\Delta-\epsilon+2J)^2} e^{-t/2\tau_{1,+}} \right). \tag{B.9}$$

The constants $a_\pm$ introduced in the main text can be identified as

$$a_- = \frac{g^2}{2\sqrt{2\pi J}(\Delta-\epsilon-2J)^2}, \tag{B.10}$$

$$a_+ = \frac{g^2}{2\sqrt{2\pi J}(\Delta-\epsilon+2J)^2}. \tag{B.11}$$

B.2.3 Sub-exponential regime: $t^{-3/2}$

Eventually, when $t \gg \tau_0, \tau_{1,\pm}$, the only surviving contribution will come from the singularities of $F(y)$, since the rapidly oscillating term e^{i2yJt} cancels out the contribution of any nonsingular part of the kernel. The singularities of $F(y)$ occurs at $y = \pm 1$. Therefore, we can approximate the kernel by any function which behaves as $F(y)$ for $y = \pm 1$, provided this function has no singularities in between both points. We consider the function $G(y)$ (see Fig. 3.11(a), green, dotted-dashed curve)

$$G(y) = \frac{\sqrt{1-y^2}}{(g/J)^4}. \tag{B.12}$$

Integrating this, the scattering amplitude in the long-time limit, $t \gg \tau_0, \tau_{1,\pm}$, is

$$c_{\mathrm{e}}^{\mathrm{s}}(t) \simeq \frac{4J^2 e^{-i\epsilon t}}{\pi g^2} \int_{-1}^{1} dy \sqrt{1-y^2} e^{i2yJt} = \frac{2Je^{-i\epsilon t}}{g^2} \frac{J_1(2Jt)}{t}, \tag{B.13}$$

being J_1 the first-kind Bessel function with $n = 1$. As $t \to \infty$, $J_1(2Jt) \to (\pi J t)^{-1/2} \cos(2Jt - 3\pi/4)$, so $P_{\mathrm{e}}^{\mathrm{s}}(t)$ decays with $(Jt)^{-3}$ in the long-time limit.

Appendix C

Cluster-decomposition principle: theorems and more

In the following sections, we derive the theorems and other results of Sect. 4.1.

C.1 The ground state of the light-matter interaction

In this appendix we demonstrate that the ground state converges to the trivial vacuum far away from the scatterer (see Eq. (4.6)). The next lemma is necessary to proof the main theorem.

Lemma 1 *Given the waveguide-QED model* (1.1)*, we have the following bounds for the expectation values on its minimum-energy state* $|\Omega_0\rangle$*,*

$$|\langle\Omega_0|a_k^\dagger a_p|\Omega_0\rangle| \leq \sqrt{\left|\frac{g_k g_p}{\omega_k\omega_p}\right|}\,\langle\Omega_0|GG^\dagger|\Omega_0\rangle\,. \tag{C.1}$$

Let us assume that $|\Omega_0\rangle$ is the minimum-energy state of H as given by Eq. (1.1), and thus $(H-E_0)\,|\Omega_0\rangle = 0$. The energy of the unnormalized state

$$|\chi\rangle = O\,|\Omega_0\rangle\ , \tag{C.2}$$

created by any operator O must be larger or equal to that of the ground state, $\langle\chi|(H-E_0)|\chi\rangle \geq 0$. Using (C.2)

$$\langle\chi|\,(H-E_0)\,|\chi\rangle = \langle\Omega_0|O^\dagger H O - O^\dagger O H|\Omega_0\rangle \tag{C.3}$$

we conclude with the useful relation

$$\langle\chi|H-E_0|\chi\rangle = \langle\Omega_0|O^\dagger[H,O]|\Omega_0\rangle \geq 0. \tag{C.4}$$

Let us take $O = a_k$. The previous statement leads to

$$\langle \Omega_0 | a_k^\dagger (-\omega_k a_k - g_k G) | \Omega_0 \rangle \geq 0, \tag{C.5}$$

or equivalently

$$0 \leq \langle \Omega_0 | a_k^\dagger a_k | \Omega_0 \rangle \leq -\frac{g_k}{\omega_k} \langle \Omega_0 | G a_k^\dagger | \Omega_0 \rangle \, . \tag{C.6}$$

Using Cauchy-Schwatz, this translates into the upper bound

$$\langle \Omega_0 | a_k^\dagger a_k | \Omega_0 \rangle \leq \frac{|g_k|}{\omega_k} \sqrt{\langle \Omega_0 | G G^\dagger | \Omega_0 \rangle \, \langle \Omega_0 | a_k^\dagger a_k | \Omega_0 \rangle}. \tag{C.7}$$

Once the diagonal elements of the correlation matrix are bounded the non-diagonal can also be bounded. The correlation matrix is positive $C \geq 0$ with $C_{kp} = \langle \Omega_0 | a_k^\dagger a_p | \Omega_0 \rangle$. A property of positive matrices is [268]

$$|C_{kp}| \leq \sqrt{|C_{kk}||C_{pp}|} \tag{C.8}$$

which implies (C.1).

With this lemma at hand we state:

Theorem 3 *Let us define $\psi^\dagger_{\bar{k}\bar{x}x}$ as the operator* (4.2) *removing the time-dependent part, where $\phi_{\bar{k}}(k)$ is infinitely differentiable with a finite support K centered around $\bar{k}$. Then, the expected value of $\psi^\dagger_{\bar{k}\bar{x}} \psi_{\bar{k}\bar{x}}$ in the minimum-energy state fulfills*

$$\langle \Omega_0 | \psi^\dagger_{\bar{k}\bar{x}} \psi_{\bar{k}\bar{x}} | \Omega_0 \rangle \to 0, \ |\bar{x}| \to \infty, \tag{C.9}$$

where we choose $x_{sc} = 0$. Moreover, if we can assume that $\langle a_k^\dagger a_p \rangle$ is an n-times differentiable function of k and p, the bound will be improved

$$\langle \Omega_0 | \psi^\dagger_{\bar{k}\bar{x}} \psi_{\bar{k}\bar{x}} | \Omega_0 \rangle \leq \mathcal{O}(|\bar{x}|^{-n}), \ |\bar{x}| \to \infty. \tag{C.10}$$

Let us compute the expectation value of the number operator for a wave packet $N := \langle \Omega_0 | \psi^\dagger_{\bar{k}\bar{x}} \psi_{\bar{k}\bar{x}} | \Omega_0 \rangle$,

$$N = \iint \langle \Omega_0 | a_k^\dagger a_p | \Omega_0 \rangle \, e^{i(k-p)\bar{x}} \varphi_{\bar{k}}(k)^* \varphi_{\bar{k}}(p) \, dk dp. \tag{C.11}$$

We can rewrite N as the Fourier transform of another function $N = \int e^{iu\bar{x}} F(u) \, du$, where

$$F(u) := \frac{1}{2} \int \varphi_{\bar{k}}((u+v)/2)^* \varphi_{\bar{k}}((u-v)/2) \, \langle a^\dagger_{(u+v)/2} a_{(u-v)/2} \rangle \, dv. \tag{C.12}$$

We are now going to assume that $\phi_{\bar{k}}(k)$ is a test function with compact support K of size $|K|$ centered around $\bar{k}$, and infinitely differentiable. We will also assume that within its support $|g_k/\omega_k|^2\langle GG^\dagger\rangle \leq C_\phi$ for some constant C_ϕ. Then we can bound

$$\int |F(u)|du \leq |K|^2 C_\phi. \tag{C.13}$$

Assuming that $\langle\Omega_0|a_k^\dagger a_p|\Omega_0\rangle$ is n-times differentiable and using the Riemann-Lebesgue theorem, we have then that

$$\left|\int e^{iu\bar{x}} F(u)du\right| \leq \mathcal{O}\left(|\bar{x}|^{-n}\right) \tag{C.14}$$

at long distances.

C.2 Approximate causality

C.2.1 Free-field causality

We first prove causal relations in a free theory. In order to do so, we work with localized wave packets $\psi_{\bar{k}\bar{x}}(t)$, Eq. (4.2). Actual calculations are done with Gaussian wave packets, Eq. (4.3). The following two lemmas are used in the demonstration of the theorem.

Lemma 2 *Let the dispersion relation ω_k have an upper bounded group velocity $v_k = \partial_k\omega_k$:*

$$|v_k| \leq c. \tag{C.15}$$

Then, the function $f(k) = kx - \omega_k t$ only has stationary points if the distance to the light cone is nonnegative. In other words

$$d_c(x,t) = |x| - c|t| > 0 \Leftrightarrow |f'(k)| > 0,\ \forall k. \tag{C.16}$$

Solving the equation $f'(k) = x - \partial_k\omega_k t = 0$ leads to the condition $\frac{x}{t} = v_k$ or $|x/t| = |v_k| \leq c$. Then, provided $f'(k) = 0$, it follows $|x| \leq c|t| \Rightarrow d_c(x,t) \leq 0$, which shows (C.16).

Lemma 3 *Assume that ω_k is n-times differentiable and that every derivative $|\omega_k^{(r\leq n)}|$ is upper bounded by an m-th order polynomial in $|k|$. Then the following integral bound applies*

$$\left|\int e^{ikx - \frac{1}{\sigma^2}(k-k_0)^2 - i\omega_k t} p(k)dk\right| = \max(\sigma^{m+n+r},1)\max(t^n,1)\mathcal{O}\left(\frac{1}{|x|^n}\right).$$

where $p(k)$ is a polynomial of degree r.

Result 5.1 from Ref. [269] states that the integral $I(x) = \int_a^b e^{ikx} q(k)\, dk$ may be integrated by parts n times, obtaining

$$I(x) = \sum_{s=0}^{n-1} \left(\frac{i}{x}\right)^{s+1} \left[e^{iax} q^{(s)}(a) - e^{ibx} q^{(s)}(b)\right] + \epsilon_n(x), \tag{C.17}$$

where the error term satisfies

$$\epsilon_n(x) = \left(\frac{i}{x}\right)^n \int e^{ikx} q^{(n)}(k) dk = o(x^{-n}) \tag{C.18}$$

provided that $q(k)$ is n-times differentiable and that $q^{(n)} \in L^1$. Based on the conditions of the lemma, this is satisfied since $q(k) = e^{-\frac{1}{\sigma^2}(k-k_0)^2 - i\omega_k t} p(k)$. The limits of the integral may be easily extended to ±∞, as explained in Result 5.2 from [269]. Since $x^{-s} q^{(s)}(a) \to 0$ when $a \to \pm\infty$, $\forall x$, we obtain

$$I(x) = \int e^{ikx} q(k)\, dk = \left(\frac{i}{x}\right)^n \int e^{ikx} q^{(n)}(k) dk, \tag{C.19}$$

Moreover, $q^{(n)}$, resulting from a product of derivatives of $\omega_k t$, $-k^2/\sigma^2$ and the polynomial $p(k)$ of degree r, is bounded by a polynomial of at most $(m + n + r)$-th order in $|k|$. Such a polynomial is integrable together with the Gaussian wave packet giving a constant prefactor. In estimating this factor, we can take the worst-case scenario for the terms in t, which appears at most n times together with $(\partial_k \omega_k)^n$, and the monomials in $|k|$, which produce another prefactor σ^{m+n+r}.

Note that it would suffice to consider $q(k)$ as a test function or even a Schwartz function since in this case all the differentiability requisites are fulfilled and $x^{-s} q^{(s)}(a) \to 0 \to 0$ when $a \to \pm\infty$, $\forall x$ still holds, because these functions and their derivatives are rapidly decreasing.

With these lemmas at hand we can prove

Theorem 4 *Let the Hamiltonian be given just by the photonic part,* $H_0 = \int dk\, \omega_k a_k^\dagger a_k$. *Let* $\psi_{\bar{k}\bar{x}}(t)$ *and* $\psi_{\bar{p}\bar{y}}(t')$ *denote two localized wave packets of the form* (4.3)*. We will assume that (i) the absolute value for the group velocity of these wave packets is upper bounded by a constant* c *within the domain of the wave packets* ($|v_k| = |\partial_k \omega_k| \leq c$) *and (ii) the dispersion relation is* n*-times differentiable and that each derivative is upper bounded by a polynomial of at most order* m*:*

$$|\partial_k^{(r\leq n)} \omega_k| \leq a_r + (|k|/b_r)^m, \ 0 < a_r, b_r < +\infty. \tag{C.20}$$

The commutator between these wave packets is small whenever they are outside of their respective light cones, that is, whenever $d = |\bar{y} - \bar{x}| - c|t' - t| \gg 0$,

$$\|[\psi_{\bar{k}\bar{x}}(t), \psi_{\bar{p}\bar{y}}(t')^\dagger]\| = \mathcal{O}\left(\frac{1}{|d|^n}\right), \ d \to \infty. \tag{C.21}$$

Let us assume that the model evolves freely according to the free Hamiltonian $H_0 = \int dk\ \omega_k a_k^\dagger a_k$. In this case, our wave packet operators have the simple form

$$\psi_{\bar{k}\bar{x}}(t) = \int e^{ik\bar{x} - i\omega_k t} \varphi_{\bar{k}}(k)^* a_k(0)\, dk, \tag{C.22}$$

and analogously for $\psi_{\bar{p}\bar{y}}(t')$. The commutator between operators reads

$$I := [\psi_{\bar{k}\bar{x}}(t), \psi_{\bar{p}\bar{y}}(t')^\dagger] = \int e^{ik(\bar{x}-\bar{y}) - i\omega_k(t-t')} \varphi_{\bar{k}}(k)^* \varphi_{\bar{p}}(k) dk. \tag{C.23}$$

Let $d = d_c(\bar{x}-\bar{y}, t-t') = |\bar{x}-\bar{y}| - c|t-t'| > 0$, using Lemma 2 we know that the exponent has no stationary point. Assuming w.l.o.g. $\bar{x} > \bar{y}$, $t > t'$ (other combinations are analogous) and writing $\tilde{\omega}_k = \omega_k - ck$, we obtain

$$I = \int e^{ik\, d_c(\bar{x}-\bar{y}, t-t') - i\tilde{\omega}_k(t-t')} \varphi_{\bar{k}}(k)^* \varphi_{\bar{p}}(k) dk. \tag{C.24}$$

The exponent $\tilde{\omega}_k = \omega_k - ck$ is n-times differentiable and is upper bounded in modulus by a polynomial of degree $m \geq 1$. Lemma 3 therefore allows us to bound the commutator by a term $\mathcal{O}(d^{-n})$.

Note that for a linear dispersion, $\omega_k = c|k|$, we can rewrite this integral as a function of the distance between world lines from Eq. (C.16), $d = (\bar{x}-\bar{y}) - c(t-t')$. Introducing $k_\pm = (\bar{k} \pm \bar{p})/2$ and using our Gaussian wave packets (4.3), we obtain

$$|I| = \exp\left[-\frac{k_-^2}{\sigma^2} - \frac{d^2\sigma^2}{4}\right]. \tag{C.25}$$

This bound is better than the one we have found but it is compatible with Lemma 3 and Theorem 4.

C.2.2 Full model causality

The causal relation (C.21) can be extended to the full model (1.1).

Theorem 5 *Let H be the light-matter Hamiltonian given by Eq.* (1.1). *We assume the conditions of Theorem 4: differentiable, polynomially bounded functions ω_k and g_k, with degrees $n \geq 2$. Then, all wave packets outside the light cone of the scatterer evolve approximately with the free Hamiltonian, H_0. More precisely, if $(\bar{x}, t_1)$ and $(\bar{x}, t_0)$ are two points outside the light cone*

$$\psi_{\bar{k}\bar{x}}(t_1) = U_0(t_1, t_0)^\dagger \psi_{\bar{k}\bar{x}}(t_0) U_0(t_1, t_0) + \mathcal{O}\left(\frac{1}{|d_{\min}|^{n-1}}\right), \tag{C.26}$$

where $d_{\min} = \min\{d(\bar{x}, t_1), d(\bar{x}, t_0)\} \gg 0$ and

$$U_0(t, t_0) = \exp(-i(t-t_0)H_0) \tag{C.27}$$

is the free-evolution operator for the photons at time t_0.

We start by building the Heisenberg equations for the operators

$$\partial_t a_k(t) = -i\omega_k a_k(t) - i g_k G(t). \tag{C.28}$$

Making the change of variables $a_k(t) = e^{-i\omega_k t} b_k(t)$, we have

$$\partial_t b_k(t) = -i g_k G(t) e^{i\omega_k t}, \tag{C.29}$$

so that the wave packet operators evolved from some initial time t_s are

$$\begin{aligned}
\psi_{\bar{k}\bar{x}}(t) &= \int e^{ik\bar{x}-i\omega_k t}\left[b_k(t_s) - i\int_{t_s}^{t} g_k G(\tau) e^{+i\omega_k \tau} d\tau\right]\varphi_{\bar{k}}(k)dk \qquad \text{(C.30)}\\
&= U_0(t,t_s)\psi_{\bar{k}\bar{x}}(t_s)U_0(t,t_s)^\dagger - i\int_{t_s}^{t}\left[\int e^{ik\bar{x}-ic(t-\tau)} g_k\varphi_{\bar{k}}(k)dk\right]G(\tau)d\tau\\
&= U_0(t,t_s)\psi_{\bar{k}\bar{x}}(t_s)U_0(t,t_s)^\dagger - i\int_{0}^{t-t_s}\left[\int e^{ik\bar{x}-ic\tau'} g_k\varphi_{\bar{k}}(k)dk\right]G(\tau)d\tau'.
\end{aligned}$$

The first part corresponds to free evolution, while the second part is an error term $\varepsilon(t)$, which can be bounded. We will assume without loss of generality $\|G\| = 1$, with $\|\cdot\|$ the Hilbert-Schmidt norm, and $|t_1| > |t_0|$. We have to choose the integration limits t and t_s so that $\text{sign}(\tau') = \text{sign(x)}$. If $x > 0$ then $t_1 > t_0 > 0$ and $(t, t_s) = (t_1, t_0)$ is a good choice. If $x < 0$ then $0 > t_0 > t_1$ and again $(t, t_s) = (t_1, t_0)$ is also a valid choice ($\tau' < 0$). This means we can introduce $\tau'' = \text{sign(x)}\tau' \geq 0$ and bound

$$\begin{aligned}
|\varepsilon(t_1)| &\leq \int_0^{|t_1-t_0|}\left|\int e^{i\,\mathrm{sign(\bar{x})kd_c(|\bar{x}|,\tau'')}} q(k)dk\right| d\tau''\\
&\leq \int_0^{|t_1-t_0|}\mathcal{O}\left(\frac{1}{d_c(|\bar{x}|,\tau'')^n}\right)d\tau''\\
&\leq \mathcal{O}\left(\frac{1}{c(n-1)}\frac{1}{(|\bar{x}|-c\tau)^{n-1}}\Bigg|_{\tau=0}^{\tau=|t_1-t_0|}\right)\\
&\leq \mathcal{O}\left(\frac{1}{d_c(|\bar{x}|,|t_1-t_0|)^{n-1}}\right).
\end{aligned} \tag{C.31}$$

Here we have taken into account that $d_c(|\bar{x}|,\tau'') \geq d_c(|\bar{x}|,|t_1-t_0|) > 0$ in the domain of integration. We can now use the fact that $d_c(|\bar{x}|,|t_1-t_0|) \geq d_c(|\bar{x}|,|t_1|) \geq \min\{d_c(\bar{x},t_1), d_c(\bar{x},t_0)\}$, obtaining the expression in the theorem.

C.2.3 Asymptotic Condition

One important limitation of Theorem 5 is that it is focused on the operators, not on the states themselves. This is a key point. For having a well defined scattering theory, the asymptotic condition must holds (see Sect 1.2 and Eq.

(1.10)). However, using Theorems 5 and 3 we have that, given a state $|\Psi\rangle \equiv \psi_{\bar{k},\bar{x}}(t_0)^\dagger|\Omega_\nu\rangle$, then

$$\begin{aligned} U(t_\pm)|\Psi\rangle &= U(t_\pm)\psi_{\bar{k},\bar{x}}(t_0)U(t_\pm)^\dagger|\Omega_\nu\rangle \\ &= U_0(t_\pm)\psi_{\bar{k},\bar{x}}(t_0)U_0(t_\pm)^\dagger|\Omega_\nu\rangle \equiv U_0(t_\pm)|\Psi_{\text{in}}\rangle \end{aligned} \tag{C.32}$$

The first equality is up to a global phase. In the second one, we have used Theorem 5. In the last equality, we can introduce input (output) states since the wave packets are well separated ($t_\pm \to \pm\infty$) from the scatterer and, by means of Theorem 3 and the conditions presented in 4.1.2 they are well defined free particle states.

This last result warrants that, under rather general conditions, the light-matter Hamiltonian (1.1) gives a physical scattering theory.

C.3 Scattering amplitude decomposition

Theorem 6 *Let us suppose the input state is*

$$|\Psi_{\text{in}}\rangle = \psi_{\text{in}}^\dagger\,|\Omega_\nu\rangle = \left(\prod_{n=1}^{N}\psi_{\bar{k}_n\bar{x}_n}^{\text{in}\,\dagger}\right)|\Omega_\nu\rangle, \tag{C.33}$$

with $|\bar{x}_n - \bar{x}_m| \to \infty\ \forall n \neq m$*. Thus, the scattering amplitude of going to*

$$|\Psi_{\text{out}}\rangle = \psi_{\text{out}}^\dagger\,|\Omega_\mu\rangle = \left(\prod_{n=1}^{N}\psi_{\bar{p}_m\bar{y}_m}^{\text{out}\,\dagger}\right)|\Omega_\mu\rangle, \tag{C.34}$$

with $|\bar{y}_n - \bar{y}_m| \to \infty\ \forall n \neq m$*, is reduced to a product of single-photon events:*

$$A = \sum_{\lambda_1,\dots,\lambda_{N-1}=0}^{M-1}\prod_{n=1}^{N}\langle\Omega_{\lambda_{n-1}}|\,\psi_{\bar{p}_n\bar{y}_n}^{\text{out}}(t_+)\psi_{\bar{k}_n\bar{x}_n}^{\text{in}}(t_-)^\dagger\,|\Omega_{\lambda_n}\rangle\,, \tag{C.35}$$

being $\lambda_0 = \mu$ *and* $\lambda_N = \nu$*, with the wave packet operators given in the Heisenberg picture for* $t = t_\pm \to \pm\infty$*.*

The proof is based directly on causality. Therefore, we find convenient to discuss it here.

The proof is done for the two-photon scattering. The generalization for N photons is straightforward. The scattering operator S is nothing but the evolution operator in the interaction picture, cf. Eq. (1.12). This permits us to write the scattering amplitudes as,

$$\begin{aligned} A = \langle\Psi_{\text{out}}|S|\Psi_{\text{in}}\rangle &= \langle\Omega_\nu|\psi_{\text{out}}U_I(t_+,t_-)\psi_{\text{in}}^\dagger|\Omega_\mu\rangle \\ &= \langle\Omega_\nu|\psi_{\text{out}}(t_+)\psi_{\text{in}}(t_-)^\dagger|\Omega_\mu\rangle, \end{aligned} \tag{C.36}$$

In the second equality we have dropped an irrelevant global phase. Here, $\psi^\dagger_{\text{in}}$ and $\psi^\dagger_{\text{out}}$ are operators creating wave packets localized far away from the scatterer. Because of Theorem 3, they are well defined N-photon wave packets.

Using Eqs. (C.33) and (C.34) the amplitude is given by

$$A = \langle \Omega_\mu | \prod_{m=1}^{2} \psi^{\text{out}}_{\bar{p}_m \bar{y}_m}(t_+) \prod_{n=1}^{2} \psi^{\text{in}}_{\bar{k}_n \bar{x}_n}(t_-)^\dagger \, |\Omega_\nu\rangle \, . \tag{C.37}$$

As $|\bar{x}_1 - \bar{x}_2|$ can be arbitrarily large, we can always choose a time t_1 such that $\psi^{\text{out}}_{\bar{p}_1\bar{y}_1}(t)^\dagger \, |\Omega_\mu\rangle$ is well separated from the scatterer for $t > t_1$, so $\psi^{\text{out}}_{\bar{p}_1\bar{y}_1}(t) \cong U_0(t,t_1)^\dagger \psi^{\text{out}}_{\bar{p}_1\bar{y}_1}(t_1) U_0(t,t_1)$. Besides, t_1 is such that the second wave packet is still far away from the scatterer. Therefore $\psi^{\text{in}}_{\bar{k}_2\bar{x}_2}(t') \cong U_0(t',t_1)^\dagger \psi^{\text{in}}_{\bar{k}_2\bar{x}_2}(t) U_0(t',t_1)$, for $t' < t_1$. Using Theorem 4, $[\psi^{\text{out}}_{\bar{p}_1\bar{y}_1}(t_+), \psi^{\text{in}}_{\bar{k}_2\bar{y}_2}(t_-)^\dagger] \to 0$ and Eq. (C.37), the amplitude equals to

$$A = \langle \Omega_\mu | \, \psi^{\text{out}}_{\bar{p}_2\bar{y}_2}(t_+) \psi^{\text{in}}_{\bar{k}_2\bar{y}_2}(t_-)^\dagger \, \psi^{\text{out}}_{\bar{p}_1\bar{x}_1}(t_+) \psi^{\text{in}}_{\bar{k}_1\bar{x}_1}(t_-)^\dagger \, |\Omega_\nu\rangle \, . \tag{C.38}$$

Finally, we insert the identity between the operators $\psi^{\text{in}}_{\bar{k}_2\bar{x}_2}(t_-)^\dagger$ and $\psi^{\text{out}}_{\bar{p}_1\bar{y}_1}(t_+)$. Assuming that there is not particle creation, just the ground states $\{|\Omega_\lambda\rangle\}_{\lambda=0}^{M-1}$ will contribute to the identity, $\sum_{\lambda=0}^{M-1} |\Omega_\lambda\rangle \langle \Omega_\lambda|$, and we arrive to (C.35).

This comes because $\psi^{\text{in}}_{\bar{k}_2\bar{x}_2}(t_-)^\dagger$ and $\psi^{\text{out}}_{\bar{p}_1\bar{y}_1}(t_+)$ asymptotically commute but not $\psi^{\text{in}}_{\bar{k}_1\bar{x}_1}(t_-)^\dagger$ and $\psi^{\text{out}}_{\bar{p}_2\bar{y}_2}(t_+)$. This is a clear signature of causality, saying which one is arriving first. Lastly, notice that if the ground state is unique, $|\Omega_{\lambda_n}\rangle = |\Omega_0\rangle$, this ordering is not important as the amplitude is simply the product of single-photon scattering amplitudes.

C.4 Scattering amplitude from Eq. (4.17)

In this appendix, we prove that (4.17) is consistent with the amplitude factorization from Theorem 6, Eq. (C.35). We do it in the two-photon subspace.

Before, we need the one-photon amplitude as an intermediate result.

C.4.1 One photon

We first need to compute the one photon amplitude. Let the one-photon input state be,

$$|\Psi^1_{\text{in}}\rangle = \psi^{\text{in}\,\dagger}_{\bar{k}_1,\bar{x}_1} |\Omega_\nu\rangle, \tag{C.39}$$

with the creation operator $\psi^{\text{in}\,\dagger}_{\bar{k}_1,\bar{x}_1}$ given by Eq. (4.2), removing the time dependence. For simplicity, we absorb the factor $e^{ik\bar{x}_1}$ into the wave packet:

$\phi_{\bar{k}_1,\bar{x}_1}(k) = e^{ik\bar{x}_1}\phi_{\bar{k}_1}(k)$. In position space, the output state will read

$$|\Psi^1_{\text{out}}\rangle = S|\Psi^1_{\text{in}}\rangle = \sum_{\mu=1}^{M}\int dydx\ (S_{yx})_{\mu\nu}\varphi_{\bar{k}_1,\bar{x}_1}(x)|y,\Omega_\mu\rangle. \tag{C.40}$$

Defining

$$\phi_{1,\mu\nu}(y) = \int dx\ (S_{yx})_{\mu\nu}\varphi_{\bar{k}_1,\bar{x}_1}(x) \tag{C.41}$$

and

$$|\xi^1_{\text{out}}\rangle_{1,\mu\nu} = \int dy\ \varphi_{1,\mu\nu}(y)|y;\Omega_\mu\rangle, \tag{C.42}$$

being $|y;\Omega_\mu\rangle = a^\dagger_y\,|\Omega_\mu\rangle$ the state with a photon at y and the scatterer in the ground state $|\Omega_\mu\rangle$, the output state (C.40) can be rewritten as

$$|\Psi^1_{\text{out}}\rangle = \sum_{\mu=1}^{M}|\xi^1_{\text{out}}\rangle_{1,\mu\nu}. \tag{C.43}$$

The probability amplitude will read

$$A_{1,\nu\to\mu} = \langle\Omega_\mu|\psi^{\text{out}}_{\bar{p}_1,\bar{y}_1}\ S\ \psi^{\text{in}\,\dagger}_{\bar{k}_1,\bar{x}_1}|\Omega_\nu\rangle = \int dy\ \varphi_{\bar{p}_1,\bar{y}_1}(y)^*\varphi_{1,\mu\nu}(y). \tag{C.44}$$

If the wave packets are monochromatic with momenta k_1 and p_1, respectively, this amplitude is

$$A_{1,\nu\to\mu} = (S_{p_1k_1})_{\mu\nu}. \tag{C.45}$$

C.4.2 Two photons

The two-photon wave packet, as sketched in Fig. 4.1, is

$$|\Psi^2_{\text{in}}\rangle = \psi^{\text{in}\,\dagger}_{\bar{k}_1,\bar{x}_1}\psi^{\text{in}\,\dagger}_{\bar{k}_2,\bar{x}_2}\,|\Omega_\nu\rangle\,. \tag{C.46}$$

By definition, the output state is

$$|\Psi^2_{\text{out}}\rangle = S|\Psi^2_{\text{in}}\rangle. \tag{C.47}$$

Here, we are interested in he limit of well separated incident photons. Thus, only the linear part of the scattering matrix S^0 is considered. We introduce the identity operator

$$|\Psi^2_{\text{out}}\rangle = \mathbb{I}S\mathbb{I}|\Psi^2_{\text{in}}\rangle, \tag{C.48}$$

with

$$\mathbb{I} = \frac{1}{2}\sum_{\mu=1}^{M}\int dx_1dx_2\ |x_1x_2;\Omega_\nu\rangle\langle x_1x_2;\Omega_\nu|, \tag{C.49}$$

being $|x_1 x_2; \Omega_\nu\rangle = a^\dagger_{x_1} a^\dagger_{x_2} |\Omega_\mu\rangle$ the symmetrized state with two photons at x_1 at x_2 and the scatterer at $|\Omega_\nu\rangle$.

Introducing (C.49) in (C.48) and considering (C.46) and (4.17) we get

$$\begin{aligned}|\Psi^2_{\text{out}}\rangle =& \frac{1}{4} \int dy_1 dy_2 dx_1 dx_2 \sum_{\mu,\lambda=1}^{M} \sum_{n,m=1}^{2} (S_{y_n x_m})_{\mu\lambda} (S_{y_{n'} x_{m'}})_{\lambda\nu} \theta(y_{n'} - y_n) \\ & (\varphi_{\bar{k}_1,\bar{x}_1}(x_1) \varphi_{\bar{k}_2,\bar{x}_2}(x_2) + \varphi_{\bar{k}_1,\bar{x}_1}(x_2) \varphi_{\bar{k}_2,\bar{x}_2}(x_1)) |y_1 y_2; \Omega_\mu\rangle. \qquad \text{(C.50)}\end{aligned}$$

with $n' \neq n$ and $m' \neq m$. Now, we have to compute integrals as

$$C = \int dx_1 dx_2 \sum_{n,m} (S_{y_n x_m})_{\mu\lambda} (S_{y_{n'} x_{m'}})_{\lambda\nu} \varphi_{\bar{k}_i,\bar{x}_i}(x_1) \varphi_{\bar{k}_j,\bar{x}_j}(x_2) \theta(y_{n'} - y_n). \qquad \text{(C.51)}$$

Using Eq. (C.41)

$$C = \sum_{n=1}^{2} (\varphi_{i,\mu\lambda}(y_n) \varphi_{j,\lambda\nu}(y_{n'}) + \varphi_{j,\mu\lambda}(y_n) \varphi_{i,\lambda\nu}(y_{n'})) \theta(y_{n'} - y_n). \qquad \text{(C.52)}$$

Following the sketch drawn in Fig. 4.1, if $x_m < x_{m'}$, then $\varphi_1(x_m)\varphi_2(x_{m'})$ is zero, so $\varphi_{1,\mu\nu}(y_n)\varphi_{2,\mu\nu}(y_{n'})$ is zero if $y_n < y_{n'}$. Therefore, choosing $i = 1$ and $j = 2$, the integral C reads

$$C = \sum_{n=1}^{2} \varphi_{2,\mu\lambda}(y_n) \varphi_{1,\lambda\nu}(y_{n'}). \qquad \text{(C.53)}$$

One can easily show that the same expression holds if we take $i = 2$ and $j = 1$. The output state, Eq. (C.50), then reads

$$\begin{aligned}|\Psi^2_{\text{out}}\rangle = \frac{1}{2} \int dy_1 dy_2 \sum_{\mu,\lambda=1}^{M} & (\varphi_{2,\mu\lambda}(y_1) \varphi_{1,\lambda\nu}(y_2) \\ & + \varphi_{2,\mu\lambda}(y_2) \varphi_{1,\lambda\nu}(y_1)) |y_1 y_2; \Omega_\mu\rangle. \qquad \text{(C.54)}\end{aligned}$$

Finally, the probability amplitude of going to the output state $\psi^{\text{out}\,\dagger}_{\bar{p}_1,\bar{y}_1} \psi^{\text{out}\,\dagger}_{\bar{p}_2,\bar{y}_2} |\Omega_\mu\rangle$ will be the overlap between this state and (C.54). Using (C.44)

$$A_{\text{in}\to\text{out}} = \langle\Omega_\mu| \psi^{\text{out}}_{\bar{p}_1,\bar{y}_1} \psi^{\text{out}}_{\bar{p}_2,\bar{y}_2} S \psi^{\text{in}\,\dagger}_{\bar{k}_1,\bar{x}_1} \psi^{\text{out}\,\dagger}_{\bar{k}_2,\bar{x}_2} |\Omega_\nu\rangle = \sum_{\lambda=0}^{M-1} A_{1,\nu\to\lambda} A_{2,\lambda\to\mu}, \qquad \text{(C.55)}$$

as expected. In the calculations, we have set $\langle\Omega_\mu| \psi^{\text{out}}_{\bar{p}_i,\bar{y}_i}\ S\ \psi^{\text{in}\,\dagger}_{\bar{k}_j \bar{x}_j} |\Omega_\nu\rangle = 0$ for $i \neq j$, since we assume that both incident wave packets are far away.

A final comment is in order. Without the step functions in (4.17), the amplitude $A_{2,\nu\to\lambda} A_{1,\lambda\to\mu}$ would appear in the final probability amplitude. This term is unphysical, because the tag 1 stands for the first incoming photon and the transition $\lambda \to \mu$ is generated by the second wave packet; the same applies for the tag 2, corresponding to the second photon, and the transition $\nu \to \lambda$, which is the first one happening.

C.5 S^0 in momentum space

Here, we show S^0 in momentum space follows Eq. (4.22). After that, we prove the Dirac-delta structure is recovered if the ground state is unique.

Let us write $(S^0_{p_1p_2k_1k_2})_{\mu\nu}$ as the Fourier transform of $(S^0_{y_1y_2x_1x_2})_{\mu\nu}$

$$(S^0_{p_1p_2k_1k_2})_{\mu\nu} = \frac{1}{(2\pi)^2}\int dy_1dy_2dx_1dx_2\ (S^0_{y_1y_2x_1x_2})_{\mu\nu} \\ \times e^{-i(p_1y_1+p_2y_2)}e^{i(k_1x_1+k_2x_2)}. \quad \text{(C.56)}$$

Due to the form of $(S^0_{y_1y_2x_1x_2})_{\mu\nu}$, (4.17), we have to compute integrals such as

$$I = \int dx\ e^{ikx}(S_{yx})_{\mu\nu}. \quad \text{(C.57)}$$

Notice that $(S_{yx})_{\mu\nu}$ is the Fourier transform of $(S_{pk})_{\mu\nu}$, Eq. (4.21). Therefore,

$$I = e^{i(k+E_\nu-E_\mu)y}t_{\mu\nu}(k). \quad \text{(C.58)}$$

Considering this in (C.56), we get

$$(S^0_{p_1p_2k_1k_2})_{\mu\nu} = \frac{1}{(2\pi)^2}\int dy_1dy_2\ e^{-i(p_1y_1+p_2y_2)} \\ \sum_{n,m=1}^{2}\sum_{\lambda=0}^{M-1} e^{i(k_ny_1+k_{n'}y_2)}e^{i[(E_\lambda-E_\mu)y_m+(E_\nu-E_\lambda)y_{m'}]} \\ \times t_{\mu\lambda}(k_n)t_{\lambda\nu}(k_{n'})\theta(y_{m'}-y_m), \quad \text{(C.59)}$$

with $n' \neq n$ and $m' \neq m$. The Fourier transform of the step function is

$$\frac{1}{\sqrt{2\pi}}\int dy\ e^{-iqy}\theta(\mp(y-y_0)) = \pm\frac{i}{\sqrt{2\pi}}\frac{e^{-iqy_0}}{q\pm i0^+}. \quad \text{(C.60)}$$

Therefore, integrating Eq. (C.59) first in y_1 and later in y_2, we get

$$(S^0_{p_1p_2k_1k_2})_{\mu\nu} = \frac{i}{2\pi}\sum_{n,m=1}^{2}\sum_{\lambda=0}^{M-1}\frac{t_{\mu\lambda}(k_n)t_{\lambda\nu}(k_{n'})}{p_m+E_\mu-k_n-E_\lambda+i0^+} \\ \times \delta(p_1+p_2+E_\mu-k_1-k_2-E_\nu), \quad \text{(C.61)}$$

which is the expression given in the main text, Eq. (4.22). This result has been recently reported for a Λ atom by Xu and Fan in [175]. Here, we show this is valid for any scatterer, provided the condition for S^0 (Eq. (4.17)) is fulfilled.

Lastly, we prove that Eq. (4.22) is formed by two Dirac-delta functions if $M = 1$. To do so, we use the following identity

$$\frac{1}{k + i0^+} = -i\pi\delta(k) + \mathcal{P}\left(\frac{1}{k}\right), \tag{C.62}$$

with $\mathcal{P}$ the principal value. Applying this identity to Eq. (4.22) we get,

$$(S^0_{p_1p_2k_1k_2})_{\mu\nu} = \frac{i}{2\pi}\sum_{n,m=1}^{2} t(k_n)t(k_{n'})\left(-i\pi\delta(p_m - k_n) + \mathcal{P}\left(\frac{1}{p_m - k_n}\right)\right) \\ \times \delta(p_1 + p_2 - k_1 - k_2). \tag{C.63}$$

Now, we sum over n and m

$$\begin{aligned}(S^0_{p_1p_2k_1k_2})_{\mu\nu} = &\frac{1}{2}t(k_1)t(k_2)\delta(p_1 + p_2 - k_1 - k_2) \\ &\times \big(\delta(p_1 - k_1) + \delta(p_1 - k_2) + \delta(p_2 - k_1) + \delta(p_2 - k_2) \\ &+ \mathcal{P}\left(\frac{1}{p_1 - k_1}\right) + \mathcal{P}\left(\frac{1}{p_1 - k_2}\right) + \mathcal{P}\left(\frac{1}{p_2 - k_1}\right) + \mathcal{P}\left(\frac{1}{p_2 - k_2}\right)\big).\end{aligned} \tag{C.64}$$

Applying the constraint imposed by the global Dirac delta to p_2 to the second row, it is straightforward to see that they cancel each other, arriving to

$$\begin{aligned}(S^0_{p_1p_2k_1k_2})_{\mu\nu} = t(k_1)t(k_2)(&\delta(p_1 - k_1)\delta(p_2 - k_2) \\ &+ \delta(p_1 - k_2)\delta(p_2 - k_1)),\end{aligned} \tag{C.65}$$

which is the usual expression in QFT for the cluster decomposition, which also holds in waveguide QED if the ground state is unique.

C.6 Fluorescence decay

In this appendix, we calculate how the correlations and thus the fluorescence decay as the distance l between the packets grows (See Figs. 4.1 and 4.2).

The input state (C.33) in momentum space is given by,

$$|\Psi_{\text{in}}\rangle = \int dk_1 dk_2\, \varphi^{\text{in}}(k_1, k_2) a^\dagger_{k_1} a^\dagger_{k_2} |\Omega_\nu\rangle, \tag{C.66}$$

with

$$\varphi^{\text{in}}(k_1, k_2) = \varphi_{\bar{k}_1}(k_1) e^{ik_2 l} \varphi_{\bar{k}_2}(k_2). \tag{C.67}$$

In these expressions, the wave packets $\phi_{\bar{k}_n}(k)$ are Lorentzian functions (see Eq. (4.4)). The out state is computed by means of Eq. (1.11)

$$|\Psi_{\text{out}}\rangle = S|\Psi_{\text{in}}\rangle = \mathbb{I}S\mathbb{I}|\Psi_{\text{in}}\rangle. \tag{C.68}$$

With $\mathbb{I}$ being the identity operator in the two-photon sector

$$\mathbb{I} = 1/2 \int dp_1 dp_2 \sum_{\mu} a^{\dagger}_{p_1} a^{\dagger}_{p_2} \left|\Omega_\mu\right\rangle \left\langle\Omega_\mu\right| a_{p_1} a_{p_2}. \tag{C.69}$$

The scattering matrix S in momentum space is $(S_{p_1p_2k_1k_2})_{\mu\nu} = (S^0_{p_1p_2k_1k_2})_{\mu\nu} + i(T_{p_1p_2k_1k_2})_{\mu\nu}$, with $(S^0_{p_1p_2k_1k_2})_{\mu\nu}$ given by Eq. (4.22) and $(T_{p_1p_2k_1k_2})_{\mu\nu} = (C_{p_1p_2k_1k_2})_{\mu\nu}\delta(p_1+p_2+E_\mu-k_1-k_2-E_\nu)$ yielding

$$\left|\Psi_{\text{out}}\right\rangle = \int dp_1 dp_2 \sum_{\mu} \varphi^{\text{out}}_{\mu}(p_1,p_2) a^{\dagger}_{p_1} a^{\dagger}_{p_2} \left|\Omega_\mu\right\rangle, \tag{C.70}$$

with

$$\begin{aligned}
&\varphi^{\text{out}}_{\mu}(p_1,p_2) \propto \\
&\sum_{n=1}^{2}\sum_{m=1}^{2}\int dk_n \left(\frac{i}{2\pi}\sum_{\lambda}\frac{t_{\mu\lambda}(k_n)t_{\lambda\nu}(p_1+p_2+E_\mu-k_n-E_\nu)}{p_m+E_\mu-k_n-E_\lambda+i0^+} + i(\tilde{C}_{p_1p_2k_n})_{\mu\nu}\right) \\
&\Big(\varphi_{\bar{k}_1}(k_n)e^{i(p_1+p_2+E_\mu-k_n-E_\nu)l}\varphi_{\bar{k}_2}(p_1+p_2+E_\mu-k_n-E_\nu) \\
&\quad + \varphi_{\bar{k}_1}(p_1+p_2+E_\mu-k_n-E_\nu)e^{ik_nl}\varphi_{\bar{k}_2}(k_n)\Big).
\end{aligned} \tag{C.71}$$

Which is nothing but Eq. (4.25) that we have rewritten here for the discussion. As said in Sect. 4.1.6, we assume that $t_{\mu\nu}(k)$ and $(C_{p_1p_2k_nk_{\bar{n}}})_{\mu\nu}$ have simple poles with imaginary parts $\{\gamma^t_n\}$ and $\{\gamma^C_n\}$ respectively. Then, this integral is solved by taking complex contours and applying the residue theorem. In order to integrate the term proportional to $e^{i(p_1+p_2+E_\mu-k_n-E_\lambda)l}$, we take the contour shown in Fig. C.1(a) so that the exponential factor does not diverge. For the same reason, for the term proportional to e^{ik_nl} we take the contour of Fig. C.1(b). As t and C have first-order poles, when integrating each pole, we just have to evaluate the rest of the function at the pole. Then, t and C give terms proportional to $e^{-|\gamma^t_n|l}$ and $e^{-|\gamma^C_n|l}$, respectively.

Now we consider the contribution to the integral of the wave packets, $\varphi_{\bar{k}_n}(k)$. We choose Lorentzian functions, with a simple pole at $k = \bar{k}_n - i\sigma_k$ (see Eq. (4.4)). In consequence, we have a term proportional to $e^{-\sigma_k l}$. Lastly, the denominator in the first term has a pole with zero imaginary part. Therefore, its contribution does not decay with l. Importantly enough, this pole enforces single-photon energy conservation giving single-photon amplitudes, $\sum_\lambda A_{1,\nu\to\lambda}A_{2,\lambda\to\mu}$.

Finally, let us mention that we do not need to impose that that $t_{\mu\nu}(k)$ and $(C_{p_1p_2k_nk_{\bar{n}}})_{\mu\nu}$ have simple poles. Higher order poles, by virtue of the Cauchy Integral formula for the derivatives, also would yield an exponential decay.

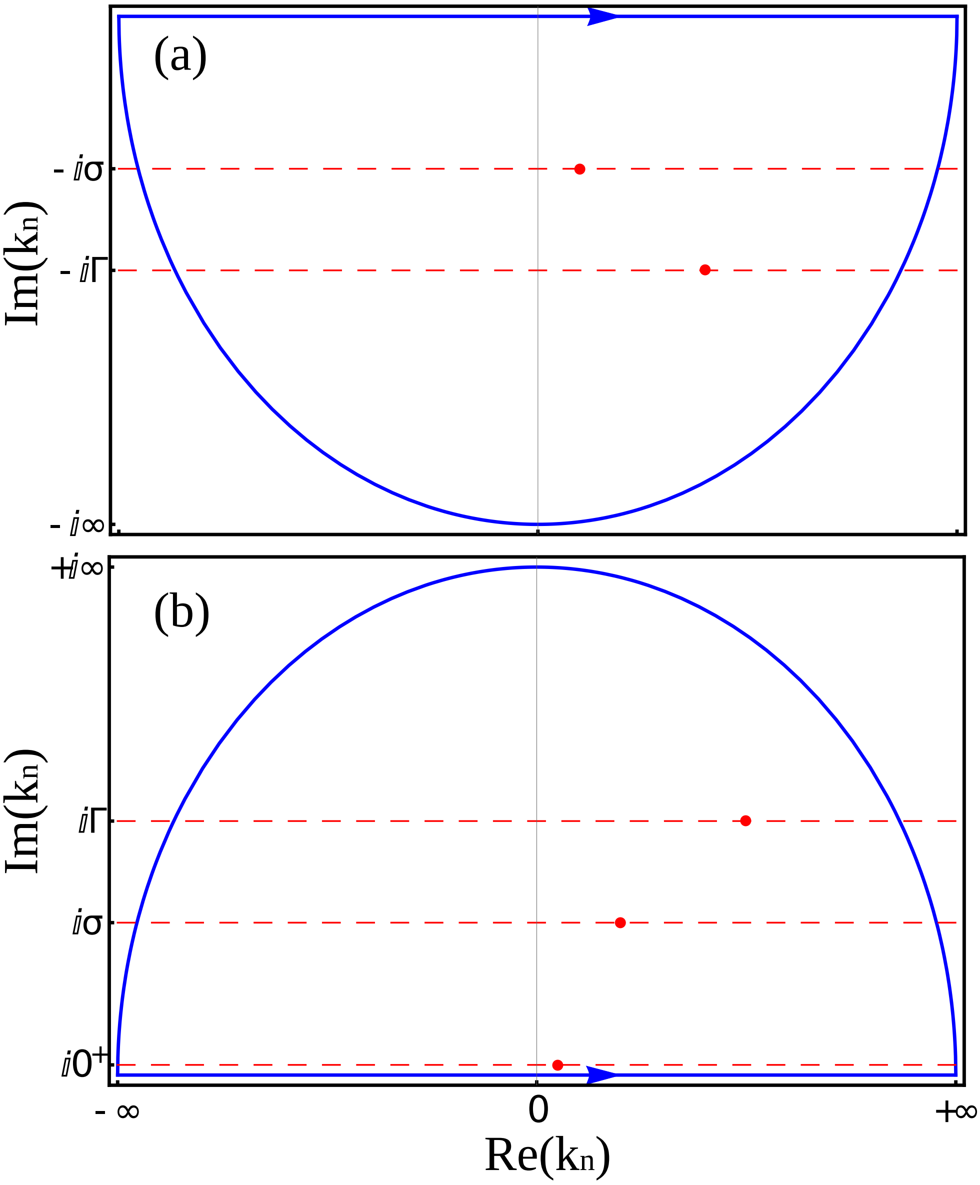

Figure C.1: (a) Lower and (b) upper contour for integrating Eq. (4.25). We show the poles coming from the Lorentzian, $\pm i\sigma_k$, those coming from one of the transmission amplitudes or from C, $\pm i\Gamma$, and those with vanishing imaginary part. The real parts are arbitrary.

Appendix D

Theorems on the linearity of the scattering matrix

In this appendix, we prove Theorems 1 and 2 of Sect. 4.2.

D.1 Proof of Theorem 1

If the scatterers are harmonic oscillators, the Hamiltonian (1.1) is linear and it can be diagonalized with a Bogolioubov-Valatin (BV) transformation,

$$H = \sum \Lambda_l \alpha_l^\dagger \alpha_l \,, \tag{D.1}$$

with $[\alpha_l, \alpha_m^\dagger] = \delta_{lm}$ and $\Lambda_l > 0 \; \forall l$. The ground state is $\alpha_l |\phi_0\rangle = 0 \; \forall l$. The BV transformation

$$\alpha_l = \sum_{i=-L}^{L} (\chi_{li}^a a_i + \eta_{li}^a a_i^\dagger) + \sum_{i=1}^{M} (\chi_{li}^c c_i + \eta_{li}^c c_i^\dagger). \tag{D.2}$$

is invertible.

Hamiltonian (D.1) commutes with $N_\alpha = \sum \alpha_l^\dagger \alpha_l$:

$$[H, N_\alpha] = 0 \,. \tag{D.3}$$

The number of α-excitations, N_α, is a good quantum number. It also conserves parity, $\mathcal{P} = \mathrm{e}^{i\pi \sum \alpha_l^\dagger \alpha_l}$:

$$[H, \mathcal{P}] = 0 \,. \tag{D.4}$$

One-photon input states, $N = 1$ in (4.41), are written in momentum space

$$|\Psi_{in}\rangle = \sum_{k>0} \tilde{\phi}_k^{\mathrm{in}} a_k^\dagger |\phi_0\rangle, \tag{D.5}$$

with $\tilde{\phi}_k^{\text{in}}$ the Fourier transform of ϕ_x^{in}. Using the transformation (D.2) and that $\alpha_l|\phi_0\rangle = 0$, we can rewrite the state (D.5) in the α-representation

$$|\Psi_{\text{in}}\rangle = \sum_l \bar{\phi}_l^{\text{in}} \alpha_l^\dagger |GS\rangle. \tag{D.6}$$

Given the input state (D.6): $N_\alpha|\Psi_{\text{in}}\rangle = |\Psi_{\text{in}}\rangle$. Since N_α is a conserved quantity [Cf. Eq. (D.3)] the time evolution is restricted to the *one α-excitation level* (D.3). The output state is then

$$|\Psi_{\text{out}}\rangle = \sum_l \bar{\phi}_l^{\text{out}} \alpha_l^\dagger |\phi_0\rangle, \tag{D.7}$$

with $\bar{\phi}_l^{\text{out}} \equiv e^{-i\Lambda_l t_{\text{out}}} \bar{\phi}_l^{\text{in}}$. Using the transformation (D.2), the output state is rewritten

$$|\Psi_{out}\rangle = \sum_l \bar{\phi}_l^{out} \left(\sum_k ((\tilde{\chi}_{lk}^a)^* a_k^\dagger + (\tilde{\eta}_{lk}^a)^* a_k) + \sum_i ((\chi_{li}^c)^* c_i^\dagger + (\eta_{li}^c)^* c_i) \right) |\phi_0\rangle, \tag{D.8}$$

with $\tilde{\chi}_{lk}^a$ and $\tilde{\eta}_{lk}^a$ the discrete Fourier transforms of χ_{li}^a and η_{li}^a in the second index. The output state (D.8) removes the possibility of having multiphoton scattering states. Therefore, the scattering events can be elastic, with transmission and reflection amplitudes t_k and r_k and inelastic, with the scatterer relaxing to an excited state $|\phi_n\rangle$. In the latter case, the photon emerges with a new momentum k_{new}, fulfilling energy conservation

$$\omega_{k_{\text{in}}} + E_0 = \omega_{k_{\text{new}}} + E_n \tag{D.9}$$

Therefore, the output state can be rewritten

$$|\Psi_{\text{out}}\rangle = \sum_{k>0} \tilde{\phi}_k^{\text{in}} (t_k a_k^\dagger + r_k a_{-k}^\dagger)|\phi_0\rangle + \sum_k \tilde{\phi}_k^{\text{new}} a_k^\dagger |\phi_n\rangle, \tag{D.10}$$

with $\tilde{\phi}_k^{\text{new}}$ a wave packet centered around k_{new}.

Let us fix our attention to the second term in the r.h.s of (D.10), which is rewritten in terms of the α-operators with the help of the BV transformation (D.2):

$$\sum_k \tilde{\phi}_k^{\text{new}} a_k^\dagger |\phi_n\rangle = \sum_l (\bar{\phi}_l^{\text{new},p} \alpha_l^\dagger + \bar{\phi}_l^{\text{new},m} \alpha_l)|\phi_n\rangle \tag{D.11}$$

Using N_α and P conservation, Eqs. (D.3)) and (D.4), $N_\alpha|\phi_n\rangle = 2n|\phi_n\rangle$ with $n \geq 1$. The first term in the r.h.s. of (D.11) has $2n+1 \geq 3$ particles. Thus, $\bar{\phi}_l^{\text{new},p} = 0$. Finally $\alpha_l|\phi_n\rangle$ is an eigenstate of (D.1) with eigen-energy $E_n - \Lambda_l$ ($\Lambda_l > 0$). The latter must equal to $\omega_{k_{\text{new}}} + E_n$ which is impossible. Therefore $\bar{\phi}_l^{\text{new},m} = 0$.

Putting all this together, the output state contains only the elastic channel,

$$|\Psi_{\rm out}\rangle = \sum_{k>0} \tilde{\phi}_k^{\rm in}(t_k a_k^\dagger + r_k a_{-k}^\dagger)|\phi_0\rangle. \tag{D.12}$$

This ends the proof.

D.2 Proof or Theorem 2

The components of the N-photon scattering matrix can be rewritten as,

$$S_{p_1 \ldots p_{N'}\,,k_1 \ldots k_N} = \langle \phi_0 | a_{p_1} \ldots a_{p_{N'}}\, a_{k_1}^\dagger(t_{\rm out}) \ldots a_{k_N}^\dagger(t_{\rm out}) | \phi_0 \rangle \tag{D.13}$$

with,

$$a_k^\dagger(t_{\rm out}) = S^\dagger a_k^\dagger S = (t_k a_k^\dagger + r_k a_{-k}^\dagger)\,. \tag{D.14}$$

In the last equality we have used *i)* linearity: the Heisenberg evolution for the operators $a_{k_n}(t)$ is independent of the input states and *ii)* Theorem 1 of Sect. 4.2.

From Eq. (D.14) and Wick's theorem:

$$\langle \phi_0 | a_{p_1} \ldots a_{p_{N'}}\, a_{k_1}^\dagger \ldots a_{k_N}^\dagger | \phi_0 \rangle = \delta_{NN'} \sum_{m_1 \neq m_2 \neq \ldots \neq m_N} \delta_{p_1\, k_{m_1}} \ldots \delta_{p_N\, k_{m_N}}\,, \tag{D.15}$$

which completes the proof.

Appendix E

Blueshift in the ultrastrong coupling regime

In this appendix we show that it is possible to describe analytically the frequency shift in the ultrastrong coupling, reminiscent of the Bloch-Siegert effect (see white line in Fig. 5.2(b)).We consider that the scatterer is the cavity-qubit system and we truncate its Hilbert space to the ground state and the couple of states which have just one particle in the low-coupling regime, that is, the polariton states, which under the RWA are

$$|\phi_1^{0/1}\rangle = (a_0^\dagger|0\rangle \pm \sigma^+|0\rangle)/\sqrt{2}. \tag{E.1}$$

A general state in this subspace is

$$|\Psi\rangle = \sum_{n\neq 0} c_n a_n^\dagger|\phi_0\rangle + f_0|\tilde{\phi}_1^0\rangle + f_1|\tilde{\phi}_1^1\rangle, \tag{E.2}$$

where $\{|\tilde{\phi}_1^i\rangle\}$ are the polariton states calculated beyond the RWA for a system comprising just one cavity plus one qubit. Taking the following ansatz we can find the scattering eigenstates

$$c_n = \begin{cases} e^{ikn} + r_k e^{-ikn} & n < 0 \\ t_k e^{ikn} & n > 0 \end{cases} \tag{E.3}$$

Solving the eigenvalue equation $H\,|\Psi\rangle = E\,|\Psi\rangle$, we show that the transmission amplitude is

$$t_k = \frac{2iG\sin k}{2e^{ik}G - 1}, \tag{E.4}$$

with

$$G = J\sum_{i=\pm} \frac{|\alpha_{i0}|^2}{\Delta_i - \omega_k}. \tag{E.5}$$

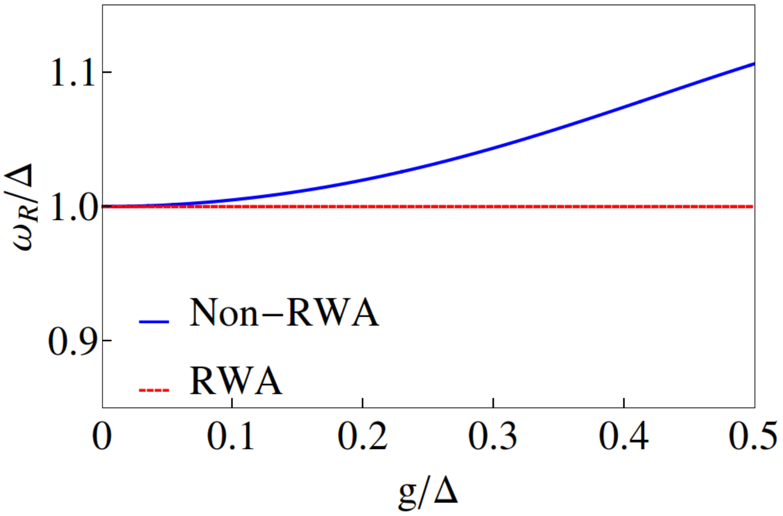

Figure E.1: **Resonant energy for perfect reflection.** ω_R shifts to larger values as g increases when computed beyond the RWA (blue, solid line), whereas it remains constant within the RWA (red, dashed line).

Here, Δ_i is the gap between $|\tilde{\phi}_1^i\rangle$ and $|\phi_0\rangle$ and $\alpha_{i0} = \langle\tilde{\phi}_1^i|a^\dagger|\phi_0\rangle$. By imposing $t_k = 0$, we find that the resonant energy for perfect reflection ω_R is

$$\omega_R = \frac{|\alpha_{+0}|^2\Delta_- + |\alpha_{-0}|^2\Delta_+}{|\alpha_{+0}|^2 + |\alpha_{-0}|^2}. \tag{E.6}$$

In the RWA, $\alpha_{\pm 0} = 1/\sqrt{2}$, and $\Delta_\pm = \Delta \pm g$, so $\omega_R = \Delta$.

However, counter rotating terms modify both the gaps and the matrix elements. Therefore, the resonant frequency shifts, as we plot in the figure E.1. As seen in the main part of the text, this result fits really well with the numerical result obtained with MPS (see the white curve in Fig.5.2(b)).

Appendix F

Losses in the one-photon scattering from a qubit in the ultrastrong

In order to estimate the influence of dissipation in the transmission processes discussed in the main text, we have considered the scattering of one photon by one qubit, when the qubit is connected to a second (upper) chain, with coupling strength g' (see the sketch of the considered geometry in Fig. F.1 (a)). This second chain acts as a lossy channel for the photons moving in the lower chain. In the weak coupling regime, this way of treating dissipation is equivalent to the usual treatment in quantum optics using master equations [5].

F.1 Hamiltonian

The Hamiltonian for the whole system is now:

$$\begin{aligned} H =&\epsilon \sum_n a_n^\dagger a_n - J \sum_n (a_n^\dagger a_{n+1} + H.c.) + \Delta \sigma^+ \sigma^- + g \sigma_x (a_0 + a_0^\dagger) \\ &+\epsilon \sum_n b_n^\dagger b_n - J \sum_n (b_n^\dagger b_{n+1} + H.c.) + g' \sigma_x (b_0 + b_0^\dagger), \end{aligned} \tag{F.1}$$

where $\{b_n\}$ is the set of bosonic annihilation operators related to the photons in the second chain of cavities.

This model can be related to the one-chain model that we consider in the text, by using the canonical bosonic transformation

$$\begin{pmatrix} \alpha_n \\ \beta_n \end{pmatrix} = \frac{1}{\sqrt{1+(g'/g)^2}} \begin{pmatrix} 1 & g'/g \\ g'/g & -1 \end{pmatrix} \begin{pmatrix} a_n \\ b_n \end{pmatrix}, \tag{F.2}$$

In terms of the new bosonic operators the Hamiltonian reads

$$\begin{aligned} H = {} & \epsilon \sum_n (\alpha_n^\dagger \alpha_n + \beta_n^\dagger \beta_n) - J \sum_n (\alpha_n^\dagger \alpha_{n+1} + \beta_n^\dagger \beta_{n+1} + H.c.) \\ & + \Delta \sigma^+ \sigma^- + \sqrt{g^2 + (g')^2} \sigma_x (\alpha_0 + \alpha_0^\dagger) \end{aligned} \tag{F.3}$$

So, the problem has been mapped into two independent chains: (i) a free chain (the one with the set of operators $\{\beta_n\}$), with no qubit present and (ii) a chain (that of the α_n's) interacting with one qubit, with a "renormalized" coupling $\hat{g} = \sqrt{g^2 + (g')^2}$. Finding the wave function in the first case is trivial, while the second problem is precisely the one that we consider in the main part of the text, so we can relate the case with dissipation to that without losses. Notice that the transformation is valid for any value of the coupling strengths g and g', so the mapping remains valid in the ultra-strong regime.

F.2 Scattering coefficients

In order to find the scattering coefficients, we express the initial wave function in terms of the new bosonic operators:

$$\begin{aligned} |\Psi_{\text{in}}\rangle &= \sum_x \varphi_x a_x^\dagger |\phi_0^+\rangle = \sum_{k>0} \tilde{\varphi}_k a_k^\dagger |\phi_0^+\rangle \\ &= \frac{1}{\sqrt{1+(g'/g)^2}} \sum_{k>0} \tilde{\varphi}_k (\alpha_k^\dagger + (g'/g)\beta_k^\dagger)|\phi_0^+\rangle, \end{aligned} \tag{F.4}$$

Where $\tilde{\varphi}_k$ is the Fourier transform of φ_x. The wave function after the scattering has occurred can be expressed in terms of the previously computed transmission and reflection coefficients, t_k and r_k, respectively:

$$\begin{aligned} |\Psi_{\text{out}}\rangle = {} & \frac{1}{\sqrt{1+(g'/g)^2}} \sum_{k>0} \tilde{\varphi}_k (t_k(\hat{g})\alpha_k^\dagger + r_k(\hat{g})\alpha_{-k}^\dagger + (g'/g)\beta_k^\dagger)|\phi_0^+\rangle \\ & + \frac{1}{\sqrt{1+(g'/g)^2}} \sum_k \tilde{\varphi}_k t_{2,k}(\hat{g}) \alpha_{k'}^\dagger |\phi_1^+\rangle \end{aligned} \tag{F.5}$$

Here $t_{2,k}$ is amplitude probability to leave the qubit in an excited state after the scattering, $|\text{exc}\rangle$ is the excited state involved in this Raman process and k' is the new photon momentum fulfilling energy conservation, $\omega_{k'} + \omega_1^+(\hat{g}) =$

$\omega_k + \omega_0^+(\hat{g})$. Transforming back to the original bosonic operators, defined in the real chains:

$$\begin{aligned}|\Psi_{\text{out}}\rangle =& \frac{1}{1+(g'/g)^2}\sum_{k>0}\tilde{\phi}_k((t_k(\hat{g})+(g'/g)^2)a_k^\dagger + r_k(\hat{g})a_{-k}^\dagger \\ &+ (g'/g)(t_k(\hat{g})-1)b_k^\dagger + (g'/g)r_k(\hat{g})b_{-k}^\dagger)|\phi_0^+\rangle \\ +& \frac{1}{1+(g'/g)^2}\sum_k \tilde{\phi}_k t_{2,k}(\hat{g})(a_{k'}^\dagger + (g'/g)b_{k'}^\dagger)|\phi_1^+\rangle \end{aligned} \tag{F.6}$$

So the scattering amplitudes in the model with losses (denoted by the superscript ^{l}) are:

$$t_k^l(g) = \frac{1}{1+(g'/g)^2}(t_k(\hat{g})+(g'/g)^2) \tag{F.7}$$

$$r_k^l(g) = \frac{1}{1+(g'/g)^2}\, r_k(\hat{g}) \tag{F.8}$$

$$t_{2,k}^l(g) = \frac{1}{1+(g'/g)^2}\, t_{2,k}(\hat{g}) \tag{F.9}$$

Fig. 5 shows the results of the calculations in two cases: $g = 0.12$, which is representative of a situation where counter-rotating terms are not playing an important role (panel b), and $g = 0.54$, as paradigmatic case of the ultra-strong regime (panel c). Panel (b) renders the elastic transmittance spectra for the case $g' = 0$, showing the null transmittance at resonance that appears when the qubit is lossless. The blue curve corresponds to $g' = g/2 = 0.06$, a value that has been chosen so that the transmission minimum is $\approx 6\%$, as in the experiments reported in [47], and the green one corresponds to $g' = 0.9g = 0.11$. The inset shows the fraction of energy that goes into the loss channel (the second waveguide). Panel (c) renders the transmittance for $g' = 0.06$, $g' = g/2 = 0.27$ and $g' = 0.9g = 0.48$, showing that the effect predicted in the main text is robust under dissipation. Even increasing the coupling into the loss channel to $g' = 0.9g$ preserves the main features found in the lossless case: a Fano resonance (with a minimum transmission that is not zero) and a high probability of Raman scattering (represented in the inset).

These results show that our predictions in the ultra-strong regime are expected to survive a moderate amount of dissipation, which can be even larger than that present in some actual realizations, as superconducting circuits.

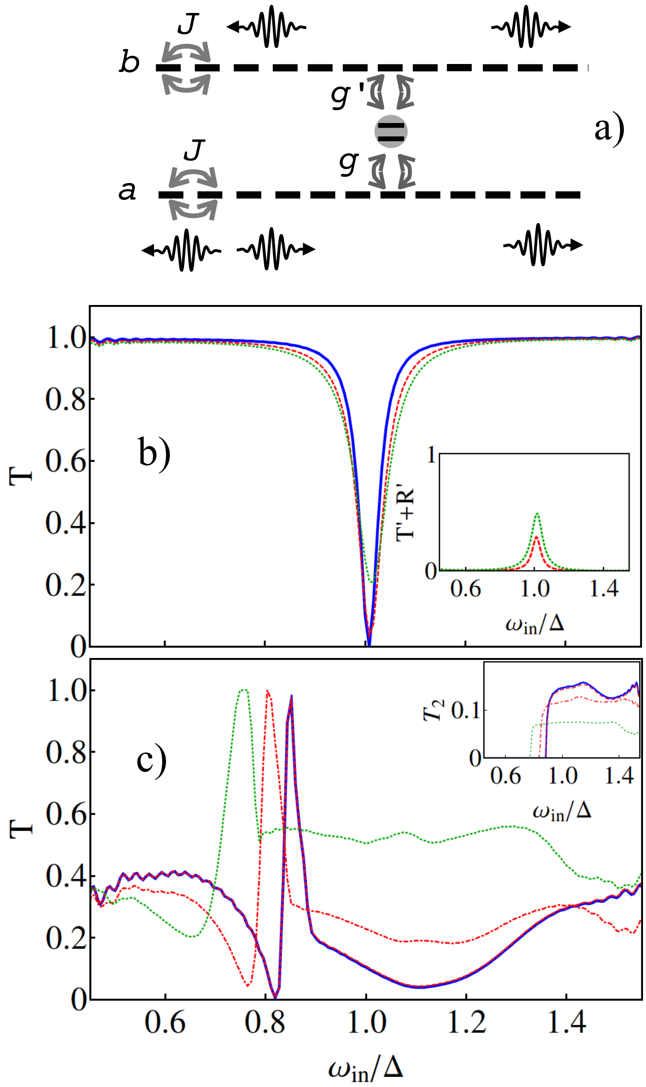

Figure F.1: Panel (a). Schematic representation of the geometry used for analyzing the effect of losses. Panel (b) Elastic transmittance spectrum for $g = 0.12$ and several values of g': $g' = 0$ (continuous blue line), $g' = 0.06$ (discontinuous red line) and $g' = 0.9\,g = 0.11$ (dotted green line). The inset shows the fraction of energy that goes into the upper waveguide. Panel (c) Elastic transmittance spectrum for $g = 0.54$ and g': $g' = 0$ (continuous blue line), $g' = 0.06$ (discontinuous red line), $g' = g/2 = 0.27$ (dot-dotted red line), and $g' = 0.9\,g = 0.48$ (dotted greed line). In this panel the inset shows the fraction of inelastically transmitted energy.

Appendix G

Cyclic-Three-Level System

G.1 Transmission calculation

We show here that the transmission amplitude for a single photon impinging into a C3LS is given by Eq. (5.20).

As explained in Sect. 5.2, we do it by means of the master-equation approach (see Sect. 2.2). In formula (2.80) we first need to compute the stationary solutions $\rho_{ij}(0)$ with constant perturbation (see the discussion below Eq. (2.80)). Since, we are assuming zero temperature, it is clear that, $\rho_{11} \sim \varrho_{22} \sim \mathcal{O}(\alpha)$ and $\varrho_{00} \sim 1 - \mathcal{O}(\alpha)$, where α is the amplitude of the coherent excitation. Taking this into, account, the solutions for the nondiagonal elements can be obtained by solving the following equations

$$\dot{\rho}_{10} = 0 = -i\Delta_{10}\rho_{10} - i\alpha G_{10} g(\omega) - \Big(\Gamma_{10} + \frac{1}{2}(\mathcal{D}_{11} - \mathcal{D}_{00})^2\Big)\varrho_{10} + \mathcal{O}(\alpha^2) \tag{G.1}$$

$$\dot{\varrho}_{20} = 0 = -i\Delta_{20}\rho_{20} - i\alpha G_{20} g(\omega) - \Big(\Gamma_{20} + \Gamma_{21} + \frac{1}{2}(\mathcal{D}_{22} - \mathcal{D}_{00})^2\Big)\rho_{20} + \mathcal{O}(\alpha^2). \tag{G.2}$$

Inserting the solutions in the general expression (2.80) together with the relation (2.73) yields Eq. (5.20) in the main text.

G.2 Effect of losses

Losses can be modeled as decays to other channels, which are characterized by input and output fields, named as b_{in} and b_{out}. Here, we take into account one additional channel (see Fig. G.1); if we consider more channels, we just have

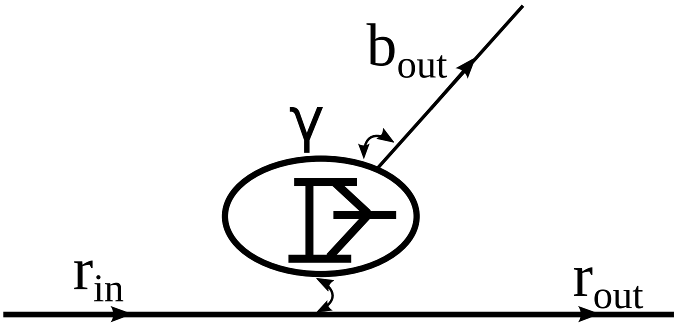

Figure G.1: Schematics for the modeling of nonradiative losses.

to add their contributions. Now the C3LS can decay into b modes, described by $H_b = \int dk\, \nu_k b_k^\dagger b_k$, interacting with the atom via

$$H_{\text{leakage}} = \sqrt{2\gamma}\, G \int dk\, (b_k^\dagger + b_k). \tag{G.3}$$

The input-output relations (2.73) must be generalized now to include this *extra* channel,

$$r_{\text{out}}(t) = r_{\text{in}}(t) - i\sqrt{2\pi} g(\omega) G(t) \tag{G.4}$$

$$b_{\text{out}}(t) = b_{\text{in}}(t) - i\sqrt{2\gamma} G(t)\,. \tag{G.5}$$

The quantity γ parametrizes a phenomenological loss rate. Besides, $b_{\text{in}}(t) = 0$ and the transmission in the b-modes read,

$$\tau(\omega) = \frac{-i\sqrt{2\gamma}\langle G\rangle}{\langle r_{\text{in}}\rangle}. \tag{G.6}$$

The total leakage is given by

$$A(\omega) = |\tau(\omega)|^2. \tag{G.7}$$

G.3 Efficiency calculations

In order to compute the reflection and leakage when the mirror is placed, we must sum over all the possible reflection, transmission, and lossy events, as shown in Figure G.2. In doing so, we define $\Phi(\omega) = \exp(ik(\omega)d)$, which is the phase accumulated by a photon with quasi momentum k traveling a distance d (this will be the distance between the mirror and the atom). Finally, we denote the reflection in the mirror as r_M.

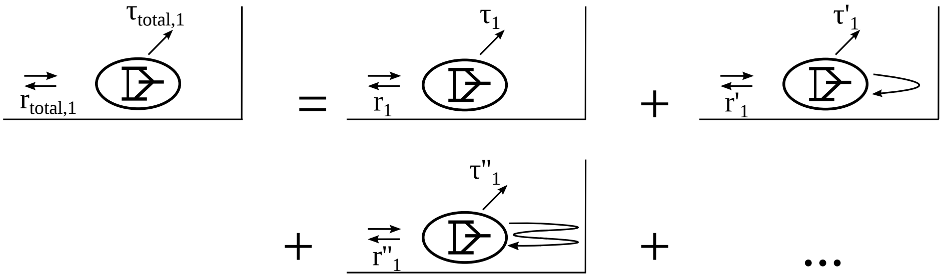

Figure G.2: Diagrammatic representation for the possible scattering events giving the total reflection.

With the mirror, $P^{(2)}(\omega)$ is written as,

$$P^{(2)}(\omega) = 1 - |r^{(1)}_{\text{tot}}(\omega)|^2 - |\tau^{(1)}_{\text{tot}}(\omega)|^2 \tag{G.8}$$

where $r^{(1)}_{\text{tot}}(\omega)$ is the *total* one-photon reflection. It should be distinguished from $r^{(1)}(\omega)$ which stands for the partial reflection occurring in every event. The coefficient $\tau^{(1)}_{\text{tot}}(\omega)$ is the amplitude of decaying in the lossy channel. Summing over all scattering events, see Figure G.2, we finally get

$$\begin{aligned} r^{(1)}_{\text{tot}}(\omega) =& r^{(1)}(\omega) + t^{(1)}(\omega)\Phi(\omega)r_M t^{(1)}(\omega) \\ &+ t^{(1)}(\omega)\Phi(\omega)r_M t^{(1)}(\omega)r^{(1)}(\omega)\Phi(\omega)r_M t^{(1)}(\omega) \\ &+ \dots \\ =& r^{(1)}(\omega) + \frac{(t^{(1)}(\omega))^2\Phi(\omega)r_M}{1 - r^{(1)}(\omega)\Phi(\omega)r_M}, \end{aligned} \tag{G.9}$$

and

$$\begin{aligned} \tau^{(1)}_{\text{tot}}(\omega) =& \tau^{(1)}(\omega) + t^{(1)}(\omega)\Phi(\omega)r_M \tau(\omega) \\ &+ t^{(1)}(\omega)\Phi(\omega)r_M t^{(1)}(\omega)r^{(1)}(\omega)\Phi(\omega)r_M \tau(\omega) \\ &+ \dots \\ =& \tau^{(1)}(\omega) + \frac{\tau(\omega)t^{(1)}(\omega)\Phi(\omega)r_M}{1 - r^{(1)}(\omega)\Phi(\omega)r_M}. \end{aligned} \tag{G.10}$$

Combining (G.9), (G.10) with (G.8) we can compute the two-photon generation $P^{(2)}(\omega)$, considering $r_M = -1$ in the calculations. The transmission into the auxiliary modes is the energy loss from the system, i.e. $A(\omega) = |\tau(\omega)|^2$ (G.7).

G.4 Simulated model, input state, and parameters used

Here we give some useful details on the numerical simulations. In particular, we present the Hamiltonian, the parameters, and the form of the input wave packet.

We first write explicitly the Hamiltonian used in the simulations, which consists of the discrete version of the waveguide (1.2), the C3LS Hamiltonian (5.5), and the dipole-field interaction term (5.6)

$$\begin{aligned} H =& \epsilon \sum_x a_x^\dagger a_x - J \sum_x (a_x^\dagger a_{x+1} + \text{H.c.}) \\ &+ \sum_{i=0}^{2} \Delta_i |i\rangle\langle i| + \sum_{i,j=0}^{2} (G_{ij} |i\rangle \langle j| + \text{H.c.})(a_0 + a_0^\dagger). \end{aligned} \tag{G.11}$$

As said in Sect. 1.1, the photonic part can be diagonalized in momentum space, giving the dispersion relation $\omega_k = \epsilon - 2J \cos k$. This implies that the density of photonic states is $g(\omega) = 1/\sqrt{2J|\sin(k(\omega))|}$. This is an essential quantity, since it appears in several expressions in Sect. 5.2, *e.g.*, in the interaction Hamiltonian (5.6).

We fix $\epsilon = 1$, $J = 1/\pi$, $\Delta_0 = 0$, $\Delta_1 = 0.59$, and $\Delta_2 = 1.10$ (these energies were obtained from the model introduced in the main part of the text). We take $L = 1000$ cavities and we place the scatterer at the center, which we define as $x_0 = 0$. The couplings used in the simulations to compute the full spectrum are $G_{01} = -0.0225$, and $G_{12} = G_{02} = 0.03$. In order to get a cleaner scattering state and due to the limitations in the time of simulations, in the calculation of the two-photon wave function we artificially increased the couplings: $G_{01} = -0.10$, $G_{12} = G_{20} = 0.13$.

We work in position space. The input state is:

$$|\Psi_{\text{in}}\rangle = \sum_x e^{ik_0 x} e^{(x-\bar{x})/2\sigma} \theta(\bar{x} - x) a_x^\dagger |\Omega\rangle, \tag{G.12}$$

up to a normalization constant, where $\bar{x}$ is the central position of the wave front, σ a measure of its width, k_0 the average wave vector, and $\theta(x)$ the Heaviside function. We fix $\bar{x} = -420$ (the chain has $L = 1000$ cavities) and $k_0 = 1.73$ (at resonance with Δ_{20}). We take $\sigma = 2$ when we wanted to obtain the full spectrum and $\sigma = 20$ for the simulation in which we compute dynamical properties. We used a bond dimension $D = 10$ and the cut-off for the cavities was $n_{\text{max}} = 3$.

Appendix H

Computation of the S matrix from a $\mathrm{V}^{(N)}$ atom

H.1 One-photon scattering

Applying Eq. (5.28) on Eq. (2.24) we obtain

$$S^{\mathrm{c}}_{pk} = \delta(p-k) - i \sum_{n=1}^{N} \sqrt{2\gamma_n} \left\langle \phi_0 | \sigma_n^-(p) | k^+ \right\rangle , \tag{H.1}$$

with $|\phi_0\rangle = |0\rangle |\mathrm{vac}\rangle$ being the ground state of the model, $|k^+\rangle$ the input state as introduced in Eq. (2.9), and $\sigma_n^-(p)$ the Fourier transform of $\sigma_n^-(t)$.

The dynamics of $\langle \phi_0 | \sigma_n^-(t) | k^+ \rangle$ is obtained by sandwiching Eq. (5.30) between $\langle \phi_0|$ and $|k^+\rangle$ and using $\langle \phi_0 | a_{\mathrm{in}}(t) | k^+ \rangle = e^{-ikt}/\sqrt{2\pi}$:

$$i \frac{d}{dt} \left\langle \phi_0 | \sigma_n^-(t) | k \right\rangle = \sum_{m=1}^{N} A_{nm} \left\langle \phi_0 | \sigma_m^-(t) | k \right\rangle + \sum_{m=1}^{N} \sqrt{2\gamma_m} \left\langle \phi_0 | c_{mn}(t) a_{\mathrm{in}}(t) | k^+ \right\rangle . \tag{H.2}$$

The last term can be easily computed using the definition of c_{nm}, Eq. (5.27). First, notice that $\langle \phi_0 | \, \sigma_n^+(t) = 0$. The calculation of the first term in c_{mn} is a little bit trickier,

$$\begin{aligned} &\langle \phi_0 | \, e^{iHt} \left(|0\rangle \langle 0| \otimes \mathbb{I}_{\mathrm{ph}} \right) e^{-iHt} a_{\mathrm{in}}(t) \, |k^+\rangle = \langle \phi_0 | \left(|0\rangle \langle 0| \otimes \mathbb{I}_{\mathrm{ph}} \right) e^{-iHt} a_{\mathrm{in}}(t) \, |k^+\rangle \\ &= \langle \phi_0 | \, e^{-iHt} a_{\mathrm{in}}(t) \, |k^+\rangle = \langle \phi_0 | \, a_{\mathrm{in}}(t) \, |k^+\rangle = \frac{e^{-ikt}}{\sqrt{2\pi}}, \end{aligned} \tag{H.3}$$

where we are using the fact that $|\phi_0\rangle$ is an eigenstate of H with energy 0 (first and third equalities), $|\phi_0\rangle = |0\rangle |\mathrm{vac}\rangle$ (second equality), and (2.30) in the last equality. Using this in (H.2) we get

$$i\frac{d}{dt}\left\langle \phi_0 | \sigma_n^-(t) | k^+ \right\rangle = \sum_{m=1}^{N} A_{nm} \left\langle \phi_0 | \sigma_m^-(t) | k^+ \right\rangle + \sqrt{\frac{\gamma_n}{\pi}} e^{-ikt}. \tag{H.4}$$

This equation can be integrated

$$\left\langle \phi_0 | \sigma_n^-(t) | k^+ \right\rangle = \frac{e^{-ikt}}{\sqrt{2\pi}} s_k^n, \tag{H.5}$$

with

$$s_k^n = \sum_{m=1}^{N} \sqrt{2\gamma_m}\, [(k - A)^{-1}]_{nm} \tag{H.6}$$

Introducing this in Eq. (H.1),

$$S_{pk}^{\mathrm{c}} = t_k^{\mathrm{c}}\, \delta(k - p), \tag{H.7}$$

$$t_k^{\mathrm{c}} = 1 - i \sum_{n=1}^{N} \sqrt{2\gamma_n}\, s_k^n, \tag{H.8}$$

where the effect of the occupation of the excited levels in the atom affects the transmission through s_k^n.

H.2 Two-photon scattering

H.2.1 Derivation of the scattering matrix

By introducing the identity $\int dk\, a_{\mathrm{in}}^\dagger(k) \left|0\right\rangle \left\langle 0\right| a_{\mathrm{in}}(k)$ between the output operators $a_{\mathrm{out}}(p_1)$ and $a_{\mathrm{out}}(p_2)$ in Eq. (5.37), we obtain

$$\begin{aligned} S_{p_1 p_2 k_1 k_2}^{\mathrm{c}} &= t_{p_1}^{\mathrm{c}} \delta(p_1 - k_1)\delta(p_2 - k_2) + \\ &+ t_{p_1}^{\mathrm{c}} \delta(p_1 - k_2)\delta(p_2 - k_1) \\ &- i t_{p_1}^{\mathrm{c}} \sum_{n=1}^{N} \sqrt{2\gamma_n} \left\langle p_1^+ | \sigma_n^-(p_2) | (k_1 k_2)^+ \right\rangle. \end{aligned} \tag{H.9}$$

The computation of $\left\langle p_1^+ | \sigma_n^-(p_2) | (k_1 k_2)^+ \right\rangle$ requires some algebraic manipulations. The crucial element in the scattering matrix is the Fourier transform of the off-diagonal element of the scatterer between different input and output states, Eq. (2.37):

$$\begin{aligned} &\left\langle p_1^+ | \sigma_n^-(p_2) | (k_1 k_2)^+ \right\rangle \\ &\qquad = \int dt\, \frac{e^{ip_2 t}}{\sqrt{2\pi}} \left\langle \phi_0 | a_{\mathrm{in}}(p_1) \sigma_n^-(t) a_{\mathrm{in}}^\dagger(k_1) a_{\mathrm{in}}^\dagger(k_2) | \phi_0 \right\rangle. \end{aligned} \tag{H.10}$$

The equations for the integrand can be found from Eq. (5.30)

$$\begin{aligned} i\frac{d}{dt}\left\langle p_1^+\right|\sigma_n^-(t)\left|(k_1k_2)^+\right\rangle = {} & \sum_{m=1}^{N} A_{nm}\left\langle p_1^+\right|\sigma_m^-(t)\left|(k_1k_2)^+\right\rangle \\ & + \sum_{m=1}^{N}\sqrt{2\gamma_m}\left\langle p_1^+\right|c_{mn}(t)a_{\text{in}}(t)\left|(k_1k_2)^+\right\rangle . \end{aligned} \tag{H.11}$$

The second term in this equation can be simplified as a transition amplitude between single-photon states

$$\left\langle p_1^+\right|c_{mn}(t)a_{\text{in}}(t)\left|(k_1k_2)^+\right\rangle = \left\langle p_1^+\right|c_{mn}(t)\left|k_1^+\right\rangle\frac{e^{-ik_2t}}{\sqrt{2\pi}} + (k_1 \leftrightarrow k_2). \tag{H.12}$$

We now expand $c_{mn}(t)$ (see Eq. (5.27))

$$\begin{aligned} & \left\langle p^+\right|c_{mn}(t)\left|k^+\right\rangle \\ & \qquad = \delta_{mn}\left\langle p^+\right|1 - \sum_{l=1}^{N}\sigma_l^+(t)\sigma_l^-(t)\left|k^+\right\rangle - \left\langle p^+\right|\sigma_m^+(t)\sigma_n^-(t)\left|k^+\right\rangle \end{aligned} \tag{H.13}$$

and use the relation

$$\left\langle p^+\right|\sigma_m^+(t)\sigma_n^-(t)\left|k^+\right\rangle = \frac{e^{i(p-k)t}}{2\pi}(s_p^m)^* s_k^n, \tag{H.14}$$

which we get introducing the identity between $\sigma_m^+(t)$ and $\sigma_n^-(t)$ and using Eq. (H.5).

We define $\mathbf{v}(t)$ as a vector whose entries are $v_n(t) = \left\langle p_1^+\right|\sigma_n^-(t)\left|(k_1k_2)^+\right\rangle$. In terms of these quantities we obtain

$$i\frac{d\mathbf{v}(t)}{dt} = A\mathbf{v}(t) + \mathbf{f}_1\frac{e^{-ik_1t}}{\sqrt{2\pi}} + \mathbf{f}_2\frac{e^{-ik_2t}}{\sqrt{2\pi}} + \mathbf{f}_{12}\frac{e^{-ipt}}{\sqrt{2\pi}}, \tag{H.15}$$

where $p = p_1 - k_1 - k_2$ and we have defined the auxiliary vectors

$$f_{1,n} = \sqrt{2\gamma_n}\,\delta(p_1 - k_2), \tag{H.16}$$

$$f_{2,n} = \sqrt{2\gamma_n}\,\delta(p_1 - k_1), \tag{H.17}$$

$$\begin{aligned} f_{12,n} = {} & -\sqrt{2\gamma_n}\sum_{m=1}^{N}\frac{1}{2\pi}(s_{p_1}^m)^*(s_{k_1}^m + s_{k_2}^m) \\ & - \sum_{m=1}^{N}\sqrt{2\gamma_m}\frac{1}{2\pi}(s_{p_1}^m)^*(s_{k_1}^n + s_{k_2}^n). \end{aligned} \tag{H.18}$$

Equation (H.15) can be readily integrated. Taking the Fourier transform in the time variable, we find,

$$\mathbf{v}(p_2) = \mathbf{v}_1 + \mathbf{v}_2 + \mathbf{v}_{12}, \tag{H.19}$$

with the vectors

$$\mathbf{v}_1 =(k_1 - A)^{-1}\,\mathbf{f}_1\,\delta(p_2 - k_1), \tag{H.20}$$

$$\mathbf{v}_2 =(k_2 - A)^{-1}\,\mathbf{f}_2\,\delta(p_2 - k_2), \tag{H.21}$$

$$\mathbf{v}_{12} =(p_2 - A)^{-1}\,\mathbf{f}_{12}\,\delta(p_2 - p). \tag{H.22}$$

Introducing this relations into Eq. (H.9), and applying (5.32), we get the expression (5.38) for $S^{\mathrm{c}}_{p_1p_2k_1k_2}$, with $T^{\mathrm{c}}_{p_1p_2k_1k_2}$ given by (5.39).

H.2.2 Symmetric form of the scattering matrix

The problem with the previous standard derivation and the final formula (5.39) is that it hides the exchange symmetry between outgoing bosons p_1 and p_2. To recover this symmetry we have to realize that it is possible to manipulate the expression for $\mathbf{s}_k$ in order to simplify all the sums. We begin by writing the innards of $\mathbf{s}_k$ explicitly

$$(k - A) = E_k^{1/2}(1 + i\mathbf{w}\mathbf{w}^\dagger)E_k^{1/2}, \tag{H.23}$$

in terms of a diagonal matrix $E_{k,nm} = (k - \Delta_n)\delta_{nm}$ and the unnormalized vector $w_n = \sqrt{\gamma_n}$. Introducing the factor

$$\alpha_k = \mathbf{w}^\dagger E_k^{-1}\mathbf{w}, \tag{H.24}$$

we arrive at the expression

$$(k - A)^{-1} = E_k^{-1}\left[1 - \frac{i}{1+\alpha_k}\mathbf{w}(E_k^{-1}\mathbf{w})^\dagger\right]. \tag{H.25}$$

We can use this simplification to write

$$\mathbf{s}_k = \frac{\sqrt{2}}{1+i\alpha_k}E_k^{-1}\mathbf{w},\ t^{\mathrm{c}}_k = \frac{1-i\alpha_k}{1+i\alpha_k}, \tag{H.26}$$

which shows that the chiral transmission coefficient is just a phase.

We can achieve a similar simplification of the two-photon scattering matrix identifying sums with scalar products

$$\sum_l \sqrt{\gamma_n}s_p^n = \mathbf{w}^\dagger\mathbf{s}_p = \frac{\sqrt{2}\alpha_p}{1+i\alpha_k}, \tag{H.27}$$

$$\sum_n (s_p^n)^* s_k^n = \mathbf{s}_p^\dagger\mathbf{s}_k = \frac{2}{(1-i\alpha_p)(1+i\alpha_k)}\beta_{pk} \tag{H.28}$$

to first transform Eq. (5.39)

$$\begin{aligned} T^{\mathrm{c}}_{p_1p_2k_1k_2} &= \frac{t^{\mathrm{c}}_{p_1}}{2\pi}\sqrt{2}(\mathbf{w}^\dagger\mathbf{s}_{p_2})[\mathbf{s}^\dagger_{p_1}(\mathbf{s}_{k_1}+\mathbf{s}_{k_2})] \\ &+ \frac{t^{\mathrm{c}}_{p_1}}{2\pi}\sqrt{2}(\mathbf{s}^\dagger_{p_1}\mathbf{w})[\mathbf{s}^T_{p_2}(\mathbf{s}_{k_1}+\mathbf{s}_{k_2})], \end{aligned} \tag{H.29}$$

and then transform it to the final expression in Eq. (5.40).

Appendix I

Two-qubit phase gate

In this appendix, we first quantify the entanglement entropy generated by the two-qubit phase gate, and later provide the expressions for the scattering amplitudes.

I.1 Entanglement

Considering the output state (5.54), we can build the density matrix $\rho_{\mathrm{out}} = |\Psi_{\mathrm{out}}\rangle \langle\Psi_{\mathrm{out}}|$ and the reduced density matrix of the first qubit

$$\begin{aligned}(\rho_{\mathrm{out}})_1 &= \mathrm{Tr}_2(\rho_{\mathrm{out}}) \\ &= \frac{1}{|\mathcal{N}|^2}\begin{pmatrix} |c_b|^2+1 & e^{-i(\delta+\phi_1)}c_a^*(e^{i\delta}+|c_b|^2) \\ e^{i(\delta+\phi_1)}c_a(e^{-i\delta}+|c_b|^2) & |c_a|^2(1+|c_b|^2) \end{pmatrix}. \end{aligned} \tag{I.1}$$

To compute the entanglement entropy S_{VN}, we need the eigenvalues of $(\rho_{\mathrm{out}})_1$ (see Eq. (2.94)). They read

$$\lambda_\pm = \frac{1}{2}(1 \pm f), \tag{I.2}$$

with f equal to

$$f = \frac{\sqrt{P_a(P_a-2)(P_b+1)^2 + (P_b^2+1)(4P_a+1) + 2P_b(1+4P_a\cos(\delta))}}{(P_a+1)(P_b+1)}, \tag{I.3}$$

being $P_x = |c_x|^2$, with $x = a, b$. The entanglement entropy S_{VN} is written as a function of f in the main text (see Eq. (5.55)). It is easy to show that $f = 1$ if $\delta = 0$ (see Fig. I.1), which implies there is no entanglement, $S_{\mathrm{VN}} = 0$ (see Eq. (5.55)), as we argued in Sect. 5.4.1. In addition, the entropy is an increasing function of δ between 0 and π. In particular, if $c_a = c_b = 1$ and $\delta = \pi$, then $f = 0$ (see again Fig. I.1) and $S_{\mathrm{VN}} = \log 2$, which is the maximum possible value for the qubit-qubit entanglement entropy.

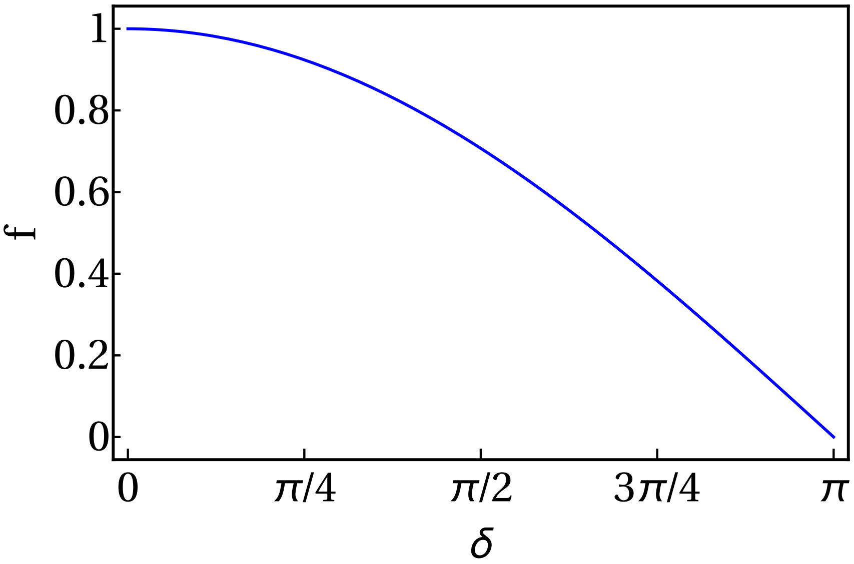

Figure I.1: Function f defined in Eq. (I.3), as a function of δ for $c_a = c_b = 1$. As seen, $f = 1$ for $\delta = 0$, so there is no entanglement at that point, and it vanishes for $\delta = \pi$, so the entropy is maximum (see Eq. (5.55)). Notice that f monotonically decreases with δ, so S_{VN} is an increasing function of δ.

I.2 $S(\bar{k} = \Delta_1, \sigma_k)$ for a V atom and two collocated two-level systems

Here we skip the tedious derivations and just write down the expressions of $S(\bar{k} = \Delta_1, \sigma_k, \Delta_1 - \Delta_2)$ for both a V atom and two collocated two-level systems. For the V atom:

$$\begin{aligned} &S(\bar{k} = \Delta_1, \sigma_k) \\ &= \frac{-8\gamma^2\sigma_k(-2i\sigma_k + \Delta_1 - \Delta_2)\left(-6\sigma_k^2 - 4i\sigma_k(\Delta_1 - \Delta_2) + (\Delta_1 - \Delta_2)^2\right)}{\left((\Delta_1 - \Delta_2)\left(3\sigma_k + \gamma\right) - 3i\sigma_k\left(3\sigma_k + 2\gamma\right)\right)\left((\Delta_1 - \Delta_2)\left(\sigma_k + \gamma\right) - i\sigma_k\left(\sigma_k + 2\gamma\right)\right)^2} \\ &+ \left(\frac{\sigma_k\left(\sigma_k - 2\gamma\right) + i\left(\Delta_1 - \Delta_2\right)\left(\sigma_k - \gamma\right)}{\sigma_k\left(\sigma_k + 2\gamma\right) + i\left(\Delta_1 - \Delta_2\right)\left(\sigma_k + \gamma\right)}\right)^2 . \end{aligned} \tag{I.4}$$

For the collocated two-level systems:

$$
\begin{aligned}
&S(\bar{k} = \Delta_1, \sigma_k) = \\
&-\frac{8\gamma^3\sigma_k\left(6\sigma_k + i\left(\Delta_1 - \Delta_2\right)\right)\left(-2i\left(\Delta_1 - \Delta_2\right)\sigma_k + \left(\Delta_1 - \Delta_2\right)^2 - 2\sigma_k^2\right) + 24i\gamma^3\sigma_k^4}{\left(\Delta_1 - \Delta_2 - 2i\left(\sigma_k + \gamma\right)\right)\left(\left(\Delta_1 - \Delta_2\right)\left(3\sigma_k + \gamma\right) - 3i\sigma_k\left(3\sigma_k + 2\gamma\right)\right)} \\
&\times \frac{1}{\left(\left(\Delta_1 - \Delta_2\right)\left(\sigma_k + \gamma\right) - i\sigma_k\left(\sigma_k + 2\gamma\right)\right)^2} \\
&+ \frac{8i\gamma^2\sigma_k\left(\Delta_1 - \Delta_2 - i\sigma_k\right)^2\left(\Delta_1 - \Delta_2 - 3i\sigma_k\right)}{\left(\sigma_k\left(\sigma_k + 2\gamma\right) + i\left(\Delta_1 - \Delta_2\right)\left(\sigma_k + \gamma\right)\right)^2\left(3\sigma_k\left(3\sigma_k + 2\gamma\right) + i\left(\Delta_1 - \Delta_2\right)\left(3\sigma_k + \gamma\right)\right)} \\
&+ \left(\frac{\sigma_k\left(\sigma_k - 2\gamma\right) + i\left(\Delta_1 - \Delta_2\right)\left(\sigma_k - \gamma\right)}{\sigma_k\left(\sigma_k + 2\gamma\right) + i\left(\Delta_1 - \Delta_2\right)\left(\sigma_k + \gamma\right)}\right)^2 . \qquad \text{(I.5)}
\end{aligned}
$$

Acknowledgments. Agradecimientos

No quiero terminar sin dar las gracias a toda la gente que ha estado allí durante todos estos años. Me voy a tomar el lujo de hacerlo en castellano

Voy a empezar por mi familia más cercana. Gracias a mis padres, Tomás y Consuelo, por haberme dado la posibilidad de llegar hasta aquí. A mi hermano Guillermo, porque si me he dedicado a la ciencia probablemente es por él. A mi hermana Irene, por haber estado allí en todo momento.

Ya que estamos, sigo con la familia. Empiezo por mis "cuñaos", Jony y Alba. Sigo por Marco, el mejor sobrino del mundo. No sabes la de buenos momentos que me has dado. Espero que leas esto cuando seas mayor. Tampoco me olvido de la familia por parte de madre: mi tía Asun, Rosa y José Miguel, Nuria, César, Sara y Álvaro (también espero que leáis esta dedicatoria cuando crezcáis), ni de la de mi padre: todas mis tías y tíos (Eva, Mercedes, Araceli, Vicenta, Emilio, Azucena, Manolo...) y primas y primos (Javi, Madalina, Eva Mari, Ana Emilia, Quique, Angelines, Miguel Ángel, Yoli, Carlos, David, Olga, Juan Emilio y Marina... espero no dejarme a nadie). Y un saludo al resto de la familia: primos, sobrinos y tíos segundos. No voy a poner todos los nombres, que si me dejo alguno me la cargo.

A Nerea, mi amor, muchas gracias por haberme apoyado en todo instante. Por rescatarme en los momentos más difíciles de la tesis. Porque sin ti no podría con esto ni de coña. Gracias. Te quiero mucho.

Un saludo también a tu familia. A Borja, por esos platos tan ricos que nos cocinas. A Pepa, por tu cariño y hospitalidad en todo momento. Antonio, esperamos que te recuperes lo antes posible. Y al pequeño Quequo, evidentemente.

Paso a dar las gracias a mis directores de tesis, Luis y David. Por haberme enseñado qué es esto de la investigación. Por haberme ayudado en todo momento y haber tenido paciencia conmigo. Por haberme enseñado tantísimo,

tanto de física como de muchas otras cosas. Porque también ha habido tiempo para echar unas risas. Porque, además de haber sido mis supervisores, me llevo un par de amigos.

Gracias también al resto de gente que me ha acompañado estos años en la investigación. Empiezo por la gente del Instituto de Física Fundamental de Madrid. Quiero hacer énfasis en Juan José García Ripoll. Muchas gracias por todo lo que me has enseñado. Por haberme acogido en Madrid varias veces. Y, sobre todo, porque si no me hubieras enseñado MPS, esta tesis no existiría. Gracias también a Andrea Cadarso por esas cuentas del "cluster". Tampoco me olvido del resto de miembros del grupo, por los buenos ratos que hemos pasado tanto en congresos como en las visitas a Madrid.

Sigo con Guifré Vidal. Gracias por haberme recibido en Waterloo para esa estancia. En esos 3 meses aprendí muchísimo. Terminaremos lo que tenemos entre manos, como te prometí. Thank you also to the members of the group (Julián, Markus, etc.). You helped me so much! También quiero agradecer a la gente que hizo que mi estancia tuviera algo más que redes tensoriales, en especial a Pol, Eduardo Barrera y Dani Remón.

Gracias a la gente del grupo: Jorge Calvo, Pablo, Fernando de León, Sergio, Tania... y a la gente que ya se ha ido, como Uta (y a Cata, ya que estamos), Fernando Quijandría y Fernando Villate. También a la gente que ha tenido un paso más fugaz, como Jorge Yago (tus visitas siempre son bien recibidas, ya lo sabes), Jesús Vergara, Luis Obís, Virginia Ciriano e Ignacio Hermoso de Mendoza (nos vemos en el ágape navideño). Gracias también a la gente del departamento, del ICMA y de la Universidad en general que me ha hecho pasar buenos momentos durante todo este tiempo. En particular, a la gente con la que he compartido docencia: David de nuevo, Juanjo Mazo, Laura Badía, Fernando López Tejeira... También al personal de secretaría y de gerencia, por haberme echado un cable en todos los trámites burocráticos. Y también gracias al servicio técnico de los "clusters" del BiFi. Habéis sido fundamentales.

No quiero dejarme a mis colegas de congreso: Carlos, Martin, Alexei, Álex... A ti, Álex Tudela, gracias otra vez por haberme recomendado en el grupo donde parece que va a seguir mi carrera científica. Y gracias, Ignacio, por haberme invitado y aceptarme.

También quiero mostrar mi agradecimiento a varias personas que me introdujeron en la investigación antes de empezar a trabajar en la tesis. A Guillermo Antorrena y Luis Morellón, del INA, por haberme dirigido la beca de aquel verano del 2010. A Pepe Esteve y Fernando Falceto, con los cuales tuve mi primera toma de contacto con la investigación en física teórica durante aquel TAD. A Jesús Gómez Gardeñes, con el que desarrollé mi primera publicación junto con David.

I acknowledge the members of the committee: Francisco José García-Vidal, Geza Giedcke, and Peter Rabl, as well as the reserve members, José G. Esteve and Fernando Falceto, for agreeing to take part of the jury in the defense. It is a honour. Thank you so much. ¡Gracias!

Gracias también por supuesto a mis amigos. Pasar ratos de cervezas, cenas y demás es necesario para poder llevar esto. Empiezo con la cuadrilla de toda la vida, contando con las incorporaciones más recientes: Nahum, Pablo, Alejandra, Aarón, Judith, Jorge, Sara, Natalia, David, Ángel, Carlos, Vanesa... Y a Valeria, Carolina y "el Chamarrico" en camino.

Tampoo me quiero olvidar del resto de gente del cole. Aunque nos veamos cada mucho tiempo, siempre es una alegría veros.

A los compañeros del balonmano: Edu, Fernando, Javiti, Loidi, Iraide, Gallardo, Valero, Francho, Bordo, "Jefe", Luisito, Adrián (pese a nuestras posiciones encontradas), Arti, los Carlos, P. López, los hermanos Orera... Me dejo muchos nombres, pero sabéis quiénes sois. Y a mis entrenadores, por supuesto: Lourdes, Raúl, César, Pablo, Miguel... También me habéis formado como persona.

A todo el Olímpico Torrero. Probablemente el mejor equipo de fútbol 7 de la Historia. Porque, gracias a vosotros, levantarse los sábados a las 7 de la mañana tenía sentido.

A la gente del instituto: Alejandro, Chema, Sara, María José, Guille, Edu, "Buda"... Hemos pasado momentos geniales. ¡No se me olvidará jamás ese viaje por Suecia y Noruega con vosotros, Álex y Chema!

Paso a los de la carrera. Gracias por estar ahí. Sabéis lo duro que puede ser esto. A los doctores Torres Sánchez (y a Laura y Arya), Santos Oliván y Martínez Martínez (and Maria, for hosting us in Düsseldorf). A Alba. Ánimo con la tesis. A la doctora Andrés Arroyo. A ver cuándo pasas por Zaragoza. Al doctor Anadón Barcelona (y a Sandra, ya que estamos). Tenemos que echar un Gwent. Al mejor organizador de partidas, también conocido como doctor Jover Galtier. A Elisa (saluda a Eduardo) y Târ (y tú a Ana). No os queda mucho, ¡un último empujón! A Adrián. Nunca olvidaré esa charla de álgebra. Cristalina. A Andrés. Te queremos pese a ser ingeniero. A Carlos. Escuchar tus locuras es una buena forma de despejar la cabeza. A Guille (o doctor Sobreviela). Por alguna razón, escribir de locuras me ha recordado a ti. A las Anas. Ánimo con esa tesis también para ambas. A Unai. El osito te manda saludos. A Pérez. No me olvido de esas sesiones de gimnnasio ni de las agujetas. A Pilar. Ya sabes que a los exámenes hay que llegar con antelación. A Paula. A Laura. A ver si nos vemos pronto. A Santi. Tus visitas por el despacho cada x meses me han alegrado muchas tardes. A Marcos. Hemos

tenido discusiones interesantísimas de física. Y nos hemos reído con muchas chorradas. También me acuerdo de gente de otras quintas y de otras carreras, con los que llegué a compartir clase y he pasado muy buenos ratos, por ejemplo hablando de política (ejem, Ignacios, Fer, Edu...).

Doy las gracias a mis profesores, desde el colegio Lestonnac hasta la carrera, pasando por el IES Miguel Servet, sin olvidarme del máster en l'Université de Cergy-Pontoise ni de mis profes del CULM.

Gracias también al ICMA, a la Universidad de Zaragoza y a su Departamento de Física de la Materia Condensada por haberme dado cobijo durante el doctorado.

Por último, gracias al Ministerio de Economía y Competitividad por haberme concedido la beca-contrato FPI con referencia BES-2012-058061, correspondiente al proyecto MAT2011-28581-C02-02. La ciencia está bien pero hay que comer, así que tener un salario no está de más.

Bibliography

[1] N. deGrasse Tyson, *Real Time with Bill Maher* (http://www.hbo.com/real-time-with-bill-maher/episodes/0/201-episode/synopsis/quotes.html, 2011).

[2] N. Bohr, *The Theory of Spectra and Atomic Constitution: Three Essays* (Cambridge University Press, 2011), ISBN 1107669812.

[3] C. Cohen-Tannoudji, J. Dupont-Roc, and G. Grynberg, *Photons and Atoms: An Introduction to Quantum Electrodynamics* (Wiley-Interscience, 1992).

[4] S. Haroche and D. Kleppner, Physics Today **42**, 24 (1989).

[5] M. H. Devoret, *Quantum Fluctuations, Volume 63 (Les Houches)* (North Holland, 1997).

[6] J. Q. You and F. Nori, Nature **474**, 589 (2011).

[7] X. Gua, A. K. Kockumb, A. Miranowiczb, Y. xi Liua, and F. Nori, eprint arXiv:1707.02046v1 (2017).

[8] M. A. Kastner, Physics Today **46**, 24 (1993).

[9] R. C. Ashoori, Nature **379**, 413 (1996).

[10] P. Lodahl, eprint arXiv:1707.02094v1 (2017).

[11] I. Aharonovich, A. D. Greentree, and S. Prawer, Nature Photonics **5**, 397 (2011).

[12] J. L. O'Brien, A. Furusawa, and J. Vučković, Nature Photonics **3**, 687 (2009).

[13] P. Benioff, Journal of Statistical Physics **22**, 563 (1980).

[14] R. P. Feynman, International Journal of Theoretical Physics **21**, 467 (1982).

[15] D. Deutsch, Proceedings of the Royal Society A: Mathematical, Physical and Engineering Sciences **400**, 97 (1985).

[16] J. I. Cirac and P. Zoller, Phys. Rev. Lett. **74**, 4091 (1995).

[17] M. A. Nielsen and I. L. Chuang, *Quantum Computation and Quantum Information* (Cambridge University Press, 2000).

[18] F. Illuminati, Nature Physics **2**, 803 (2006).

[19] C. Noh and D. G. Angelakis, Reports on Progress in Physics **80**, 016401 (2016).

[20] T. E. Northup and R. Blatt, arXiv preprint arXiv:1708.00424v1 (2017).

[21] P. Zoller, T. Beth, D. Binosi, R. Blatt, H. Briegel, D. Bruss, T. Calarco, J. I. Cirac, D. Deutsch, J. Eisert, et al., The European Physical Journal D **36**, 203 (2005).

[22] C. H. Bennett, G. Brassard, and A. K. Ekert, Scientific American **267**, 50 (1992).

[23] N. Gisin and R. Thew, Nature Photonics **1**, 165 (2007).

[24] V. Giovannetti, Science **306**, 1330 (2004).

[25] A. Kuhn, M. Hennrich, and G. Rempe, Physical Review Letters **89** (2002).

[26] A. A. Houck, D. I. Schuster, J. M. Gambetta, J. A. Schreier, B. R. Johnson, J. M. Chow, L. Frunzio, J. Majer, M. H. Devoret, S. M. Girvin, et al., Nature **449**, 328 (2007).

[27] D. Bozyigit, C. Lang, L. Steffen, J. M. Fink, C. Eichler, M. Baur, R. Bianchetti, P. J. Leek, S. Filipp, M. P. da Silva, et al., Nature Physics **7**, 154 (2010).

[28] W. F. Kindel, M. D. Schroer, and K. W. Lehnert, Phys. Rev. A **93**, 033817 (2016).

[29] P. Forn-Díaz, C. W. Warren, C. W. S. Chang, A. M. Vadiraj, and C. M. Wilson, arXiv preprint arXiv:1706.06688v1 (2017).

[30] J. I. Cirac, P. Zoller, H. J. Kimble, and H. Mabuchi, Phys. Rev. Lett. **78**, 3221 (1997).

[31] A. Acín, J. I. Cirac, and M. Lewenstein, Nature Physics **3**, 256 (2007).

[32] H. J. Kimble, Nature **453**, 1023 (2008).

[33] S. Ritter, C. Nölleke, C. Hahn, A. Reiserer, A. Neuzner, M. Uphoff, M. Mücke, E. Figueroa, J. Bochmann, and G. Rempe, Nature **484**, 195 (2012).

[34] B. Hensen, H. Bernien, A. E. Dréau, A. Reiserer, N. Kalb, M. S. Blok, J. Ruitenberg, R. F. L. Vermeulen, R. N. Schouten, C. Abellán, et al., Nature **526**, 682 (2015).

[35] Y. He, Y.-M. He, Y.-J. Wei, X. Jiang, K. Chen, C.-Y. Lu, J.-W. Pan, C. Schneider, M. Kamp, and S. Höfling, Phys. Rev. Lett. **119**, 060501 (2017).

[36] B. Vermersch, P.-O. Guimond, H. Pichler, and P. Zoller, Phys. Rev. Lett. **118**, 133601 (2017).

[37] Z.-L. Xiang, M. Zhang, L. Jiang, and P. Rabl, Phys. Rev. X **7**, 011035 (2017).

[38] D. Roy, C. M. Wilson, and O. Firstenberg, Rev. Mod. Phys. **89**, 021001 (2017).

[39] T. Lund-Hansen, S. Stobbe, B. Julsgaard, H. Thyrrestrup, T. Sünner, M. Kamp, A. Forchel, and P. Lodahl, Phys. Rev. Lett. **101**, 113903 (2008).

[40] M. Arcari, I. Söllner, A. Javadi, S. Lindskov Hansen, S. Mahmoodian, J. Liu, H. Thyrrestrup, E. H. Lee, J. D. Song, S. Stobbe, et al., Phys. Rev. Lett. **113**, 093603 (2014).

[41] A. Goban, C.-L. Hung, S.-P. Yu, J. D. Hood, J. A. Muniz, J. H. Lee, M. J. Martin, A. C. McClung, K. S. Choi, D. E. Chang, et al., Nature Communications **5**, 3808 (2014).

[42] A. Javadi, I. Söllner, M. Arcari, S. Lindskov Hansen, L. Midolo, S. Mahmoodian, G. Kirsanske, T. Pregnolato, E. H. Lee, J. D. Song, et al., Nature Communications **6**, 8655 (2015).

[43] I. Söllner, S. Mahmoodian, S. Lindskov Hansen, L. Midolo, A. Javadi, G. Kirsanske, T. Pregnolato, H. El-Ella, E. H. Lee, J. D. Song, et al., Nature Nanotechnology **10**, 775 (2015).

[44] A. B. Young, A. C. T. Thijssen, D. M. Beggs, P. Androvitsaneas, L. Kuipers, J. G. Rarity, S. Hughes, and R. Oulton, Phys. Rev. Lett. **115**, 153901 (2015).

[45] P. Lodahl, S. Mahmoodian, and S. Stobbe, Reviews of Modern Physics **87**, 347 (2015).

[46] J. D. Hood, A. Goban, A. Asenjo-Garcia, M. Lu, S.-P. Yu, D. E. Chang, and H. J. Kimble, Proceedings of the National Academy of Sciences **113**, 10507 (2016).

[47] O. Astafiev, A. M. Zagoskin, A. Abdumalikov, Y. A. Pashkin, T. Yamamoto, K. Inomata, Y. Nakamura, and J. Tsai, Science **327**, 840 (2010).

[48] I.-C. Hoi, C. M. Wilson, G. Johansson, T. Palomaki, B. Peropadre, and P. Delsing, Phys. Rev. Lett. **107**, 073601 (2011).

[49] A. F. van Loo, A. Fedorov, K. Lalumière, B. C. Sanders, A. Blais, and A. Wallraff, Science **342**, 1494 (2013).

[50] I.-C. Hoi, A. F. Kockum, T. Palomaki, T. M. Stace, B. Fan, L. Tornberg, S. R. Sathyamoorthy, G. Johansson, P. Delsing, and C. M. Wilson, Phys. Rev. Lett. **111**, 053601 (2013).

[51] I.-C. Hoi, C. M. Wilson, G. Johansson, J. Lindkvist, B. Peropadre, T. Palomaki, and P. Delsing, New Journal of Physics **15**, 025011 (2013).

[52] M. Haeberlein, F. Deppe, A. Kurcz, J. Goetz, A. Baust, P. Eder, K. Fedorov, M. Fischer, E. P. Menzel, M. J. Schwarz, et al., arXiv preprint arXiv:1506.09114 (2015).

[53] P. Forn-Díaz, J. J. García-Ripoll, B. Peropadre, J.-L. Orgiazzi, M. A. Yurtalan, R. Belyansky, C. M. Wilson, and A. Lupascu, Nature Physics **13**, 39 (2017).

[54] Y. Liu and A. A. Houck, Nature Physics **13**, 48 (2017).

[55] Y. Tsuchimoto, P. Knüppel, A. Delteil, Z. Sun, M. Kroner, and A. Imamoglu, eprint arXiv:1707.02195v1 (2017).

[56] D. Reitz, C. Sayrin, R. Mitsch, P. Schneeweiss, and A. Rauschenbeutel, Phys. Rev. Lett. **110**, 243603 (2013).

[57] R. Mitsch, C. Sayrin, B. Albrecht, P. Schneeweiss, and Rauschenbeutel, Nature Communications **5**, 5713 (2014).

[58] J. Petersen, J. Volz, and A. Rauschenbeutel, Science **346**, 67 (2014).

[59] A. V. Akimov, A. Mukherjee, C. L. Yu, D. E. Chang, A. S. Zibrov, P. R. Hemmer, H. Park, and M. D. Lukin, Nature Physics **450**, 402 (2007).

[60] A. L. Falk, F. H. L. Koppens, C. L. Yu, K. Kang, N. de Leon Snapp, A. V. Akimov, M.-H. Jo, M. D. Lukin, and H. Park, Nature Physics **10**, 475 (2009).

[61] R. Kolesov, B. Grotz, G. Balasubramanian, R. J. Stöhr, A. A. L. Nicolet, P. R. Hemmer, F. Jelezko, and J. Wrachtrup, Nature Physics **5**, 470 (2009).

[62] A. Cuche, O. Mollet, A. Drezet, and S. Huant, Nano Letters **10**, 4566 (2010).

[63] A. Huck, S. Kumar, A. Shakoor, and U. L. Andersen, Phys. Rev. Lett. **106**, 096801 (2011).

[64] N. P. de Leon, M. D. Lukin, and H. Park, IEEE Journal of Selected Topics in Quantum Electronics **18**, 1781 (2012).

[65] N. C. Lindquist, P. Nagpal, K. M. McPeak, D. J. Norris, and S.-H. Oh, Reports on Progress in Physics **75**, 036501 (2012).

[66] S. J. P. Kress, P. Richner, S. V. Jayanti, P. Galliker, D. K. Kim, D. Poulikakos, and D. J. Norris, Nano Letters **14**, 5827 (2014).

[67] S. J. P. Kress, F. V. Antolinez, P. Richner, S. V. Jayanti, D. K. Kim, F. Prins, A. Riedinger, M. P. C. Fischer, S. Meyer, K. M. McPeak, et al., Nano Letters **15**, 6267 (2015).

[68] H. Siampour, S. Kumar, and S. I. Bozhevolnyi, ACS Photonics **4**, 1879 (2017).

[69] S. Faez, P. Türschmann, H. R. Haakh, S. Götzinger, and V. Sandoghdar, Phys. Rev. Lett. **113** (2014).

[70] P. Türschmann, N. Rotenberg, J. Renger, I. Harder, O. Lohse, T. Utikal, S. Götzinger, and V. Sandoghdar, Nano Letters **17**, 4941 (2017).

[71] A. Sipahigil, R. E. Evans, D. D. Sukachev, M. J. Burek, J. Borregaard, M. K. Bhaskar, C. T. Nguyen, J. L. Pacheco, H. A. Atikian, C. Meuwly, et al., Science **354**, 847 (2016).

[72] M. K. Bhaskar, D. D. Sukachev, A. Sipahigil, R. E. Evans, M. J. Burek, C. T. Nguyen, L. J. Rogers, P. Siyushev, M. H. Metsch, H. Park, et al., Phys. Rev. Lett. **118**, 223603 (2017).

[73] J. Thompson, T. Tiecke, N. de Leon, J. Feist, A. Akimov, M. Gullans, A. Zibrov, V. Vuletić, and M. Lukin, Science **340**, 1202 (2013).

[74] A. Goban, C.-L. Hung, J. D. Hood, S.-P. Yu, J. A. Muniz, O. Painter, and H. J. Kimble, Phys. Rev. Lett. **115**, 063601 (2015).

[75] J. A. H. Stotz, R. Hey, P. V. Santos, and K. H. Ploog, Nature Materials **4**, 585 (2005).

[76] S. Hermelin, S. Takada, M. Yamamoto, S. Tarucha, A. D. Wieck, L. Saminadayar, C. Bäuerle, and T. Meunier, Nature **477**, 435 (2011).

[77] R. P. G. McNeil, M. Kataoka, C. J. B. Ford, C. H. W. Barnes, D. Anderson, G. A. C. Jones, I. Farrer, and D. A. Ritchie, Nature **477**, 439 (2011).

[78] M. M. de Lima Jr and P. V. Santos, Rep. Progr. Phys. **68**, 1639 (2005).

[79] M. J. A. Schütz, E. Kessler, G. Giedke, L. Vandersypen, M. Lukin, and J. Cirac, in *Quantum Dots for Quantum Information Processing: Controlling and Exploiting the Quantum Dot Environment* (Springer International Publishing, 2016), pp. 143–196.

[80] M. J. A. Schuetz, J. Knörzer, G. Giedke, L. M. K. Vandersypen, M. D. Lukin, , and J. I. Cirac, arXiv preprint arXiv:1705.04860v1 (2017).

[81] R. Yalla, M. Sadgrove, K. P. Nayak, and K. Hakuta, Phys. Rev. Lett. **113**, 143601 (2014).

[82] T. Peyronel, O. Firstenberg, Q.-Y. Liang, S. Hofferberth, A. V. Gorshkov, T. Pohl, M. D. Lukin, and V. Vuletic, Nature **488**, 57 (2012).

[83] O. Firstenberg, T. Peyronel, Q.-Y. Liang, A. V. Gorshkov, M. D. Lukin, and V. Vuletić, Nature **502**, 71 (2013).

[84] D. E. Chang, V. Vuletić, and M. D. Lukin, Nature Photonics **8**, 685 (2014).

[85] M. Schiró, M. Bordyuh, B. Öztop, and H. E. Türeci, Phys. Rev. Lett. **109** (2012).

[86] M. Schiró, M. Bordyuh, B. Öztop, and H. E. Türeci, Journal of Physics B: Atomic, Molecular and Optical Physics **46**, 224021 (2013).

[87] M. Fannes, B. Nachtergaele, and R. F. Werner, Communications in Mathematical Physics **144**, 443 (1992).

[88] S. Östlund and S. Rommer, Phys. Rev. Lett. **75**, 3537 (1995).

[89] S. Rommer and S. Östlund, Phys. Rev. B **55**, 2164 (1997).

[90] G. Vidal, Phys. Rev. Lett. **91**, 147902 (2003).

[91] G. Vidal, Phys. Rev. Lett. **93**, 040502 (2004).

[92] J. J. García-Ripoll, New Journal of Physics **8**, 305 (2006).

[93] F. Verstraete, V. Murg, and J. I. Cirac, Advances in Physics **57**, 143 (2008).

[94] R. Orús, Annals of Physics **349**, 117 (2014).

[95] C. W. Gardiner and M. J. Collett, Phys. Rev. A **31**, 3761 (1985).

[96] S. Fan, Ş. E. Kocabaş, and J. T. Shen, Phys. Rev. A **82**, 063821 (2010).

[97] C. Cohen-Tannoudji, J. Dupont-Roc, and G. Grynberg, *Atom-Photon Interactions: Basic Processes and Applications* (Wiley-Interscience, 1992).

[98] R. W. Boyd, *Nonlinear Optics, Second Edition* (Academic Press, 2003), 2nd ed.

[99] J.-T. Shen and S. Fan, Optics Letters **30**, 2001 (2005).

[100] J.-T. Shen and S. Fan, Phys. Rev. Lett. **95**, 213001 (2005).

[101] J.-T. Shen and S. Fan, Phys. Rev. A **76**, 062709 (2007).

[102] L. Zhou, Z. R. Gong, Y. X. Liu, C. P. Sun, and F. Nori, Phys. Rev. Lett. **101**, 100501 (2008).

[103] P. Longo, P. Schmitteckert, and K. Busch, Phys. Rev. Lett. **104**, 023602 (2010).

[104] H. Zheng and H. U. Baranger, Phys. Rev. Lett. **110**, 113601 (2013).

[105] T. Shi, D. E. Chang, and J. I. Cirac, Phys. Rev. A **92**, 053834 (2015).

[106] P. Forn-Díaz, J. Lisenfeld, D. Marcos, García-Ripoll, E. Solano, C. J. P. M. Harmans, and J. E. Mooij, Phys. Rev. Lett. **105**, 237001 (2010).

[107] T. Niemczyk, F. Deppe, H. Huebl, E. P. Menzel, F. Hocke, M. J. Schwarz, J. J. Garcia-Ripoll, D. Zueco, T. Hümmer, E. Solano, et al., Nature Physics **6**, 772 (2010).

[108] S. J. Bosman, M. F. Gely, V. Singh, D. Bothner, A. Castellanos-Gomez, and G. A. Steele, Phys. Rev. B **95**, 224515 (2017).

[109] G. Günter, A. A. Anappara, J. Hees, A. Sell, G. Biasol, L. Sorba, S. D. Liberato, C. Ciuti, A. Tredicucci, A. Leitenstorfer, et al., Nature **458**, 07838 (2009).

[110] T. Schwartz, J. A. Hutchinson, C. Genet, and T. W. Ebbesen, Phys. Rev. Lett. **106**, 196405 (2011).

[111] C. Ciuti, G. Bastard, and I. Carusotto, Phys. Rev. B **72**, 115303 (2005).

[112] S. De Liberato and C. Ciuti, Phys. Rev. B **77**, 155321 (2008).

[113] K. Le Hur, Phys. Rev. B **85**, 140506 (2012).

[114] G. Romero, D. Ballester, Y. M. Wang, V. Scarani, and E. Solano, Phys. Rev. Lett. **108**, 120501 (2012).

[115] B. Peropadre, D. Zueco, D. Porras, and J. J. García-Ripoll, Phys. Rev. Lett. **111**, 243602 (2013).

[116] U. Naether, J. J. García-Ripoll, J. J. Mazo, and D. Zueco, Phys. Rev. Lett. **112**, 074101 (2014).

[117] S. De Liberato, Phys. Rev. Lett. **112**, 016401 (2014).

[118] E. Sánchez-Burillo, D. Zueco, J. J. García-Ripoll, and L. Martín-Moreno, Phys. Rev. Lett. **113**, 263604 (2014).

[119] T. Shi, Y. Chang, and J. J. García-Ripoll, arXiv preprint arXiv:1701.04709 (2017).

[120] J. R. Taylor, *Scattering Theory: The Quantum Theory of Nonrelativistic Collisions* (John Wiley & Sons, New York, 1972).

[121] K. Chang, *Maryam Mirzakhani, Only Woman to Win a Fields Medal, Dies at 40* (https://www.nytimes.com/2017/07/16/us/maryam-mirzakhani-dead.html, 2017).

[122] S. Xu and S. Fan, Phys. Rev. A **91**, 043845 (2015).

[123] R. Loudon, *The Quantum Theory of Light* (Oxford University Press, 2000).

[124] C. Gonzalez-Ballestero, A. Gonzalez-Tudela, F. J. Garcia-Vidal, and E. Moreno, Phys. Rev. B **92**, 155304 (2015).

[125] P.-O. Guimond, H. Pichler, A. Rauschenbeutel, and P. Zoller, Phys. Rev. A **94**, 033829 (2016).

[126] T. Ramós, B. Bermersch, P. Hauke, H. Pichler, and P. Zoller, Phys. Rev. A **93**, 062104 (2016).

[127] E. Rephaeli, Ş. E. Kocabaş, and S. Fan, Phys. Rev. A **84**, 063832 (2011).

[128] E. Sánchez-Burillo, L. Martín-Moreno, D. Zueco, and J. J. García-Ripoll, Phys. Rev. A **94**, 053857 (2016).

[129] F. Guinea and J. A. Vergés, Phys. Rev. B **35**, 979 (1987).

[130] A. Rivas and S. F. Huelga, *Open Quantum Systems* (Springer Berlin Heidelberg, 2012).

[131] A. A. Belavin, B. Y. Zel'oovich, A. Perelomov, and V. S. Popov, Zh. Eksp. Teor. Fiz **56**, 264 (1969).

[132] A. Kossakowski, Reports on Mathematical Physics **3**, 247 (1972).

[133] G. Lindblad, Communications in Mathematical Physics **48**, 119 (1976).

[134] V. Gorini, Journal of Mathematical Physics **17**, 821 (1976).

[135] J. L. Garcia-Palacios, arXiv preprint arXiv:cond-mat/0701242v1 (2007).

[136] C. Eckart and G. Young, Psychometrika **1**, 211 (1936).

[137] D. Poulin, A. Qarry, R. Somma, and F. Verstraete, Phys. Rev. Lett. **106** (2011).

[138] C. H. Bennett, H. J. Bernstein, S. Popescu, and B. Schumacher, Phys. Rev. A **53**, 2046 (1996).

[139] L. Bombelli, R. K. Koul, J. Lee, and R. D. Sorkin, Phys. Rev. D **34**, 373 (1986).

[140] J. Eisert, M. Cramer, and M. B. Plenio, Revs. of Mod. Phys. **82**, 277 (2010).

[141] K. G. Wilson, Reviews of Modern Physics **47**, 773 (1975).

[142] S. White, Phys. Rev. Lett. **69**, 2863 (1992).

[143] M. Suzuki, Journal of Mathematical Physics **32**, 400 (1991).

[144] I. P. McCulloch, Journal of Statistical Mechanics: Theory and Experiment p. 10014 (2007).

[145] B. Pirvu, V. Murg, J. I. Cirac, and F. Verstraete, New Journal of Physics **12**, 025012 (2010).

[146] W. Heisenberg, *The Physical Principles of the Quantum Theory (Dover Books on Physics)* (Dover Publications, 2013), ISBN 978-0486601137.

[147] S. John, Phys. Rev. Lett. **53**, 2169 (1984).

[148] S. John, Phys. Rev. Lett. **58**, 2486 (1987).

[149] S. John and J. Wang, Phys. Rev. Lett. **64**, 2418 (1990).

[150] Q.-J. Tong, J.-H. An, H.-G. Luo, and C. H. Oh, Journal of Physics B **43**, 155501 (2010).

[151] Q.-J. Tong, J.-H. An, H.-G. Luo, and C. H. Oh, Phys. Rev. A **81**, 052330 (2010).

[152] W. L. Yang, J.-H. An, C. Zhang, M. Feng, and C. H. Oh, Phys. Rev. A **87**, 022312 (2013).

[153] Y.-Q. Lü, J.-H. An, X.-M. Chen, H.-G. Luo, and C. H. Oh, Phys. Rev. A **88**, 012129 (2013).

[154] G. Calajó, F. Ciccarello, D. Chang, and P. Rabl, Phys. Rev. A **93**, 033833 (2016).

[155] T. Shi, Y.-H. Wu, A. González-Tudela, and J. I. Cirac, Phys. Rev. X **6**, 021027 (2016).

[156] A. González-Tudela and J. I. Cirac, arXiv preprint arXiv:1705.06677v1 (2017).

[157] A. González-Tudela and J. I. Cirac, arXiv preprint arXiv:1705.06673v1 (2017).

[158] P. Longo, P. Schmitteckert, and K. Busch, Phys. Rev. A **83**, 063828 (2011).

[159] B. Gaveau and L. S. Schulmann, Journal of Physics A **28**, 7359 (1995).

[160] D. Braak, Phys. Rev. Lett. **107**, 100401 (2011).

[161] M. Hirokawa and F. Hiroshima, arXiv preprint arXiv:1207.4020 (2012).

[162] E. Sánchez-Burillo, D. Zueco, L. Martín-Moreno, and J. J. García-Ripoll, Phys. Rev. A **96**, 023831 (2017).

[163] F. Lombardo, F. Ciccarello, and G. M. Palma, Phys. Rev. A **89**, 053826 (2014).

[164] S. Garmon, T. Petrosky, L. Simine, and D. Segal, Fortschritte der Physik **61**, 261 (2013).

[165] W. Greiner and J. Reinhardt, *Field Quantization* (Springer, 1996), ISBN 978-3540780489.

[166] M. E. Peskin and D. V. Schroeder, *An Introduction to Quantum Field Theory* (ABP, 1995), ISBN 978-0201503975.

[167] L. A. Khalfin, Soviet Physics JETP **6**, 1053 (1958).

[168] C. B. Chiu, E. C. G. Sudarshan, and B. Misra, Phys. Rev. D **16**, 520 (1977).

[169] R. G. Winter, Physical Review **123**, 1503 (1961).

[170] G. García-Calderón and J. Villavicencio, Phys. Rev. A **73**, 062115 (2006).

[171] S. Longhi, Phys. Rev. Lett **97**, 110402 (2006).

[172] A. D. Dente, R. A. Bustos-Marún, and H. M. Pastawski, Phys. Rev. A **78**, 062116 (2008).

[173] S. Longhi, Phys. Rev. A **74**, 063826 (2006).

[174] *A talk with Lisa Randall*, `archive.boston.com/bostonglobe/ideas/articles/2008/12/14/a_talk_with_lisa_randall/`.

[175] S. Xu and S. Fan, Phys. Rev. A **95**, 063809 (2017).

[176] S. Weinberg, in *Conceptual foundations of quantum field theory. Proceedings, Symposium and Workshop, Boston, USA, March 1-3, 1996* (1996), pp. 241–251, `hep-th/9702027`.

[177] E. H. Wichmann and J. H. Crichton, Phys. Rev. **132**, 2788 (1963).

[178] S. Weinberg, *The Quantum Theory of Fields*, vol. 1 (Cambridge University Press, Cambridge, 1995), ISBN 9781139644167.

[179] E. H. Lieb and D. W. Robinson, Communications in Mathematical Physics **28**, 251 (1972).

[180] S. Bravyi, M. B. Hastings, and F. Verstraete, Phys. Rev. Lett. **97**, 050401 (2006).

[181] B. Nachtergaele and R. Sims, Communications in Mathematical Physics **265**, 119 (2006).

[182] M. Cramer, A. Serafini, and J. Eisert, arXiv:0803.0890v2 (2008).

[183] M. B. Hastings, Journal of Statistical Mechanics: Theory and Experiment **2007**, P08024 (2007).

[184] E. Sánchez-Burillo, A. Cadarso, L. Martín-Moreno, J. J. García-Ripoll, and D. Zueco, arXiv preprint arXiv:1705.09094v1 (2017).

[185] E. Sánchez-Burillo, J. García-Ripoll, L. Martín-Moreno, and D. Zueco, Faraday discussions **178**, 335 (2015).

[186] M. B. Hastings and T. Koma, Commun. Math. Phys. **265**, 781 (2006).

[187] B. Nachtergaele, H. Raz, B. Schlein, and R. Sims, Journal of Statistical Physics **286**, 1073 (2009).

[188] D. Poulin, Phys. Rev. Lett. **104**, 190401 (2010).

[189] B. Barthel and M. Kliesch, Phys. Rev. Lett. **108**, 230504 (2012).

[190] J. Jünemann, A. Cadarso, D. Pérez-García, A. Bermúdez, and J. García-Ripoll, Phys. Rev. Lett. **111**, 230404 (2013).

[191] E. Sánchez-Burillo, L. Martín-Moreno, J. J. García-Ripoll, and D. Zueco, Phys. Rev. A **94**, 053814 (2016).

[192] R. H. Dicke, Phys. Rev. **93**, 99 (1954).

[193] T. Hümmer, G. Reuther, P. Hänggi, and D. Zueco, Phys. Rev. A **85**, 052320 (2012).

[194] J.-T. Shen and S. Fan, Phys. Rev. Lett. **98**, 153003 (2007).

[195] D. Roy, Phys. Rev. A **87**, 063819 (2013).

[196] T. Shi, S. Fan, and C. P. Sun, Phys. Rev. A **84**, 063803 (2011).

[197] M. A. Benarde, *Our Precarious Habitat (Second Edition)* (W. W. Norton & Company, 1973), ISBN 0393063607.

[198] M. O. Scully and M. S. Zubairy, *Quantum Optics* (Cambridge University Press, 1997).

[199] P. Kolchin, R. F. Oulton, and X. Zhang, Phys. Rev. Lett. **106**, 113601 (2011).

[200] S. Xu, E. Rephaeli, and S. Fan, Phys. Rev. Lett. **111**, 223602 (2013).

[201] T. Shi and C. P. Sun, Phys. Rev. B **79**, 205111 (2009).

[202] V. I. Yudson and P. Reineker, Phys. Rev. A **78**, 052713 (2008).

[203] H. Zheng, D. J. Gauthier, and H. U. Baranger, Phys. Rev. A **82**, 063816 (2010).

[204] H. Zheng, D. J. Gauthier, and H. U. Baranger, Phys. Rev. Lett. **107**, 223601 (2011).

[205] H. Zheng, D. J. Gauthier, and H. U. Baranger, Phys. Rev. A **85**, 043832 (2012).

[206] H. Zheng and H. U. Baranger, Phys. Rev. Lett. **110**, 113601 (2013).

[207] Y.-L. L. Fang, H. Zheng, and H. U. Baranger, EPJ Quantum Technology **1**, 3 (2014).

[208] D. Roy, Phys. Rev. Lett. **106**, 053601 (2011).

[209] D. Roy, Phys. Rev. A **83**, 043823 (2011).

[210] J.-Q. Liao and C. K. Law, Phys. Rev. A **82**, 053836 (2010).

[211] Şükrü Ekin Kocabaş, Phys. Rev. A **93**, 033829 (2016).

[212] B. Peropadre, J. Lindkvist, I. C. Hoi, C. M. Wilson, J. J. García-Ripoll, P. Delsing, and G. Johansson, New Journal of Physics **15**, 035009 (2013).

[213] E. Rephaeli and S. Fan, Phys. Rev. Lett. **108**, 143602 (2012).

[214] M. F. Yanik, S. Fan, M. Soljačić, and J. D. Joannopoulos, Optics Letters **28**, 2506 (2007).

[215] D. E. Chang, A. S. Sørensen, E. A. Demler, and M. D. Lukin, Nature Physics **3**, 807 (2007).

[216] L. Zhou, H. Dong, Y. X. Liu, C. P. Sun, and F. Nori, Phys. Rev. A **78**, 063827 (2008).

[217] D. Zueco, F. Galve, S. Kohler, and P. Hänggi, Phys. Rev. A **80**, 042303 (2009).

[218] L. Zhou, L.-P. Yang, Y. Li, and C. P. Sun, Phys. Rev. Lett. **111**, 103604 (2013).

[219] J. Lu, L. Zhou, L.-M. Kuang, and F. Nori, Phys. Rev. A **89**, 013805 (2014).

[220] G. Romero, J. J. García-Ripoll, and E. Solano, Phys. Rev. Lett. **102**, 173602 (2009).

[221] B. Peropadre, G. Romero, G. Johansson, C. M. Wilson, E. Solano, and J. J. García-Ripoll, Phys. Rev. A **84**, 063834 (2011).

[222] P. Longo, P. Schmitteckert, and K. Busch, Journal of Optics A: Pure and Applied Optics **11**, 114009 (2009).

[223] F. Guinea, E. Bascones, and M. J. Calderon, American Institute of Physics Conference Series **438**, 1 (1998).

[224] Y. D. Chong, L. Ge, H. Cao, and A. D. Stone, Phys. Rev. Lett. **105**, 053901 (2010).

[225] K. Koshino, K. Inomata, T. Yamamoto, and Y. Nakamura, Phys. Rev. Lett. **111**, 153601 (2013).

[226] K. Inomata, K. Koshino, Z. R. Lin, W. D. Oliver, J. S. Tsai, Y. Nakamura, and T. Yamamoto, Phys. Rev. Lett. **113**, 063604 (2014).

[227] Y.-x. Liu, J. Q. You, L. F. Wei, C. P. Sun, and F. Nori, Phys. Rev. Lett. **95**, 087001 (2005).

[228] Y.-x. Liu, H.-C. Sun, Z. H. Peng, A. Miranowicz, J. S. Tsai, and F. Nori, Scientific Reports **4**, 7289 (2014).

[229] S. R. Sathyamoorthy, A. Bengtsson, S. Bens, M. Simoen, P. Delsing, and G. Johansson, Phys. Rev. A **93**, 063823 (2016).

[230] K. Koshino, Phys. Rev. A **79**, 013804 (2009).

[231] P. Král and M. Shapiro, Phys. Rev. Lett. **87**, 183002 (2001).

[232] Y. Chen, C. Neill, P. Roushan, N. Leung, M. Fang, R. Barends, J. Kelly, B. Campbell, Z. Chen, B. Chiaro, et al., Phys. Rev. Lett. **113**, 220502 (2014).

[233] É. Dumur, B. Küng, A. K. Feofanov, T. Weissl, N. Roch, C. Naud, W. Guichard, and O. Buisson, Phy. Rev. B **92**, 020515 (2015).

[234] J. Koch, T. Yu, J. Gambetta, A. Houck, D. Schuster, J. Majer, A. Blais, M. Devoret, S. Girvin, and R. Schoelkopf, Phys. Rev. A **76**, 042319 (2007).

[235] R. Paškauskas and L. You, Phys. Rev. A **64**, 042310 (2001).

[236] A. Muthukrishnan, G. S. Agarwal, and M. O. Scully, Phys. Rev. Lett. **93**, 093002 (2004).

[237] D. Zueco, J. J. Mazo, E. Solano, and J. J. García-Ripoll, Phys. Rev. B **86**, 024503 (2012).

[238] S. J. Srinivasan, A. J. Hoffman, J. M. Gambetta, and A. A. Houck, Phys. Rev. Lett. **106** (2011).

[239] D. Jaksch, J. I. Cirac, P. Zoller, S. L. Rolston, R. Côté, and M. D. Lukin, Phys. Rev. Lett. **85**, 2208 (2000).

[240] M. D. Lukin, M. Fleischhauer, R. Cote, L. M. Duan, D. Jaksch, J. I. Cirac, and P. Zoller, Phys. Rev. Lett. **87**, 037901 (2001).

[241] M. Saffman, T. G. Walker, and K. Mølmer, Rev. Mod. Phys. **82**, 2313 (2010).

[242] S. E. Harris, Phys. Today **50(7)**, 36 (1997).

[243] D. D. Smith, H. Chang, K. A. Fuller, A. T. Rosenberger, and R. W. Boyd, Phys. Rev. A **69**, 063804 (2004).

[244] D. Witthaut and A. S. Sørensen, New Journal of Physics **12**, 043052 (2010).

[245] M. Pletyukhov and V. Gritsev, New Journal of Physics **14**, 095028 (2012).

[246] J. R. Taylor, *The Quantum Theory on Nonrelativistic Collisions* (John Wiley & Sons, Inc., Boulder, Colorado, 1972).

[247] P. Zhou and S. Swain, Phys. Rev. Lett. **77**, 3995 (1996).

[248] Y.-L. L. Fang and H. U. Baranger, Physica E **78**, 92 (2016).

[249] J. L. O'Brien, Science **318**, 1567 (2007).

[250] T. D. Ladd, F. Jelezko, R. Laflamme, Y. Nakamura, C. Monroe, and J. L. O'Brien, Nature **464**, 45 (2010).

[251] H. Zheng, D. J. Gaunthier, and H. U. Baranger, Phys. Rev. Lett. **111**, 090502 (2013).

[252] W. Gao, P. Fallahi, E. Togan, A. Delteil, Y. Chin, J. Miguel-Sanchez, and A. Imamoğlu, Nature Communications **4** (2013).

[253] A. Delteil, Z. Sun, W.-b. Gao, E. Togan, S. Fält, and A. Imamoğlu, Nature Physics **12**, 218 (2015).

[254] A. Delteil, Z. Sun, S. Fält, and A. Imamoğlu, Phys. Rev. Lett. **118**, 177401 (2017).

[255] R. Johne and A. Fiore, Phys. Rev. A **86**, 063815 (2012).

[256] Q. A. Turchette, C. J. Hood, W. Lange, H. Mabuchi, and H. J. Kimble, Phys. Rev. Lett. **75**, 4710 (1995).

[257] L.-M. Duan and H. J. Kimble, Phys. Rev. Lett. **92** (2004).

[258] E. Knill, R. Laflamme, and G. J. Milburn, Nature **409**, 46 (2001).

[259] R. H. Lehmberg, Phys. Rev. A **2**, 883 (1970).

[260] G.-Y. Chen, N. Lambert, C.-H. Chou, Y.-N. Chen, and F. Nori, Phys. Rev. B **84**, 045310 (2011).

[261] A. González-Tudela, D. Martín-Cano, E. Moreno, L. Martín-Moreno, C. Tejedor, and F. J. García-Vidal, Phys. Rev. Lett. **106**, 020501 (2011).

[262] D. Martín-Cano, A. González-Tudela, L. Martín-Moreno, F. J. García-Vidal, C. Tejedor, and E. Moreno, Phys. Rev. B **84**, 235306 (2011).

[263] K. Lalumière, B. C. Sanders, A. F. van Loo, A. Fedorov, A. Wallraff, and A. Blais, Phys. Rev. A **88**, 043806 (2013).

[264] C. Gonzalez-Ballestero, E. Moreno, and F. J. Garcia-Vidal, Phys. Rev. A **89**, 042328 (2014).

[265] V. Paulisch, A. González-Tudela, H. J. Kimble, and J. I. Cirac, New Journal of Physics **19**, 043004 (2017).

[266] P. Facchi, S. Pascazio, F. V. Pepe, and K. Yuasa, arXiv preprint arXiv:1705.01967v1 (2017).

[267] B. Maddox, *Rosalind Franklin: The Dark Lady of DNA* (Perennial, 2003).

[268] R. A. Horn and C. R. Johnson, *Matrix Analysis* (Cambridge University Press, Cambridge, 1985).

[269] F. Olver, *Asymptotics and special functions.* (Academic press, New York, 2014).